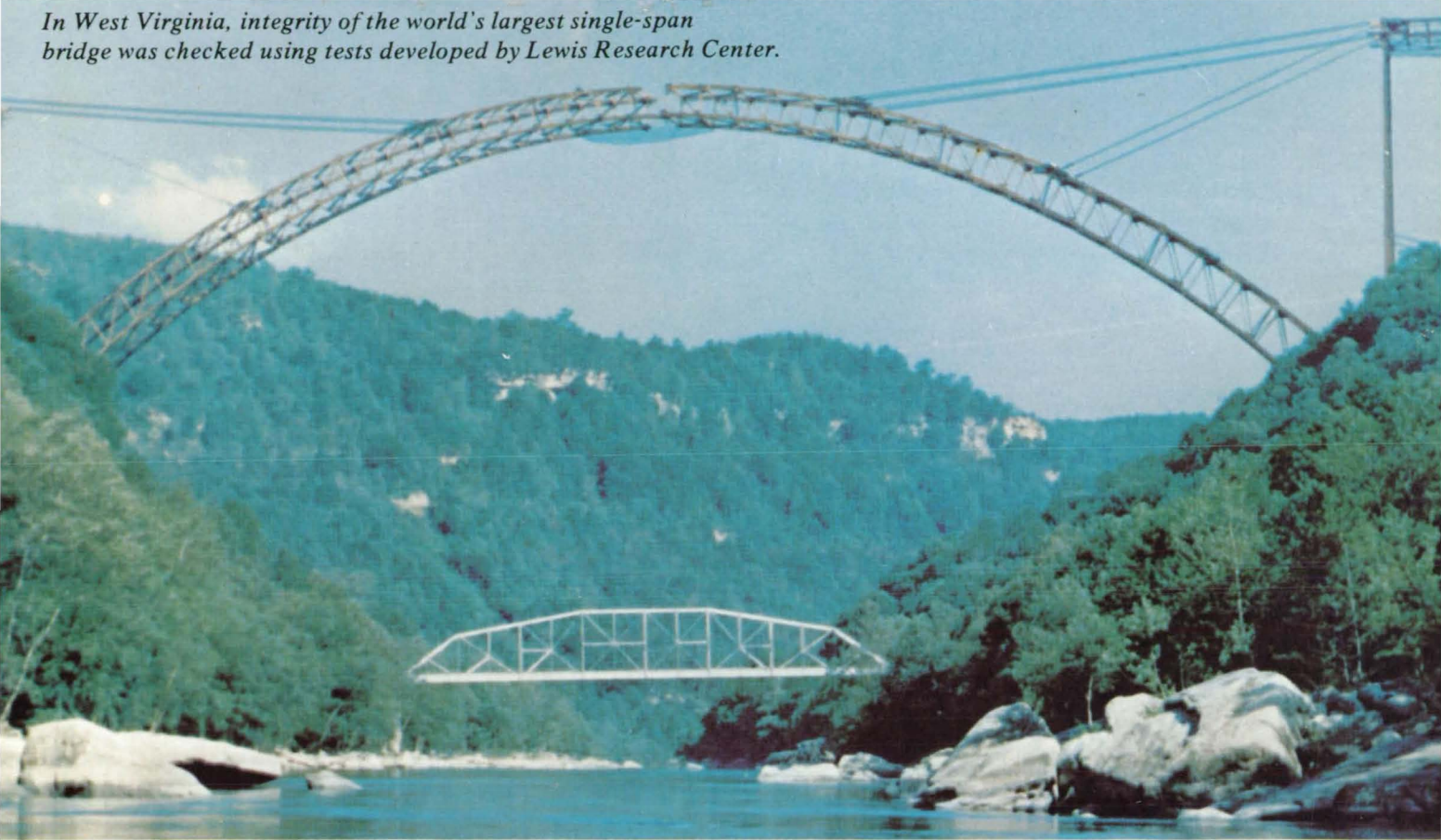


NASA Tech Briefs

National
Aeronautics and
Space
Administration

In West Virginia, integrity of the world's largest single-span bridge was checked using tests developed by Lewis Research Center.



A flame-retarding coating, used for manned-spacecraft shields, helps protect this tank farm from fire.

About the NASA Technology Utilization Program

The National Aeronautics and Space Act of 1958, which established NASA and the United States civilian space program, requires that "The Administration shall provide for the widest practicable and appropriate dissemination of information concerning its activities and the results thereof."

To help carry out this objective the NASA Technology Utilization (TU) Program was established in 1962. It offers a variety of valuable services to facilitate the transfer of aerospace technology to nonaerospace applications, thus assuring American taxpayers maximum return on their investment in space research; thousands of spinoffs of NASA research have already occurred in virtually every area of our economy.

The TU Program has worked for engineers, scientists, technicians, and businessmen. And it can work for you.

NASA Tech Briefs

Tech Briefs is published quarterly and is free to any U.S. citizen or organization. It is both a current-awareness medium and a problem-solving tool. Potential products ... industrial processes ... basic and applied research ... shop and lab techniques ... computer software ... new sources of technical data ... concepts ... you will find them all in NASA Tech Briefs. The first section highlights a few of the potential new products contained in Tech Briefs. The remainder of the volume is organized by technical category to help you quickly review new developments in your areas of interest. Finally, a subject index makes each issue a convenient permanent reference file.

Further Information on Innovations

Although many articles are complete in themselves, others are backed up by Technical Support Packages (TSP's). TSP's are available without charge and may be ordered by simply completing the enclosed TSP Request Card. Further information on some innovations is available for a nominal fee from other sources, as indicated at the ends of the articles. In addition, Technology Utilization Officers at NASA Field Centers will assist you directly when necessary. (See page A4.)

Patent Licenses

Many of the inventions described are under consideration for patents or have been patented by NASA. Unless NASA has decided not to apply for a patent, the patent status is described at the end of each article. For further information about the Patent Program see page A8.

Other Technology Utilization Services

To assist engineers, industrial researchers, business executives, city officials, and other potential users in applying space technology to their problems, NASA sponsors six Industrial Applications Centers. Their services are described on page A6. In addition, an extensive library of computer programs is available through COSMIC, the Technology Utilization Program's outlet for NASA-developed software. (See page A5.)

Applications Program

To help solve public-sector problems in such areas as safety, health, transportation, and environmental protection, NASA TU Applications Teams, staffed by professionals from a variety of disciplines, work with Federal agencies, local governments, and health organizations to identify critical problems amenable to technical solutions. Among their many significant contributions are a rechargeable heart pacemaker, a lightweight fireman's breathing apparatus, aids for the handicapped, and safer highways.

Reader Feedback

We hope you find the information in NASA Tech Briefs useful. A reader feedback card has been included because we want your comments and suggestions on how we can further help you apply NASA innovations and technology to your needs. Please use it, or if you need more space, write us a letter.

NASA TU Services

A3

Technology Utilization services that can assist you in learning about and applying NASA technology.



New Product Ideas

A9

A summary of selected innovations of value to manufacturers for the development of new products.



Tech Briefs

297

Electronic Components and Circuits



321

Electronic Systems



333

Physical Sciences



349

Materials



357

Life Sciences



369

Mechanics



389

Machinery



397

Fabrication Technology



409

Mathematics and Information Sciences



Subject Index

417

Items in this issue are indexed by subject; a cumulative index will be published yearly.



COVERS: The photographs on the front and back covers illustrate recent developments by NASA and its contractors that resulted in commercial and nonaerospace spinoffs. You can use the TSP Request Card at the end of this issue to find out more about "Fracture-Toughness Test Procedures" [Circle 48], the "Flame-Retarding Coating" [Circle 49], and the "Electronic Truck-Weighing System" [Circle 50].

About This NASA Publication

NASA Tech Briefs, a quarterly publication, is distributed free to U.S. citizens to encourage commercial application of U.S. space technology. For information on publications and services available through the NASA Technology Utilization Program, write to the Director, Technology Utilization Office, P. O. Box 8756, Baltimore/Washington International Airport, Maryland 21240.

"The Administrator of National Aeronautics and Space Administration has determined that the publication of this periodical is necessary in the transaction of the public business required by law of this Agency. Use of funds for printing this periodical has been approved by the Director of the Office of Management and Budget through December 31, 1977."

This document was prepared under the sponsorship of the National Aeronautics and Space Administration. Neither the United States Government nor any person acting on behalf of the United States Government assumes any liability resulting from the use of the information contained in this document, or warrants that such use will be free from privately owned rights.

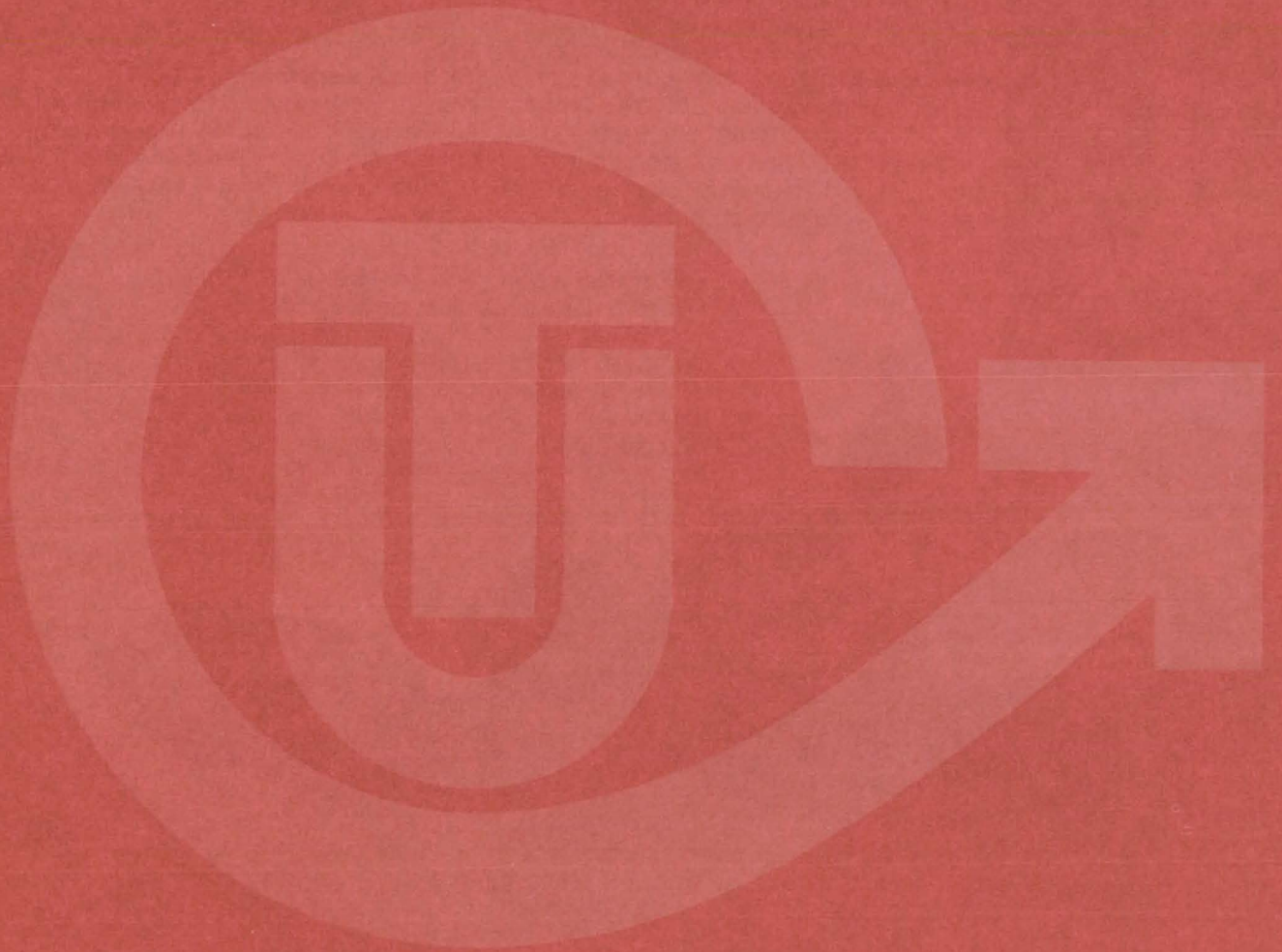
Change of Address

Change of Address: If you wish to have NASA Tech Briefs forwarded to your new address, use one of the Subscriptions cards enclosed in the back of this volume of NASA Tech Briefs. Be sure to check the appropriate box indicating change of address.

Communication Concerning Editorial Matter

For editorial comments or general communications about NASA Tech Briefs, you may use the self-addressed Feedback card in the back of NASA Tech Briefs, or write to: The Publications Manager, Technology Utilization Office (Code KT), NASA Headquarters, Washington, DC 20546. Technical questions concerning specific articles should be directed to the Technology Utilization Officer of the sponsoring NASA Center (addresses listed on page A4.)

NASA TU SERVICES



THE NASA TECHNOLOGY UTILIZATION OFFICERS

They will help you apply the innovations described in Tech Briefs.

The Technology Utilization Officer (TUU)

Each NASA Center has a Technology Utilization Officer — An applications engineer whose job is to help you make use of new technology developed at his center. He brings you the NASA Tech Briefs and other special publications, sponsors conferences, and arranges for expert assistance in solving technical problems.

Technical Assistance

Working together with NASA Scientists and Engineers and the Industrial Applications Centers, the center TUO's can answer specific questions about innovations and related NASA technology.

Technical Support Package (TSP's)

For many of the innovations described in Tech Briefs, the center TUO has prepared additional material that will help you in detailed evaluation and actual use or construction of the new technology. You may get TSP's free of cost by using the TSP Request Card or writing the center TUO.



Who to Contact. Of course, many technical questions about Tech Briefs are answered in the TSP's, but when no TSP is available, or you have further questions, write the Technology Utilization Officer at the center that sponsored the research at the address listed below.

Charles K. Kubokawa
Ames Research Center
Code AU: 230-2
Moffett Field, CA 94035
(415) 965-5554

Clinton T. Johnson
Hugh L. Dryden Flight Research Center
P. O. Box 273
Edwards, CA 93523
(805) 258-3311, Ext. 568

Donald S. Friedman
Goddard Space Flight Center
Code 704.1
Greenbelt, MD 20771
(301) 982-6242

John T. Wheeler
Johnson Space Center
Code AT3
Houston, TX 77058
(713) 483-3809

Raymond J. Cerrato
John F. Kennedy Space Center
Code SA-RTP
Kennedy Space Center, FL 32899
(305) 867-2780

John Samos
Langley Research Center
Mail Stop 139A
Hampton, VA 23665
(804) 827-3281

Paul Foster
Lewis Research Center
21000 Brookpark Rd.
Cleveland, OH 44135
(216) 433-4000, Ext. 6832

Aubrey D. Smith
Marshall Space Flight Center
Code AT01
Marshall Space Flight Center, AL 35812
(205) 453-2224

John C. Drane
NASA Resident Legal Office-JPL
4800 Oak Grove Drive
Pasadena, CA 91103
(213) 354-6420

Gilmore H. Trafford
Wallops Flight Center
Wallops Island, VA 23337
(804) 824-3411, Ext 201

Louis Mogavero, Director
Technology Utilization Office
Code KT
NASA Headquarters
Washington, DC 20546
(202) 755-3103

COSMIC

(Computer Software Management & Information Center)

AN ECONOMICAL SOURCE OF COMPUTER PROGRAMS DEVELOPED BY THE GOVERNMENT.

COSMIC is sponsored by NASA to give you access to over 1400 computer programs developed by NASA and the Department of Defense, and selected programs from other government agencies. It is one of the Nation's largest software libraries.

COSMIC charges very reasonable fees for programs to help cover part of their expenses—and NASA pays for the remainder. Programs generally cost from \$500 to \$1000, but a few are more expensive and many are less. Documentation is available separately and very inexpensively.

COSMIC collects and stores software packages, insures that they are complete, prepares special announcements (such as Tech Briefs), publishes an indexed software catalog, and reproduces programs for distribution. COSMIC helps customers to identify their software needs, follows up to determine the successes and problems, and provides updates and error corrections. In some cases, NASA engineers can offer guidance to users in installing or running a program.

COSMIC programs range from management (pert scheduling) to information science (retrieval systems) and computer operations (hardware and software). Hundreds of engineering programs perform such tasks as structural analysis, electronic circuit design, chemical analysis, and design of fluid systems. Others determine building energy requirements, optimize mineral exploration, and draw maps of water-covered areas using NASA satellite data. In fact, the chances are, if you use a computer, you can use COSMIC.

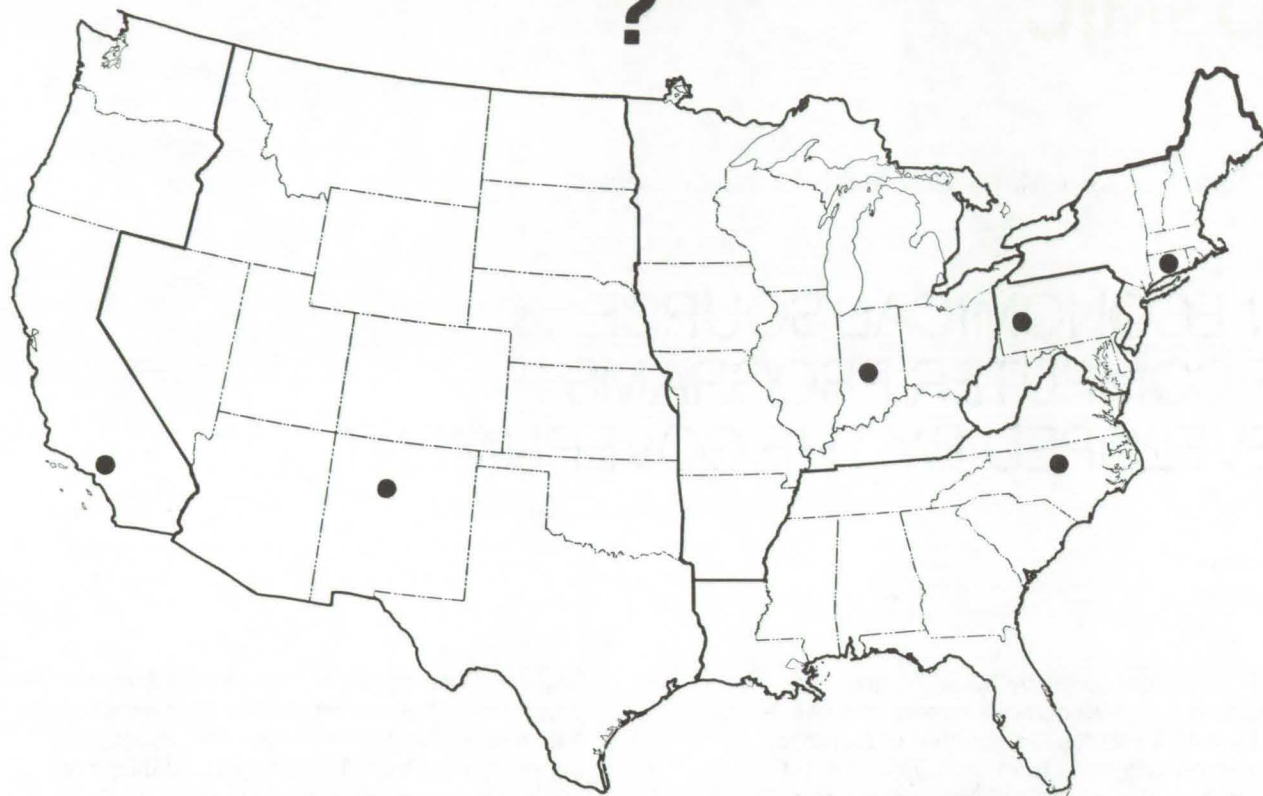
COSMIC is eager to help you get the programs you need. For more information about services or software available from COSMIC, fill out and mail the COSMIC Request Card in this issue.

COSMIC: Computer Software Management and Information Center

Suite 112, Barrow Hall, University of Georgia, Athens, Georgia 30602 Phone: (404) 542-3265

WHERE IS THE WORLD'S LARGEST BANK OF TECHNICAL DATA

?



It's in Bloomington and Pittsburgh, it's in Storrs, Connecticut and Research Triangle Park, North Carolina; and it's in Albuquerque and Los Angeles.

NASA IAC's — INDUSTRIAL

You can get more information and more data on more technical subjects through NASA's network of IAC's than anywhere else in the world. About 8,000,000 documents and growing at the rate of 50,000 more each month!

Major sources include:

- 750,000 NASA Technical Reports
- Selected Water Resources Abstracts
- NASA Scientific and Technical Aerospace Reports
- Air Pollution Technical Information Center
- NASA International Aerospace Abstracts
- Chem Abstracts Condensates
- Engineering Index
- Nuclear Science Abstracts
- NASA Tech Briefs
- Government Reports Announcements

and many other specialized files on food technology, textile technology, metallurgy, medicine, business, economics, social sciences, and physical science.

The IAC's are one of the most economical ways of staying competitive in today's world of exploding technology. The help available from the network ranges from literature searches through expert technical assistance.

Literature Searches

Help in designing your search, typically from 30 to 300 abstracts in as narrow or broad an area as you need, and complete reports when you need them. The most complete "search before research" available!

Current Awareness

Consult with our applications engineers to design your personal program — selected monthly or quarterly abstracts on new developments in your speciality. It's like having your own journal!

Technical Assistance

Our applications engineers will help you evaluate and apply your literature-search results. They can help find answers to your technical problems and put you in touch with scientists and engineers at NASA Field Centers.

To obtain more information about how NASA's IAC's can help you — Check the IAC box on the TSP Request Card in this issue, Or write or call the IAC nearest you.

APPLICATIONS CENTERS

How to get reports and other documents discussed in this issue of Tech Briefs

Many of the innovations in Tech Briefs are described in detail in reports available at a reasonable cost through one or more of the IAC's. To order a report, call or write the IAC referenced at the end of the Tech Brief article at the address below. Be sure to list the titles and accession numbers (N76-..., N75-..., etc.) of those you wish to purchase.

Aerospace Research Application Center (ARAC)
Indiana University-Purdue University at Indianapolis
1201 E. 38th St.
Indianapolis, IN 46205
E. Guy Buck, Director
(317) 264-4644

Knowledge Availability Systems Center (KASC)
University of Pittsburgh
Pittsburgh, PA 15260
Dr. Edmond Howie, Director
(412) 624-5211

New England Research Application Center (NERAC)
Mansfield Professional Park
Storrs, CT 06268
Dr. Daniel U. Wilde, Director
(203) 486-4533

North Carolina Science & Technology
Research Center (NC/STRC)
P. O. Box 12235
Research Triangle Park, NC 27709
Peter J. Chenery, Director
(919) 549-0671

Technology Application Center (TAC)
University of New Mexico
Albuquerque, NM 87131
Stanley A. Morain, Director
(505) 277-4000

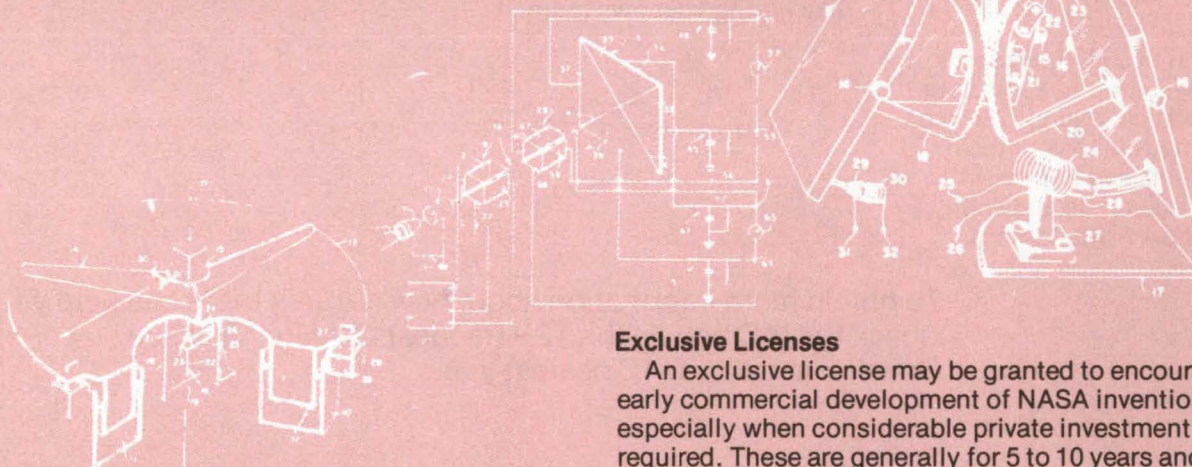
Western Research Application Center (WESRAC)
901 Exposition Boulevard, Room 205
University of Southern California
University Park
Los Angeles, CA 90007
Radford King, Director
(213) 741-6132

NASA INVENTIONS AVAILABLE FOR LICENSING

Over 3,500 NASA inventions are available for licensing in the United States - both exclusive and nonexclusive.

Nonexclusive Licenses

Nonexclusive licenses for commercial use are encouraged to promote competition and to achieve the widest use of inventions. They must be used by a negotiated target date but are usually royalty free.



Exclusive Licenses

An exclusive license may be granted to encourage early commercial development of NASA inventions, especially when considerable private investment is required. These are generally for 5 to 10 years and usually require royalties based on sales or use.

The NASA patent licensing program also provides for licensing of NASA-owned foreign patents. In addition to inventions described in Tech Briefs, "NASA Patent Abstract Bibliography," containing abstracts of all NASA inventions, can be purchased from: National Technical Information Service, Springfield, Va., 22161. This document is updated semi-annually.

Patent Licenses and the NASA Tech Brief

Many of the inventions reported in Tech Briefs are patented or are under consideration for a patent at the time they are published. When this is the case, the current patent status is described at the end of the article; otherwise, there is no statement about patents. **If you want to know more about the patent program or are interested in license for a particular invention, write the Patent Counsel at the NASA Field Center that sponsored the research. Be sure to refer to the NASA reference number in parenthesis at the end of the Tech Brief.**

Robert F. Kempf
NASA Headquarters, Code GP
400 Maryland Ave., S.W.
Washington, DC 20546
(202) 755-3932

Darrell G. Brekke
Ames Research Center
Mail Code: 200-11A
Moffett Field, CA 94035
(415) 965-5104

John O. Tresansky
Goddard Space Flight Center
Mail Code: 204
Greenbelt, MD 20771
(301) 982-2351

Marvin F. Matthews
Lyndon B. Johnson Space Center
Mail Code: AM
Houston, TX 77058
(713) 483-4871

James O. Harrell
John F. Kennedy Space Center
Mail Code: SA-PAT
Kennedy Space Center, FL 32899
(305) 867-2544

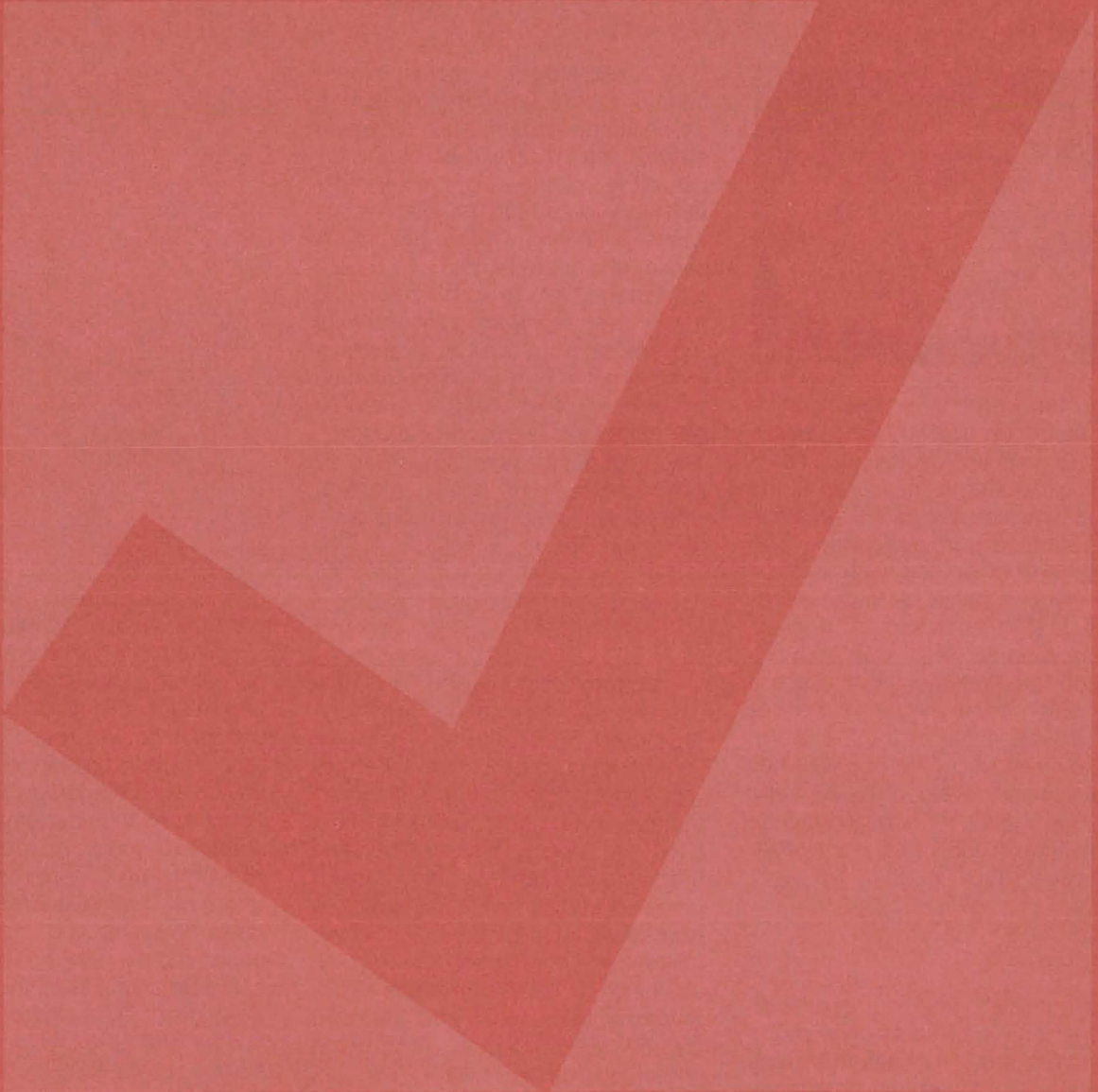
Howard J. Osborn
Langley Research Center
Mail Code: 313
Hampton, VA 23665
(804) 827-3725

Norman T. Musial
Lewis Research Center
Mail Code: 500-113
21000 Brookpark Road
Cleveland, OH 44135
(216) 433-4000

Leon D. Wofford, Jr.
Marshall Space Flight Center
Mail Code: CC01
Marshall Space Flight Center, AL 35812
(205) 453-0020

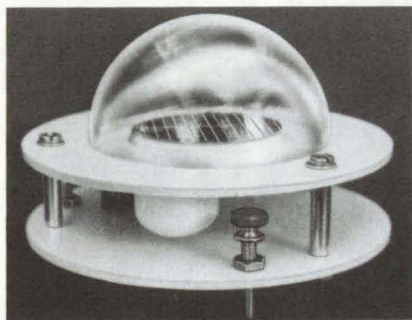
Monte F. Mott
NASA Resident Legal Office-JPL
4800 Oak Grove Drive
Pasadena, CA 91103
(213) 354-2700

NEW PRODUCT IDEAS



NEW PRODUCT IDEAS are just a few of the many innovations described in this issue of NASA Tech Briefs and having promising commercial applications. Each is discussed further on the referenced page in the appropriate section in this issue. If you are interested in developing a product from these or other NASA innovations, you can receive further technical information by requesting the TSP referenced at the end of the full-length article or by writing the Technology Utilization Office of the sponsoring NASA center (see page A4). NASA's patent-licensing program to encourage commercial development is described on page A8.

Solar Meter With Silicon Photocell



An instrument for measuring the light falling on a given spot uses a simple silicon photovoltaic cell as its sensing element. It measures all the light at the location: direct, scattered, reflected, or reradiated. The silicon cell is coated with a thick antireflecting layer of silicon monoxide and is enclosed in a glass dome. A large heat sink reduces temperature fluctuations, and accuracy within a few percentage points over a wide angle of the Sun's arc across the sky. The device has recently been developed as a kit and has been used in school science curriculums and club activities. (See page 299.)

Measuring Solar-Cell Quality

An automatic method for checking the quality of solar cells promises to make cell manufacture more economical, efficient, and reliable. The method is based on the measurement of minority-carrier lifetime — a good indicator of cell future performance. A cell, as it comes off the production line, is exposed to light, and its behavior is compared with that of a cell of known quality. If the new cell doesn't measure up, it is rejected. The method is fast and automatic and its flexible enough to be adapted to a variety of solar-cell types. (See page 371.)

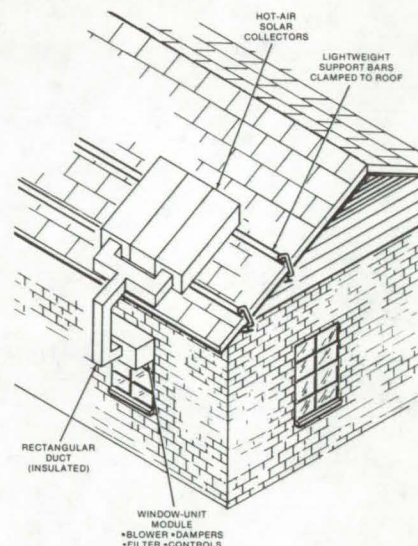
Solid-Sensor Technique for Detecting Ozone

A solid-sensor chemiluminescence technique for measuring ozone concentration is sensitive and easy to use. It should be useful for detecting ozone in the Earth's atmosphere and other environments where ozone may be a hazard. A sensor film coated with a solid (such as rubrene) reacts with ozone; the film is then heated to produce light (chemiluminescence) in proportion to the amount of reacted material on the sensor. Tests have shown that the technique is specific to ozone. Trace quantities as small as 1 to 10 ppm ozone have been detected, using only 10⁻⁴ gram of rubrene. (See page 351.)

Modular Multiapertures for Light Sensors

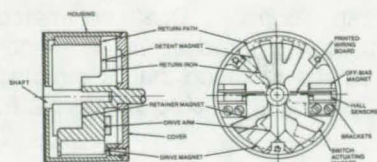
Electroforming is used in a new process for fabricating precisely-registered multiaperture masks for light-sensor systems. Developed for Sun and star sensors in spacecraft attitude-and-bearing control systems, the process can also be used for masks in automation and surveillance systems when a precise, wide-angle field of view is needed. Large and small apertures are prealigned on a beryllium copper substrate by photoresist and then are formed by electroplating outside the photoresist areas. Initially, the cavity between the apertures is filled with a conductive material. In the final module, the filler is dissolved to provide a fixed spacing between the aperture masks. A quartz window or discardable plastic disk can be placed over the openings to protect the edges and to keep contamination out of the module. (See page 403.)

Window-Mounted Auxiliary Solar Heater



A hot-air collector and a window unit that looks something like a simplified air-conditioner are proposed as a potentially-inexpensive and easily-installed solar-heating unit that could service one or two rooms. The proposed system should be easily fabricated and installed. It could probably be developed and marketed long before hot-water collectors and more complex systems for heating entire homes and other buildings find their way into general use. The hot-air collector could be clamped to the roof above a window. The window unit would contain the only moving part in the system, a fractional horsepower fan for directing airflow through the collector and into the room. Two thermocouples control the fan and actuate it when the temperature in the collectors is higher than in the room. By using lightweight prefabricated collectors and short pieces of duct, the system could be installed by homeowners without disturbing the existing roofing. (See page 344.)

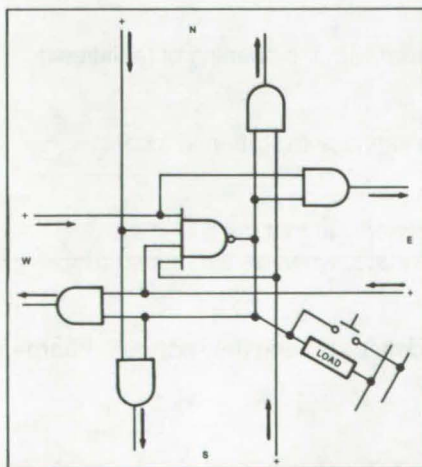
Magnetic Rotary and Toggle Switches



A family of rotary and toggle switches uses Hall-effect elements and magnets instead of mechanical contacts, detents, and springs. The switches provide fast positive action with no contact bounce. Since they eliminate contact wear, material fatigue, and arcing, they may be useful for high-duty-cycle applications such as television channel selectors. The single-chip Hall element includes a Hall transducer, an amplifier, and trigger circuitry. When the user flips the toggle or rotary drive, a magnet is moved in the vicinity of the Hall element to turn the switch on or off. The switches occupy the same or less panel space as conventional switches and can operate under severe conditions of temperature, vibration, and shock.

(See pages 300 and 301.)

Individual Control of Relays in a Matrix



A suggested control-logic approach for a crossbar matrix of relays would control individual relays and display their status. Readily available IC's are used, and simple SPST pushbutton switches are used for programming. The relay status indicators are LED's and reed relays

are used for isolation. The same panel is used for programming and for display with a light-indicating push-button at each x-y matrix intersection. The system is expandable, employs general-purpose multiple-pole relays, and could be equipped with program control.

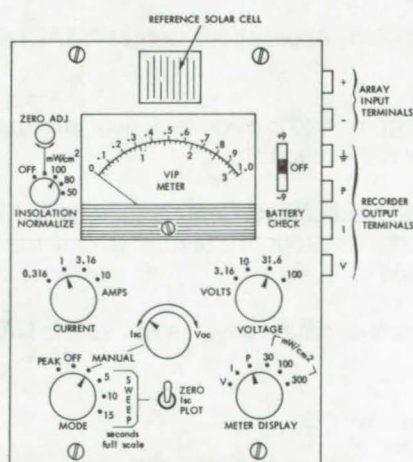
(See page 302.)

Flame and Acid Resistant Polyamide Fibers

An economical process can improve the flame resistance and resistance to acids of polyamide fibers, without modifying their colors or mechanical properties. The process improves the general safety of garments and other items made from polyamide fibers and makes them suitable for applications requiring exposure to an oxygen-rich atmosphere or corrosive acids. Halo-olefins are added to the surface of the fibers by photoaddition in a sealed chamber. Gas pressure, including that of the halo-olefin and a diluent, is around 1 atmosphere; temperatures may vary from 0° to 150° C. In addition to the fibers, the process could be used with films and other forms of polyamide.

(See page 353.)

Solar-Cell Measurements in the Field

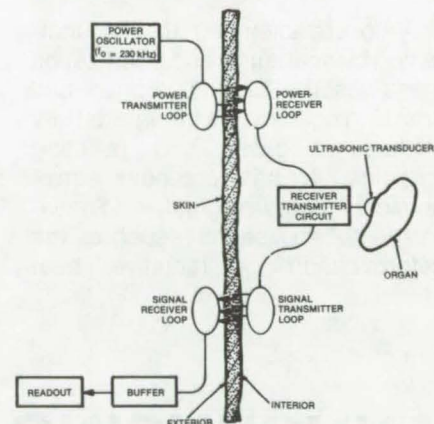


A portable instrument evaluates the performance of photovoltaic solar-cell arrays in the field as well as in the laboratory. The compact

instrument, which measures only 5 by 7 by 2 inches, contains circuitry that determines peak current, voltage, and power in a fraction of a second. A built-in reference solar cell is included to determine the ambient light level and to scale the array current up or down accordingly. Although designed primarily for solar cells, the instrument can be used for other dc sources, such as batteries and fuel cells.

(See page 372.)

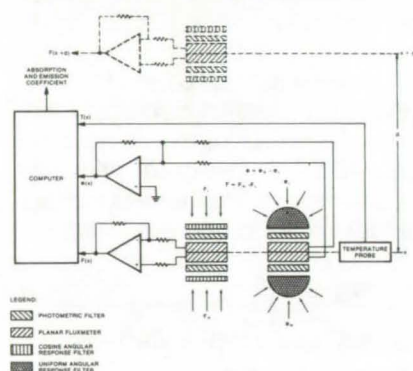
Batteryless Implanted Echosonometer



A miniature ultrasonic echosonometer implanted within a laboratory animal does not use a built-in active power source. Instead, it has an induction loop that couples power from an external RF power oscillator. Its output data are picked up by an external RF signal receiver. Thus, periodic battery reactivation or replacement is not necessary, and no leads project through the skin of the animal, avoiding infection that can arise at these sites. The echosonometer is therefore safe for long periods of real-time observation. The RF energy picked up by the power receiver loop is converted to a stream of high-voltage ultrasonic pulses that drive a piezoelectric crystal transducer stitched to the organ being studied. The echo signal is analyzed to provide an image of the organ.

(See page 361.)

Instrument Gives True Radiation Coefficients



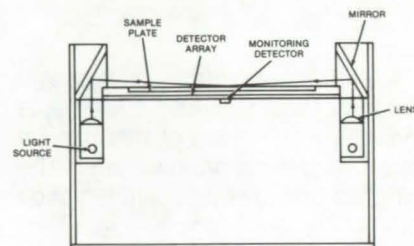
A novel radiometer that is unaffected by scattering and polarization measures the true absorption and emission coefficients for an arbitrary mixture of gases and polluting particles. It has potential astronomical, meteorological, and environmental applications, such as the determination of radiative heat

budget, aerosol relative concentration, and the morphology of cloud, haze, and fog formations. Other uses are in determining the "greenhouse" factor and the state of radiative equilibrium of a medium. The radiometer uses only simple experimental procedures; planar fluxmeters and angular response filters determine the net planar flux and net spherical flux in a selected region within the medium. These data along with a measurement of temperature can be coupled directly to a small computer for online calculation of the radiation coefficients. (See page 339.)

Dust-Contamination Monitor

A compact instrument gives an instantaneous reading of the accumulation of small particles on a glass plate. The instrument is sensitive to particles as small as 100

microns and should be adaptable to monitoring particulate air pollution or dust levels in semiconductor "clean rooms." Dual collimated light sources produce highly monochromatic radiation that is directed at a grazing angle onto a glass plate.



Dust particles on the plate reflect the light at a sharp angle where it is intercepted by an array of light detectors. The instrument measures only about 10 by 7 by 4 inches, consumes only 14 watts of electrical power, and is sensitive to as few as seven 100-micron particles. (See page 308.)

ANNOUNCING . . .

A NEW NASA TECHNOLOGY UTILIZATION SERVICE in Cooperation With STATE GOVERNMENTS

NASA recently inaugurated a State Technology Applications Center (STAC) program with the opening of facilities in Florida and Kentucky.

The purpose of the experimental STAC program is to provide technical information services to state and local government agencies as well as to industry within each state.

The STAC's differ from the NASA Industrial Applications Centers (see page A7) primarily in that the STAC's are integrated into existing state technical assistance programs and serve only the host state, whereas the Industrial Applications Centers serve multistate regions.

The STAC's have access to several commercial data bases, as well as the NASA data base, and they normally charge a fee for their services.

Persons wishing **further information** should write to:

In Florida

NASA/Florida State Technology Applications Center (STAC)
311 Weil Hall
University of Florida
Gainesville, Florida 32611

or phone, Gainesville: (904) 392-6760
Orlando: (305) 275-2706
Tampa: (813) 974-2499

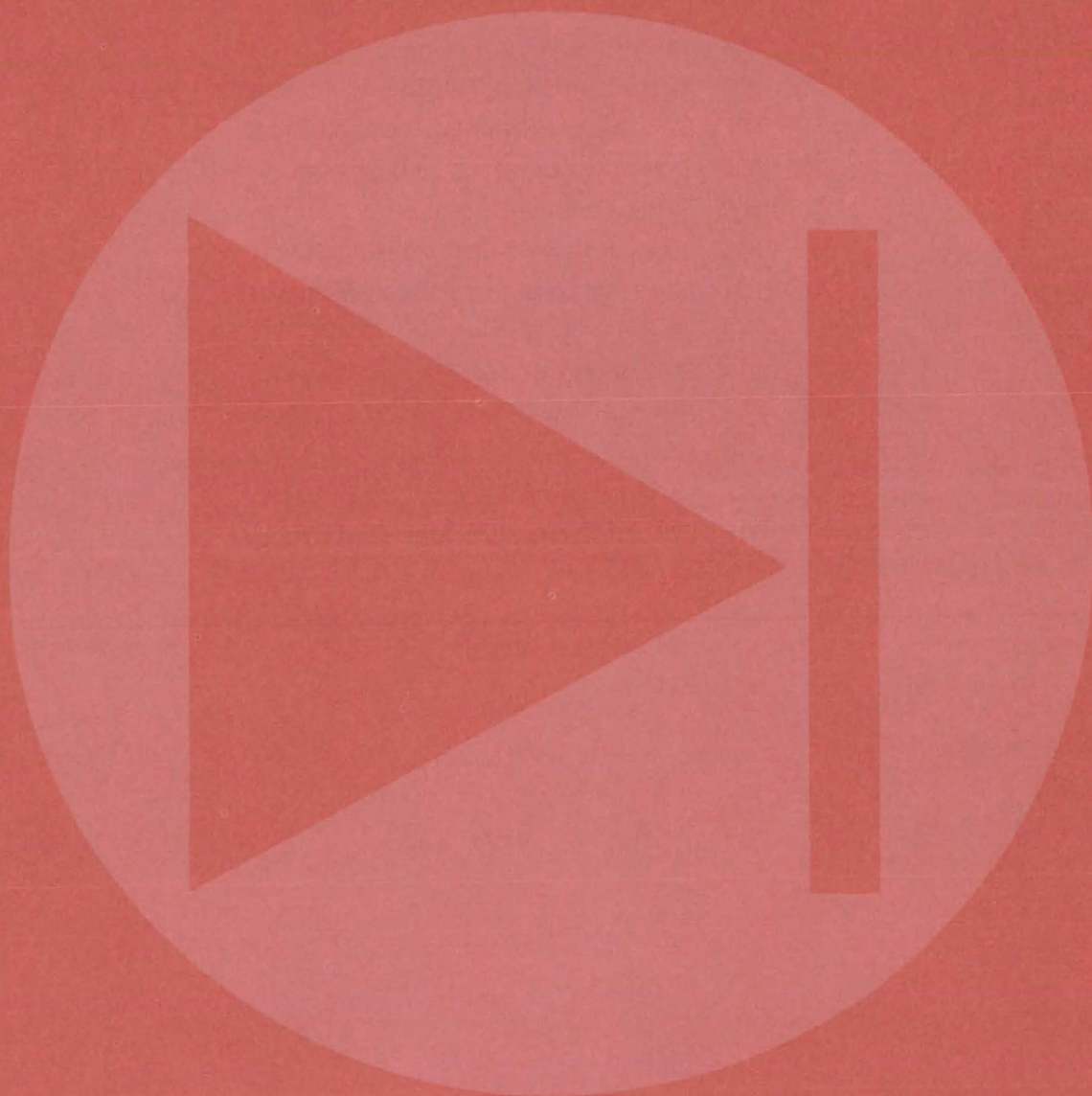
or contact the local State Department of Commerce
Business Development Representative

In Kentucky

NASA/University of Kentucky State Technology Applications Program (STAP)
109 Kinkead Hall
University of Kentucky
Lexington, Kentucky 40506

phone: (606) 258-4632

Electronic Components and Circuits



Hardware, Techniques, and Processes

- 299 Solar Meter With Silicon Photocell
- 300 Hall-Effect Toggle Switch
- 301 Magnetic Rotary Switch
- 302 Individual Control of Relays in a Matrix
- 304 Versatile Solid-State Relay
- 305 Inexpensive Pulse-Train Converter Measures Analog Voltage
- 307 Extrasensitive Phase-Locked-Loop Circuit
- 308 Capacitive Connectors for Digital-Data Lines
- 309 Simple Constant-Current-Regulated Power Supply
- 310 Inexpensive Solid-State Monitoring Circuit
- 311 Bias-Field Equalizer for Bubble Memories
- 312 Double-Duty Loudspeaker
- 313 DC Transformer Uses Magnetoresistors
- 314 Precision Voltage Division Without Precision Parts
- 316 Low-Inductance Bus Lines
- 318 Low-Insertion-Resistance Current Monitor
- 318 Op-Amp Gyrator Simulates High Q Inductor

Books and Reports

- 320 Safe Handling Practices for Electrostatic-Sensitive Devices

Solar Meter With Silicon Photocell

Device measures total insolation accurately over a wide solar arc.

Caltech/JPL, Pasadena, California

An instrument for measuring the Sun's energy falling on a given spot on the Earth uses a simple silicon photovoltaic cell as its sensing element. The instrument — a pyranometer — measures all the light at the location, whether direct sunlight or light that has been scattered, reflected, or reradiated from the surroundings, clouds, or the atmosphere itself.

The silicon cell is thickly coated with an antireflection layer of silicon monoxide to ensure that it absorbs virtually all the light falling on it. The

cell is enclosed in a glass dome (see Figure 1). The combination of the dome, the antireflective layer, and a large photovoltaic surface makes the instrument accurate over a wide angle of the Sun's arc across the sky. It is accurate within a few percentage points as the Sun's angle varies from $+65^\circ$ to -65° from the vertical.

The cell is 2 inches (5 cm) in diameter and generates about 0.5 volt. The current varies directly with the light input. Thus the voltage measured by a voltmeter across the

cell shunt resistor corresponds to the light level (see Figure 2).

Although the cell output voltage varies with temperature, the instrument is designed to keep such variations to a minimum. The reference temperature is 28°C . If the cell were allowed to heat up to 60°C , its readings would be off by about 3 percent. However, the cell is mounted on a heat sink to keep it at or near the ambient temperature. The silicon photovoltaic device is suitable for general solar-energy monitoring and thermal-energy measurements as well as for insolation measurements.

Because silicon photovoltaic cells are somewhat color-sensitive and because the color of the light reaching the Earth's surface depends on the thickness of atmosphere, the instrument response is different at high noon from that in early morning or late afternoon. (The cell peak response is at a wavelength of 0.9 nanometer, well into the infrared region.) However, this variation in response does not introduce any serious error since the solar radiation is most intense during the midday hours; in the morning and afternoon, there is not a lot of radiation by comparison. A small correction factor can be applied to the data.

This device has recently been developed as a kit. Several schools have assembled the units and are incorporating the instrument in their science curriculum or club activities.

This work was done by Gilbert Yanow of Caltech/JPL. For further information, Circle 1 on the TSP Request Card.
NPO-14136

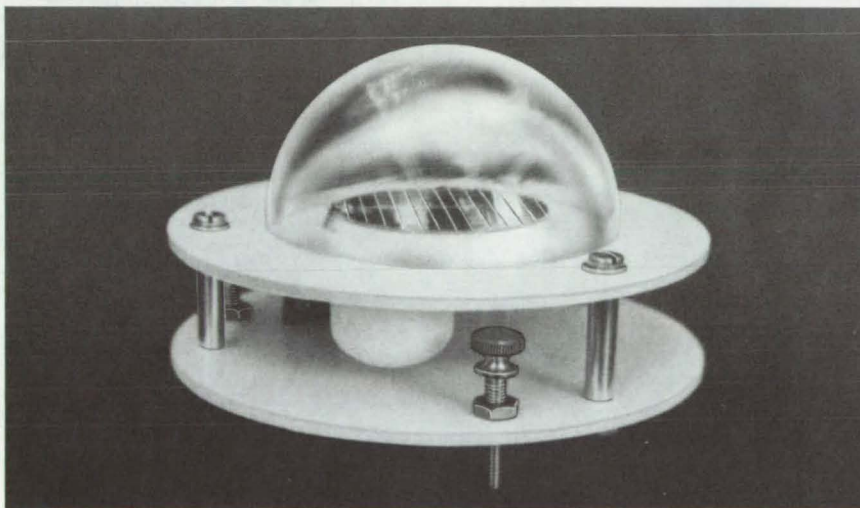


Figure 1. Glass Dome Protects Silicon Cell while large heat sink (white disks) minimizes temperature rise.

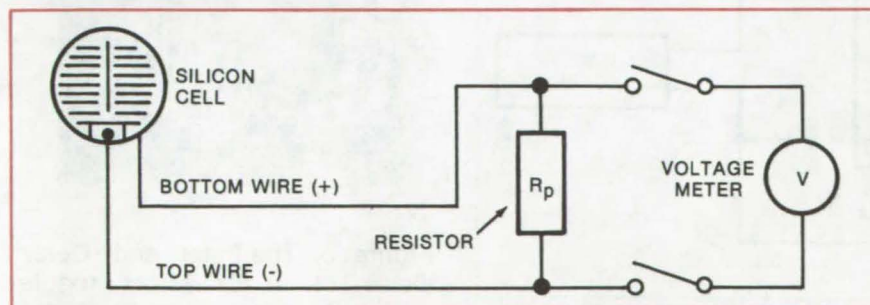


Figure 2. The **Pyranometer Circuit** includes a silicon photocell with an output current proportional to total light energy it receives. Current produces a voltage drop across resistor, and drop is measured by voltage meter.

Hall-Effect Toggle Switch

Solid-state switching element eliminates problems of mechanical contacts and operates in severe environments.

Lyndon B. Johnson Space Center, Houston, Texas

Solid-state toggle switches that operate by the Hall effect eliminate the contact bounce, arcing, contamination, and slow operation inherent in switches containing mechanical contacts. The Hall-effect toggle switches perform the same switching functions as mechanical switches, occupy the same or less panel space, require only one power source (which is compatible with the load), and can operate

under severe conditions of temperature, vibration, and shock.

The Hall switch is an integrated chip consisting of a Hall transducer, an amplifier, and trigger circuitry. The Hall transducer is a semiconductor device that generates voltage as a function of control current and magnetic field (see Figure 1). As control current is passed along one axis of the semiconductor, the Hall voltage appears transverse to the

control current. The voltage level is a function of the magnetic flux passing through the chip perpendicular to both the control current and output voltage. The Hall transducer has a low output voltage — on the order of 50 millivolts — so an amplification stage is necessary between the transducer and switch output circuitry. The control current required for the Hall transducer is in the range from 5 to 20 milliamperes, and the Hall chip requires an operating power of approximately 30 milliwatts.

A typical current-sourcing solid-state toggle switch is shown in Figure 2. A permanent magnet (Alnico V, or equivalent) mounted in the toggle mechanism produces the magnetic field necessary to activate the Hall chip (see Figure 3). Logic-level switches (5 Vdc, 20 mA)

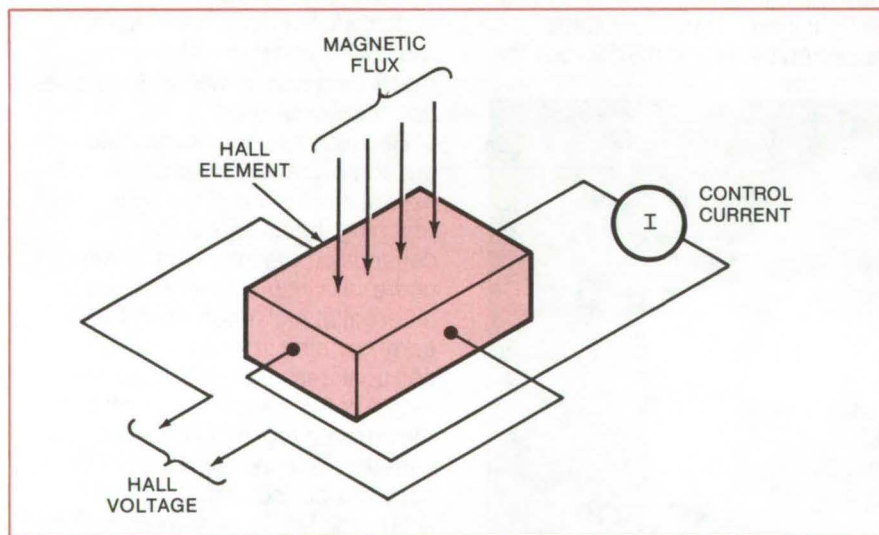


Figure 1. A **Hall-Effect Transducer** produces an output voltage when driven by a control current in the presence of a magnetic field.

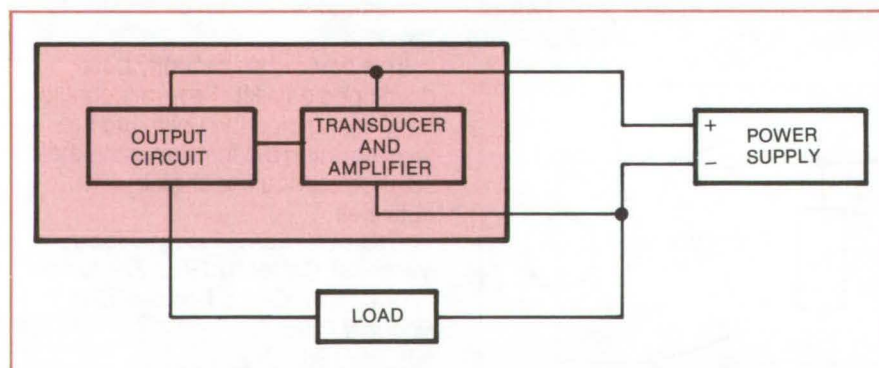


Figure 2. This **Hall-Effect Toggle Switch** for power applications uses a transistor for amplification of the transducer output; for logic-level applications, the Hall chip suffices by itself. A mechanical detent provides the tactile feel required by many operators.

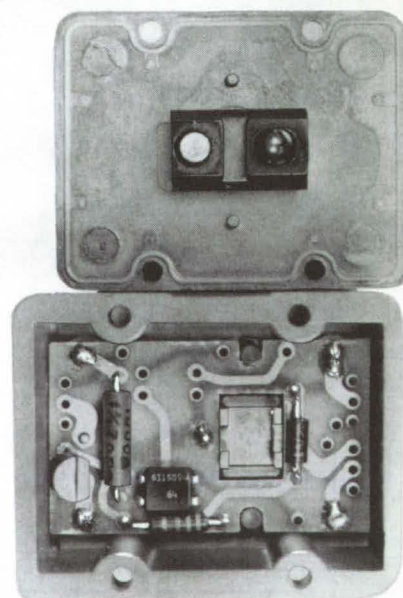


Figure 3. The **Inner and Outer Views** of a Hall-effect toggle switch are seen in this photograph. The switch occupies the same panel space as a standard mechanical toggle switch.

consist only of the Hall chip, while power switches (>20 mA) require an additional transistor external to the Hall chip for amplification. The Hall chip provides sufficient base drive to saturate the output transistor that carries the output load. Existing state-of-the-art permits maximum switching of 30 Vdc at 1.5 A at -54° to +25° C for power switches; logic-level switches operate at -54° to +85° C. Maximum operation for 5-Vdc switches is 0.300 A at -54° to +65° C.

The solid-state toggle switch can be mounted in existing mechanical-switch panel spaces. A mechanical

detent, although not needed for actuation, is housed in one cavity of the toggle case. The mechanical portion (detent) of the switch and tactile feel are provided by a standard toggle-switch contact design consisting of a plunger and a spring (Figure 3). The chip is capable of actuation through any nonmagnetic material, thereby simplifying the process of hermetically sealing the switch.

Because no moving contacts are required for switching, billions of operations at very high speeds are possible without the worry of de-

grading contacts. Contact bounce, arcing, and false actuation (or no actuation) because of contamination are all eliminated. Rise time is less than 10 microseconds.

Another Hall-effect switch is described in the following article (Magnetic Rotary Switch, MSC-16624).

This work was done by Shirley A. Chevalier and Aaron B. Olsen of Johnson Space Center and Charles A. Vittorio of Honeywell Inc. No further documentation is available.
MSC-16354

Magnetic Rotary Switch

Three different magnets are used to provide spring action, detent, and switch actuation.

Lyndon B. Johnson Space Center, Houston, Texas

Magnets replace the springs, detents, and mechanical contacts in a rotary switch of novel design. Electrical switching is performed by Hall-effect elements that are controlled by the presence or absence of magnet fields, so contact wear and resistance change are eliminated. The use of magnetic springs and magnetic detents eliminates

material wear and fatigue. Therefore this design may be useful in high-duty-cycle switches and control devices such as television channel selectors.

Figure 1 shows the switch assembly. The color-tinted rotary drive arm, which carries the drive magnets, is attached to the knob that the operator twists. The gray-

tinted rotary arm, which carries the magnets that can actuate the Hall elements, is free to turn about the same axis as the drive arm; the detent magnets normally hold this arm in the off position shown. When the operator turns the knob (and thus the drive arm), however, the drive magnet is moved toward the actuating magnet, and the opposing

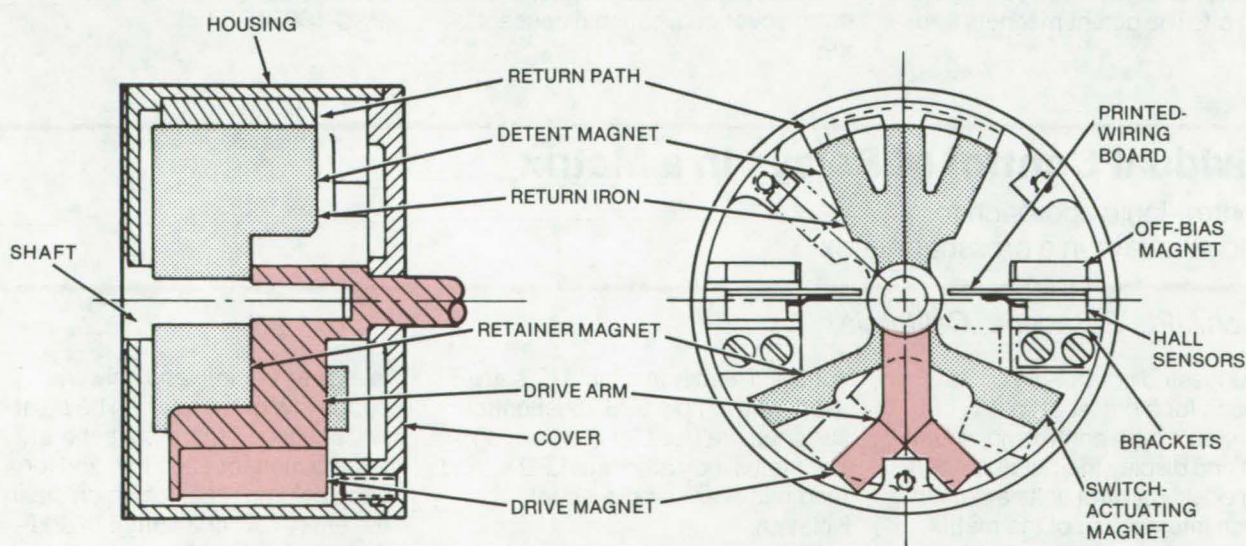


Figure 1. This **Magnetic Rotary Switch** uses a solid-state Hall-effect sensor to turn an electrical circuit on or off. The Hall device, normally held off by a small bias magnet, turns on when the strong actuating magnet comes into proximity. The drive magnet moves the actuating magnet against the restraint of a detent magnet.

(continued on next page)

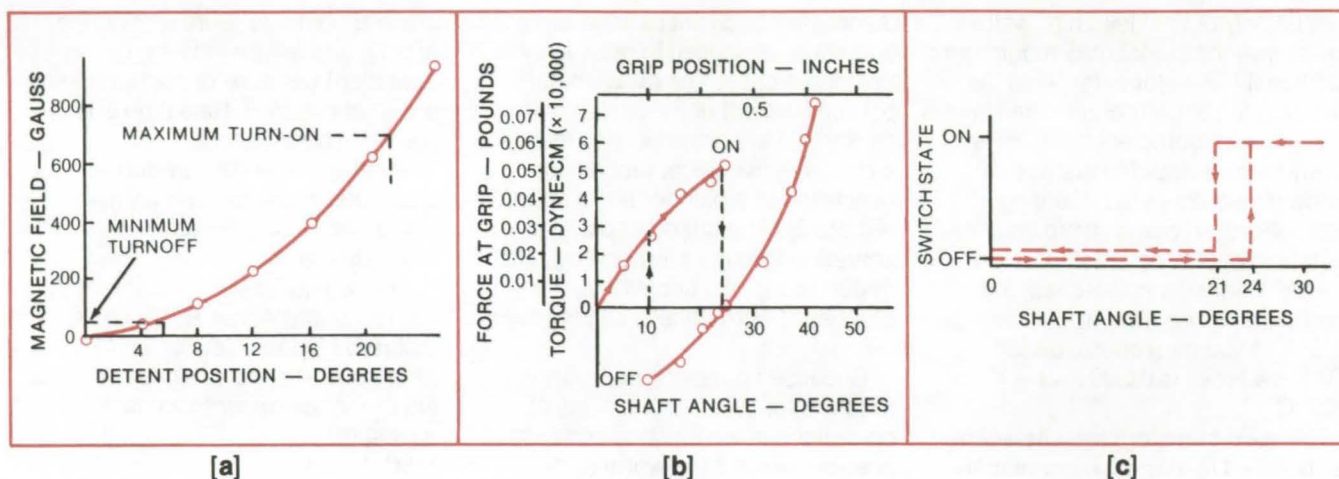


Figure 2. The **Performance Characteristics** of a developmental magnetic rotary switch show (a) magnetic field vs. detent position, (b) torque vs. shaft position, and (c) switch state vs. shaft position.

force between the two increases to overcome the restraining force of the detent. At this point the actuating-magnet arm snaps to the next detent position.

When the actuating magnets are in the position shown in Figure 1, the Hall-effect sensors are biased off by a small bias magnet. However, when the drive magnet forces the actuating magnet over the Hall device, the stronger field of the actuating magnet turns the sensor on. Continued travel of the drive magnet does not change the state of the Hall switch.

The action is identical when the shaft rotation is reversed to turn the switch off. The detent magnets and

return iron are designed to assure that the switch deactuates before the drive arm has returned to the neutral or off position. The turn-on and turnoff points can be adjusted by varying the size of the drive magnets, the angular relationship of the drive and actuating magnets, the size of the detent magnets, the airgap, and the number of poles in the detent. Figure 2 shows the characteristics of a developmental model of the magnetic rotary switch. The unit occupied a box 1-1/8 in. (2.9 cm) square and 13/16 in. (2 cm) deep, with a 0.09-in. (0.23-cm) shaft protruding 0.42 in. (1.1 cm).

Advantages of the magnetic switch over conventional concepts are:

- No mechanical coupled parts for the detent or drive mechanism and therefore no wear-out mode;
- Simplicity and low parts count, resulting in small size and low cost;
- Constant performance parameters (no mechanical fatiguing of springs or sliding surfaces);
- High reliability; and
- Elimination of contact bounce.

Another Hall-effect switch is described in the preceding article (Hall-Effect Toggle Switch, MSC-16354).

This work was done by John K. Sarkinen of Honeywell Inc. for Johnson Space Center. No further documentation is available.
MSC-16624

Individual Control of Relays in a Matrix

IC control-logic approach for individual relays in a crossbar matrix

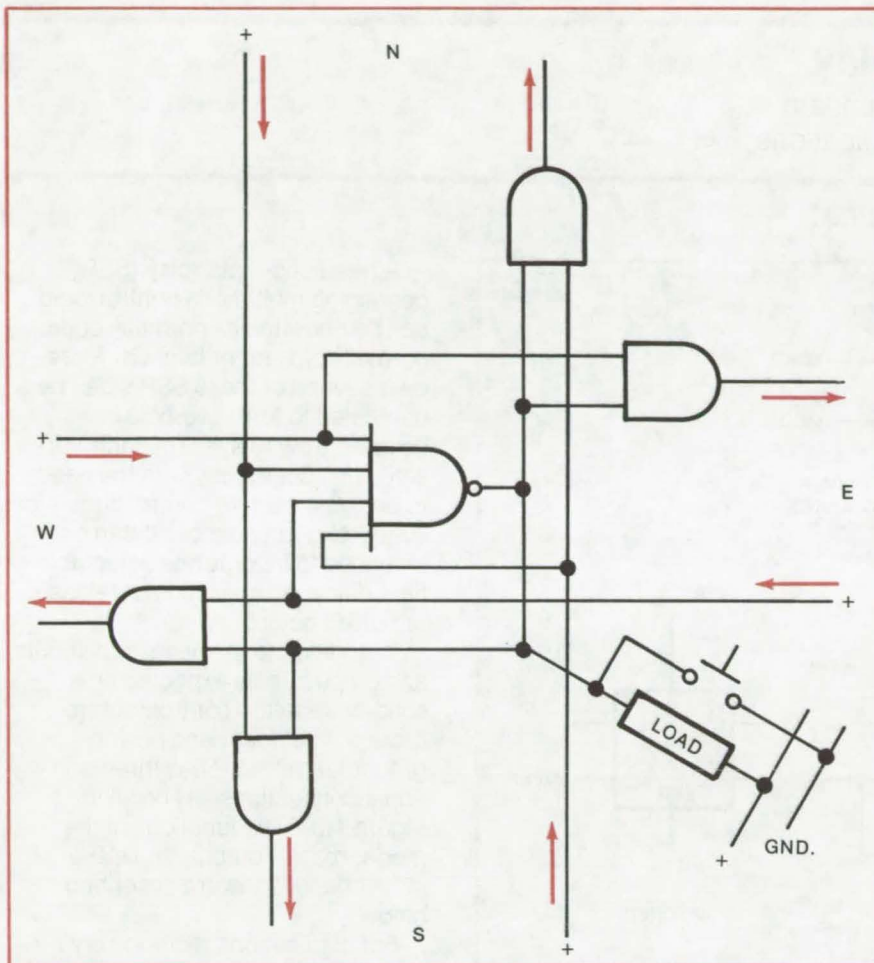
Caltech/JPL, Pasadena, California

A suggested control-logic approach for a crossbar matrix of relays would both control individual relays and display their status. Identical modular control units are used for each intersection of the matrix; their design is independent of the size or form of the relays. The system is expandable, employs general-purpose multiple pole relays, and could be equipped with program

control. Readily available IC's are used, and simple SPST pushbutton switches are used for programing. The status indicators are LED's, and reed relays are employed for isolation.

The same panel would be used for programing and for display with a light-indicating pushbutton at each x-y matrix intersection. As the system is designed, only one button

in a given column and only one button in a given row can be on at any one time. There is a separate reset button for each row and for each column, each of which clears the entire row or column. In addition, a common reset button clears the entire board, and a single key switch could be used to disable all pushbuttons once the board is programed.



In the **Control Circuit in a Matrix-Intersection** configuration, the output of the latching four-input open-collector NAND gate is connected to an isolating reed relay and the intersection pushbutton. In a matrix assembly, edge and corner circuits will require fewer gates, since they originate the control lines. Collective row or column reset buttons operate on the respective control-line originating points, and the control-board disable switch operates on the line connecting the ground side of all intersection pushbuttons.

Because logical control of the coil current through the relay contacts can result in an oscillating system, the control system is segregated from the relay contacts. It is also isolated from the coils through an intermediate relay, to allow the coils to operate at a different voltage and from a less filtered and less regulated supply. The status indicators are controlled by a relay contact (in a dual-purpose configuration).

The control logic (see figure) is inspired by functionally-similar relay coil and contact designs in which the positive and negative coil voltages are fed to the intersection from opposite directions over the contacts of neighboring relays. If a latch circuit at a matrix intersection is set, all identical latches to the N, S, E, and W shall be released (N, S, E, and W representing four arbitrary directions on the control board). This arrangement requires four outbound control lines and four inbound control lines on each circuit. These lines originate at each matrix-edge circuit.

The illustrated control circuit is shown as one matrix-intersection unit; when a particular latch is set, it will provide release lines to all others with the same x coordinate or with the same y coordinate. The feed-through control lines will enable the latch just set to remain set. This allows the latch to be implemented simply by a single four-input gate at the intersection. If more than one latch are set momentarily, they will all be released sequentially and will provide hold signals to the last latch set.

This work was done by Tage O. Anderson of Caltech/JPL. For further information, Circle 2 on the TSP Request Card.
NPO-14095

Versatile Solid-State Relay

Multimode control logic permits a standard unit to be used in many different applications.

Marshall Space Flight Center, Alabama

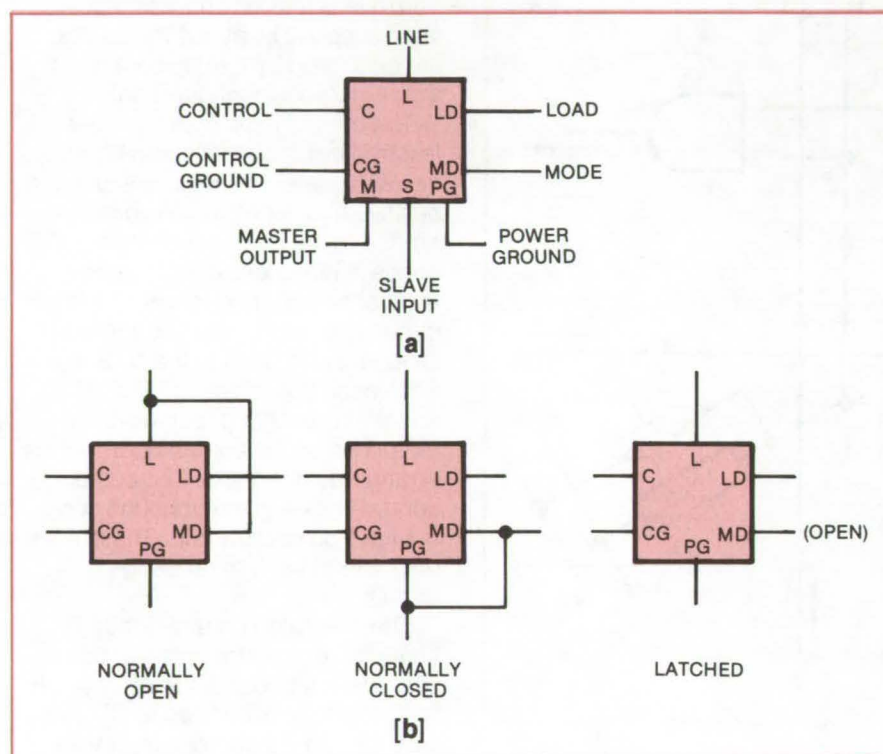


Figure 1. **Solid-State Relay** has the expected input and output terminals (control, control ground, line, load, and power ground) plus three more (a). The connection of the mode terminal determines whether the relay operates normally open, normally closed, or latched (b). The master output and slave input terminals allow interconnection of any number of these relays to form multipole and double-throw configurations, as shown in Figure 2.

A new solid-state relay (SSR), containing multimode control logic, can be operated as normally open, normally closed, or latched. Moreover several of these SSR's can be paralleled to form two-pole or double-throw relays. Thus this versatile unit does away with the need to design a custom control circuit for every relay application. It can be extended to incorporate selectable time delay, on operation or release, or pulsed output.

In addition to the necessary inputs and outputs to be expected on a solid-state relay (control, control ground, line, load, and power ground), each SSR has three additional connections as shown in Figure 1(a). The functions of the mode, master output, and slave input connections are described below.

For applications requiring only one SSR, the mode control determines whether the relay operates normally open (N.O.), normally closed (N.C.), or latched. Connections for each of these functions are shown in Figure 1(b).

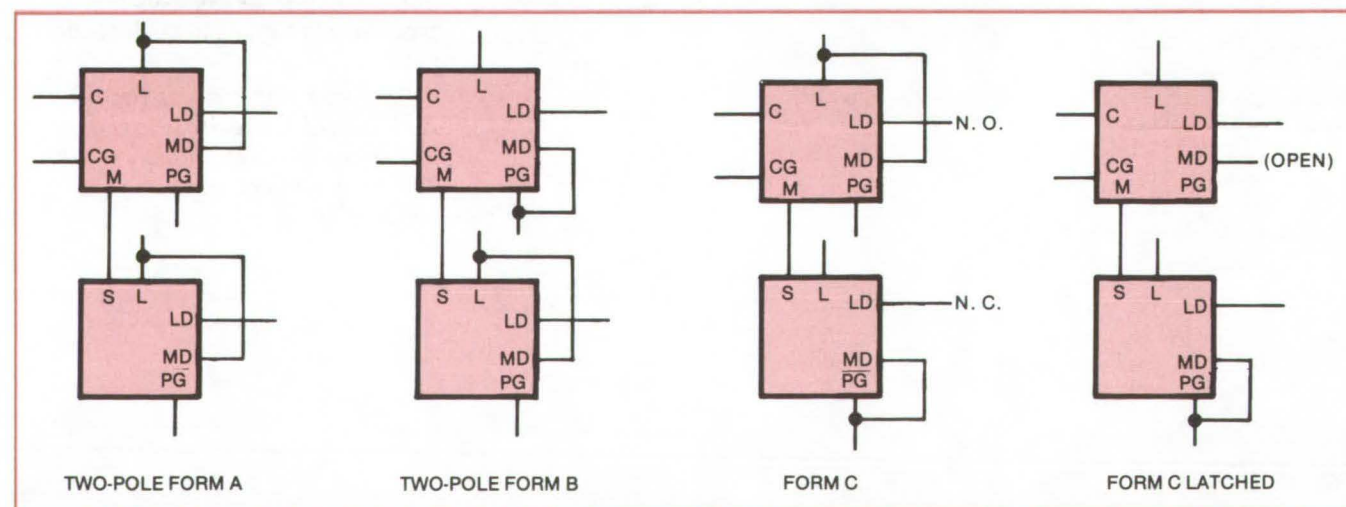


Figure 2. In **Multiple-Circuit Operations** requiring more than one solid-state relay, the master output (M) of one unit is connected to the slave inputs (S) of the others. Connections for four different switch configurations are shown here.

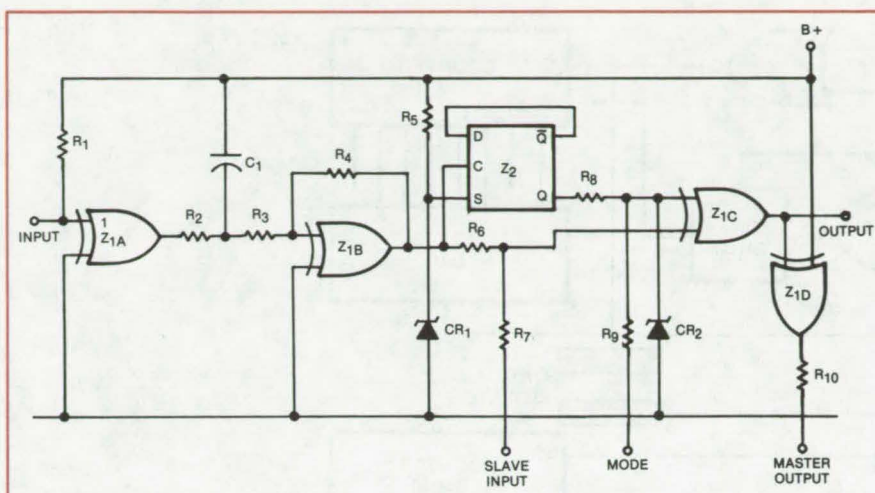


Figure 3. The **Multimode Control Logic**, which drives the output power switch inside the solid-state relay, consists of a quad exclusive-OR gate and a flip-flop. The relay output changes state when a falling edge is applied to the control input.

For multiple-circuit configurations requiring more than one SSR, one device is designated as the "master." The other units are designated as "slaves." The mode con-

trol for the master unit operates in the same manner as for single units, selecting N.O., N.C., or latched operation. The mode control for the slave units selects inverting or non-

inverting operation. The master output of the master unit is then connected to the slave inputs of the slave units. Connections of four switch configurations are shown in Figure 2; note that the control inputs of the slave units are not used.

The schematic diagram of the control circuit, which is the logic inside the SSR, is shown in Figure 3. This logic circuitry interfaces the low-level control circuit and the output power switch. As can be seen, it requires only a quad exclusive-OR gate and a flip-flop.

This work was done by D. A. Fox of Westinghouse Electric Corp. for Marshall Space Flight Center. For further information, including a detailed description of the multimode control logic circuit operation complete with waveforms, Circle 3 on the TSP Request Card. MFS-23632



Inexpensive Pulse-Train Converter Measures Analog Voltage

Analog voltage with very large common-mode voltage is measured with simple circuit having only one optoisolator.

Lewis Research Center, Cleveland, Ohio

A pulse-train converter has been developed for measuring small voltages or currents in the presence of very large common-mode voltages (thousands of volts ac or dc). The advantages of this converter are its low power consumption, transmission via a single isolated channel, simplicity, and operation from a single-polarity power supply. Examples of the types of voltage relationship measured are the cathode discharge supply of an ion engine (40 V), which floats 1 to 2 kV off ground, or the bias voltages of an electron gun (1 to 100 V) operating at -20 kV off ground.

This converter measures an input voltage (or current) by converting it into a pulse train. The number of pulses in the train is directly proportional to the analog input. No external clock signals are required, and the converter can run continuously. This makes it possible to

couple the output pulse train across a large voltage differential using a single optical isolator. An additional purpose is to make the above function simple and at a low power level so that in some cases the circuit can be powered from the signal voltage being measured. This eliminates the need for bulky, high-voltage isolated power supplies.

Prior complex techniques for making these voltage measurements required the use of analog-to-digital converters and voltage-to-frequency converters, which were isolated by using multiple high-voltage isolation transformers or optoisolators. They needed considerable power to operate and required several isolated transmission channels to provide timing or synchronization signals across the high-voltage interface.

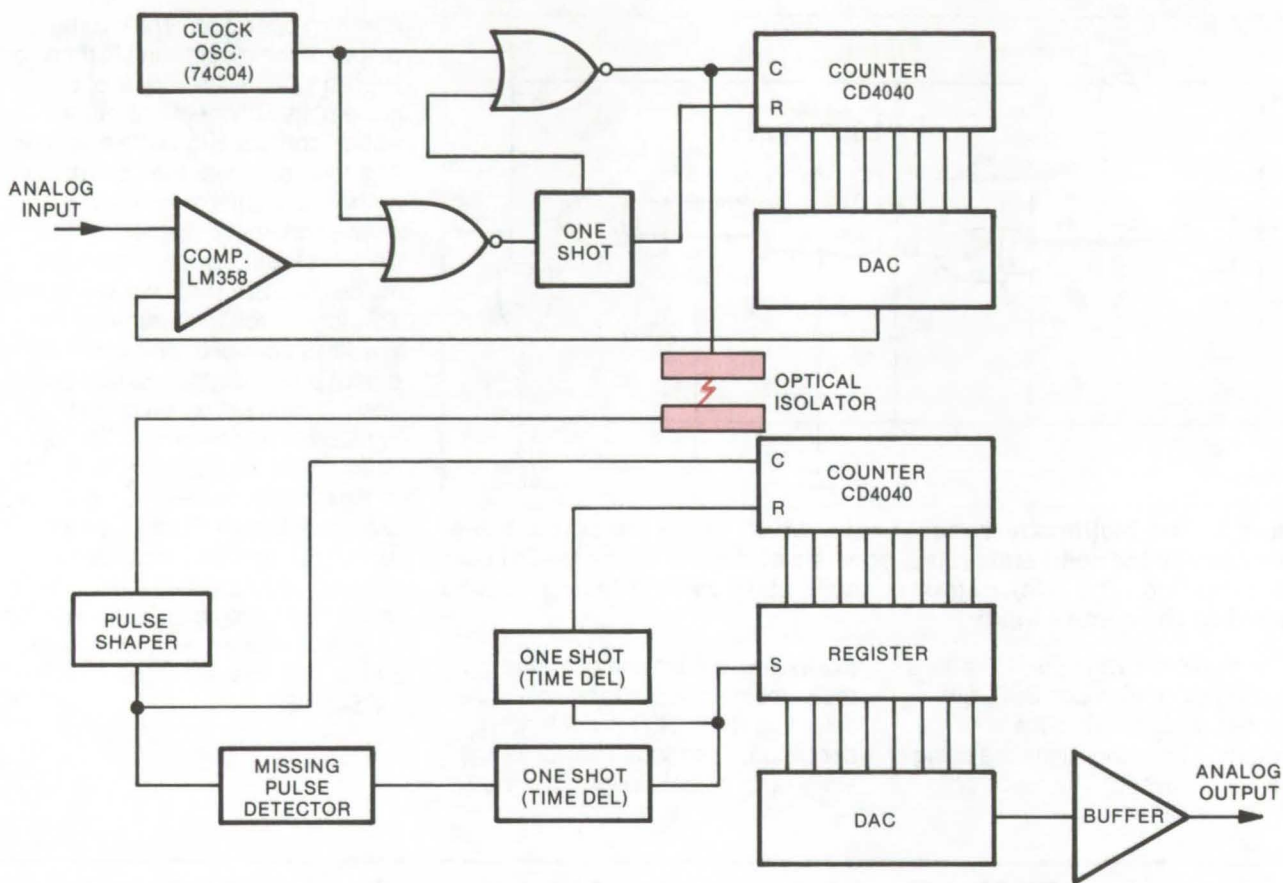
The converter circuit shown in the block diagram operates as follows:

Two inverters of a 74C04 are used to generate a highly asymmetric clock. This clock signal, when gated by the comparison operational amplifier LM358, is counted in a CD4040 counter. The counter output drives a DAC that produces an analog feedback signal proportional to the instantaneous count in the counter. This signal is compared to the input by the LM358 op amp used as a comparator. When the feedback signal slightly exceeds the input, the counter is reset, and the conversion process starts over again.

The output, which is derived from the gated pulse train into the counter, is a continuous train of pulses with two missing every time the counter resets. An optical coupler is driven by this pulse train.

Reconversion of the pulse train to an analog voltage referenced to ground is done in a fashion similar to

(continued on next page)



The **Pulse-Train Converter** measures analog voltages with a very high common-mode voltage by converting the analog input into a pulse train with a length proportional to the input voltage. The pulse train is optically coupled to another circuit that converts the pulse train into an analog signal proportional to the voltage.

the encoding process. The photo-coupler pulses are first shaped and then fed to a circuit that detects the missing pulse. Absence of a pulse causes the lower CD4040A counter to be reset. It then counts pulses until another missing pulse is detected. At this time, two things happen. First, the count in the 4040A is loaded into an 8-bit holding register consisting of two DC4042 latches. After this, the counter is reset, and the cycle repeats. Except for the few microseconds when data are being transferred into the register, there is always a digital count proportional to the input stored in the register. Conversion of this count to an analog voltage is done by the DAC3851-8 DAC that provides the analog output.

Only one power supply voltage (+15 V) is required for either the high or low side of the circuit. All circuitry is CMOS, making the power consumption extremely low.

Several forms of the converter have been built. One is powered by an isolated power supply that must withstand the common-mode voltage of the system. This unit is capable of operation to 4 kV. A second unit was built to measure the cathode discharge voltage of an ion engine. Because of the combination of low power requirements and the capability of operation from a single-polarity power supply, it was possible to power this unit from the signal being measured. A third system powers multiple measuring

systems from a single isolated power supply. Other alternates include multiplexed data channels operating into one converter and the use of different means of transmitting the pulse train across the high-voltage interface. An example of the latter would be the use of fiber optics, which would increase the isolation voltage capabilities to a million volts or more.

*This work was done by John C. Sturman of **Lewis Research Center**. No further documentation is available.*

Inquiries concerning rights for the commercial use of this invention should be addressed to the Patent Counsel, Lewis Research Center [see page A8]. Refer to LEW-12912.

Extrasensitive Phase-Locked-Loop Circuit

Modified form of PLL obtains fast positive lock under marginal signal-to-noise conditions.

Lyndon B. Johnson Space Center, Houston, Texas

A modified phase-locked-loop (PLL) circuit can lock on an incoming signal that is 2 dB below the noise in the signal bandwidth. The lock-detection voltage is nearly independent of gain variations in the PLL, and the output phase is accurate to within 1° .

The superior signal-acquisition characteristic of this circuit results from the technique used to detect locking: Instead of a coherent amplitude detector to detect lock and turn off the sweep of the voltage-controlled oscillator (VCO), a dither oscillator, a dither band-pass filter, and a correlator are used. This arrangement, shown in the block diagram (Figure 1), minimizes the effects of the threshold phase-detector gain variations in the lock-detection process. The basic equations that define the operation of the dither signal in relation to the PLL parameters are shown in Figure 2.

The dither oscillator produces a reference signal that is used in the dither correlator and produces a dither signal that is used to modulate the VCO in the PLL. When the incoming data are phase locked to the dither-modulated VCO signal, the output of the phase detector contains a component of the dither signal. When the loop is unlocked, the output of the phase detector contains only components of the sum and difference frequencies of the input data and VCO signal; the dither appears as modulation sidebands on these signals.

Once the data and VCO are phase locked, the detected dither signal (derived from the output of the phase detector) is filtered in a narrow-band active filter, is amplified, and then is correlated against the reference dither signal. When the detected dither signal has the same frequency and phase ($0^\circ \pm 10^\circ$) as the reference signal, the correlator output dc level changes. This change in dc level is

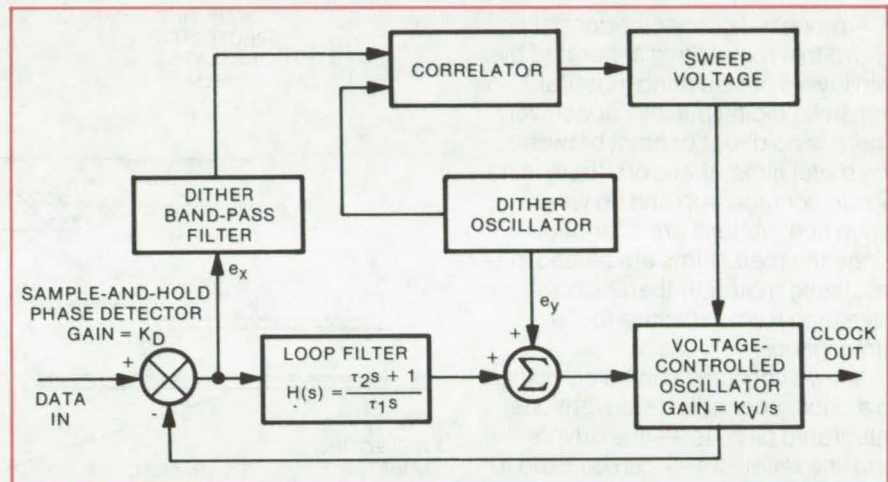


Figure 1. **Modified Phase-Locked Loop** generates clock from an incoming data signal. To minimize the effects of the threshold phase-detector gain variations, the PLL uses a dither oscillator, a dither band-pass filter, and a correlator instead of a coherent amplitude detector.

DITHER-SIGNAL EQUATIONS

$$(1) \quad \frac{e_y}{e_x} = \frac{-(s^2 \tau_1 + s \tau_2 GL + GL)}{s GL \tau_1}$$

$$(2) \quad \theta = \text{phase of } e_y/e_x = \tan^{-1} \left[\frac{(GL/\tau_1 - \omega^2)}{GL \tau_2/\tau_1} \right]$$

$$(3) \quad A = |e_y/e_x| = \left[\left(\frac{\tau_2}{\tau_1} \right)^2 + \left(\frac{GL/\tau_1 - \omega^2}{\omega GL} \right)^2 \right]^{1/2}$$

Where: e_x = detected dither signal
 e_y = input dither signal to VCO
 $GL = K_V K_D$ = phase-lock-loop gain
 $s = j\omega$ = dither frequency in radians

Figure 2. The **Phase and Amplitude** functions (Equations 2 and 3) show that a dither-signal frequency, much lower than the natural resonant frequency of the loop, $\omega_n = [GL/\tau_1]^{1/2}$, makes the detected dither signal amplitude and phase nearly independent of gain variations in the phase-locked loop.

then used to turn off the sweep of the VCO and to indicate loop lock.

To make the detected dither-signal amplitude and phase nearly independent of gain variations in the phase-lock loop, the dither frequency is chosen much lower than

the natural resonant frequency of the loop.

This work was done by Ernest J. Nyiri of Motorola, Inc., for **Johnson Space Center**. No further documentation is available.
 MSC-16770

Capacitive Connectors for Digital-Data Lines

Thin-film, flat-conductor connection resists wear and corrosion, yet should cost less than conventional connectors.

Goddard Space Flight Center, Greenbelt, Maryland

A proposed connector consisting of two thin metal films separated by thin layers of insulating material transmits digital pulses capacitively. There is no direct contact between the metal films; therefore there is no ohmic contact drop and no wear when connections are changed. Since the metal films are sealed in insulating material, there is no corrosion from exposure to the atmosphere.

Many such films can be combined in a cable connector. Conventional integrated circuits — line drivers and line receivers — can be used to send signals through the connector. Since the connector does not transmit direct current, it has a high level of electrical isolation.

The flat conductor is etched or printed on an insulating substrate with an overlying insulating film. The capacitive electronic connection is made by superimposing matched areas on the input and output cables. This technique overcomes some limitations of conventional pin or spring mating connectors. No soldering is required at the connector, and the absence of inter-metallic contact reduces corrosion.

The connector elements are shown in Figure 1, one way of implementing this capacitive-connector scheme. Further refinement is possible by surrounding each connecting area with a grounded-ring conductor, which may be extended down the length of the conductor to the source and to the load (see Figure 2). This serves to reduce "crosstalk," or mutual interference, between signal paths. For best results, pairs of conducting areas could be used for each signal path to

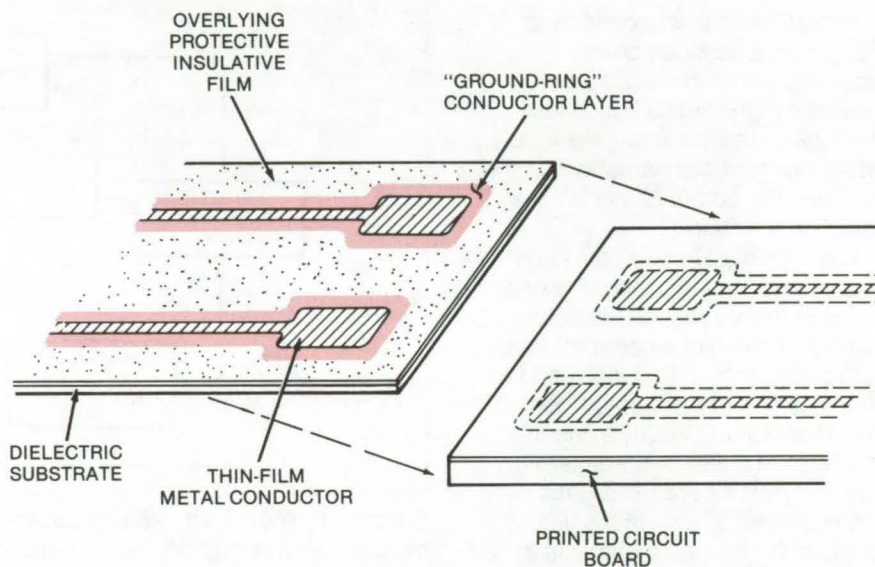


Figure 1. A **Magnetically Clamped Connector** is one possible implementation of the thin-film capacitive connector. Since the capacitance is an inverse function of spacing, improved results might be obtained by clamping thin conductors and insulating films with a rubber-based magnet. The magnet would apply a uniformly distributed pressure conforming to variations in surface flatness on the connecting surfaces.

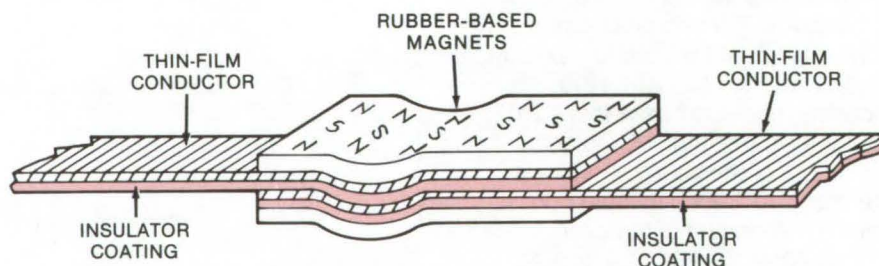


Figure 2. **Pairs of Conducting Areas** could be used for each signal path. This approach has the advantage of improved noise cancellation.

gain the benefits of differential action (i.e., one goes high when the other goes low).

Capacitive coupling is not new in itself, but the concept of using thin-film insulated conductors as the direct circuit connection adds desir-

able simplicity and economy to the technique. In addition to reducing wear, the dielectric film can have the advantage of a high dielectric constant. This can improve the coupling and reduce the effect of surface imperfections. Another

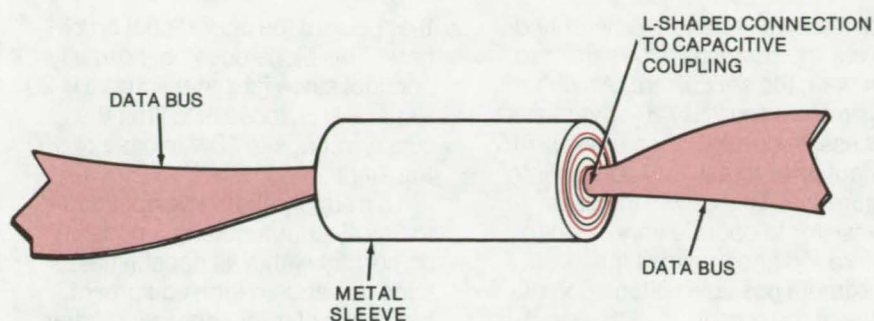


Figure 3. **Rolled Connectors** are another suggested method of stabilizing, securing, and isolating the capacitive plates. To keep the conductors from producing or sensing external signals, relatively-large-area thin-plate conductors are superimposed and then rolled and slipped into a metal cylinder. Each strip is terminated in an L-shaped pattern to facilitate packaging.

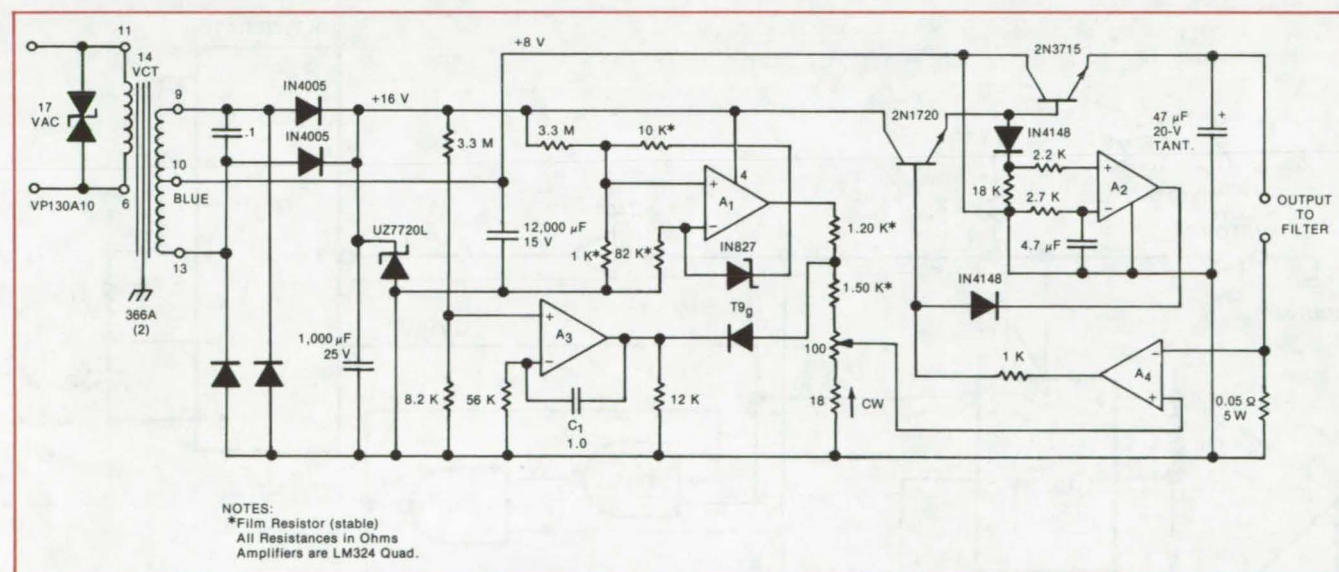
advantage lies in the fact that the input and output are open-circuited to direct current. Thus, electrical isolation is enhanced, and common mode problems are reduced.

*This work was done by Philip A. Studer of **Goddard Space Flight Center**. No further documentation is available.*
GSC-12238

Simple Constant-Current-Regulated Power Supply

Constant-current supply features "soft-start" circuit.

Lewis Research Center, Cleveland, Ohio



The **Constant-Current-Regulated Power-Supply Circuit** can be modified to operate over a wide range of voltages and currents. It is limited only by the maximum supply voltage for the operational amplifier and by the maximum current of the pass transistor.

A relatively-simple current-regulated power supply will supply up to 5 A and 5.5 Vdc. Current ripple is less than 0.01 percent at 5 A, and current regulation is better than 0.05 percent for a 60-percent change in load resistance. The supply also incorporates a soft-start circuit that slowly ramps the current up to the set point at turn-on.

The operation of electron guns

often requires the cathode to be maintained at a constant temperature. Circuitry to measure cathode temperature, or some related parameter, and to hold it constant is not generally available commercially. A simple but often viable solution is to regulate the heater current to a constant value. This method has the added advantage of eliminating the large surge currents

drawn by metallic filaments when first turned on.

As shown in the figure, the supply consists of a full-wave rectifier, a regulating pass transistor, a current feedback circuit, and a quad single-supply operational-amplifier circuit providing the control. Amplifier A₁ provides a closely-regulated reference output of about 6 V, which is used as the system reference.

Operational amplifier A_3 is the slow startup circuit. At turn-on, its output is low, pulling down the comparison voltage reference. Capacitor C_1 begins to charge as operational amplifier A_3 integrates the current flowing through the 56-k Ω resistor, producing a positive-going ramp at its output. When its output exceeds the normal voltage at the tap on the reference voltage divider, the T9_g germanium diode becomes back biased, decoupling the startup circuit from the reference supply.

Amplifier A_4 is the regulating amplifier. It compares the voltage across the 0.05- Ω current feedback resistor with the set point voltage

from the 100- Ω potentiometer and drives the series pass transistor to maintain the set current. Amplifier A_2 protects the 2N1720 driver from excessive current when the 2N3715 output pass transistor is driven into saturation. This allows the pass transistor to operate very close to saturation and provides the maximum possible voltage compliance at the output.

Protection against circuit transients from arcs in the electron gun has been provided by incorporating a transient-voltage suppressor across the line and a protective zener diode across the 16-V supply

that powers the operational amplifiers. This diode does not normally conduct since its zener voltage is 20 V. Its only purpose is to limit the supply voltage to 20 V in case of a transient.

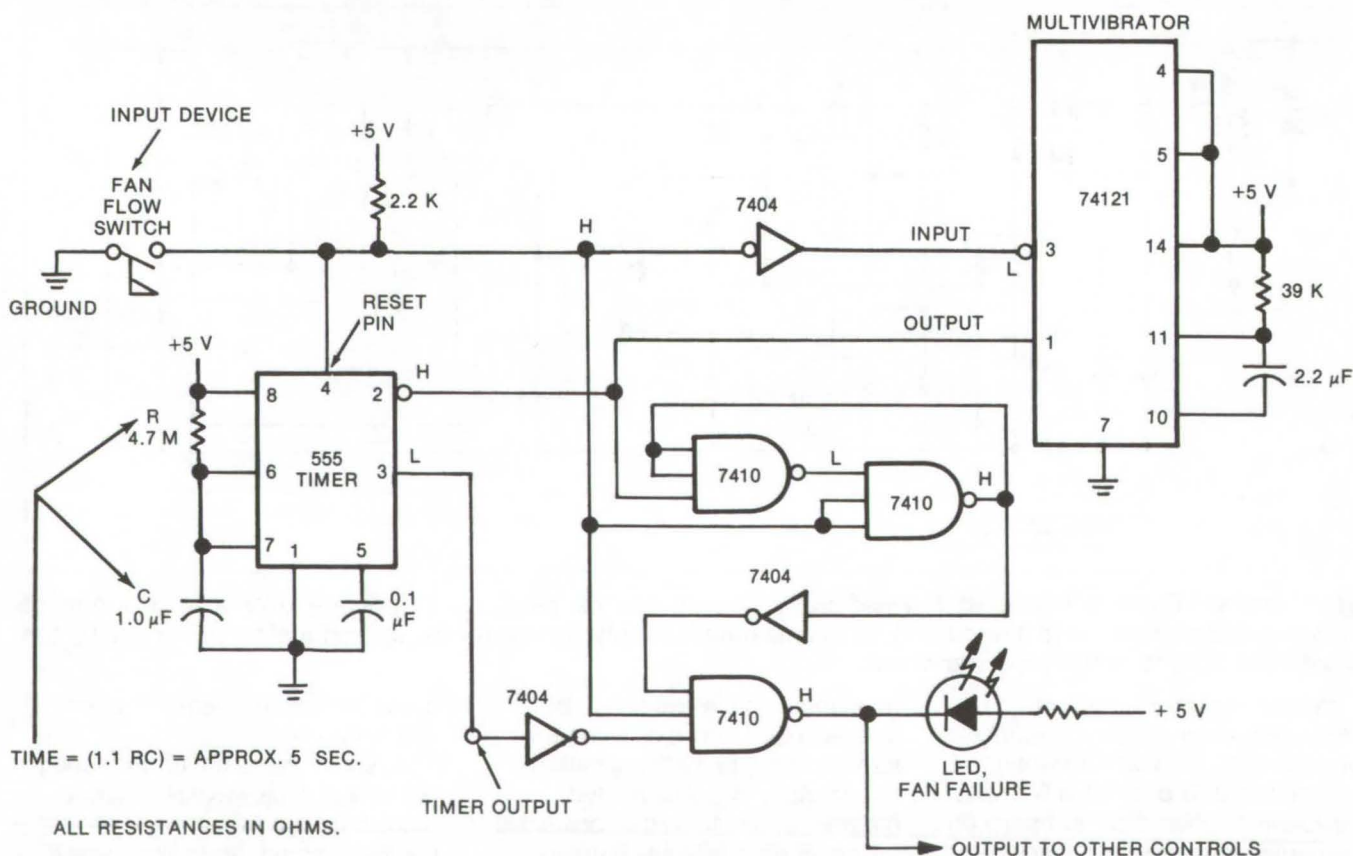
This supply should be applicable to any system requiring a constant dc current within its capabilities, such as vacuum tube equipment, heaters, or battery chargers. It has also been used to supply constant current for instrument calibration.

This work was done by Donald H. E. Priebe and John C. Sturman of Lewis Research Center. No further documentation is available.
LEW-12894

Inexpensive Solid-State Monitoring Circuit

Short-term switch interruptions due to contact flutter are ignored, and equipment is shut down only in response to longer "opens."

Lewis Research Center, Cleveland, Ohio



The **Solid-State Monitoring Circuit** is used to reduce intermittent fan-flutter openings in an airflow switch. The circuit ignores brief switch openings due to contact oscillations; however, if the switch is open longer than a selected interval, the control circuit shuts down the system and sounds an alarm.

A lightweight inexpensive solid-state electronic antibounce or anti-flutter monitoring circuit recognizes and compensates for short-duration contact flutter (repeated closings/openings) during startup or operation of a process control system. These contact oscillations are inherent in mechanical-contact switching components.

The equipment controlled by these components, unless monitored by such an antinuisance circuit, can be turned on and off repeatedly by the contact oscillations, thus disrupting intended operation. This new circuit contains a preset timer that ignores these nuisance interrupts but monitors the switch to detect interrupts longer than the preset time.

The changeover from past relay controls to the more reliable current-day solid-state controls created the need for an inexpensive, simple, antibounce circuit readily adaptable to other solid-state control circuits.

A typical application is shown in the figure. In this example, the monitoring circuit is used to prevent inadvertent shutdown or alarm caused by intermittent fan-flutter openings of an airflow switch. The control circuit will shut down the system and sound an alarm only if the flow switch remains open longer than the preselected time.

As shown in the figure, the circuit is in a quiescent state, and TTL (transistor-transistor logic) devices are used for the controls. When the fan is turned on manually, the airflow pressure closes the flow switch. If the airflow switch bounces or flutters during startup or opens for short durations due to back pressure during normal fan run conditions, the antinuisance circuit will ignore these short-time interrupts of the airflow switch. If the airflow switch remains open longer than the preset time, the antibounce circuit timer will automatically turn the output on. Closing the flow switch causes pin 4

of the timer and the input of the inverter to go to ground. When the input of the inverter goes to ground, the inverter output voltage goes high. If the flow switch opens, the input to the multivibrator changes back to low or ground level.

It is this transition of voltage from high to low on the input pin 3 of the multivibrator that causes its output pin 1 to pulse momentarily and start the timer. If the flow switch remains open longer than the time setting of the timer, the timer will be allowed to time-out; and the LED will light, giving visual indication of fan failure.

This same output could be used to sound an alarm and to act as a logic input signal to other solid-state control circuits that may be used in a process control system, thus shutting some devices off and turning others on.

This work was done by Donald H. Hardy of Lewis Research Center. No further documentation is available.
LEW-12848



Bias-Field Equalizer for Bubble Memories

Magnetoresistive sensor controls electromagnets that keep bias field constant.

Marshall Space Flight Center, Alabama

The perpendicular magnetic bias field required to maintain cylindrical magnetic domains or "bubbles" in a bubble memory must be held constant to within ± 16 percent. With too high a perpendicular field, the bubbles will collapse; with too low a field, the bubbles will elongate to serpentine domains.

Permanent magnets are the preferred source for the perpendicular bias field because they weigh less than equivalent bias-field coils, they require no operating power, and they are relatively nonvolatile. However, over long periods of time, the magnetization of the permanent magnet may change enough to affect adversely the operating margins of the memory by either collapsing or overly expanding the bubbles.

A new magnetoresistive Permalloy sensor monitors the bias field that is required to maintain a bubble memory; the sensor provides an error signal that, in turn, corrects the magnitude of the bias field. The error signal from the sensor can be used to control the magnitude of the bias field in either of two ways:

- An auxiliary set of bias-field coils may be provided around the permanent magnet field. The sensor output can be used to control the magnetizing current through the auxiliary coils to aid the existing permanent magnet field.
- The current in the small coils can be used to remagnetize the permanent magnet by a very infrequent, short, high-current pulse or a short sequence of pulses. These magnetizing current pulses consume very little power over the life of the memory.

For maximum sensitivity, the sensor geometry should be chosen so that the sensor magnetization is oriented at an angle of 45° to the measuring current for the nominal value of bias field. As an example, for a 100-oersted bias field and a sensor thickness of 1,000 angstroms, the sensor width should be 5 microns.

This work was done by G. E. Keefe of IBM Corp. for Marshall Space Flight Center. For further information, Circle 4 on the TSP Request Card.

Inquiries concerning rights for the commercial use of this invention should be addressed to the Patent Counsel, Marshall Space Flight Center [see page A8]. Refer to MFS-23189.

Double-Duty Loudspeaker

Two independent coils transmit voice messages and warning tones through the same speaker.

Lyndon B. Johnson Space Center, Houston, Texas

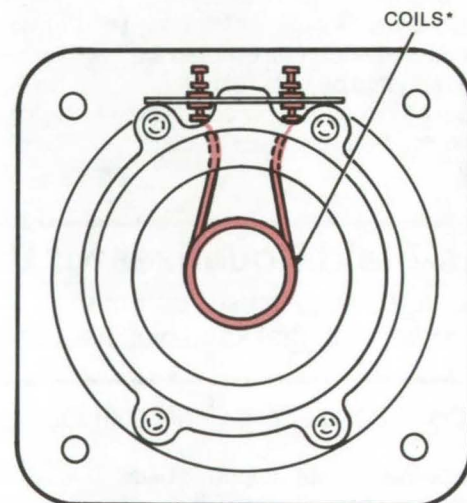
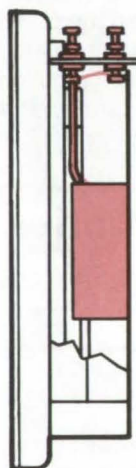
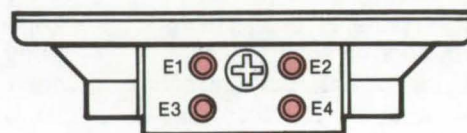
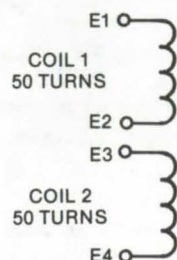
A loudspeaker with two coils handles both audible-warning signals and intercom messages, saving much of the space and weight of two separate speakers. The dual-coil speaker should be useful in applications where space is limited. For example it could be used to give audio indications of malfunctions or danger over a car radio.

Although they are mounted on the same diaphragm, the two coils operate independently. Thus, it is not necessary for the intercom circuitry to be turned on for a warning tone to sound.

The two coils are wound on the same voice-coil form with no sacrifice in speaker efficiency or power-handling capability. Interaction between the two coils is minimal; signals in one coil do not affect the circuits associated with the other coil.

The speaker developed to demonstrate dual-coil operation is a standard commercially available model with a cone 2 in. (5 cm) in diameter. The standard coil was replaced by two coils of 50 turns each. The original magnet was replaced by an Alnico VIII magnet, which has higher efficiency and reduced weight by 0.2 lb (91 g). Frequency response is about the same as in the original speaker, which is specified as flat between 500 and 2,000 Hz.

This work was done by Ed Joscelyn of Instrument Systems Corp. for Johnson Space Center. No further documentation is available.
MSC-16263



*50TURNS EACH, 2 LAYERS (26 AND 24 TURNS) BIFILAR WOUND, BONDABLE WITH TWO COATS ADHESIVE, ACTIVATED WITH METHYL ALCOHOL TO BOND TOGETHER, BAKING VARNISH APPLIED

Dual-Coil Speaker can transmit warning signals and intercom messages. It saves power by allowing warning signals to be heard with the intercom electronics turned off.

DC Transformer Uses Magnetoresistors

Flux motion in a superconductor/insulator/magnetoresistor sandwich provides transformer action.

Marshall Space Flight Center, Alabama

A new study predicts that a dc transformer can be constructed by using a combination of superconducting and magnetoresistive materials. Until now, the generation of a steady voltage in a secondary circuit in response to the application of a dc voltage in a primary has been realized only by using superconducting materials. If the new device is successful, it will extend the temperature range over which dc transformers can operate; and since it is less susceptible to pinning forces and eddy-current losses, it will be more efficient.

The conventional dc transformer uses the phenomenon of magnetic-flux motion in a superconductor/insulator/superconductor thin-film sandwich (Figure 1) to generate primary and secondary voltages. When a steady magnetic field, above a minimum critical value, is applied transverse to a superconducting film, flux lines penetrate in tiny cylindrical bunches known as flux quanta. If a steady transport current is simultaneously applied, the flux quanta begin to move across the film and induce a voltage in the direction of the current flow. This effect generates the primary voltage in the film sandwich. As the flux quanta move across the primary, they induce flux motion across the secondary and generate a voltage that provides transformer action.

The new study investigated the effects of flux motion across non-superconducting, magnetoresistive materials. While magnetoresistance (magnetic-field-induced resistance) is observed in virtually all metals and semiconductors, it is quite small in monovalent metals such as copper and silver but can be large in semi-metals such as bismuth and antimony, particularly at low temperatures. Voltages analogous to flux-flow voltages in superconductors were observed, indicating that it might be possible to build a dc

transformer with a magnetoresistor as the secondary.

In the study, thin plates of various materials were moved across a transverse magnetic field, while the induced voltage was monitored between pairs of contacts. Typical results are shown in Figure 2. Figures 2(a), 2(b), and 2(c) were obtained at helium temperature (4.2 K). They show the induced voltage as a function of time across bismuth, copper, and lead, respectively. Figure 2(d) shows the voltage across bismuth at room temperature. Each graph shows an initial positive voltage spike followed by a

negative voltage spike. In the case of bismuth at room temperature and copper at helium temperature, neither of which shows strong magnetoresistance, the spikes are roughly equal in magnitude so that the integrated voltage signal is zero. In the case of lead (a superconductor) at helium temperature, the spikes do not cancel, as a result of the flux-flow voltage. In the case of bismuth at helium temperature, the spikes also do not cancel, indicating for the first time that an effect similar to flux-flow voltage can occur in a magnetoresistive material.

These results suggest that if a

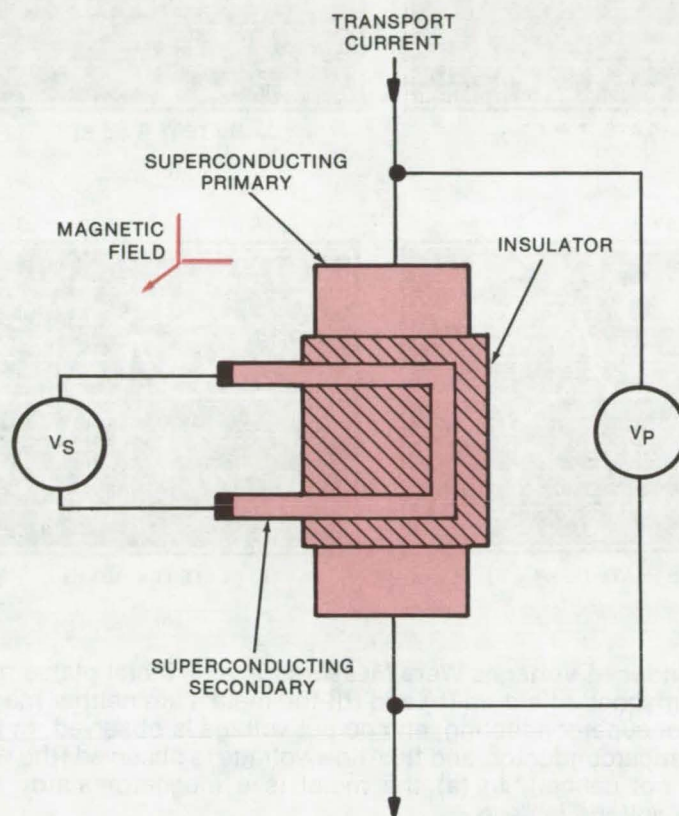


Figure 1. A conventional **DC Transformer** is formed by a superconductor/insulator/superconductor thin-film sandwich. The combination of applied magnetic field and transport current in the primary produces magnetic-flux flow that generates a voltage in the secondary layer. A new study indicates that the secondary could be formed out of a magnetoresistive material, creating a transformer with wider operating-temperature range and improved efficiency.

(continued on next page)

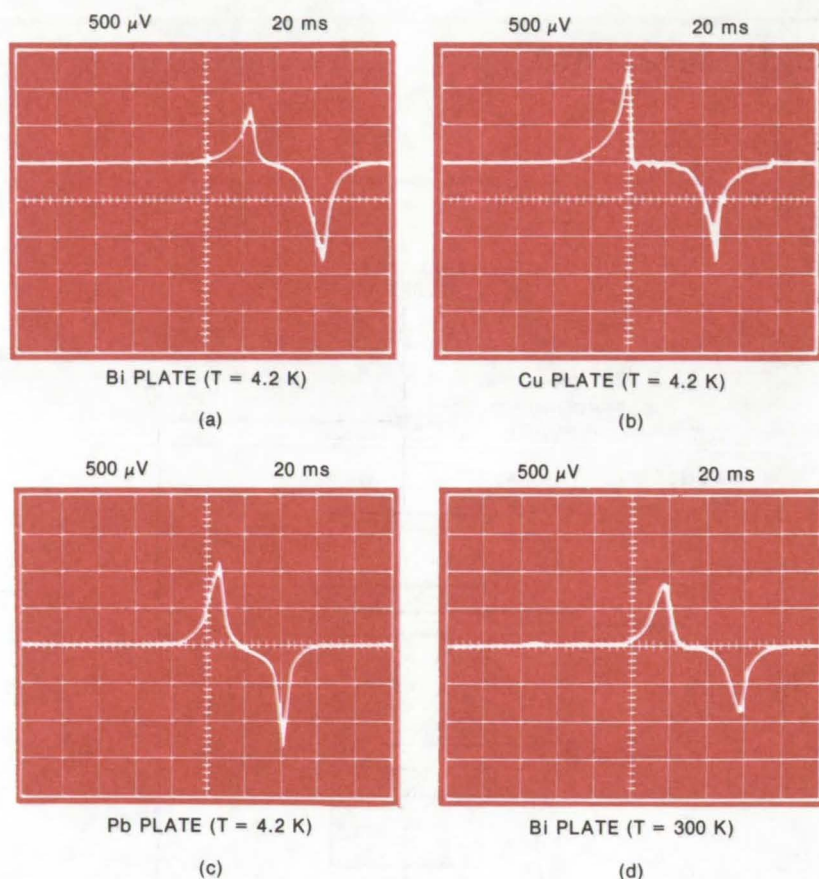


Figure 2. Induced Voltages Were Measured across metal plates moving through a magnetic field. In (b) and (d) the metals are neither magnetoresistive nor superconducting, and no net voltage is observed. In (c) the metal is a superconductor, and flux-flow voltage is observed (the voltage spikes do not cancel). In (a) the metal is a magnetoresistor, and a similar net voltage is seen.

superconductor/insulator/magnetoresistor sandwich is placed in a transverse magnetic field and a transport current is passed through the superconducting layer, then flux quanta moving through the primary would couple to the magnetoresistor to generate a secondary voltage.

In the all-superconductor transformer, the circuit could only be operated below the superconducting transition temperature of the secondary. In the proposed device, no such restriction exists, and the transformer could be operated at any temperature below the transition temperature of the primary. In addition, the all-superconducting transformer is limited by pinning forces that tend to restrict the free motion of the flux quanta in the secondary. Since this limit does not appear to exist for the magnetoresistor, efficiency could be improved. Also, eddy-current losses in regions where flux changes occur during flux motion in the secondary would be much reduced in the new transformer.

This work was done by S. M. Khanna and E. W. Urban of Marshall Space Flight Center. For further information, Circle 5 on the TSP Request Card.

This invention is owned by NASA, and a patent application has been filed. Inquiries concerning nonexclusive or exclusive license for its commercial development should be addressed to the Patent Counsel, Marshall Space Flight Center [see page A8]. Refer to MFS-23659.

Precision Voltage Division Without Precision Parts

Inexpensive solid-state devices supplant costly precision resistors.

Goddard Space Flight Center, Greenbelt, Maryland

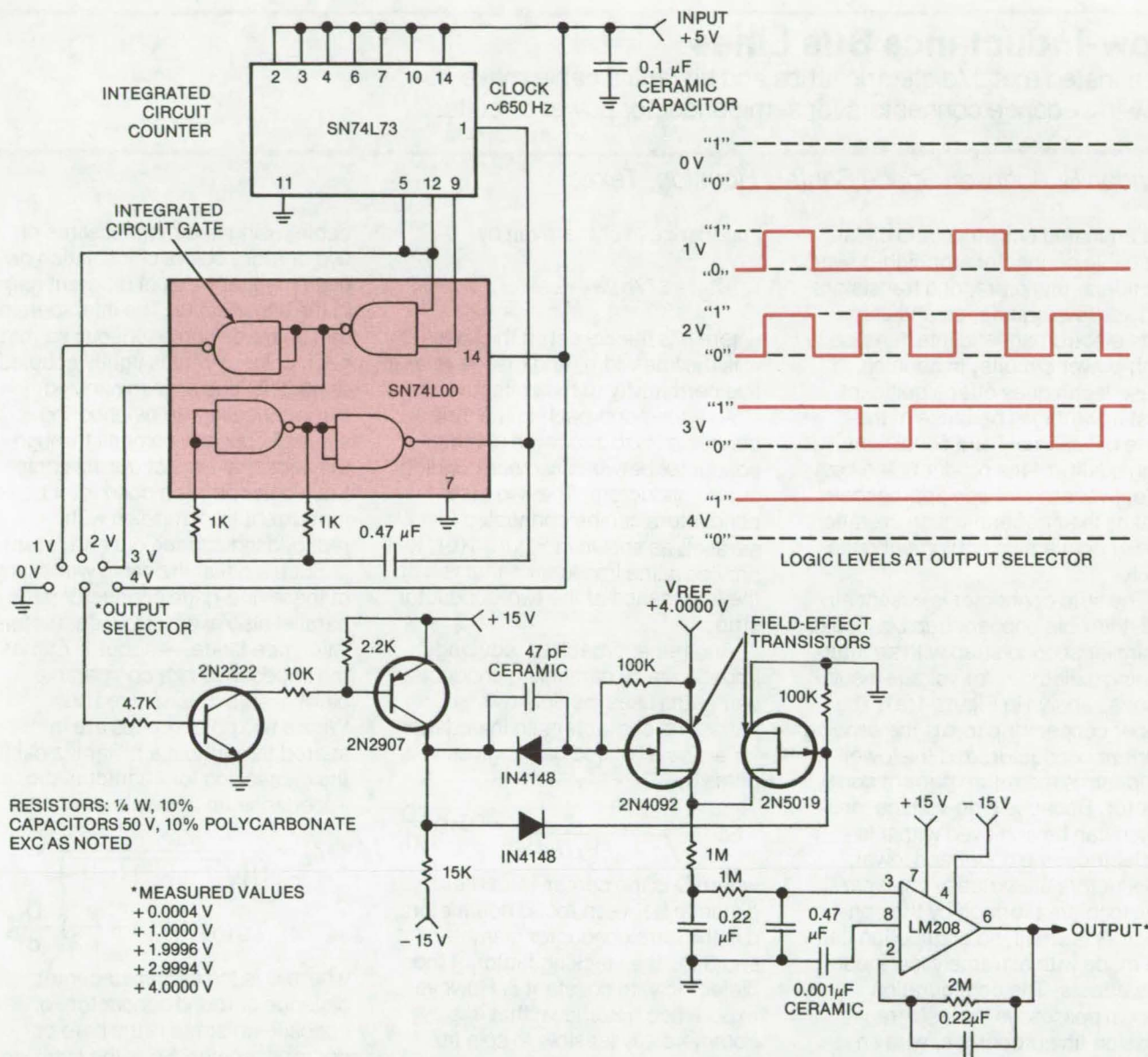
A precision voltage divider uses pulse-width modulation circuitry instead of a conventional voltage-division network. With ordinary solid-state components and 10-percent-tolerance resistors, the new source divides an input reference voltage with a typical long-term accuracy of ± 0.05 percent. For similar precision, a conventional

voltage-divider network would need highly-stable precision resistors that cost more than the entire new voltage source.

The new "active" circuit is compact and greatly reduces errors from drifting component values. It was designed for a precision calibrator in aerospace instrument systems; however, the principle is suited for

use in laboratory voltage and current references and in switchable references for programmed calibration equipment.

Simple digital circuitry can produce pulse trains with very stable on/off-time ratios. For precision voltage division, it is only necessary to select a logic signal having a duty cycle proportional to the desired



Active Voltage Divider applies different logic signals to FET switches to generate various voltage levels at the output. Waveforms of logic levels at the output selector show that a 50-percent-duty-cycle signal, for example, produces a 2-volt output, or one-half of the V_{REF} value used. The actual measured value was 1.9996 volts, corresponding to an error of only 0.02 percent.

voltage, to stabilize its amplitude, and to integrate the resulting waveform. The circuit shown illustrates the principle. The SN74L73 comprises a two-stage ripple counter. The SN74L00 gate package generates a clock signal and also decodes the counter so that waveforms of 0, 25, 50, 75, and 100 percent duty cycle are available. The FET switches fix the amplitude, and the resulting signal is averaged

by the two-pole low-pass filter and is then buffered. The 1-V output steps are accurate to well within 1 mV. Noise level is under 0.3 millivolt p-p, and stabilization time is about 10 seconds.

The logic can be designed to provide any number of output steps to meet particular requirements. Some design tradeoffs are evident. Stabilization time can be cut by reducing the averaging-filter time

constant, but this will increase output ripple unless a proportionally higher clock rate is used. Much higher clock frequencies will require higher-speed FET switching circuitry to avoid duty-cycle errors and corresponding division errors.

This work was done by Maxwell G. Strange of Goddard Space Flight Center. No further documentation is available.
 GSC-12182

Low-Inductance Bus Lines

Laminated metal/dielectric strips and bifilar litz cable make low-impedance connectors for semiconductor power circuits.

Lyndon B. Johnson Space Center, Houston, Texas

Laminated bus strips and bifilar litz cable connectors for high-power rectifiers, thyristors, and transistors provide low inductance and eliminate electromagnetic interference in high-power circuits. In addition, these techniques offer significant cost advantages because of the ease of assembly and consistent high quality of the product. The cost effectiveness of these approaches makes their general usage in static power conversion equipment quite likely.

The strip connector is essentially a flat flexible copper strap bonded to a similar second strap with an intervening dielectric, for voltage insulation, as shown in Figure 1(a). The upper copper strip forms the sending current conductor, and the lower strip forms the return current conductor. Because high-voltage insulation can be achieved with thin dielectrics, the upper and lower conductors are virtually coplanar. The loop area formed by the conductors is small, so connection can be made with extremely low inductive effects. The configuration shown possesses intrinsic transmission-line properties, with an

impedance in ohms given by

$$Z_0 = 377h/w \cdot \frac{1}{\sqrt{\epsilon}}$$

where h is the dielectric thickness, w is the line width, and ϵ is the relative permittivity of the dielectric.

A second approach to the strip connector is to sandwich a center conductor between two surrounding outer conductors. The two outer conductors can be connected in parallel, as shown in Figure 1(b), to provide a line impedance that is half the impedance of the two-conductor strip.

Another approach to reducing impedance by paralleling conductor-pair paths uses multiple twisted pairs. The characteristic impedance for a single twisted pair is given in ohms by

$$Z_0 = \frac{276}{\sqrt{1 + (SF)(\epsilon - 1)}} \cdot \log_{10} \frac{2D}{d}$$

where D is the center-to-center distance between round conductors, d is the bare conductor diameter, and SF is the stacking factor of the dielectric with constant ϵ . However, experience has shown that it is commercially feasible to spin litz

cable, using fine magnet wires of two or more colors of insulation or even magnet wires of different gage in the same cable. The interspersing can be made homogeneous so that each color of wire is tightly coupled (inductive loop area minimized) symmetrically with neighboring wires of opposite color all through the sectional area of the litz cable. Each color pair is a conductor pair for current transmission with reduced inductance out and return.

Such a bifilar litz cable with many of these fine-gage conductor pairs in parallel also exhibits low characteristic impedance — about 1.7 times the impedance of a comparable parallel strip or laminated bus. Where two color groups are interspersed throughout a bifilar litz cable, the expression for characteristic impedance, in ohms, is

$$Z_0 = \frac{552}{N \left(\sqrt{1 + (SF)(\epsilon - 1)} \right)} \times \log_{10} \left[\left(1.218 + \frac{\pi}{N^2} \right) \frac{D}{d} \right]$$

where D is the center-to-center distance of round conductors of opposite colors, d is the bare conductor diameter, SF is the stacking factor of dielectric of constant ϵ , and N is the number of strands of both colors together in the bifilar litz cable.

Where the width of the laminated bus cannot be tolerated, such as in a small opening or in toroidal winding, the bifilar litz approach is the next best alternative for the elimination of inductance.

Another configuration often considered to be a low-inductance conductor pair is the round insulated wire lying on a ground-return plane. Its characteristic impedance is

$$Z_0 = \frac{138}{\sqrt{1 + (SF)(\epsilon - 1)}} \cdot \log_{10} \frac{4H}{d}$$

where H is the height of the round conductor center above the ground plane.

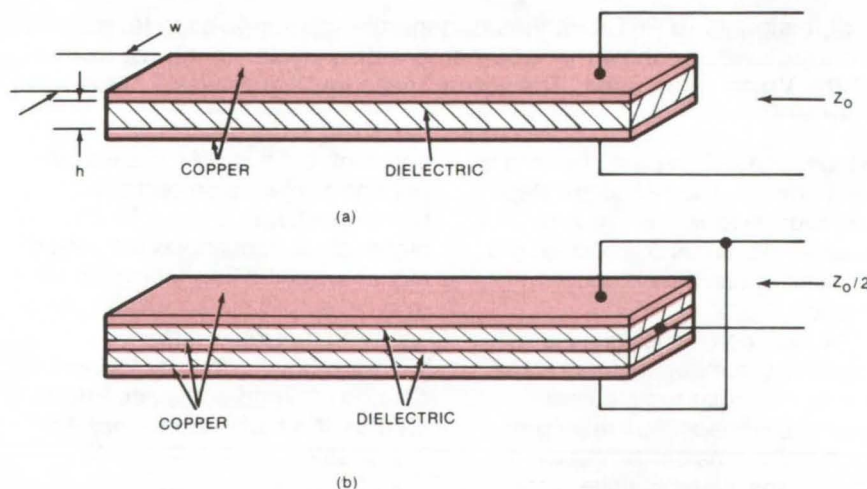


Figure 1. **Laminated Bus** consists of flexible copper strips separated by a thin layer of dielectric. The two-conductor structure (a) has a low characteristic impedance; paralleling, as shown in (b), halves this impedance.

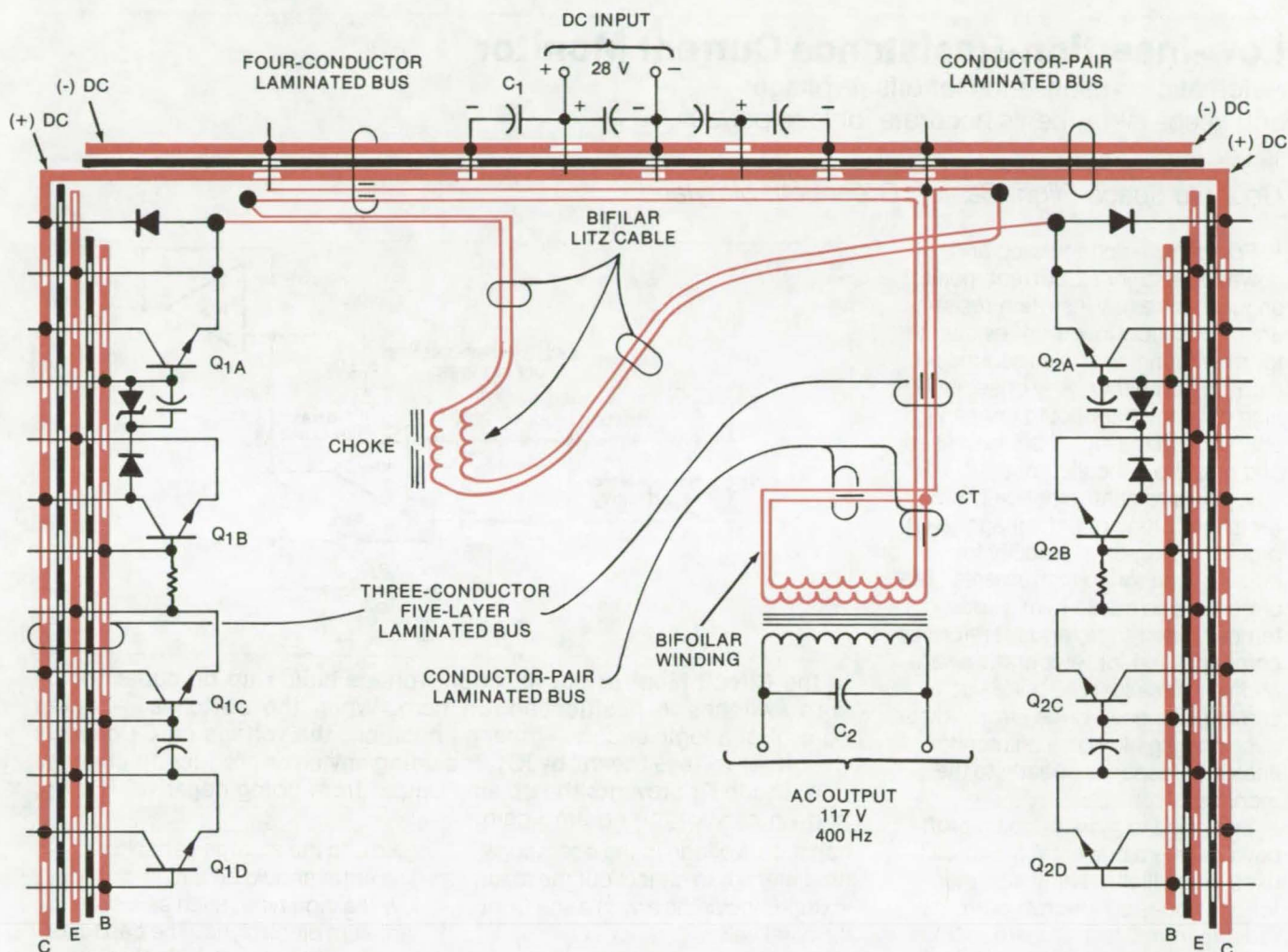


Figure 2. To **Prevent Losses and EMI**, this power static inverter circuit uses laminar strips and bifilar litz cable for low-inductance connectors. The concentric "swiss-cheese" holes in the laminated bus are for clearances and creepage. The choke is wound with bifilar litz cable, which also extends as low-inductance self-leads a sufficient distance from the cores to make connections practical; because the bifilar litz cable has been spun with two colors of insulation, separation of the many strands into the separate windings is a simple production procedure. The points at which the separation of cable strands is done are chosen with great care. Choke remote nodal points are connected by straight litz leads of one color that are but a fraction of an inch long. Self-leads and primary winding of the power transformer are by parallel-strip conductor pair; this winding procedure is known as "bifilar."

Impedances of the four different conductor-pair configurations are compared in the accompanying table.

The laminated bus and bifilar litz cable low-inductance connectors are used in the center-tapped power stage shown in Figure 2. Each of the

two transistorized power brackets has four 250-ampere switching devices in matched sets directly connected in parallel and with commutating diodes upon a five-layer laminated bus. The two power brackets are joined noninductively by a two-conductor laminated-bus transmission line, into which the input-filter capacitors are tapped.

This work was done by Andress Kernick of Westinghouse Electric Corp. for Johnson Space Center. No further documentation is available.
MSC-16730

Impedances of Various Conductor Pairs*		
Conductor Pair	Z ₀ (Ohms)	Conductor Dimensions
Laminated Bus	0.29	0.005 inch by 2 inches
Bifilar Litz Cable	0.48	(133) 0.0142-inch wires
Twisted Leads	64.5	0.1144-inch diameter
Lead-Over-Ground Plane	26.0	0.1144-inch diameter

*With 0.003-inch Kapton insulation

Low-Insertion-Resistance Current Monitor

Automatic compensation for offset voltage drift keeps instruments accurate for long periods.

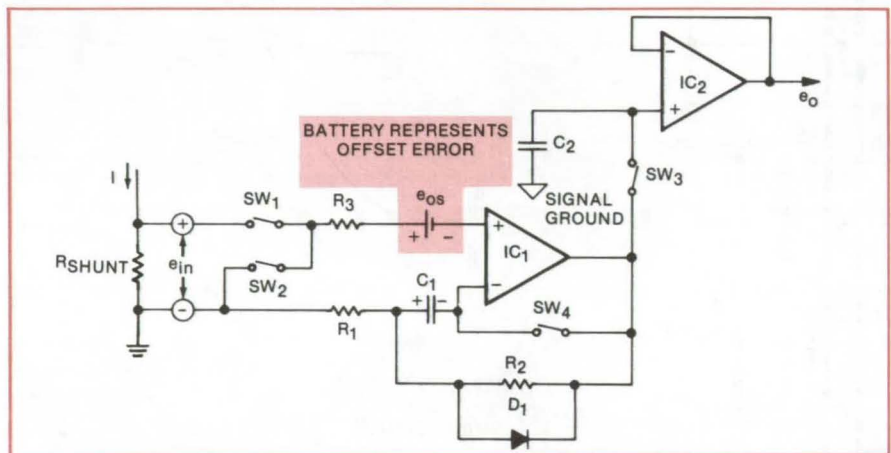
Goddard Space Flight Center, Greenbelt, Maryland

For low line-voltage drop and power dissipation, a current monitor should have a low insertion resistance. But a low insertion resistance for monitoring currents requires a high gain amplifier. Any offset in the high gain amplifier could conceivably exceed the signal being sensed and must be cancelled out.

A new circuit automatically corrects for drifting offset voltage (e_{os}), providing long-term stability for current-monitoring instruments. The circuit is also stable over a wide temperature range, and therefore no compensation for temperature variations is necessary. Besides consuming little power, the circuit introduces negligible noise on monitored lines and responds linearly to the monitored current.

Designed to monitor spacecraft power system currents, the circuit uses 2.5 milliohm shunts for monitoring various spacecraft currents ranging from 0 to 1 ampere to 0 to 20 amperes. The 0 to 1 ampere range requires a gain of 2,000 for a 0 to 5 volts output. Under such conditions, a conventional monitoring circuit would create a 2-volt error in the output for a 1 millivolt offset, if it were not corrected manually.

The figure shows the basic circuit for automatically correcting offset voltage drift. Essentially, the circuit is a switching arrangement that allows capacitor C_1 to charge to the offset voltage; then it applies the



In the **Circuit Monitor** above, offset voltage builds up on capacitor C_1 with switches in position shown here. When the switches — under control of a logic circuit — change position, the voltage on C_1 cancels the offset voltage “seen” by IC_1 , including any error-production changes in it. Diode D_1 prevents the op amp output from going negative. R_1 , R_2 , and R_3 control the op amp gain.

capacitor voltage to the operational amplifier IC_1 to cancel out the offset voltage, including any change from its initial value.

IC_1 produces a voltage proportional to the current through the shunt resistor. Operational amplifier IC_2 buffers the output signal for transmission to the data system for display, recording, or data processing. The cycle repeats: switches SW_1 and SW_3 open, SW_2 and SW_4 close, and so forth.

The integrated circuits are used for the operational amplifiers and for the switch control. A few discrete components are necessary, such as the resistors for adjusting op amp

gain and the storage capacitor C_1 . The latter should be a high-capacity, low-leakage type, such as a solid tantalum electrolytic. The capacitor voltage rating is not critical, since it “sees” only the offset voltage, which varies typically from 0 to ± 5 millivolts. The circuit reacts fairly quickly to current changes. Its reaction speed depends largely on the type of op amp and the oscillator frequency.

This work was done by John Paulkovich of Goddard Space Flight Center. For further information, Circle 6 on the TSP Request Card.
GSC-12278

Op-Amp Gyrator Simulates High Q Inductor

Practical operational-amplifier circuit facilitates inductorless filter synthesis.

Marshall Space Flight Center, Alabama

A gyrator circuit consisting of a dual operational amplifier and four resistors inverts the impedance of a

capacitor to simulate an inductor. This synthetic inductor has a high Q factor, good stability, wide band-

width, and an easily determined value of inductance that is independent of frequency. It readily

lends itself to integrated-circuit applications, including filter networks.

The gyrator circuit is shown in Figure 1, with a capacitor C connected across its output terminals. The impedance seen looking into its input terminals is very nearly $j\omega R^2C$, where R is the value of each of the four resistors in the circuit. Thus the input appears to be an inductor of value R^2C . (These formulas assume ideal characteristics for the operational amplifiers — infinite gain and infinite input impedance. However, practical op amps provide performance that is very close to ideal.)

To demonstrate the use of the capacitor-loaded gyrator to simulate an inductance, it was used in a simple narrow-band parallel L-C band-pass filter network. The test filter network is shown in Figure 2(a), and the experimental test data are plotted in Figure 2(b). The measured data agree closely with calculated data in the band pass. The bandwidth and curve shape are also very close. The effect of the operational-amplifier parameters on frequency response is to shift the center frequency slightly.

The usefulness of this gyrator circuit is limited to simulating inductors with one side grounded. However, it is possible to simulate a floating inductor by connecting two gyrators in series; this method is used quite extensively with all transistor gyrator circuits.

This work was done by William C. Sutherland of **Marshall Space Flight Center**. Further information may be found in NASA TM-X-64995 [N76-20367], "The Practical Operational-Amplifier Gyrator Circuit for Inductorless Filter Synthesis," a copy of which may be obtained at cost from the New England Research Application Center [see page A7]. MFS-23514

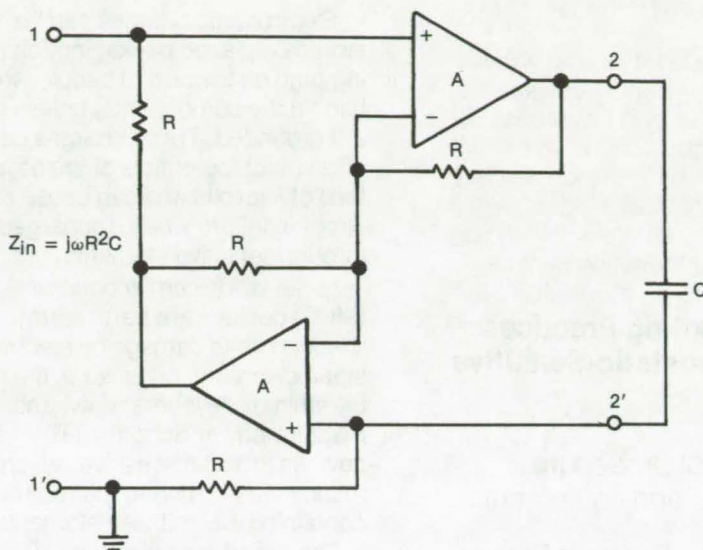
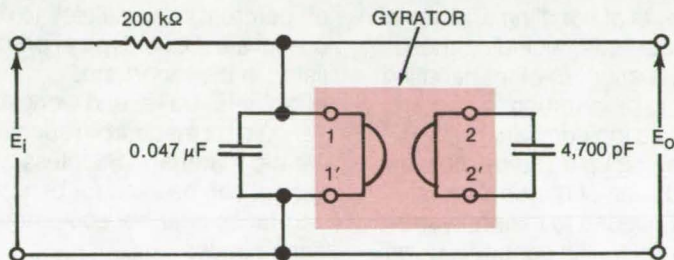
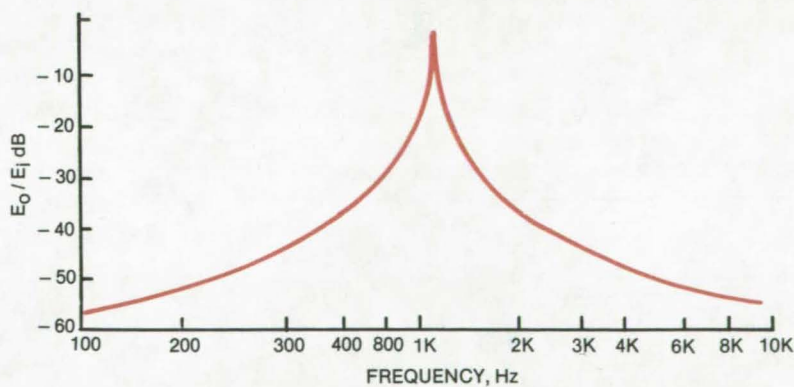


Figure 1. A **Gyrator Circuit** presents an input impedance that is reciprocal to the load across its output terminals. Thus this capacitor-loaded gyrator simulates an inductor of value $L = R^2C$. The thermal coefficients of the resistors determine temperature stability. Should dc inputs be expected in a particular application, a large blocking capacitor could be placed in series with the input for stability.



[a]



[b]

Figure 2. This **Narrow-Band L-C Filter** uses a gyrator-simulated inductance for L . The gyrator is represented by its standard symbol in the circuit diagram (a), and the filter response is shown in (b). The gyrator diagramed in Figure 1 provides stable, high Q inductance over a wide frequency range.

Books and Reports

These reports, studies, and handbooks are available from NASA as Technical Support Packages (TSP's) when a Request Card number is cited; otherwise they are available from one of NASA's Industrial Application Centers or the National Technical Information Service.

Safe Handling Practices for Electrostatic-Sensitive Devices

A review of procedures, materials, and equipment

A review, "Protective Requirements for Electro-Static Sensitive Components," is a detailed compilation of safe handling practices for MOS circuit elements and other devices that are susceptible to damage by electrostatic discharge. The review lists safety procedures for all aspects of handling and use of these components, including those for design, testing, in-plant handling, storage, and preparation for delivery. Also included are guidelines for setting up a static-free work station and a list of materials and equipment needed to maintain anti-static protection. An appendix gives the names and addresses of vendors of these items.

Electrostatic charges can be stored on plastic packaging, clothing, and on the skin of people who handle the components, unless they are grounded. These charges can often reach potentials of the order of tens of kilovolts and can cause catastrophic failure when discharged through sensitive elements.

Metal-oxide semiconductor (MOS) devices are particularly susceptible to damage by electrostatic discharge because of their ultrathin oxide layers. Low- and medium-power Schottky TTL devices are also sensitive, as are monolithic and hybrid microcircuits containing any of these elements.

The report compiles over 50 procedures that affect workers, packaging materials, equipment, and work areas. These procedures assure that there is a good conducting path to ground nearby sensitive components. Such a path is essential to allow static charge to leak off before it accumulates to dangerous levels. Some typical procedures listed in the report are:

- Cabinets, trays, and work surfaces should be made from special anti-static materials. Stainless-steel sheet can be used for bench work surfaces near hot equipment and chemicals.
- Ionized air blowers can be used to direct a stream of ionized (con-

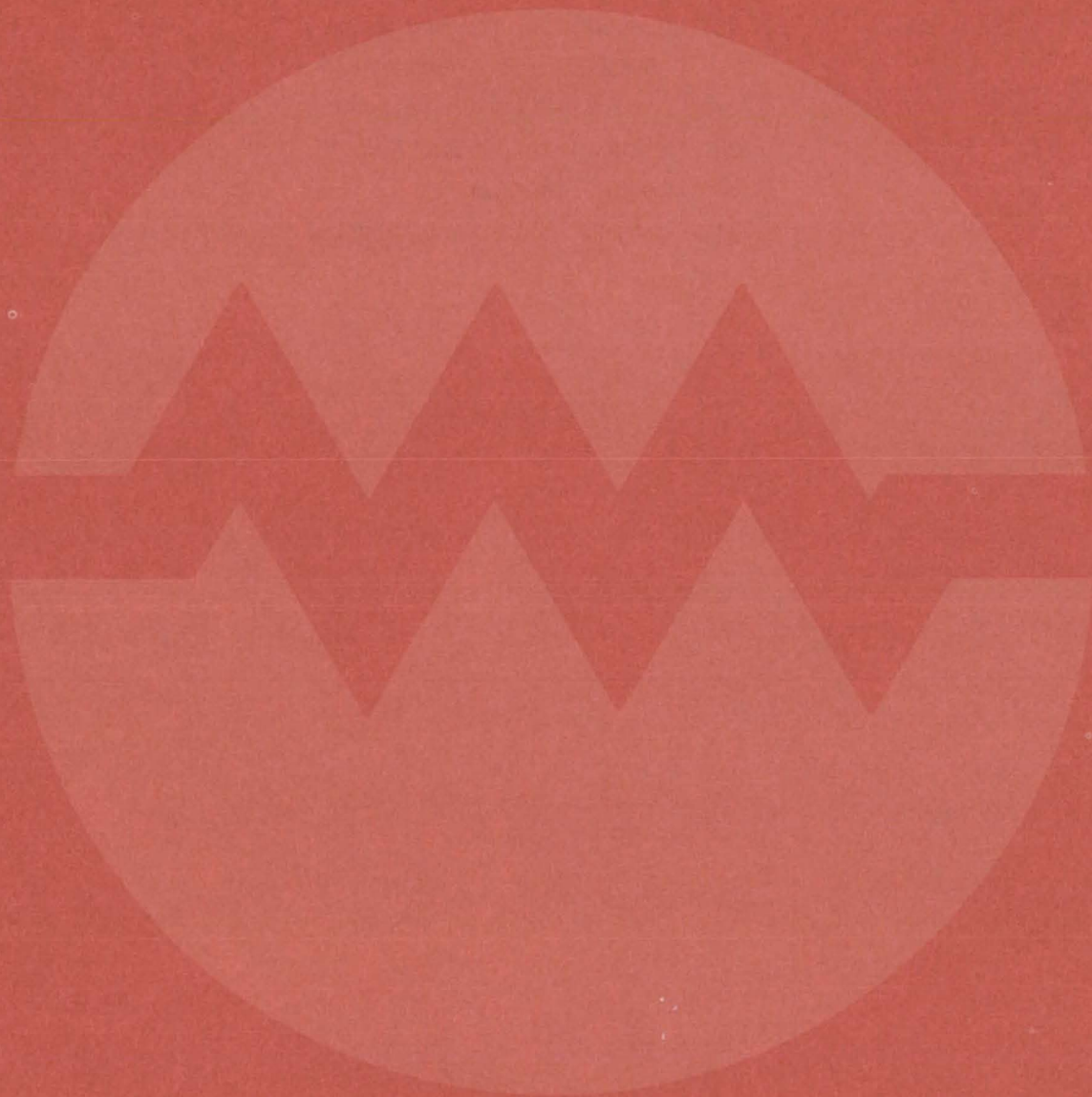
ducting) air over work areas.

- No nylon, permanent-press, or other synthetic clothing should be worn. Cotton clothing is preferred.
- No plastic-coated or otherwise-insulated handtools should be used.
- Circuit assemblers and test personnel should be grounded via wrist or ankle straps through a 0.25- to 2.0-megohm isolation resistor.

The review describes antistatic materials that have been developed for use in place of standard packaging materials and for the construction of boxes, cabinets, and trays. One such material is pink polyethylene, which obtains its antistatic properties from an impregnated liquid that migrates to the surface and forms a conductive layer. Orange nylon has similar antistatic properties but has superior physical and thermal properties in ultraclean applications. Another electrostatic-free material is black polyolefin, which contains impregnated carbon particles to give volume conductivity.

This work was done by Leigh L. Herring of Rockwell International Corp. for Johnson Space Center. To learn how to obtain a copy of the review, Circle 7 on the TSP Request Card.
MSC-16642

Electronic Systems



Hardware, Techniques, and Processes

- 323 "Printed-Circuit" Rectenna
- 324 Changing Sunlight to Microwaves: A Concept
- 325 Emergency-Vehicle VHF Antenna
- 326 Satellite-Based Interference Analyzer
- 327 Inkjet Color-Printer Control Interface
- 328 Measurement of Bit-Error Rate
- 330 Multiline Radar Scan
- 331 Changing NRZ Data to Biphase Logic

"Printed-Circuit" Rectenna

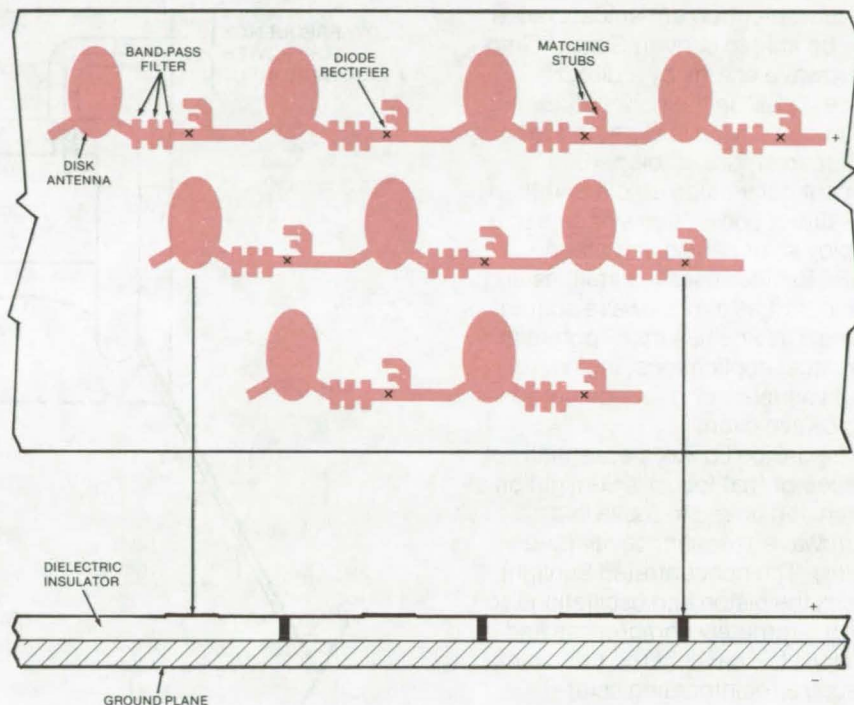
A proposed printed-circuit-like rectifier/antenna with reduced bulk could help pave the way toward transmission of microwave power.

Caltech/JPL, Pasadena, California

One of the possible "waves" of the future, microwave transmission of electric power, is the subject of extensive work at NASA's Caltech/JPL research labs. Recently, a printed-circuit rectifying antenna has been proposed as a less bulky structure for absorbing transmitted microwave power and converting it into electrical current. Most of today's rectennas are bulky dipole devices requiring special orientation for the absorption of significant amounts of power.

The printed-circuit approach, using microstrip technology and a circularly polarized antenna, would make polarization orientation unimportant and would allow much smaller arrays for a given performance. Copper-plate elements etched on a dielectric substrate would be flexible enough to conform to the surface shape of a vehicle. This would be particularly useful with proposed electric vehicles powered by beam microwaves. This approach is sufficiently promising that NASA plans to test it with an electrically powered aircraft in the near future.

A schematic of the proposed array is shown in the figure. The substrate is a Teflon/fiberglass (the dielectric); the microwave circuit elements are etched on it, using the printed-circuit techniques. These elements include circularly-polarized disk antennas (which replace horizontally or vertically polarized dipoles in earlier devices), band-pass filters, diode rectifiers, and matching stubs. These elements form a rectenna. Duplicate rectennas are cascaded and connected in series/parallel to make up an array.



"Printed" Rectifying Antenna is a pattern of disks, filters, and stubs fabricated by conventional photolithographic printed-circuit technology. Semiconductor diodes interspersed in the pattern change the received energy to direct current.

The rectenna array, including the ground plane, can be mounted integrally with the metal surface of a vehicle. The skin is integrated with the microstrip dielectric; the ground plane is the negative dc output terminal to which the negative terminals of the diodes are mounted. The microstrip etched plate forms the positive dc output terminal. The ground plane would, in most cases, be an aluminum or copper sheet or a foil backing on the dielectric, connected electrically to the vehicle metal skin. RF transparent coatings

could be applied over the microstrip for aerodynamic flow and the protection of etched circuit elements.

This work was done by Richard M. Dickinson of **Caltech/JPL**. For further information, Circle 8 on the TSP Request Card.

This invention is owned by NASA, and a patent application has been filed. Inquiries concerning nonexclusive or exclusive license for its commercial development should be addressed to the Patent Counsel, NASA Resident Legal Office-JPL [see page A8]. Refer to NPO-13886.

Changing Sunlight to Microwaves: A Concept

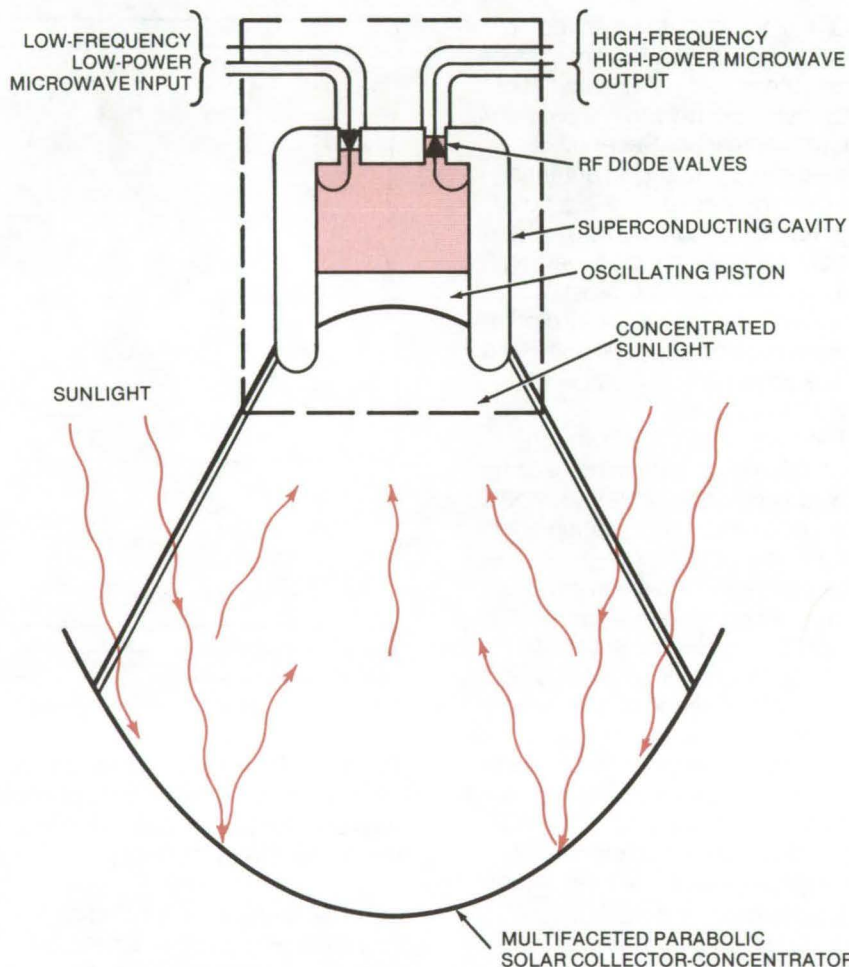
A suggested method for using light to compress an electromagnetic microwave field and thereby increase its energy

Caltech/JPL, Pasadena, California

A new electromechanical device may be able to convert Sunlight into microwave energy by a direct process. Still in the conceptual stage, the device is expected to be lighter and more efficient (90 percent conversion efficiency) than less-direct conversion systems that employ solar panels and magnetrons. Besides uses in satellites and spacecraft as a microwave source, the new device has many potential terrestrial applications, including use in a fuel-saving Sun-powered microwave oven.

The device consists essentially of a reflector that focuses Sunlight on a piston that is free to move in a microwave-resonant cavity (see figure). The concentrated Sunlight forces the piston into oscillations so that it alternately compresses and expands the cavity. (The principles of such a reciprocating solar-powered piston are well understood.) In effect, the piston compresses the electromagnetic field in the cavity created by electromagnetic waves flowing through it. In so doing, the piston increases the energy of the waves — they exit at higher frequency and power than they entered.

Until recently, it has been impossible to contain electromagnetic radiation long enough for it to interact with a mechanical system. In fact, if it were made of ordinary metals, the device in the figure simply wouldn't work. The microwave energy (at frequencies of billions of cycles per second) would dissipate into the walls before the piston (operating at only hundreds of cycles per second) could move more than a negligibly small distance. However, the superconducting materials now available, cooled to liquid helium temperatures, can contain the microwaves long enough for interaction.



Concentrated Sunlight Makes a Piston Oscillate in a microwave cavity. In so doing, the light increases the microwave energy in the cavity. The cavity is cooled to liquid helium temperature to make it superconducting.

The device operation is based on the Boltzmann-Ehrenfest theorem: Under conditions of adiabatic deformation, the number of photons contained in a lossless resonator remains constant. Since the energy in a cavity is the product of the number of photons and the instantaneous characteristic frequency, decreasing the volume of the cavity (thereby increasing its characteristic frequency) will increase the energy. For example, if the cavity is com-

pressed to one-tenth its original volume, its frequency and energy content would increase 10 times. If the compression is repeated at a high rate, a small amount of power at a low microwave frequency becomes a large amount of power at a high microwave frequency.

In another version of the device, the piston could be moved by a rotating crank instead of by Sunlight. Mechanical energy could then be converted directly into microwave

energy; or conversely, microwaves could be converted directly into kinetic energy. It may even be possible to design a self-excited device in which no external microwave energy need be added.

However, certain technical problems must be solved before any

devices can be built. A way must be found to cool the moving piston to cryogenic temperatures, and superconducting alloys of adequate strength must be developed.

This work was done by Richard M. Dickinson of Caltech/JPL. For

further information, Circle 9 on the TSP Request Card.

Inquiries concerning rights for the commercial use of this invention should be addressed to the Patent Counsel, NASA Resident Legal Office-JPL [see page A8]. Refer to NPO-14068.

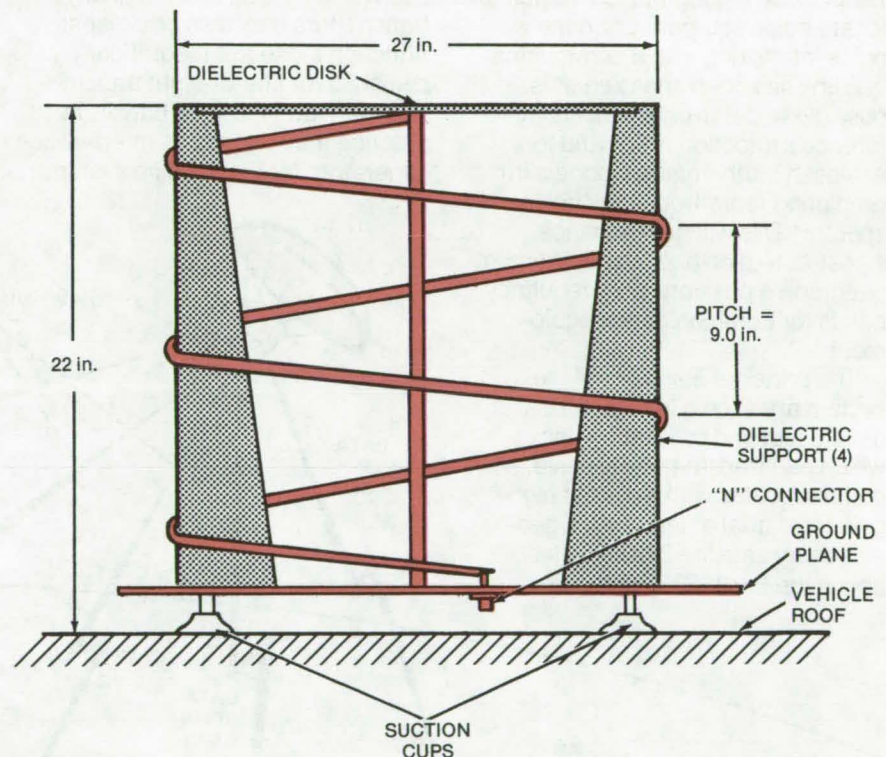
Emergency-Vehicle VHF Antenna

Roof-mounted antenna that provides two-way communication requires no pointing.

Marshall Space Flight Center, Alabama

A VHF antenna mounted on the roof of a moving vehicle can provide two-way communication while the vehicle moves at high speed. The antenna, which was originally designed to communicate with a distant station via an earth satellite, does not have to be aimed. Instead, its wide-beamwidth characteristic, sufficient off-axis gain, and generally right circularly polarized signal allow continuous communication with a fixed vertical axis. The antenna, is strong and small to withstand vehicle speeds up to 70 miles per hour (112.7 km/h); it has proved extremely successful in electrocardiogram transmission tests between a medical services vehicle and a hospital emergency room.

The antenna used in the medical application is shown in the figure. It is a low-gain helix with reduced spacing between turns to decrease its height and increase stability. Two and one-half turns of 5/8-in. (1.59-cm) copper tubing are wound around four dielectric supports. The circumference of each loop is equal to one wavelength at a frequency that is midway between the receive and transmit frequencies (135.675 and 149.195 MHz, respectively). The unit is assembled on an aluminum ground plane 35 in. (88.9 cm), in diameter or 8 in. (20.3 cm) larger than the element diameter. Inherent in the design is the use of the vehicle roof as an extension of the ground plane.



Helical VHF Antenna Mounts on the Roof of a moving vehicle to communicate with distant stations via an Earth satellite. The antenna requires no pointing and can provide two-way communication while the vehicle moves at high speed.

Initial tests revealed an antenna gain of 6.5 dB axially and 4.5 dB in the direction of the satellite (elevation 48°). The antenna had sufficient circular polarization to permit two-way operation while pointed vertically.

This work was done by R. E. Anderson, A. W. Carlson, and J.

Lewis of General Electric Co. for Marshall Space Flight Center. No further documentation is available. MFS-23638

Inquiries concerning rights for the commercial use of this invention should be addressed to the Patent Counsel, Marshall Space Flight Center [see page A8]. Refer to MFS-23638.

Satellite-Based Interference Analyzer

Mobile system can locate and measure terrestrial noise sources.

Goddard Space Flight Center, Greenbelt, Maryland

A satellite-based system can identify terrestrial sources of radio-frequency interference and measure their frequency spectra and amplitudes. The system, which was designed to protect satellite communication networks, measures the entire noise spectrum over a selected frequency band and can raster-scan a geographical region to locate noise sources. Once the noise interfering with a communication link has been analyzed, it is possible to determine realistic interference protection ratios and to establish mathematical models for predicting radio-frequency noise spectra. This will help enhance signal-detection and locate optimum geographic positions and frequency bands for communication equipment.

The principal elements of the system are shown in Figure 1. A mobile test and calibration unit, which can transmit and receive, communicates with a distant high-gain terrestrial antenna via a geostationary satellite 22,000 miles above the Earth. The high-gain

antenna may be located outside the region being scanned and communicates with a base station containing data-storage and processing equipment. In a typical application, the satellite is one element of a larger communication network that includes several Earth-based antennas. Radio-frequency sources such as television and telephony transmitters may also be present. Although these are theoretically designed for line-of-sight transmission with low side-lobe power, in practice they can act as interference generators for the satellite system.

The noise analysis is carried out while other communication signals are blocked. A synchronization signal is broadcast through the system to initiate a calibration sequence. In the proposed system, which is designed to operate around 6 GHz, signals of known power level are transmitted from the mobile unit to the satellite and are received at the downlink high-gain antenna.

Typically, four power levels within each 10-MHz frequency band are used, with the calibration points being 100 MHz apart. These data are converted to digital form and are

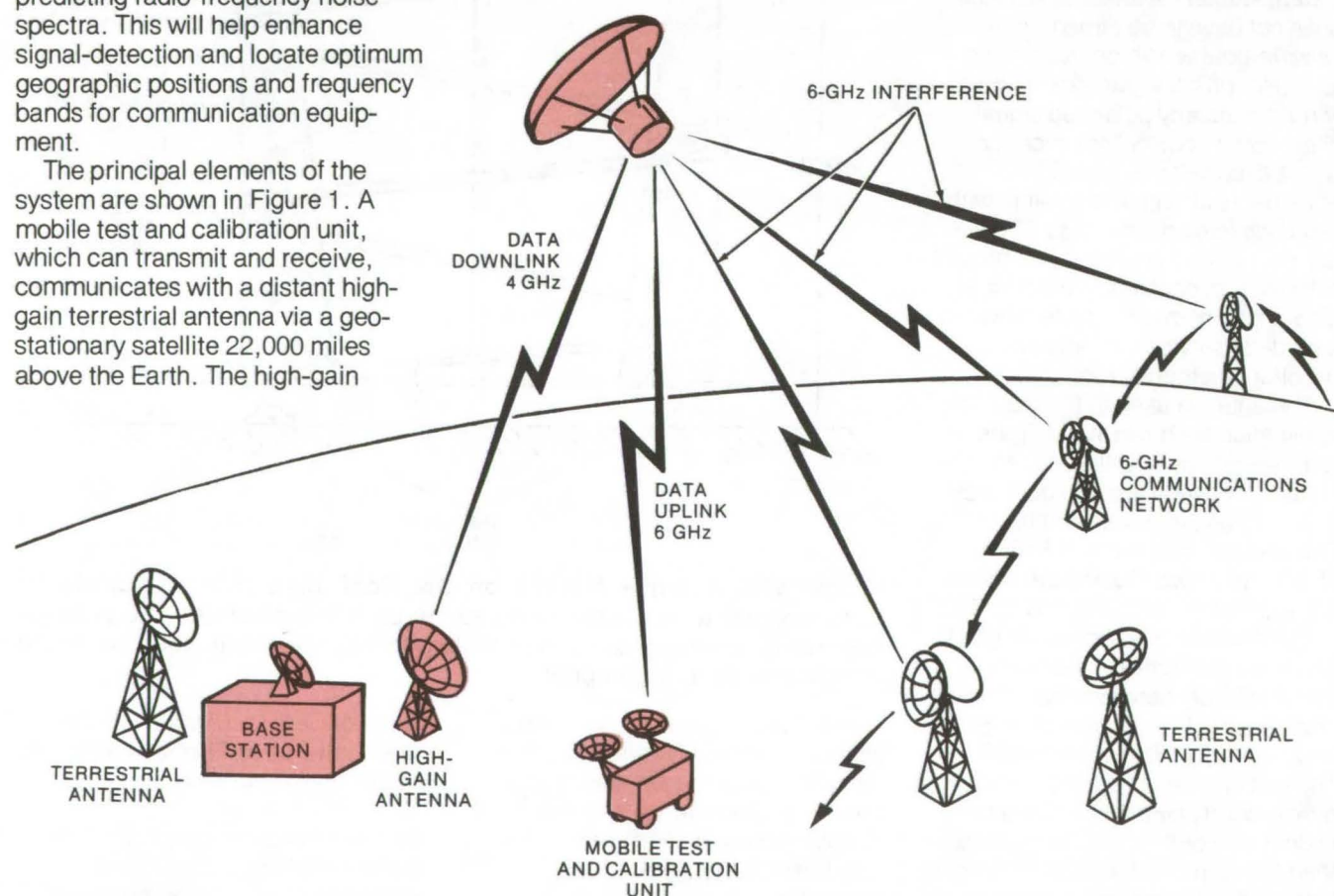


Figure 1. **Radio-Frequency Interference Sources**, such as the 6-GHz communications network shown, can be located and analyzed in frequency and amplitude by this satellite-based system. Calibration signals from the mobile unit are transmitted via the satellite to a computer in the base station. These are compared with the noise input to the satellite. The satellite is part of a larger communications network that includes the terrestrial antennas shown.

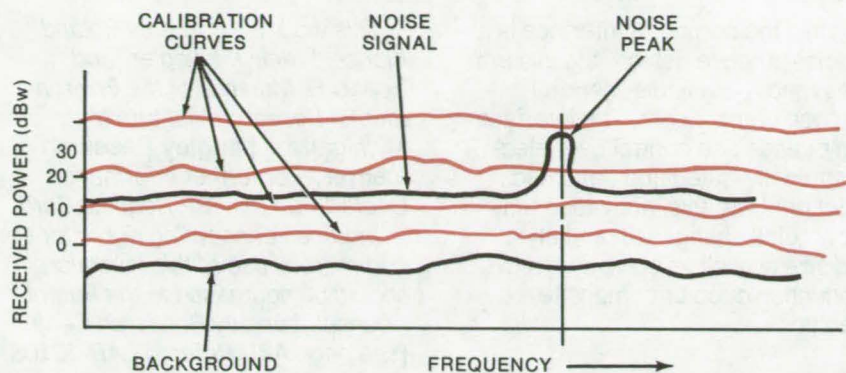


Figure 2. Calibration Traces Are Compared With the Noise Signal to determine the amplitude of the noise spectrum. The background signal is obtained with the antenna pointing at a low-noise source such as the ocean.

stored in the base computer memory. In this way, four calibration traces at different power levels are permanently recorded (Figure 2). These can then be compared with noise signals recorded by the antenna while transmission from the mobile unit is blocked. For the noise sampling, the entire frequency band is covered in 10-KHz intervals.

Thirty-nine samples are taken in each interval, averaged, and compared with the calibration traces to determine the noise spectrum. The computer is programmed to reject points with excess scatter about the average.

In the proposed system, detailed scanning is carried out over a roughly-oval-shaped geographical

area of approximately 200 by 50 mi (322 by 805 km). When scanning is complete, the mobile unit can be relocated in a new, not necessarily contiguous, region. An overview of noise sources can be made by gross raster scanning of relatively large regions, such as the 48 contiguous States. When a signal peak is observed, it is converted from a set of time displacements to the spatial position of the noise source. Detailed scanning can then be carried out at that position.

This work was done by Henry Varice of **Goddard Space Flight Center** and Klaus Johannsen and Samuel Sabaroff of Hughes Aircraft Corp. For further information, Circle 10 on the TSP Request Card.

This invention is owned by NASA and a patent application has been filed. Inquiries concerning nonexclusive or exclusive license for its commercial development should be addressed to the Patent Counsel, Goddard Space Flight Center [see page A8]. Refer to GSC-12150.



Inkjet Color-Printer Control Interface

Computer-driven interface efficiently controls inkjet printer.

Langley Research Center, Hampton, Virginia

A special-purpose interface that permits computer-driven control of inkjet printers has been developed and is believed to be the first device of this kind in operation in the United States. Because impact printers, due to physical limitations inherent in such electromechanical systems, cannot achieve operational speeds commensurate with the data-processing and data-transfer capabilities of computers, inkjet printers appear to be an answer to the problem of high-speed peripheral output devices for computer systems. The inkjet-printer control interface was developed to provide high-resolution color-classification maps quickly and economically from multispectral data.

The inkjet printer uses three color-negative inkjet streams, which are electrostatically controlled with pulse-duration modulation, to produce an image on a sheet of paper. The printer produces a picture element size of 0.008 by 0.008 in. (0.2 by 0.2 mm) for a picture sheet size up to the standard 8-1/2 by 11 in. (21.5 by 28 cm), or up to 1,000 x 1,400 elements per sheet. Each pixel is printed by three separate inkjets using three color-negative primary colors: magenta, cyan, and yellow. Each primary color can be pulse controlled in its density over 40 quanta, providing a color range per element of approximately 64,000 (40^3) separate colors. The printer operates at a rate of approximately 50 μ s per pixel.

The computer interface has two major parts. One part turns the three inkjets on and off; the other part controls the stepper motor. The inkjets are controlled by turning them on for a period of $n/128 \times 50 \mu$ s, where n is under computer control. The stepper motor can cause the printer to slew right or left, to make a large number of steps while not in the print mode, to step at the end of each line of print, and to step while printing.

The interface permits efficient control of the 10 signal lines in the inkjet printer. Six of these lines are input to the printer:

- drum motor on,
- stepper motor direction,
- stepper motor step,
- ink color 1 on,

(continued next page)

- ink color 2 on, and
- ink color 3 on.

Three of the other four printer signals are:

- power on,
- print head at left margin, and
- print head at right margin.

The remaining signal indicates that the rotating drum is at the proper position to start a line of print.

While the computer interface is a special-purpose design, the system uses readily-available, general-purpose components. The interface can provide fine control over electrostatically-gated and deflected inkjet printers; this innovation may allow quick changes in print style and size as well as computerized production of color composite graphics.

This work was done by Roland Kistler, Frank J. Kriegler, and Robert E. Marshall of the Environmental Research Institute of Michigan for **Langley Research Center**. For further information, Circle 11 on the TSP Request Card.

Inquiries concerning rights for the commercial use of this invention should be addressed to the Patent Counsel, Langley Research Center [see page A8]. Refer to LAR-12103.

Measurement of Bit-Error Rate

Bit-tracking threshold is determined by length of pseudorandom code sequence, not by bit rate.

Lyndon B. Johnson Space Center, Houston, Texas

The bit-error rate of an RF digital communication link can be measured at low signal-to-noise ratios by a new technique. In this method, as in earlier ones, identical pseudorandom sequences of pulses are generated at the transmitter and receiver of the link. However, comparison of the two sequences at the receiver involves an integration that makes the bit-tracking threshold depend on the length of the pseudorandom sequence, rather than on the actual rate of transmission of individual bits.

The pseudorandom generator, shown in Figure 1, consists of a shift register and an Exclusive-OR gate driven by a clock signal. It outputs a pulse-coded signal to the link transmitter to simulate pulse-code-modulated data. The signal is transmitted to the receiver site where it is processed in a tracking loop with a match filter to detect logical 1's and 0's.

The tracking loop, indicated in color in Figure 2, locks to the incoming waveform so that the tracking code matches bit for bit with the incoming code. The tracking loop can track the incoming signal well above the threshold if the code is long enough.

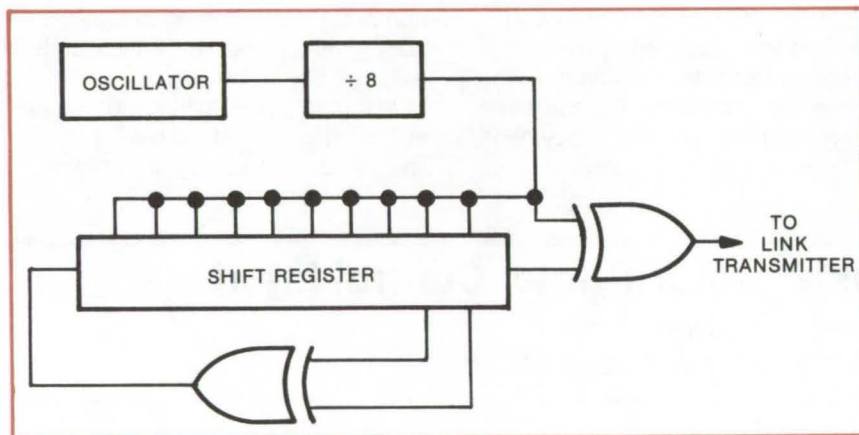


Figure 1. The **Pseudorandom Code Generator** applies a sequence of logical ones and zeros to the input of the RF transmitter, simulating pulse-code modulation, as a test signal to the digital communication link. The code generator consists of a shift register and an Exclusive-OR driven by a clock signal.

In the circuit of Figure 2, the received signal is multiplied by a tracking clock that has been shifted by 90° . The demodulated waveform with noise is integrated every other bit (interleaved). The received signal is integrated over the total bit period and then is dumped. The integrate, hold, and dump command is sampled at the end of each bit and is stored, a procedure that results in a delayed pseudorandom bit.

Bit-error rate is measured by comparing each generated pseudorandom-code bit with the delayed bit. Identical bits indicate no error; if the bits differ, a level change occurs. Bit-error rate produced by sampling is the total number of errors divided by the total number of bits received and can be measured for various signal-to-noise ratios. The technique thus is used to optimize the performance of link

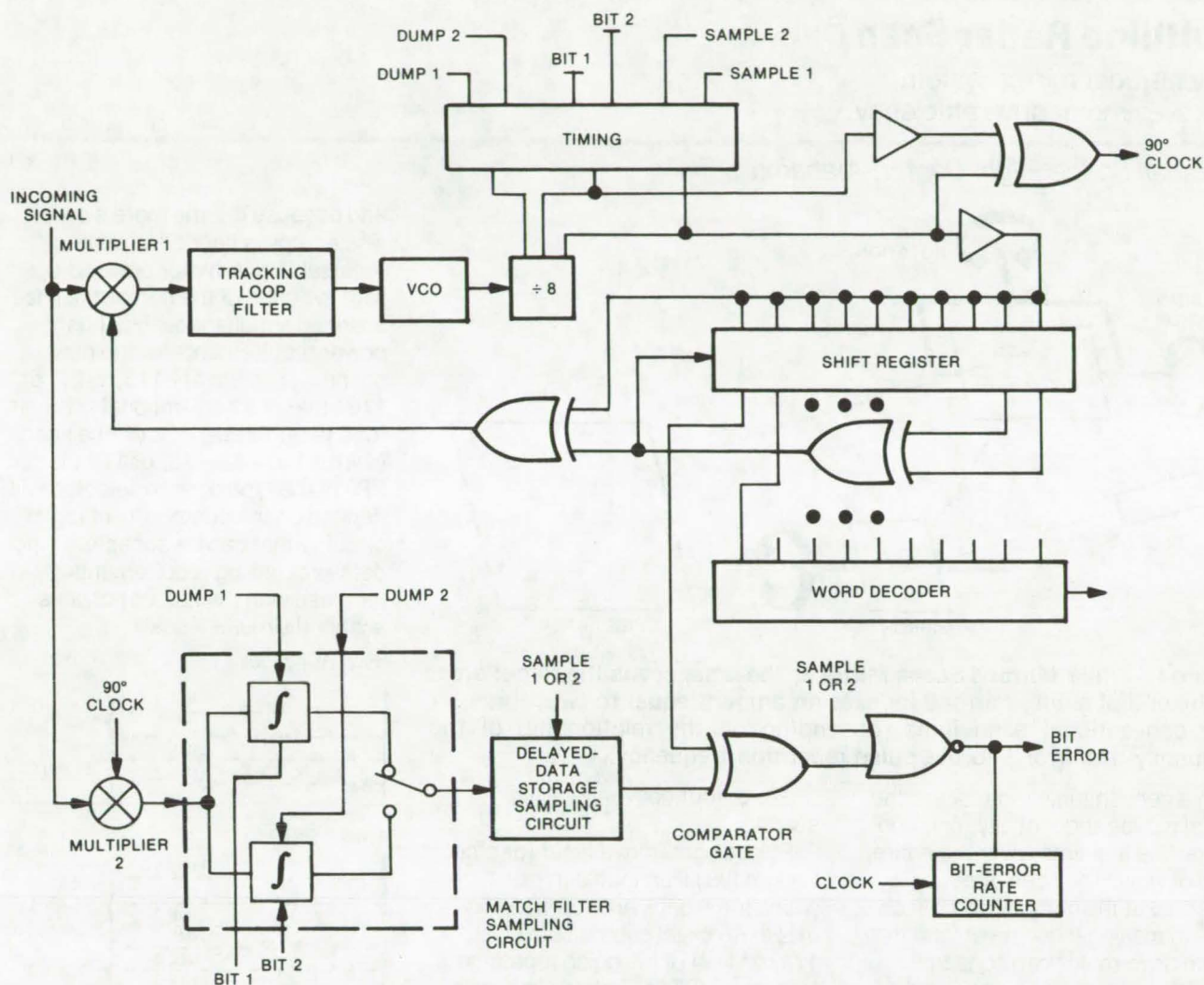


Figure 2. **Bit-Error Rate** is measured at the receiving site by the circuit shown above. The signal is fed via multiplier 1 to the tracking loop/filter and voltage-controlled oscillator (VCO) that begin to track the incoming signal. A shift register and an Exclusive-OR gate reproduce the pseudorandom code in response to the VCO. The register shortly matches the test code so that the reproduction of the test signal matches the test signal itself. (Matchup occurs when the incoming signal is in phase quadrature relative to the split-phase tracking signal.) The incoming signal then is routed through multiplier 2 by a 90° clock signal to produce an output that is alternately integrated in the match filter sampling circuit, then is sampled and stored in the delayed-data storage circuit. Circuit output does not define whether the incoming digital pulse is a "1" or a "0"; rather, it represents the probability that the detected bit is in one particular state. A comparator gate compares, bit by bit, the reproduction of the test signal from the shift register with the output from the delayed-data storage circuit. When the two input signals differ, the NOR gate delivers a pulse to a bit-error rate counter; the counter increments in response to the NOR gate.

system subassemblies and components comprising the link, via the adjustment of filters, clipping levels, and phase linearity to bring the link closer to its theoretical limit of bit-error probability.

This work was done by Joe Fowler and Herbert S. Kobayashi of Johnson Space Center and William Kurple of Lockheed Electronics Co., Inc. For further information, Circle 12 on the TSP Request Card.

This invention is owned by NASA, and a patent application has been filed. Inquiries concerning nonexclusive or exclusive license for its commercial development should be addressed to the Patent Counsel, Johnson Space Center [see page A8]. Refer to MSC-12743.

Multiline Radar Scan

Optical-radar mirror system improves motor drive efficiency.

Marshall Space Flight Center, Alabama

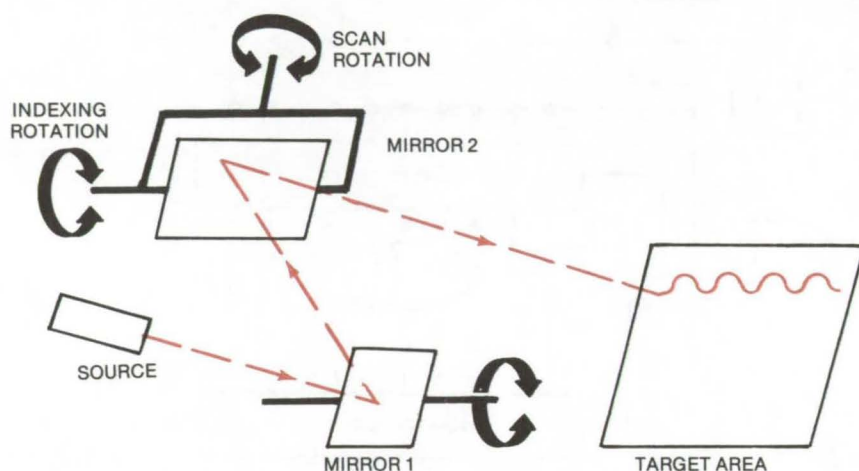


Figure 1. While **Mirror 1 Scans Mirror 2**, the latter scans the target area. At the end of a line, mirror 2 indexes an amount equal to two, three, or four conventional scan lines, depending on the relationship of the frequency of mirror 1 to the pulse repetition frequency.

In a conventional radar scan, the beam moves sequentially, one horizontal line at a time, over the entire field of view. The scan direction is reversed at the completion of each line. In making these reversals, the beam drive motor can consume considerable energy since it must repeatedly decelerate and then reaccelerate.

A new scanning scheme is considerably more efficient than conventional scanning. Originally designed for optical radar in space vehicles, the scheme may also find uses in site-surveillance security systems and in other industrial applications. It should be particularly useful when a system must run on battery energy, as would be the case during power outages.

The scheme uses two mirrors to reflect the light beam. One mirror scans a small angle at a high frequency; the other moves slowly at right angles to the first (see Figure 1). The motion of the first mirror has a precise relationship to the repetition frequency and phase of the optical-radar pulses. Depending on the relationship, a single line scan of the mirrors is equivalent to two,

three, or four conventional line scans.

Pulsed light from a laser (or other transmitter) illuminates mirror 1, which turns back and forth on its axis at an exact submultiple ($1/2$, $1/3$, or $1/4$) of the pulse repetition frequency (PRF). To keep in phase with the pulses, the mirror starts its cycle on the leading edge of a pulse.

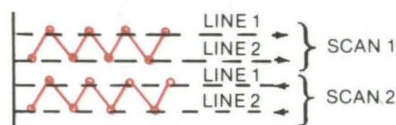
Mirror 1 thus directs a reciprocating beam of pulsed light on mirror 2. The latter mirror moves the beam at constant angular velocity across the width of the target area. At the end of a line, mirror 2 indexes to the next line. The process repeats until the entire target area has been scanned.

With mirror 1 rapidly reciprocating and mirror 2 slowly turning, the beam traces zigzag patterns across the target area. If mirror 1 reciprocates at $1/2$ the pulse repetition frequency, each horizontal traversal of the beam covers two ordinary scan lines; if it reciprocates at $1/3$ or $1/4$ the PRF, the beam covers three or four ordinary scan lines (see Figure 2).

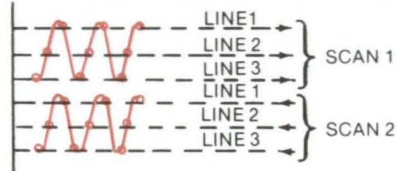
Since mirror 2 reverses less frequently than in a conventional scan

and because it turns more slowly, less energy is needed to make a reversal. Drive-motor power drops with the cube of the number of lines scanned simultaneously. Thus, power requirements for the new scanning system are $1/8$, $1/27$, or $1/64$ that of a conventional scanner for a two-, three-, or four-line scan (mirror 1 at $1/2$, $1/3$, or $1/4$ the PRF). The type of scan selected will depend on the complexity of logic circuitry that can be accepted, since data-processing requirements increase with the number of lines scanned simultaneously.

TWO-LINE SCAN



THREE-LINE SCAN



FOUR-LINE SCAN

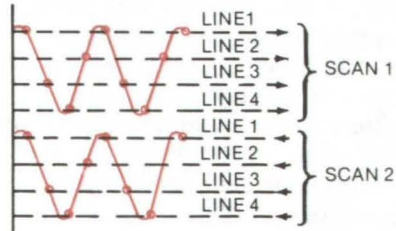


Figure 2. Pulsed Beam Traces a Zigzag Course over two, three, or four lines of the target area, according to whether mirror 1 is synchronized at $1/2$, $1/3$, or $1/4$ the radar pulse repetition frequency.

This work was done by Samuel Levinson of United Aircraft Corp. for Marshall Space Flight Center. For further information, Circle 13 on the TSP Request Card.
MFS-23252

Changing NRZ Data to Biphase Logic

An inexpensive circuit converts a nonreturn-to-zero data stream into a biphase data stream.

Lyndon B. Johnson Space Center, Houston, Texas

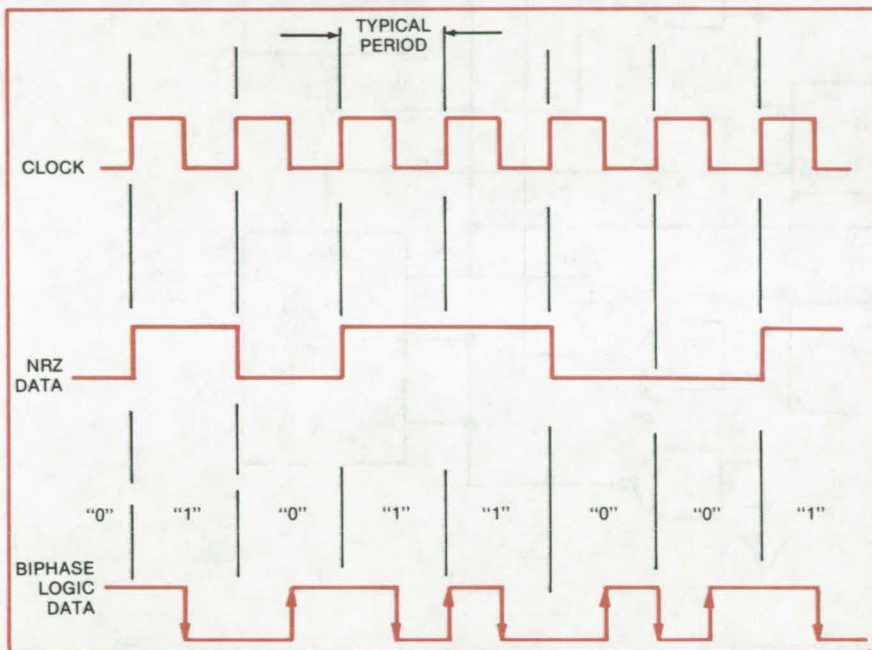


Figure 1. The Coding of Data in nonreturn-to-zero (NRZ) and biphase logic formats is illustrated here. Logic states are represented by high or low levels in NRZ and by positive or negative transitions (at period midpoint) in biphase.

A simple arrangement of four integrated circuits can change a stream of binary data from nonreturn-to-zero (NRZ) coding to biphase logic coding. The NRZ format represents logic states by high or low signal levels — high for logic "1" and low for logic "0" — and the level does not change between successive "1's" or successive "0's." Biphase logic represents states by appropriately-timed signal transitions: Logic "1" is indicated by a transition from high level to low level at the midpoint of the clock period; and logic "0," by a midpoint transition from low to high level. The clock stream should have a positive edge at the beginning of a period and a negative edge at

midpoint. Figure 1 illustrates the NRZ and biphase formats in a comparative presentation.

The concept of the circuit for converting NRZ to biphase format is extremely simple. First, sense the state of the NRZ data, and set the data output level to the same state (i.e., "1" = "1"). Second, at mid-clock period, change the output state to the opposite state (i.e., "1" to "0" or "0" to "1"). The implementation is also simple, as can be seen in the circuit diagram in Figure 2. The conversion requires a clock stream of 50 percent duty cycle, an NRZ data stream, and an inverted NRZ data stream. The inversion is done in a shift register. Each of the two NRZ data streams biases a

two-input NAND gate (G_1 and G_2) to inhibit or enable paths to the 'preset' and 'clear' inputs of an output register. A "1" in the data ("0" in the inverted data) enables a path to the preset input; a "0" enables the clear input. The data streams have no other function in this circuit.

The negative edge of the input clock triggers one-shot "A," the 150-nanosecond output of which is passed through the enabled gate to activate the register. The clock positive edge triggers one-shot "B," the 150-nanosecond output of which is passed through a two-input NAND gate (G_3) to the clock input of the register. This causes the register output to change state and complete the conversion. The two one-shots are used in order to provide trigger pulses that activate the output register but do not inhibit succeeding actions. Action is started by the clock negative edge to insure that the input data have become stable before the register is operated, thus insuring a valid output. A clock stream for the biphase logic is output with the data. A twin register (same package) is 'preset' (Q output raised) at the same time data are sensed and is clocked simultaneously with the data register. The waveforms in Figure 2 illustrate the operation of the circuit.

This circuit is implemented using four transistor-transistor logic (TTL) integrated-circuit modules with multiple circuits per module. This selection of integrated circuits and wiring enables the control and balancing of propagation delay without requiring excessive and expensive hardware. The circuit configuration exhibits typical propagation delays of half a clock period plus 32 ± 5 nanoseconds.



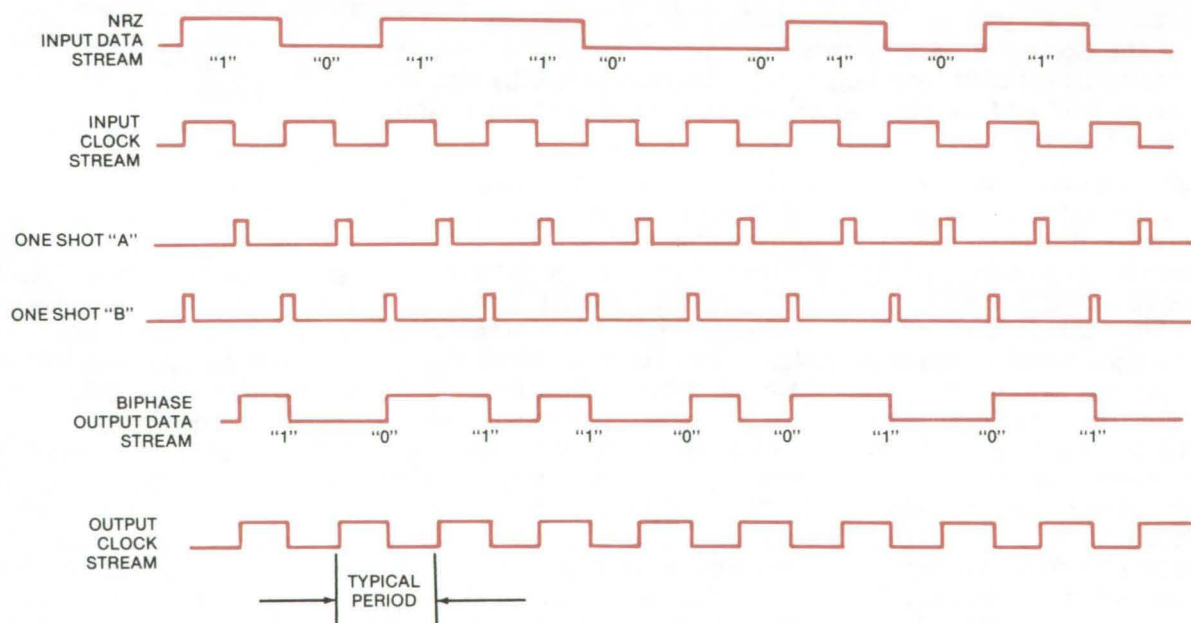
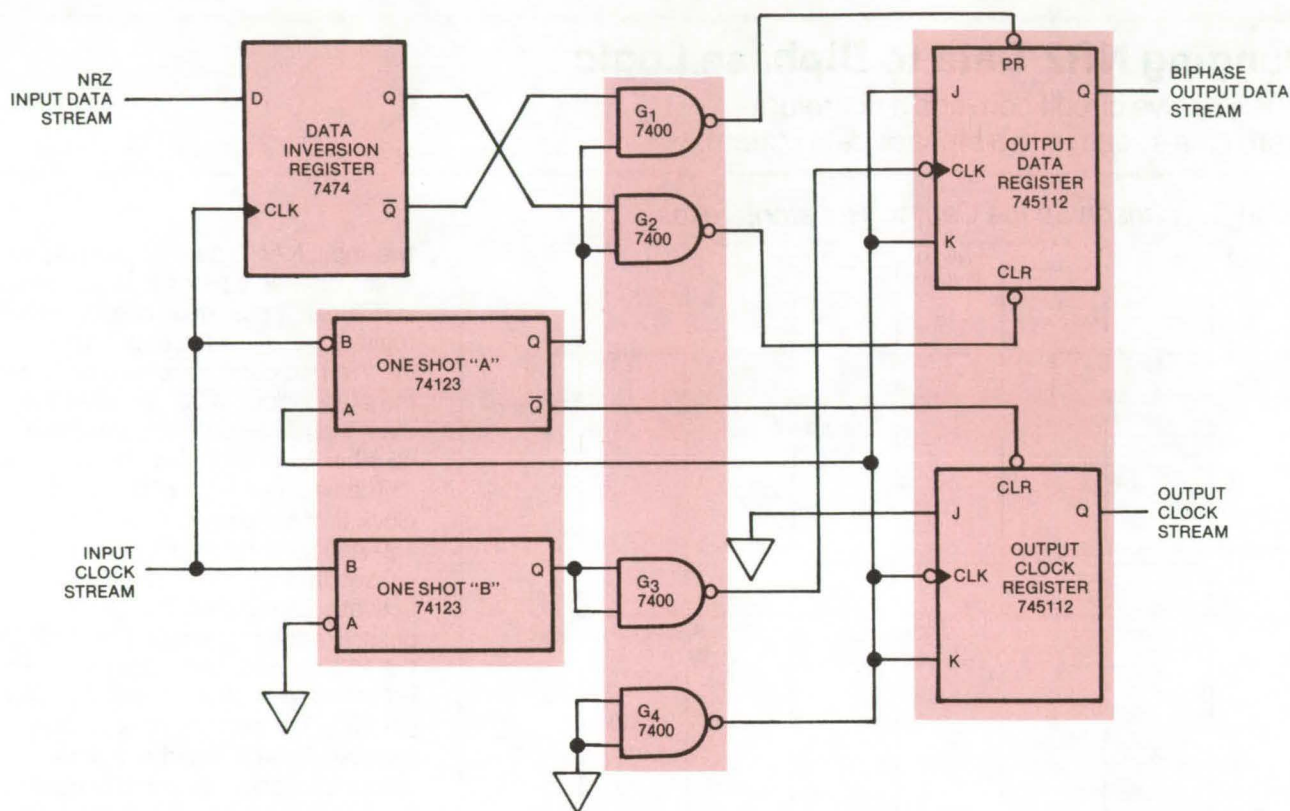
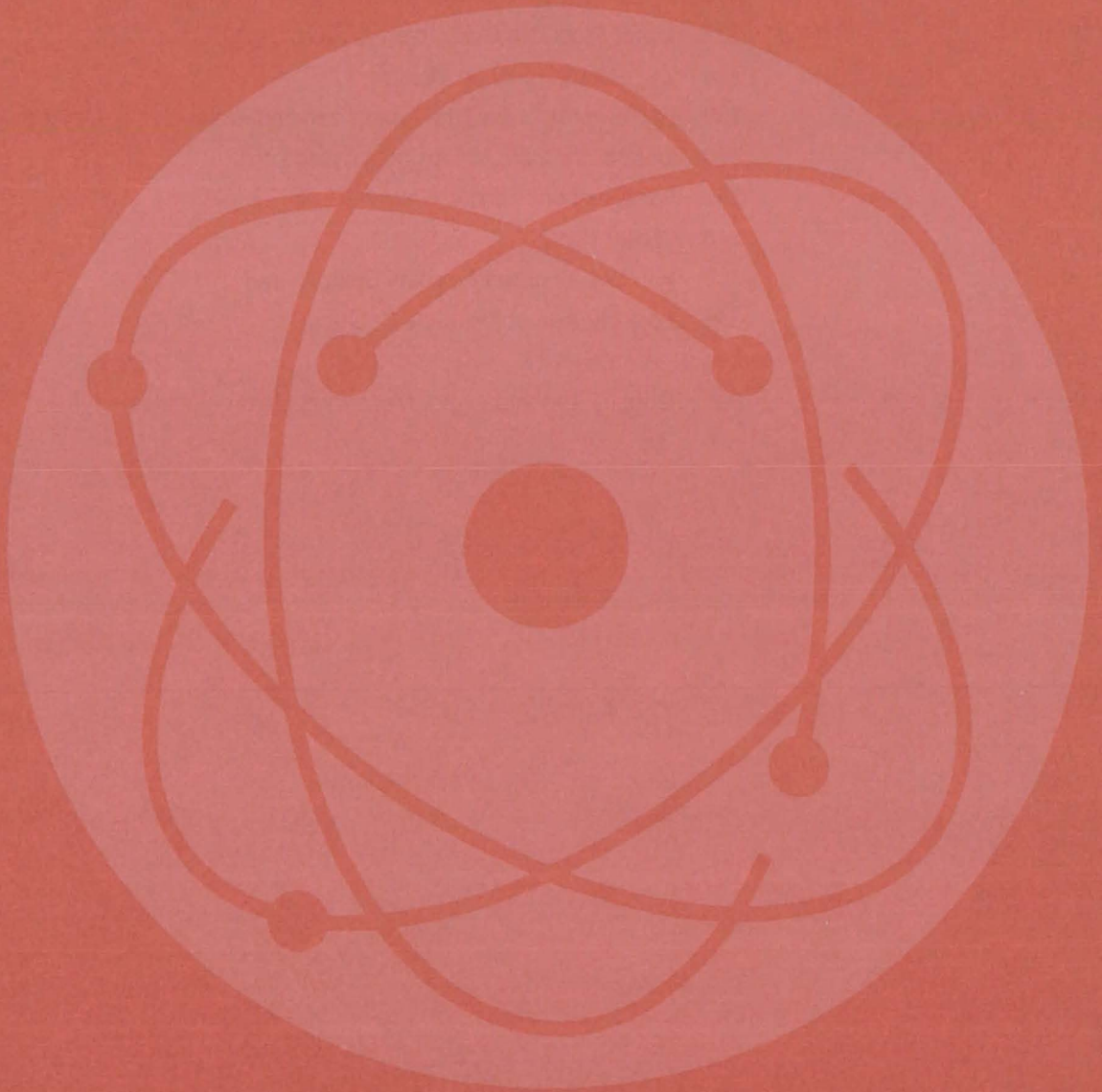


Figure 2. This **Conversion Circuit** changes a data stream from NRZ format to biphasic logic format. Only four integrated circuits are required for precision conversion in this simple inexpensive method. It sets the output level equal to the NRZ level at the beginning of each period and opposite to the NRZ level at the midpoint of the period. The waveforms show the timing of the circuit elements.

This work was done by Elwood B. Baker, Kenneth G. Harf, and William L. McHenry of The Singer Co. for Johnson Space Center. No further documentation is available.
 MSC-16688

Physical Sciences



Hardware, Techniques, and Processes

- 335 Optical Scanning System for Laser Velocimeter
- 336 Faster Optical-Spectra Recording and Analysis
- 337 Laser Produces Color Images From Digital Data
- 338 Dust-Contamination Monitor
- 339 Radiometer Gives True Absorption and Emission Coefficients
- 340 Differential Optical Proximity Detector
- 342 Fast-Response Cloud Chamber
- 343 "Solar Ponds"
- 344 Window-Mounted Auxiliary Solar Heater
- 346 Portable Aerosol-Particle Counter

Books and Reports

- 347 Doppler Techniques for Measuring Fluid Velocities

Optical Scanning System for Laser Velocimeter

Rapid, 16-position coaxial scanner
used with LV system for vortex analysis

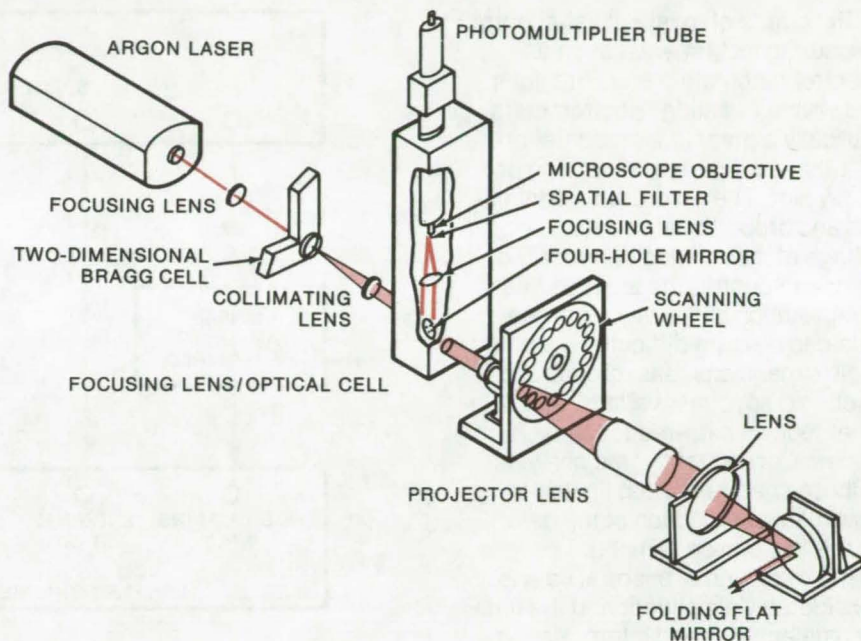
Langley Research Center, Hampton, Virginia

Wake and vortex flow associated with large aircraft present a severe hazard to nearby small aircraft. Tests at the Langley Research Center Vortex Research Facility, using towed models of large aircraft with smaller trailing models through a still-air test zone, have been designed to analyze wake vortex phenomena.

Pressure probes and hot wires disturb the flow field and are difficult to use, making the laser velocimeter (LV) preferable in measuring velocities at several locations across the vortex. By analyzing velocity profiles as a function of time, information is developed on the generation and decay of the wake vortex. Because of vortex decay, rapid measurements are necessary, dictating the use of a fast, scanning, backscatter LV.

For this purpose, an optical system was developed to provide fast incremental scanning of a back-scattered focus point over a 36-cm distance. The system measures flow velocities at 16 positions along its optical axis and scans these 16 positions at a rate of up to 30 times per second. Dwell time at each position is approximately 2 milliseconds, and sample volumes are typically 0.2 mm in diameter by 1.4 cm in length.

The scanning LV incorporates a two-dimensional ultrasonic Bragg cell coupled with a unique rotational scanning technique to attain the high scan rate. The optical system, shown in the diagram, uses a rotating wheel containing plane parallel quartz windows of different thicknesses. The beam from a CW



The Coaxial Optical Scanning System is an improvement over currently-available LV products and is anticipated to have many applications in research and commercial projects.

argon-ion laser is focused by a 2-diopter lens into the center of the Bragg cell. The laser beams from the Bragg cell are collimated and then imaged to a primary focus within the dead airspace of an optical cell. The beams emerging from the cell pass through the windows of the scanning wheel and are refracted, causing an apparent shift of the focus within the optical cell that is projected into the test zone. Backscattered light from the focus in the test zone is concurrently collected and imaged back through the same optical path that projected the primary focus. The imaged backscattered light containing the velocity information is collected and focused onto a photomultiplier

detector to complete the scanned LV optical system.

The amount of apparent LV focal shift varies with the thickness of the plane windows and their refractive indices. Since the refractive index of all the windows is the same, the apparent shift is dependent on window thickness that must be identified. A minicomputer is used to reduce the measured LV data to velocity data on a real-time basis. Each of the windows is identified by an optical shaft encoder attached to the scan wheel hub.

This work was done by David B. Rhodes of Langley Research Center. For further information, Circle 14 on the TSP Request Card. LAR-12143

Faster Optical-Spectra Recording and Analysis

Multichannel analyzer and programable calculator combine to speed data reduction and interpretation.

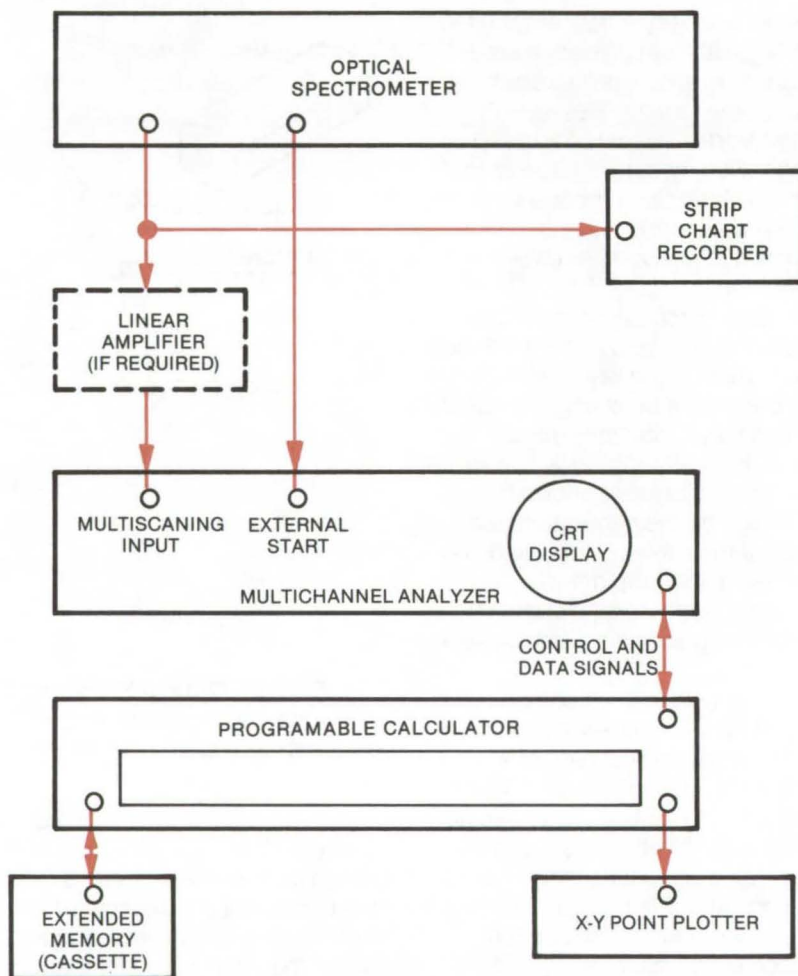
Lyndon B. Johnson Space Center, Houston, Texas

The output of most optical-spectra measuring instruments, such as spectrophotometers and ultraviolet and visible radiation spectrometers, is usually a graphic representation — either a strip-chart recording or an x-y plot. The recording is continuous and proportional to the analog voltage of the sensing detector. For complex spectra, the analysis and interpretation of the raw recorded data can be quite difficult, requiring scale expansions, background subtractions, spectral overlays, and other tedious data-reduction techniques. Consequently, the analysis of these spectra is often limited to slow manual reduction of the data from a few choice samples.

The reduction of spectral data is considerably simplified, and the time for data analysis and interpretation is reduced by at least 50 percent, by a new technique that uses a multichannel analyzer (MCA) in conjunction with a programable desk-top calculator, cassette memory, and point plotter. The system can be programmed to perform most of the tedious and time-consuming operations necessary to analyze optical spectra. Included among its unique features are:

- CRT display of optical spectra;
- Automatic analog-to-digital conversion of the detector output;
- Storage capacity for several hundred spectra for immediate or delayed data reduction and analysis;
- Automation of background subtraction, scale expansion, spectral overlays, spectrum stripping, and other data-reduction methods; and
- Improved accuracy and more efficient personnel utilization and productivity.

The system, shown in the figure, has a linear amplifier that expands the output of the x-y plotter to cover the input range of the multichannel analyzer (generally 0 to 10 volts).



Optical Spectra Are Recorded and Rapidly Analyzed by a system that links a multichannel analyzer and desk-top programable calculator. Cassette-memory storage is also provided. The system can be programmed to automate background subtraction, axis expansion, and other data-analysis techniques and can store several hundred spectra for immediate or delayed analysis and comparisons.

The MCA is operated in the multi-scaling mode, with time as the abscissa and voltage as the ordinate. Its scan time is set to be at least as long as that of the spectrometer. The scan is started by a synchronization pulse from the spectrometer.

The MCA gives a CRT display of the spectrum and provides a digital output that is fed to the calculator along with the MCA control signals.

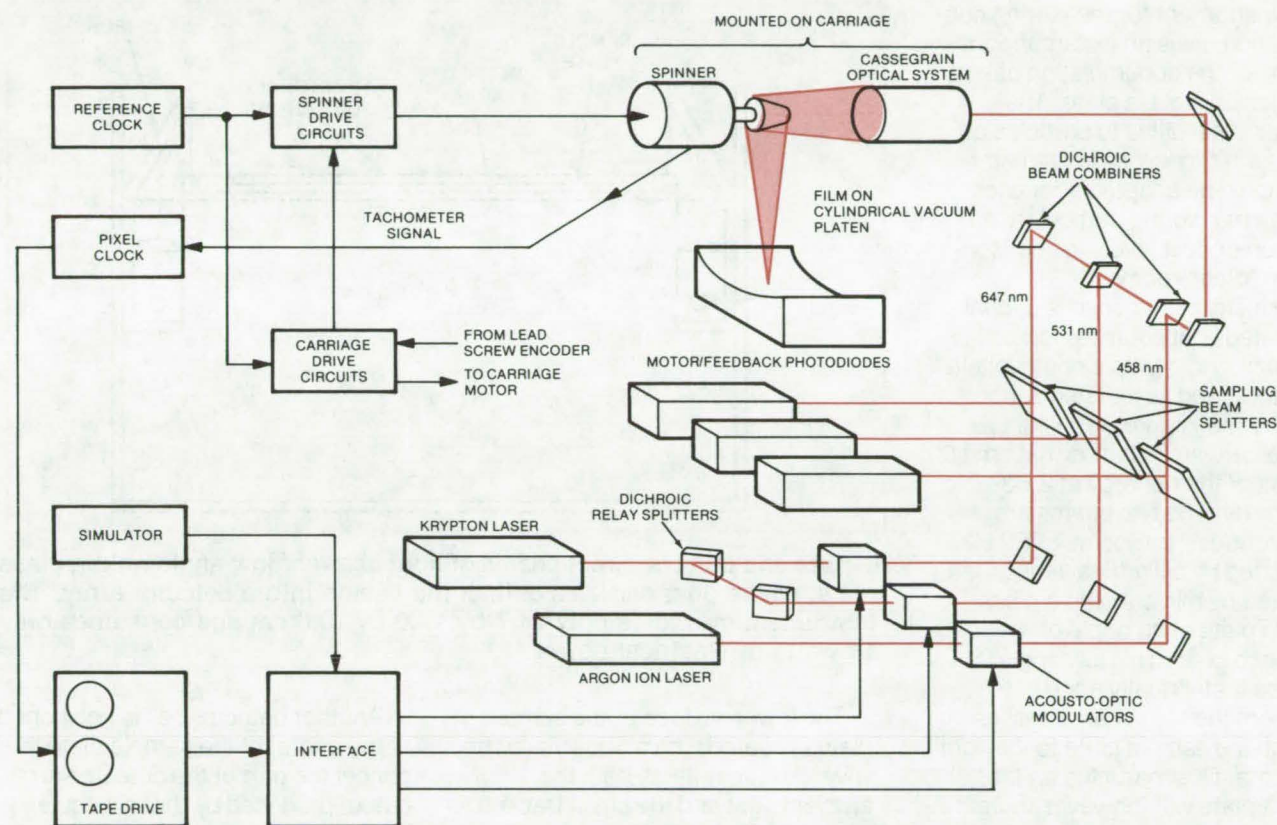
The calculator outputs are tied to a cassette memory and an x-y point plotter. The system can be implemented by combining readily available equipment and is suitable for integrating as a product-line or custom-design item.

This work was done by Robert G. Richmond of Johnson Space Center. No further documentation is available.
MSC-16729

Laser Produces Color Images From Digital Data

Two lasers form three beams that produce multicolor images on film.

Goddard Space Flight Center, Greenbelt, Maryland



Color Recorder uses two lasers to generate three beams, each a different color. Modulators vary the intensity of each beam according to information stored on magnetic tape. Together, the three beams are sufficient to reproduce virtually any colors on photographic film. The tape synchronizes the motion of the beam-writing carriage with the modulation imposed on the beams.

A two-laser system generates high-resolution color images directly from data stored on magnetic tape. A research model was developed to demonstrate the feasibility of using three color laser beams, each a different color, to reproduce images from data sent by satellites. The new system is expected to be useful in storing and reproducing true-color images in a variety of applications. In medicine, for example, the system might be used in patient diagnosis and student training.

The two-laser system does not make color separations and therefore avoids registration problems. It records on a 9-inch-square frame with a resolution of 4,820 picture elements (pixels) per line and 4,820

lines per frame. It can record as many as 409,600 pixels per line if required. The recording speed (8.5 lines per second) is limited largely by the tape transport speed. The recorded spot size is 20 microns. Colors are repeatable within ± 5 percent.

Beams from krypton and argon lasers are used to form a third light beam (see figure). The three beams — each different color — are modulated according to the digital data and are combined to produce the required color. The combined beam is scanned across a color film to produce the image.

The film carriage and the spinner (which projects pixels on the film) are synchronized by pulses from a

crystal oscillator reference clock. Frequency dividers allow the pulse frequency to be programmed so that the image size can be varied as required. Lookup tables are stored in the system for calibration and ensure that light levels stored on the magnetic tape are recorded on film at the correct level. The system can thus compensate for variations in film response. The lookup tables also make it easy to manipulate the recorded data for special effects, such as image enhancement or contouring.

This work was done by Arnold R. Shulman of Goddard Space Flight Center. For further information, Circle 15 on the TSP Request Card. GSC-12198

Dust-Contamination Monitor

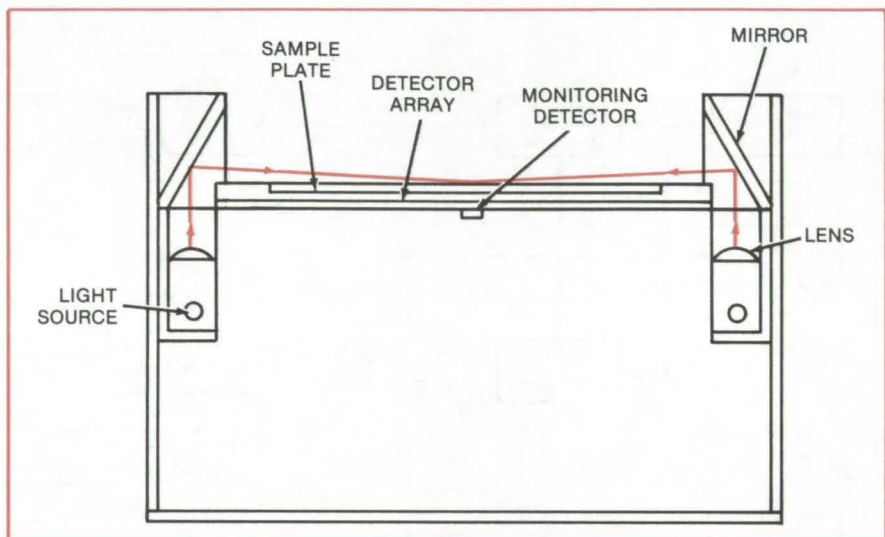
Compact instrument senses light reflected by particles falling on a glass plate

Marshall Space Flight Center, Alabama

An instrument for measuring contamination gives an instantaneous reading of the accumulation of small particles on a glass plate. The monitor is sensitive to particles as small as 100 microns in diameter and should be adaptable for uses such as measuring particulate air pollution or dust levels in semiconductor "clean rooms."

The instrument consists of dual collimated light sources, lenses, optical filters, multiple photovoltaic detectors, and associated support circuitry (see figure). The light sources are small lamps that emit 90 percent of their energy at 2,537 angstroms. The two beams are synchronously pulsed at 1,000 Hz, collimated by cylindrical lenses, and reflected by mirrors onto a glass sample plate at an angle of incidence of 4° . This low angle ensures that virtually none of the light from the twin beams passes through the sample plate to the light detectors. Dust particles on the sample plate will, however, reflect light from the beams at a sharp angle and will deflect it through the plate in proportion to the amount of dust present.

The reflected light is intercepted by the light detectors. These are a 7×7 array of closely-spaced solar cells each 2 cm square. The cells are coated with a fluorescent paint, which converts the 2,537-Å light to visible yellow where the cells are more responsive. The cells are sensitive to as few as seven 100-micron particles.



Lenses and Mirrors direct beams of light at a very low angle onto a glass plate, where dust particles deflect the beams into a detector array. The instrument measures only 24.7 by 17.0 by 10.0 cm and consumes only 14 watts of electrical power.

The lower surface of the sample plate is coated with a 500-Å layer of silver, which reflects both the ambient light and the small fraction of the direct beams that penetrate the glass. Only 0.005 percent of the ambient light and 0.001 percent of the undeflected beam light pass through the silver layer. Beam light scattered by dust, however, is at an angle that easily penetrates the reflective coating. Transmission is 42 percent at a 90° angle of incidence, decreasing to 18 percent at 30° . The sample plate itself is made of selected high-quality quartz with low bubble content to minimize internal scattering.

Another detector cell is positioned at the center of the sample plate to cancel the part of the detector-array output produced by the miniscule amount of directly transmitted light. It also monitors the lamp intensities to compensate for fluctuations.

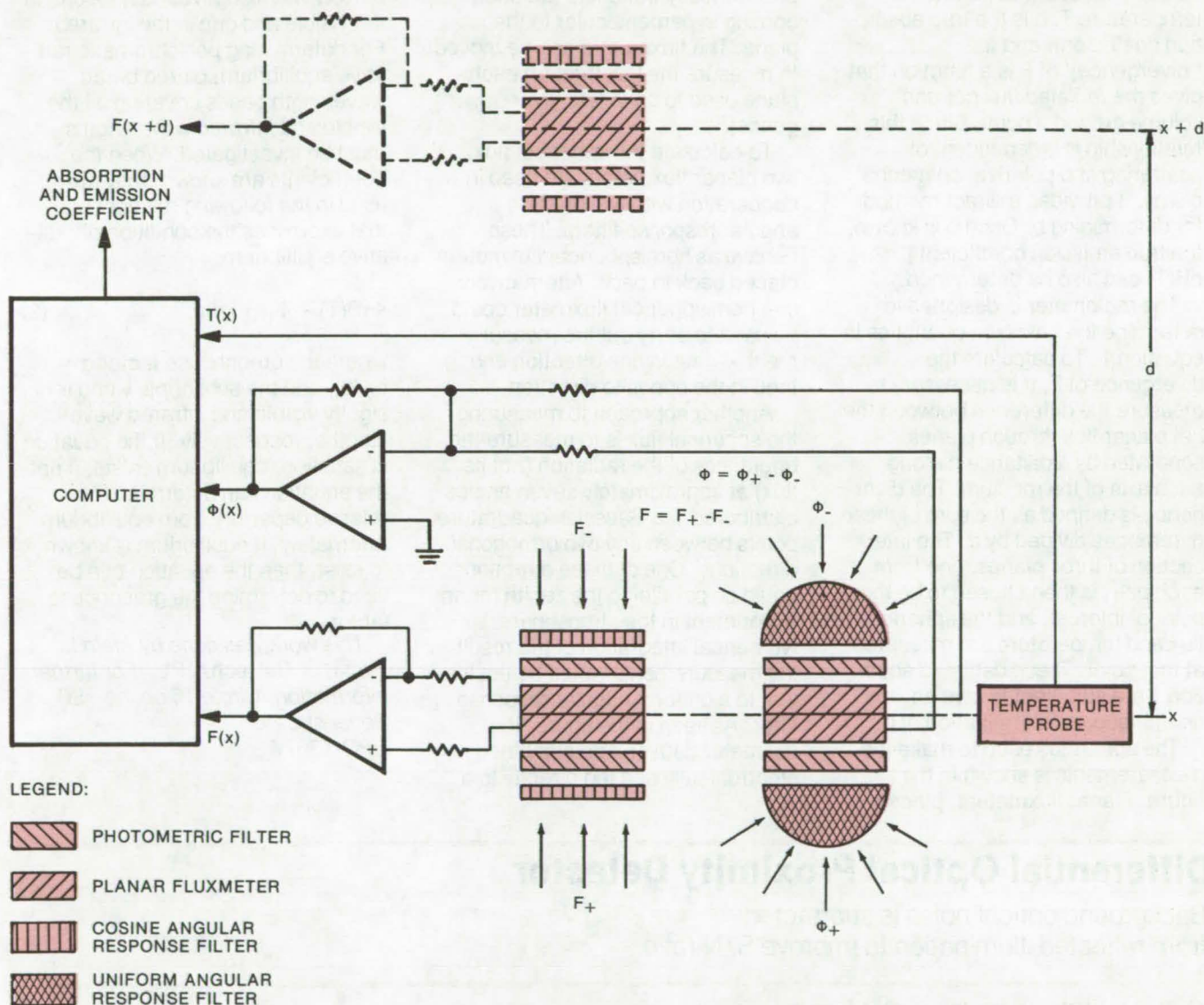
This work was done by C. R. Claysmith of General Dynamics for Marshall Space Flight Center. No further documentation is available.

Inquiries concerning rights for the commercial use of this invention should be addressed to the Patent Counsel, Marshall Space Flight Center [see page A8]. Refer to MFS-23702.

Radiometer Gives True Absorption and Emission Coefficients

A radiometer that is unaffected by scattering and polarization has potential astronomical, meteorological, and environmental applications.

Caltech/JPL, Pasadena, California



A Radiometer for Determining True Absorption and Emission Coefficients measures net planar flux and net spherical flux across planes parallel to each axis of inhomogeneity of a medium. The planar flux must be measured across pairs of parallel planes such as the planes at x and $x+d$ shown here; the spherical flux is measured around a point on one of the planes. The coefficients can be used to determine whether or not the medium is in monochromatic or polychromatic radiative equilibrium.

A novel technique that is not affected by scattering and polarization effects can measure radiation absorption and emission coefficients at any wavelength for an arbitrary mixture of gases and polluting particles. Since the technique can determine the true absorption and emission coefficients of an unknown

environment from simple experimental procedures, it has potential applications to astronomical, meteorological, and environmental problems, such as the determination of radiative heat budget, aerosol relative concentration, and the morphology of cloud, haze, and fog

formations. When used in cooperation with a prescribed analytical procedure, the method can determine the state of radiative equilibrium of a medium.

The key to the application of the new method is a relationship between the net planar flux (F) and

(continued next page)

the net spherical flux (Φ) at points within the medium. The relationship takes the form:

$$\text{Divergence}(F) = -b[\Phi - 4\pi B(T)]. \quad (1)$$

Here, $B(T)$ is the Planck spectral intensity function, dependent on temperature T , b is the true absorption coefficient, and the "divergence" of F is a function that gives the radiated flux per unit volume around a point. Since this relationship is independent of scattering and polarization mechanisms, it provides a direct method for determining b . Once b is known, the true emission coefficient $j = bB(T)$ can also be determined.

The radiometer is designed to determine the unknown quantities in equation 1. To calculate the divergence of F , it is necessary to measure the difference between the net planar flux through planes separated by a distance d along each axis of the medium. The divergence is defined as the sum of these differences divided by d . The intersection of three planes, one from each pair, is then chosen to be the point of interest, and the spherical flux and temperature are measured at that point. These data and equation 1 are sufficient to give an unambiguous determination of b .

The apparatus used to make the measurements is shown in the figure. Planar fluxmeters, placed

back to back, determine the flux crossing a plane from both sides. Each fluxmeter is equipped with a photometric filter to permit the selection of wavelengths at which the measurements are made and a cosine angular response filter that preferentially transmits radiation coming in perpendicular to the plane. The fluxmeters can be moved to measure the flux through each plane used to calculate divergence(F).

To calculate the spherical flux, two planar fluxmeters are used in cooperation with two uniform angular response filters. These behave as hemispherical fluxmeters placed back to back. Alternatively, one hemispherical fluxmeter could be used to carry out the measurement — first in one direction and then in the opposite direction.

Another approach to measuring the spherical flux is to measure the brightness of the radiation (not its flux) at approximately seven angles distributed like Gaussian quadrature points between any two orthogonal directions. One of these directions could be parallel to the zenith for an experiment in the atmosphere. Numerical integration of the resulting measurements would be equivalent to a uniform angular response filter. As seen in the figure, the fluxmeter data can be combined electronically and fed directly to a

computer for an online calculation of the absorption coefficients.

To determine whether the medium is in monochromatic radiative equilibrium, the absorption coefficients are measured for pairs of wavelengths (single wavelengths or very narrow wavelength bands) — one in the visible and one in the infrared. For determining polychromatic radiative equilibrium, paired broad wavelength bands covering all the visible and infrared wavelengths must be investigated. When the coefficients are known, they are used in the following relationship that expresses the condition of radiative equilibrium:

$$4\pi B(T) = \Phi_{ir} + g\Phi_v \quad (2)$$

where the greenhouse factor $g = b_v/b_{ir}$ and the subscripts v and ir signify visible and infrared wavelengths, respectively. If the equation is satisfied, equilibrium exists; if not, the equation can determine the relative departure from equilibrium. Alternately, if equilibrium is known to exist, then the equation can be used to determine the greenhouse factor.

This work was done by Alain L. Fymat of Caltech/JPL. For further information, Circle 16 on the TSP Request Card. NPO-13677

Differential Optical Proximity Detector

Background optical noise is subtracted from reflected illumination to improve S/N ratio.

Caltech/JPL, Pasadena, California

In an earlier optical proximity sensor, a beam of coherent light was used to illuminate a field of view for sensed objects. When an object entered the intersection volume of the beam and an aimed optical detector, reflected light would be sensed to indicate the presence of the object within that volume. When operated with background illumination, however, the signal-to-noise (S/N) ratio of the detector was degraded, and thus its ability to sense an object was hampered.

An updated optical proximity detector has two new features: It can operate under ambient light, and it uses multiple detectors to locate objects in several different spatial volumes. Detector sensitivity (and thus the S/N ratio) is improved by scanning the field-of-view scene twice: once with the coherent light source turned on and once with background light only. The detector outputs for the two cases are amplified and subtracted for each photo-

diode sensor in an array, to eliminate the effect of background light. The detector is configured to react to an object in any of several "detection volumes" by using single LED source and an array of detectors (or with multiple LED's and a single detector, or multiple detectors and LED's).

The multidetector system uses a commercially available array of 16 silicon photodiodes that are scanned sequentially via a 16-stage shift

(continued next page)

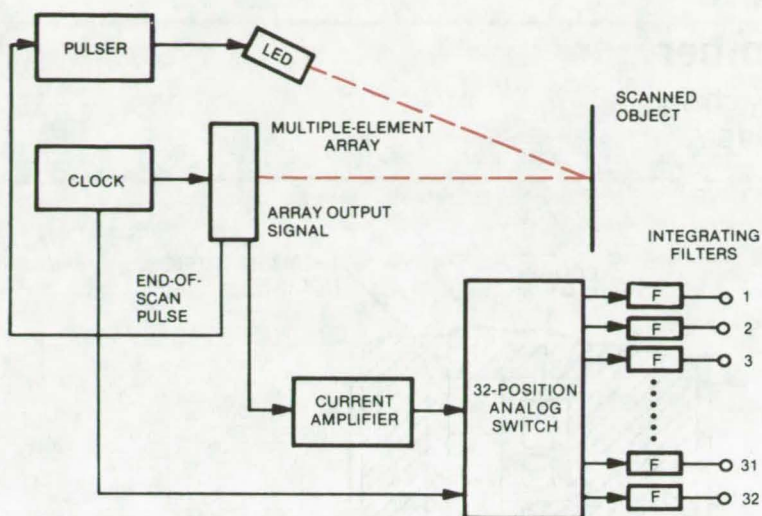


Figure 1. **Background-Illumination Noise is Eliminated** by subtracting output signals with and without LED illumination. Output signals are boosted by a current amplifier and are multiplexed by the analog switch to 1 of 32 filters for storage. The filter elements can consist of a simple integrating (R/C) network. The outputs of filters 1 and 16, 2 and 17, 3 and 18, and so forth are subtracted from each other to derive a signal with an improved signal-to-noise ratio.

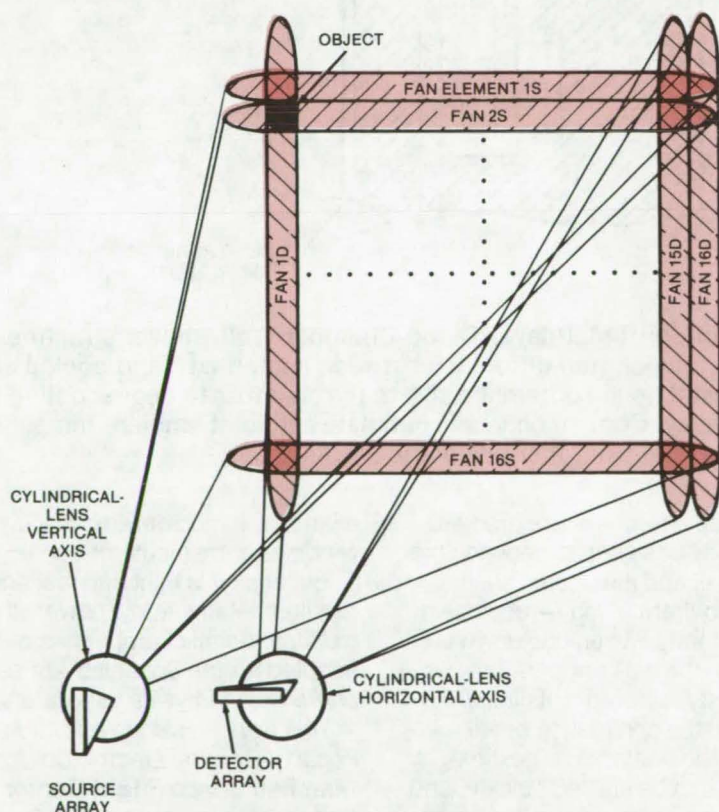


Figure 2. A **Multidimensional Optical Proximity Sensor** uses multiple detectors and multiple LED's with adjacent detection volumes for more precise location of an object within the instrument field of view. When scanned, a small object like that indicated produces a return from 1D (detector 1 field) and 2S (source 2 field). The detected return results in a 1 (yes) in the 1,2 position in the output data matrix. An extended object results in a 1 in each position in the output matrix included by object boundaries.

register driven by a TTL clock. An end-of-scan pulse is used to synchronize the array scan with other circuits. Operated in its charge mode, the array is first scanned by an LED with ambient light, then by ambient light alone. The differences between the two outputs for each element are used in that part of the array in which the axis of an object lies.

One arrangement of the single-point LED source (relative to the object under scan and the array) is shown in Figure 1. As each end-of-scan pulse is generated, the pulser is triggered to turn the LED on, alternately for one full scan and then off for one full scan. The output signal from each detector element is sequentially boosted by a current amplifier and then is stored in a filter. Each of the photodiode outputs is guided to a discrete filter element via a single-pole, 32-position analog switch. Each clock pulse advances the current amplifier output one switch position to connect each diode output to its appropriate filter in a series of 32 filters. Diode signals stored in filter pairs 1 and 17, 2 and 18, 3 and 19, etc., are subtracted, the differences are amplified, compared to a threshold level, and loaded into registers as binary bits.

As shown in Figure 2, the object is located in the sensor field of view by noting which combination of detector-array elements is excited. Each element (light or detector) functions independently as in the single-point proximity detector. A cylindrical lens spreads the beam from each LED and detector element into a thin fan. This fan can be made 20° or 30° in the long dimension and from 1° to 3° in width, the angles as seen from the lens.

This work was done by Alan R. Johnston, Katsunori Shimada, and Harry H. Tippins, Jr., of **Caltech/JPL**. For further information, Circle 17 on the TSP Request Card.

Inquiries concerning rights for the commercial use of this invention should be addressed to the Patent Counsel, NASA Resident Legal Office-JPL [see page A8]. Refer to NPO-13939.

Fast-Response Cloud Chamber

The temperature of lightweight multilayer chamber walls can be controlled quickly and uniformly.

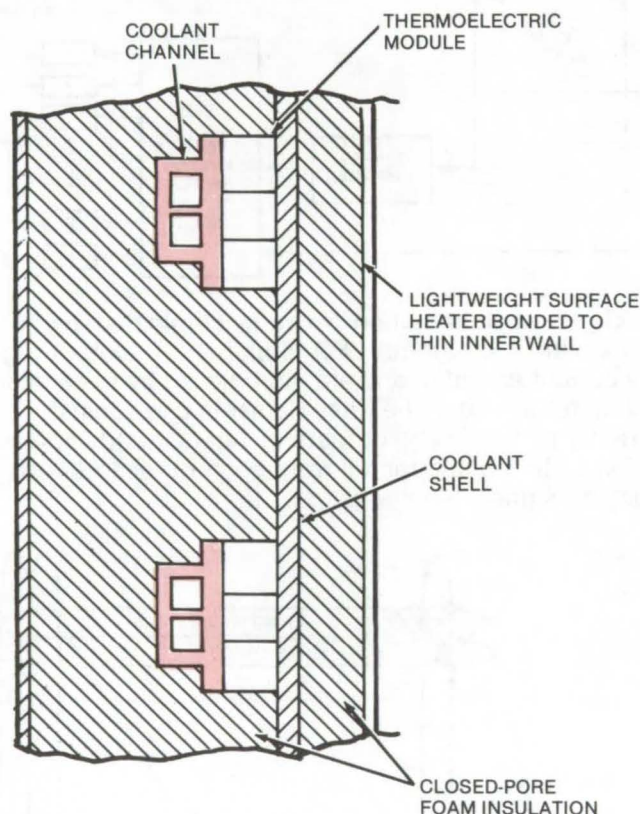
Marshall Space Flight Center, Alabama

The containment of "clouds" in cloud chambers poses some tricky engineering problems. Meteorologists studying fog and clouds and physicists studying subatomic particles require a chamber with walls that can be held at a constant, uniform temperature but that can also be cooled rapidly (at rates up to 15° C per minute), while wall temperature is kept uniform within $\pm 0.01^\circ\text{C}$ over its entire area.

In the past, massive chamber walls have provided the required temperature uniformity. However, large mass is not compatible with rapid change. Consequently, it was necessary to pump coolant at high flow rates (and high power consumption) through the walls. Even then, thermal lag caused excessive delays in the transition from steady-state to cooldown operation.

A new thermal-isolation chamber with multilayer walls eliminates such "brute force" methods. The inner surface of the wall consists of metal foil with an integral layer of resistance-heating material (see figure). Backing up this layer are a thin layer of insulation (for temperature stability) and — most important — a metal shell that is cooled by efficient thermoelectric modules. (A refrigerated liquid coolant can be substituted for the modules, but this means more weight and power for the auxiliary equipment.) A relatively thick layer of closed-pore insulation isolates the cool and warm layers from the outside world.

During steady-state operation, the resistance-heating material maintains the chamber inner wall at the required constant temperature — uniformly over the wall. Then, during cooldown, power to the heater is reduced, and the cooled shell quickly removes heat from the wall.



Cross section of **Multilayer Cloud-Chamber Wall** shows structure that sets up a temperature difference between heated wall and cooled shell. This preestablished difference allows the chamber to begin cooling with no time delay. Coolant channels circulate a fluid at ambient temperature to remove heat from thermoelectric modules.

Because a temperature gradient has already been set up between the heated wall and the cooled shell, there is no thermal lag — cooldown starts instantly. When cooldown is complete, the wall temperature can be promptly restored to its initial value with the application of full power to the heater. The next experiment can be started quickly, and more experiments can be done per hour.

A chamber can be constructed with either flat or curved sections of multilayer wall panels, each section controlled independently. Sections can be moved readily to change the chamber configuration — for

example, to add or remove viewing windows or manipulator openings.

Because it is light and fast and requires relatively low power, the multilayer-wall chamber has been adopted for the Spacelab Atmosphere Cloud Physics Laboratory.

This work was done by Gordon L. Fogal of General Electric Co. for Marshall Space Flight Center. For further information, Circle 18 on the TSP Request Card.

Inquiries concerning rights for the commercial use of this invention should be addressed to the Patent Counsel, Marshall Space Flight Center [see page A8]. Refer to MFS-23588.

"Solar Ponds"

Economical approach to
large-scale heat collection

Caltech/JPL, Pasadena, California

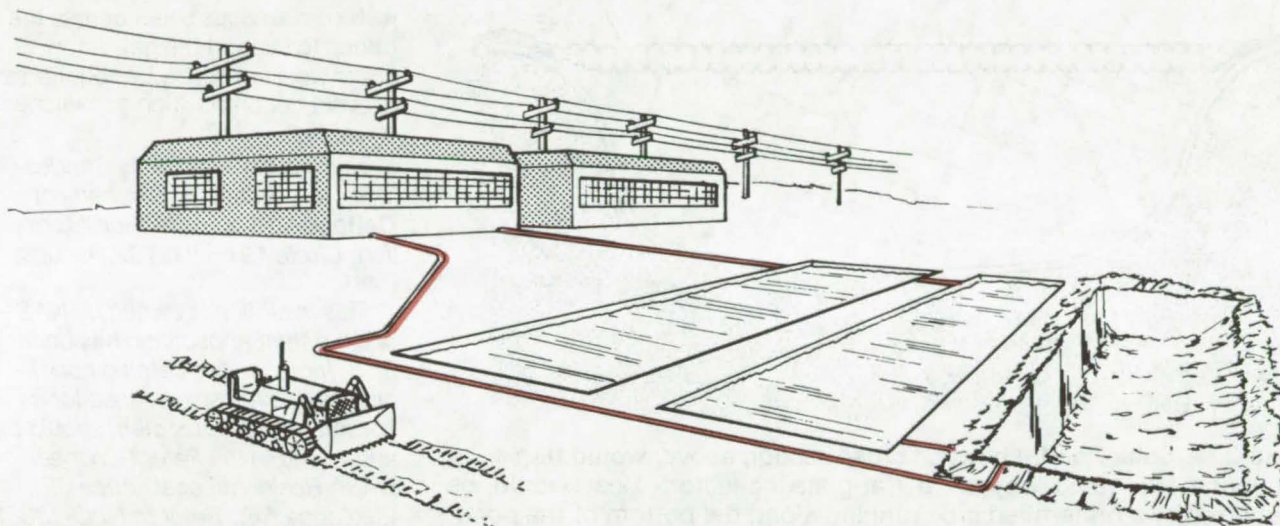


Figure 1. A **Solar Pond Array** would use low-cost materials and heavy-construction methods to make the collection and storage of solar energy economical on the large scale required for commercial operation. A series of long trenches could be dug side by side over an area large in comparison to the heat diffusivity of the soil.



The collector of solar energy on a large scale for powerplants or major facilities magnifies the incompletely-solved technical and economic problems of residential solar-utilization systems. It has been suggested that large ponds of water, made with bulldozers, could be used to collect and store solar heat. The ponds would act much like conventional collectors.

Solar ponds have a number of problems:

- The liquid must be kept free of dust that would impair transparency.
- The hot fluid at the bottom of the pond must not circulate (convection) to bring the heat close to the exposed upper surface of the pond for where it is cooled by the air
- Heat-releasing evaporation should be minimized.

It is also difficult to extract heat from such ponds, since the removal (to a heat exchanger) and subsequent replacement of the hot bottom liquid induces convection, which partially defeats the purpose of the pond.

In the concept illustrated in Figure 1, cost-effective solar ponds might be constructed inexpensively by digging narrow elongated trenches. These ditches would be lined with black plastic to enhance absorptivity and to keep water from seeping into the earth. The heat-transfer medium would be water pumped through thin-walled plastic tubes on the bottom of the pond. This would solve many of the problems with convection. To ensure good thermal contact with the liner in the trench, the fluid in the tubing should be made denser by adding a salt.

The free water in the trench, separate from the hot brine in the plastic tubing, would be kept clean and free from dust by an independent circulation system. The top of the ditch would be covered with an inexpensive, transparent low-heat-transfer film that would also decrease evaporation.

Figure 2 is a cross section of a typical trench. The soil in the trench is covered with black polyethylene

sheeting, and the tubing could be thin-walled clear polyethylene hose connected to a pump and heat exchanger (or directly connected to a heat engine). As the black liner is heated by the Sun, the brine in the tubing is heated by conduction from the hot liner across an intervening thin film of plastic. Heat is also absorbed by the ground surrounding the trenches, and if the overall area of the assembly of trenches is large compared to their depth, both the ponds and the surrounding earth can store heat efficiently. For many soils, the time to reach temperature equilibrium in such a storage arrangement is many weeks, and the stored energy can heat the pond during extended periods of Sunless days. It would also compensate for diurnal variations.

A cover should be placed over the trench to reduce heat loss and to prevent evaporation. A number of approaches could be followed: A layer of Blister Pack, or the equivalent, might be used; alternatively,

(continued next page)

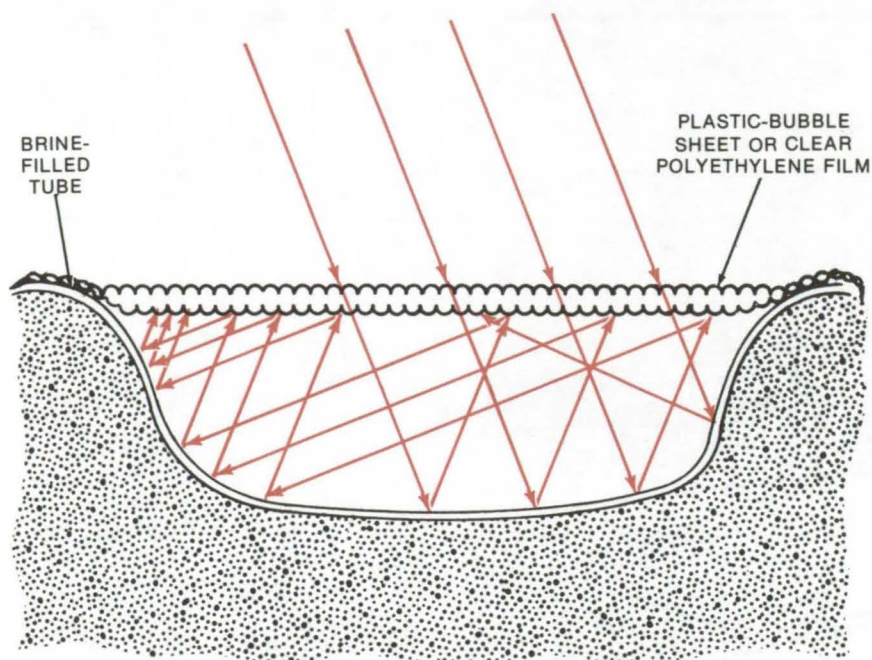


Figure 2. A **Solar Pond**, shown in cross section above, would trap solar heat much the same way as a flat-plate collector. Heat would be transported by a brine-filled pipe running along the bottom of the pond. The temperature of the brine could be expected to reach about 90° C.

the water just above the top of the hose may be filled with a transparent gelatin that would prevent the re-radiation of heat. The gel might be produced by mixing a gelatinizing agent with the water; costs are estimated at 1.6 cents per square foot. This would require the use of a water-impervious sheet across the trench to support the gel. A top cover would probably be required to prevent decomposition occasioned by rainfall.

*This work was done by Charles G. Miller and James B. Stephens of **Caltech/JPL**. For further information, Circle 19 on the TSP Request Card.*

This invention is owned by NASA, and a patent application has been filed. Inquiries concerning nonexclusive or exclusive license for its commercial development should be addressed to the Patent Counsel, NASA Resident Legal Office-JPL [see page A8]. Refer to NPO-13581.

Window-Mounted Auxiliary Solar Heater

Proposed inexpensive and easily installed unit could heat one or two rooms.

Marshall Space Flight Center, Alabama

Although there is a great deal of interest in the installation of auxiliary solar-heating units in existing homes and other buildings, actual implementation is hampered by costs and by the lack of a well-developed industry experienced in the many problems that arise in the installation of these relatively-complex piping systems on the roofs or other surfaces of buildings. A recently-proposed hot-air collector and a window unit that looks something like a vastly simplified version of an air-conditioner appear to be a promising approach to bypassing some of the costs and installation problems of systems generally under consideration, at the sacrifice of some capacity and efficiency.

The unit could consist of simply a hot-air collector that is clamped onto a roof above a window, a short length of duct, and an enclosed window fan with a thermostat switch. The unit mounted as shown in Figure 1 could be manufactured as modules including the window unit shown in Figure 2, ducts, and modular hot-air collectors.

The hot-air collectors could be made from aluminum or molded black plastic frames with interior baffles to direct the airflow and increase the thermal absorption. Clear plastic or glass covers could be installed by the homeowner or sold as an integral part of the modules. Knockout holes and short pieces of duct could be used to con-

nect modules, and prefabricated ducting connecting to the window fan could be installed through additional knockouts in the collector panels. Such collectors, made of lightweight plastic (or aluminum) panels, could be easily installed by homeowners on a supporting bar clamped to the roof, thereby eliminating the need to disturb the roofing (one of the significant practical problems in installing hot-water collectors).

The window unit would contain the only moving part in the system, a fractional horsepower fan. Two thermocouples would control the fan: one on the collector plate and one on the inside face of the window

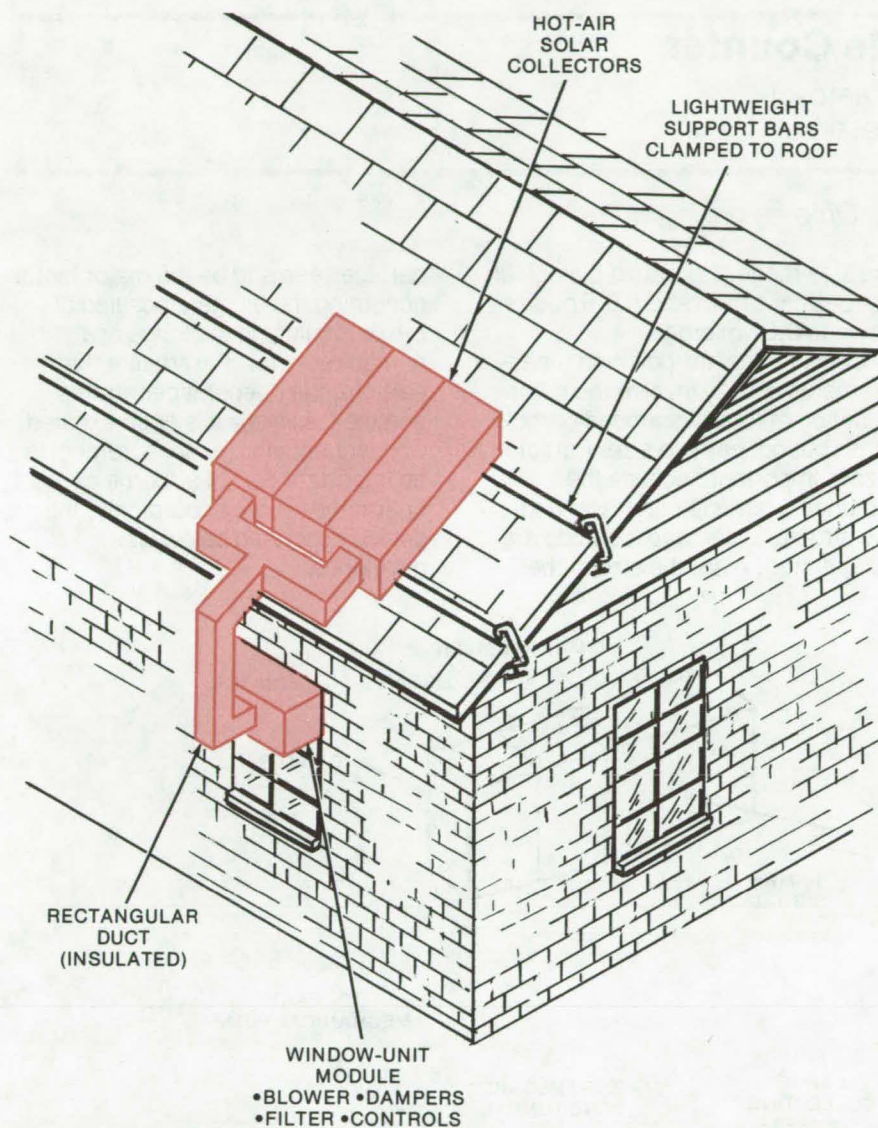


Figure 1. A **Proposed Window-Mounted Solar-Heating System** uses hot-air collectors, no thermal storage, and a fan with thermostat switches. At the cost of heating efficiency, this unit could conceivably be manufactured and sold at a price that would allow its immediate entry to the market as an auxiliary heating system. Its simplicity would allow homeowner installation, and maintenance would be minimal.

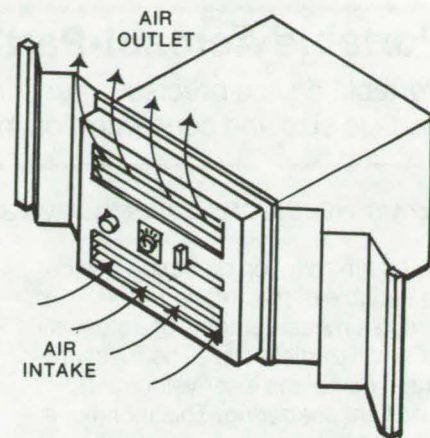


Figure 2. The **Window-Fan Unit** could have the shape and appearance of a window-mounted air-conditioner, but would contain only a fan, dampers, filters, and a few simple controls.

unit to monitor the interior air temperature. When the collector temperature is greater, the fan is switched on, and the resulting air pressure opens dampers. The same unit might be used as a kind of a window fan in summer evenings when the indoor air is hotter, by drawing air from within the room through the cooler collectors (acting as radiators).

Although such a unit has yet to be constructed and tested, its ease of fabrication and installation suggest that it could be developed and marketed long before hot-water collectors and other more complex systems could find their way into general use. The major factor yet to be determined is, of course, whether a unit with all of these cost-saving simplifications will provide enough heat to quickly pay back its purchase cost.

*This work was done by Kenneth G. Anthony and Earl P. Herndon of **Marshall Space Flight Center**. No further documentation is available. MFS-23719*

Portable Aerosol-Particle Counter

Portable device precisely measures aerosol-particle size and concentration in real time.

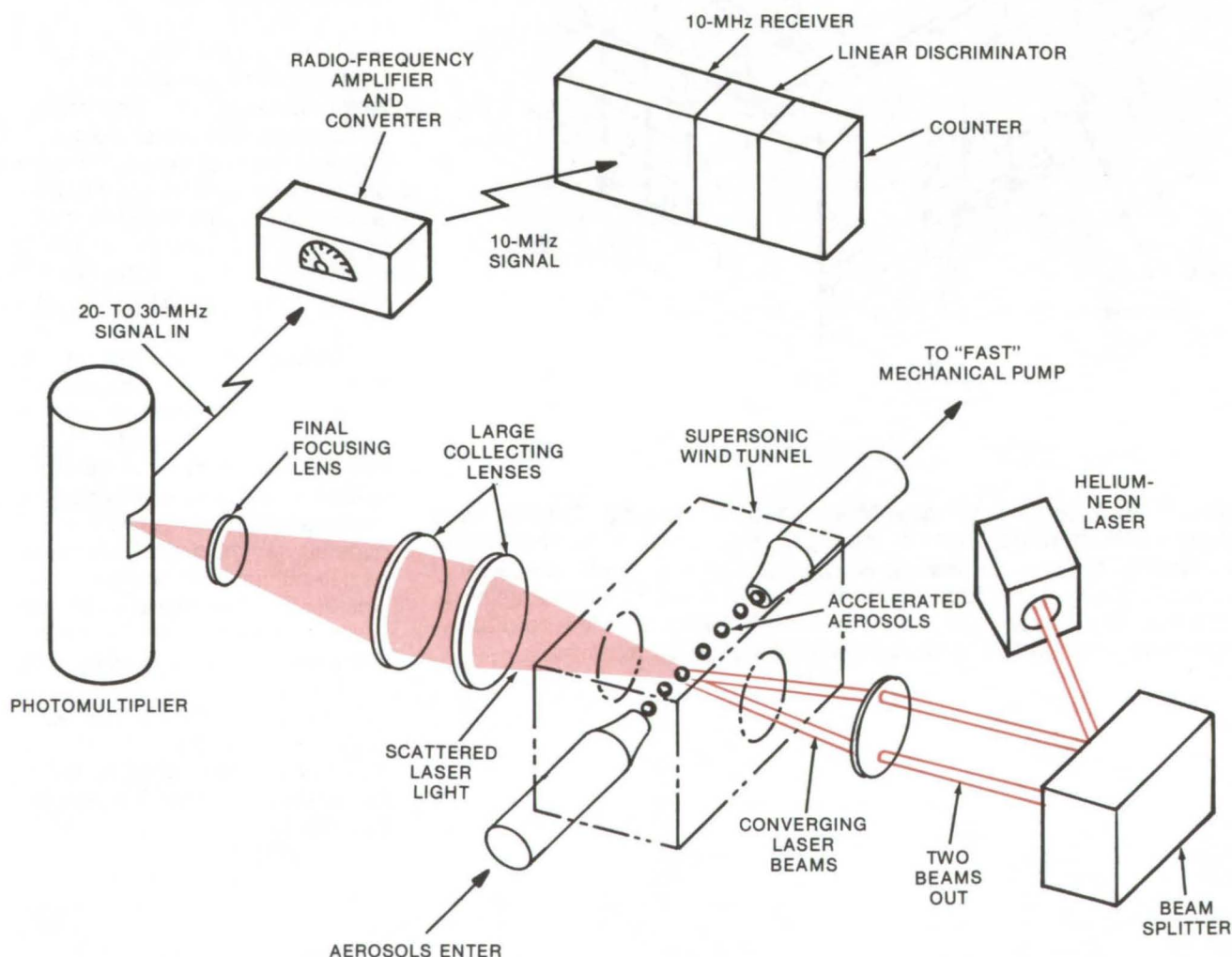
Lewis Research Center, Cleveland, Ohio

An air-pollution detection device is capable of making real-time, precise measurements of aerosols of small particle size. The measurement combines laser velocimetry and light scattering. This technique offers advantages over a number of other currently practiced techniques: It measures aerosol size in real time; it measures size precisely; and it has high sensitivity in

the size range of greatest biological concern, viz from about 0.5 micron down to 0.01 micron.

Conventional air-pollution measurements usually involve the determination of total suspended particle mass but not particle size. Particle size is important because the distance a particle can travel and the structural damage it can do are size related. Also, the size of the

particle seems to be the major factor governing the ultimate position of the particulate in the lungs of a human receptor; the smaller the particle, the deeper it penetrates and the less likely it is to be exhaled. Consequently, size measurement is an important part of airborne aerosol characterization; accordingly, the device described below was developed.



Particle-Size and Concentration Measurements are made with a laser-Doppler technique. Scattered-light frequency depends on particle velocity, which in turn depends on particle size. The converter is set at a frequency corresponding to a selected particle size; a particle of that size passing through the focal point triggers the 10-MHz signal and an audible "pop" is heard. The number of "pops" per second can be related to the concentration of particles of that particular size.

Light from a low-powered helium-neon laser (see figure) is split into two parallel beams by an optically-flat and parallel (to within a half wavelength) beam splitter. These two parallel beams are then focused by a converging lens of 10-centimeter focal length. The focal point is positioned so as to strike the particles as they pass through the supersonic microwind tunnel. The particles are preferentially accelerated by the supersonic nozzle of the wind tunnel; the smaller the particle, the greater the acceleration.

Because the particles travel at different speeds, according to their size, the light that is scattered from each particle as it passes through the focal point is scattered at a different frequency by the Doppler effect. (The Doppler effect works in very much the same way for light as it does for sound.) Thus the scattered light has the particle-size information desired. This light is collected over large solid angles and is focused upon a photomultiplier sensitive to the red wavelength of

the He-Ne laser. The electrical output of the photomultiplier then passes to an RF amplifier and a frequency converter.

The converter has a multiposition switch for selecting receive frequency; output is a fixed 10 MHz. When a particular-sized particle scatters light, it does so at a particular frequency. When the converter is set at that frequency, the 10-MHz signal is generated and passes to a 10-MHz fixed-frequency communications receiver, and an audible "pop" is heard. The converter settings can be calibrated directly in terms of particle size. When the converter is set to a particular size, the number of "pops" per second corresponds directly to the number of particles per second of that particular size that pass through the focal point of the converging lens. By measuring the input flow rate, the concentration of that particular particle size can be calculated.

This technique has excellent small-size measuring capability, relative to conventional light scat-

tering, because the size information is in terms of a particular frequency and narrow band-pass amplifiers may be used. In conventional light scattering, the size information is carried in the height of the electrical pulse from the photomultiplier, requiring that broad band-pass amplifiers be used; and the characteristic noise of the photomultiplier obliterates the small signal from small particles. Based on present limited use of this new system, it appears that there is a twofold to tenfold improvement in small-size measurement over conventional light scattering.

*This work was done by Faustin N. Weber, Jr., of the University of South Alabama for **Lewis Research Center**. Further information may be found in NASA CR-146064 [N76-15438], "Laser Doppler Spectrometer Method of Particle Sizing," a copy of which may be obtained at cost from the New England Research Application Center [see page A7]. LEW-12130*



Books and Reports

These reports, studies, and handbooks are available from NASA as Technical Support Packages (TSP's) when a Request Card number is cited; otherwise they are available from one of NASA's Industrial Application Centers or the National Technical Information Service.

Doppler Techniques for Measuring Fluid Velocities

An overview of the features and applications of current laser- and acoustic-Doppler methods

A report that gives a detailed overview of current laser- and acoustic-Doppler techniques can be

used as a reference for the application of this technology to the measurement of fluid velocities. The report provides background information that will be useful to persons unfamiliar with Doppler methods. It gives a detailed summary of specific laser- and acoustic-Doppler techniques, with emphasis on the advantages and disadvantages of each, hardware design and setup, error sources, and the appropriateness of each method for particular applications.

Doppler methods have been under development since the early 1960's as a means for remotely measuring the velocities of free and confined moving fluids, such as atmospheric and oceanic currents, and blood, wind-tunnel, pipe, and

channel flows. In the laser systems, coherent visible or infrared radiation is scattered by particles suspended in the moving fluid. In the acoustic systems, sound waves are scattered by fluid temperature or velocity gradients. The fluid velocity is determined by measuring the frequency difference between the scattered radiation and the incident beam. This frequency change is directly proportional to the component of the velocity of the scatterer along the line bisecting the angle between the incident and scattered beams. If the scatterer moves at the same velocity as the fluid, or if the relationship between the velocities is known, then the fluid velocity can be determined from the Doppler frequency shift.

(continued next page)

Since the laser systems are of much higher frequency and shorter wavelength than the acoustic systems, they are superior for defining small-resolution volumes and for long-range applications, such as measuring atmospheric flows at distances up to 10 km. The acoustic techniques, on the other hand, give frequency changes that are much simpler to measure electronically and thus can be used for nondestructive remote investigation of confined flows, such as the measurement of blood velocity profiles in veins and arteries.

The review discusses continuous-wave and pulsed-laser techniques, including pulsed-coaxial, local-oscillator focused-forward and backscatter systems, and

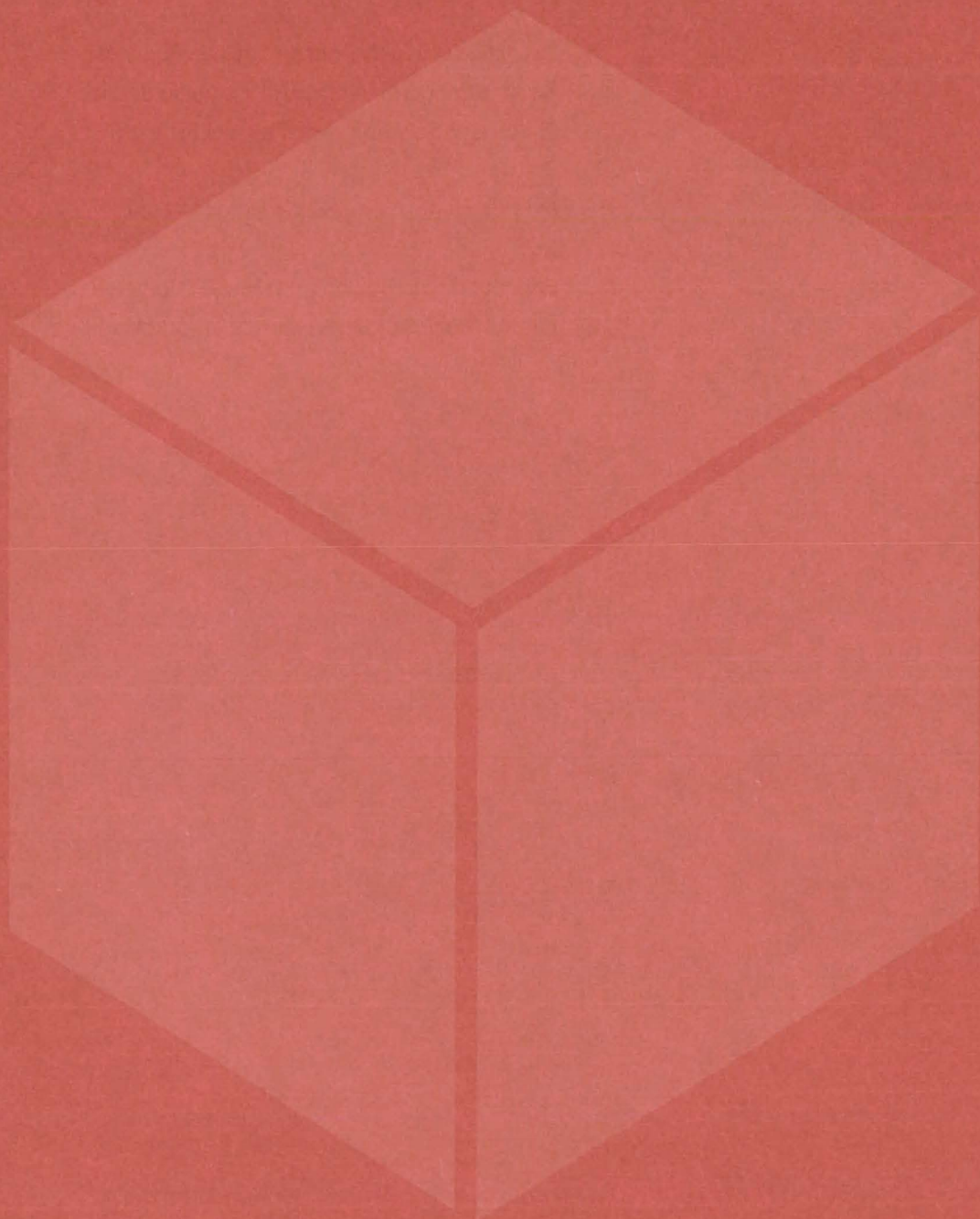
continuous-wave and single-particle dual-beam systems. A section that outlines typical wavelengths and common uses of helium neon, argon, and CO₂ lasers is also included, and scanning methods for obtaining two- and three-dimensional velocity information are described in detail. Laser-Doppler measurements are compared with simultaneous velocity measurements, using hot-wire anemometry in a gaspipe flow and with propeller-and-cup anemometry in atmospheric flows.

The report describes continuous and pulsed acoustic-Doppler techniques and gives a schematic of a three-dimensional continuous-wave system. The application of a pulsed system to the measurement of

horizontal atmospheric-flow velocities at an elevation of 150 meters is compared with measurements obtained from conventional wind sensors. The use of a pulsed ultrasonic system at frequencies up to 40 MHz to investigate blood flow is also described.

*This work was done by William C. Cliff of **Marshall Space Flight Center**. Further information may be found in NASA TM-X-64932 [N75-235130] "Laser and Acoustic Doppler Techniques for the Measurement of Fluid Velocities," a copy of which may be obtained at cost from the New England Research Application Center [see page A7].*
MFS-23289

Materials



Hardware, Techniques, and Processes

- 351 Simplified Ozone Detection by Chemiluminescence
- 352 Tough Strong Iron Alloys for Cryogenic Service
- 353 Flame and Acid Resistant Polyamide Fibers
- 354 Control of Electro-osmotic Flow
- 355 Electrically-Nonlinear Composite Material

Books and Reports

- 355 Effects of Hydrogen on Iron/Nickel/Cobalt Alloy
- 356 Kinetic Studies of Stress-Corrosion Cracking

Simplified Ozone Detection by Chemiluminescence

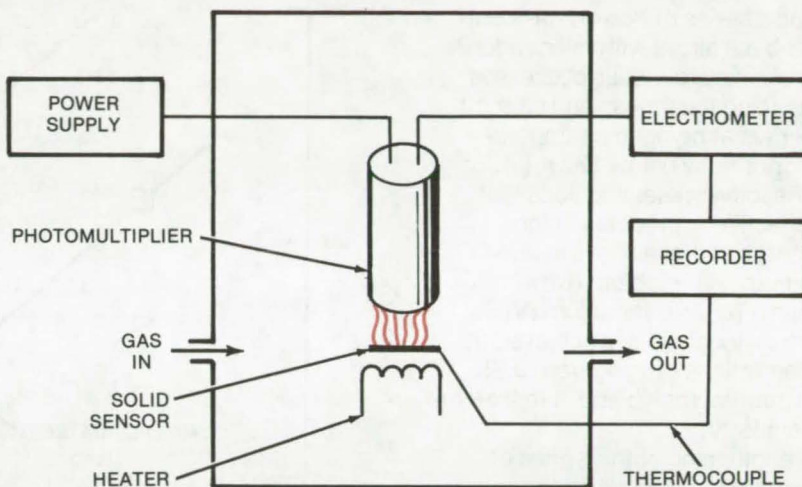
Thermally-induced gas-solid reaction at atmospheric pressure produces light in proportion to amount of ozone present.

Langley Research Center, Hampton, Virginia

A new chemiluminescence method detects and quantifies ozone in the environment, using a gas-solid reaction. The measuring apparatus can be used to sense ozone in the Earth's atmosphere, inside an aircraft or a spacecraft, in the wake of high-flying aircraft, or in any other environment where ozone may be a hazard because of its toxicity.

Current methods for detecting ozone include a chemiluminescence method involving a gas-phase reaction (e.g., O_3 with NO), a colorimetric and a coulometric method (both utilizing KI solutions), ultra-violet photometry, and the cracking of stressed rubber strips by ozone. Of these, only the chemiluminescence method is specific for ozone; for example, most of the others measure total oxidants present. The chemiluminescence method most commonly used, the gas-phase reaction of ozone with nitrous oxide, is limited in application. The reaction must take place at reduced pressure (1 torr or 130 N/m²), requiring an evacuated reaction vessel plus a pressurized container and metering system for the nitrous oxide. Atmospheric sampling is accomplished through a calibrated leak; therefore, changes in atmospheric pressure present problems making high-altitude sampling difficult.

Using an instrument as outlined in the figure, the sample gas is passed over the dry sensitive solid (which may be rubrene, polyethylene, 2,6 naphthalene dicarboxylate, or 9,10 diphenyl anthracene) for 2 to 5 minutes. The gas flow is stopped, and the solid is heated to 200° C. Light is emitted during the heating process and is detected by a photomultiplier tube; the total integrated light intensity measured during the



Ozone Is Detected by using a film coated with a solid, such as rubrene, that reacts with the ozone to a degree proportional to its concentration in the sample gas. The gas flow is stopped, and the film is heated to produce light (chemiluminescence) in proportion to the amount of reacted material on the sensor.

heating cycle is a measure of the concentration of ozone in the sample gas. The solid may be mounted in the detector as a film-strip with fresh areas exposed sequentially for consecutive sampling.

Tests made in the presence of other gases, such as H_2S , CO, NO, NO_2 , SO_2 , and N_2 , indicate that this device is specific for ozone. Trace quantities of ozone can be detected, using very small amounts of the sensitive solid; e.g., 1 to 10 ppm O_3 have been detected, using only 10-4 gram of rubrene.

In addition, multisampling can be performed, using only one instrument: Samples of the sensitive solid can be placed in various locations, exposed to the gas, collected, and placed in the heater chamber for the measurement of light output. This delayed readout capability is unique to this gas-solid reaction method.

This innovative chemiluminescence method utilizing a gas-solid reaction is very sensitive, specific to ozone, and very easy to use to detect ozone and to measure its concentration.

This work was done by Edmund J. Conway and Robert S. Rogowski of Langley Research Center and R. Ronald Richards of Greenville College. Further information may be found in the U.S. Patent referenced below, which may be purchased from the U.S. Patent and Trademark Office, Washington, D. C. 20230, for \$0.50 a copy.

This invention has been patented by NASA [U.S. Patent No. 3,977,831]. Inquiries concerning nonexclusive or exclusive license for its commercial development should be addressed to the Patent Counsel, Langley Research Center [see page A8]. Refer to LAR-11405.

Tough Strong Iron Alloys for Cryogenic Service

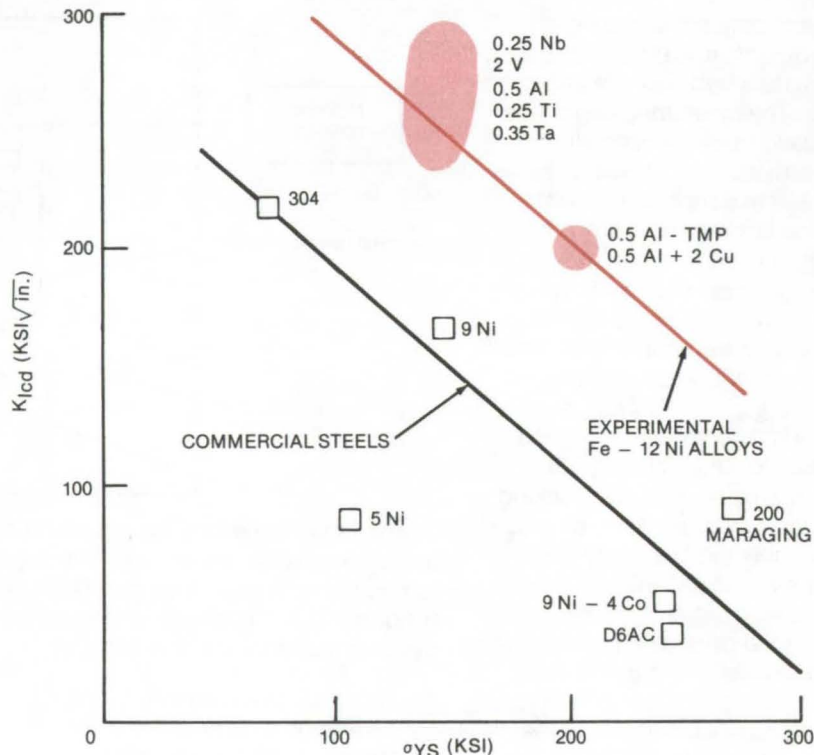
Reactive metals added to iron/nickel alloys improve strength and toughness at low temperatures.

Lewis Research Center, Cleveland, Ohio

A new series of iron/12-percent-nickel-base alloys with minor additions of reactive metals possesses outstanding toughness and strength properties at cryogenic temperatures [primarily below 172 K (-150° F)]. Reactive metal additions that are effective in producing high toughness in these alloys include aluminum (Al), niobium (Nb), titanium (Ti), and vanadium (V). Optimum toughness is achieved at concentrations ranging from 0.25 atom percent for Nb and Ti to 2 atom percent for V.

Strengthening of this series of alloys can be achieved by thermomechanical processing and by precipitate strengthening while maintaining a high level of toughness. The alloys are readily fabricable and can be finish-rolled to sheet form at room temperature after initial ingot breakdown by hot rolling. Welding studies of alloys with additions of Al, Ti, or V have indicated a high level of toughness and strength in the weld-metal and heat-affected zone.

A comparison of toughness and strength at 77 K (-320° F) of the new experimental alloys with several commercial steels is shown in the figure. A general trend noted for all of the alloys is a decrease in toughness with increase in strength. At a strength level comparable to the 9-percent Ni steel [near 140×10^3 psi (980×10^6 N/m²)], the new alloys exhibit 40 to 80 percent higher toughness than the commercial steel. By thermomechanical processing or by precipitate strengthening with the addition of copper (Cu), the yield strength can be increased to near 200×10^3 psi ($1,400 \times 10^6$ N/m²), with only a modest reduction in toughness, to a level near 200×10^3 psi√in. (220×10^6 N/m²√m). At this higher strength level, an advantage in toughness near 100 percent is indicated for the experimental alloys compared to the trend developed by commercial alloys.



Toughness/Strength Comparison of experimental alloys with commercial steels at 77 K (-320° F) indicates the enhanced properties of the new alloys. The fracture toughness (K_{ICd}) was determined by the equivalent energy method from slow bend tests on precracked subsize Charpy specimens (0.4 by 0.25 by 2 in.).

Possible applications for these alloys include liquefied natural-gas storage and transmission, structural members in superconducting machinery, and welding rod for other alloys such as 9-percent Ni steels.

These iron/12-percent-nickel-base alloy compositions can be further modified by the various reactive metal additions cited above or by combinations of these metals to change the toughness range and weldability of the alloy. The strength range of the alloys can be increased by changing processing techniques or by adding additional alloying elements.

This work was done by Joseph R. Stephens and Walter R. Witzke of **Lewis Research Center**. Further information may be found in:

NASA TN-D-8232 [N76-24392], "Effect of Minor Reactive Metal Additions on Fracture Toughness of Iron-12% Nickel Alloy at -196° and 25° C," and NASA TN-D-8403 [N77-18249], "Weldability of High-Toughness Iron-12-Percent-Nickel Alloys with Reactive Metal Additions of Titanium, Aluminum or Niobium."

Copies of these reports may be obtained at cost from the New England Research Application Center [see page A7].

This invention is owned by NASA, and a patent application has been filed. Inquiries concerning nonexclusive or exclusive license for its commercial development should be addressed to the Patent Counsel, Lewis Research Center [see page A8]. Refer to LEW-12726.

Flame and Acid Resistant Polyamide Fibers

Surface photoaddition of halo-olefins improves the flame and acid resistance of aromatic polyamide fibers.

Lyndon B. Johnson Space Center, Houston, Texas

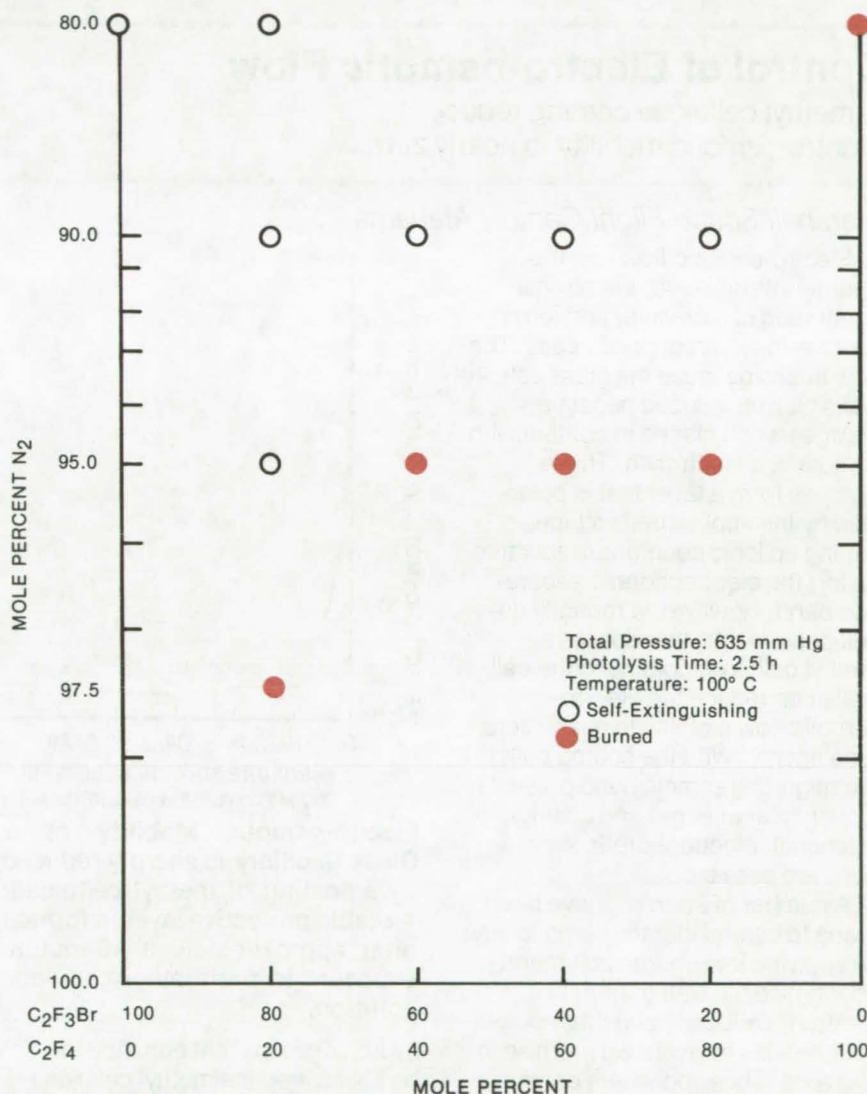
A modification of aromatic polyamide fibers improves their flame resistance and resistance to acids, without modifying their colors or mechanical properties. Aromatic polyamides, such as, poly(m-phenyleneisophthalamide), are used to make garments and similar items. The economical photoaddition of halo-olefins to the fiber surface improves the general safety of these fibers and makes them suitable for applications involving exposure to an oxygen-rich atmosphere or corrosive acids.

The photoaddition is carried out in a vacuum-sealed chamber into which a mixture of halo-olefins and an inert-gas diluent are introduced. Suitable halo-olefins include tetrafluoroethylene or bromotrifluoroethylene. The diluent (e.g., nitrogen, argon, or helium) probably inhibits both homopolymerization of the halo-olefin and photo-oxidation that would occur were the reaction conducted in the presence of oxygen. The composition of a suitable mixture of gases is 10 mole-percent of a bromotrifluoroethylene and tetrafluoroethylene with about 90 mole-percent nitrogen.

Total gas pressure should be around 1 atmosphere, but will vary depending on other process parameters. Temperatures may vary from 0° up to 150° C. Higher temperatures may damage the polyamide substrate or result in homopolymerization of the halo-olefins.

A suitable ultraviolet radiation source has a wavelength of about 1,800 Å. The polyamide should be kept at a fairly constant distance from the UV source. For instance the UV light could be in the middle of the chamber and the polyamide placed around it.

The photoaddition is believed to occur via the formation of free radical sites on the polyamide surface, followed by addition of the



Flammability Characteristics of the treated fibers can be seen in the results of vertical flame tests. Tests were conducted in a mixture of 31 percent oxygen and 69 percent nitrogen at 10 psia (69×10^3 N/m²). Various fluoro-olefins were used to treat polyamide poly(m-phenyleneisophthalamide).

unsaturated halogen-containing compound. The relatively low energy of the UV source restricts the reaction to the fiber surface, and also prevents any extensive homopolymerization.

In addition to fibers, the process could be used with films or other forms of polyamide. There are a

wide variety of conditions and halogen compounds that might be used. The particular choice will depend on the polyamide and other factors.

Vertical flame testing of treated poly(m-phenyleneisophthalamide) fibers in a highly oxygenated environment revealed that the degree of

flame resistance depends on the ratio and composition and amount of halo-olefin on the fiber surface (see illustration).

This work was done by Roger S. Stringham and Madeline S. Toy of

Science Applications, Inc., for **Johnson Space Center**. For further information, Circle 20 on the TSP Request Card.

This invention is owned by NASA, and a patent application has been

filed. Inquiries concerning nonexclusive or exclusive license for its commercial development should be addressed to the Patent Counsel, Johnson Space Center [see page A8]. Refer to MSC-16074.

Control of Electro-osmotic Flow

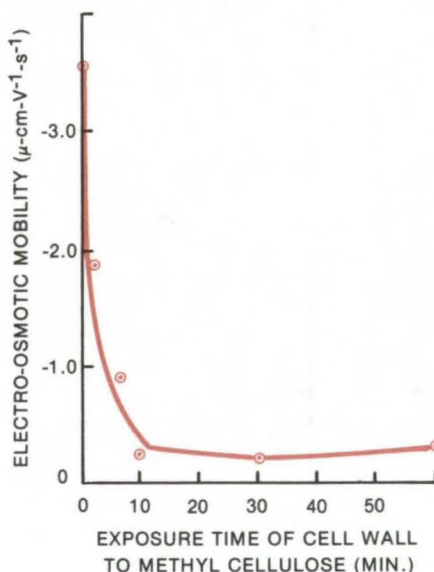
A methyl cellulose coating reduces electro-osmotic mobility to nearly zero.

Marshall Space Flight Center, Alabama

Electro-osmotic flow can frequently interfere with the normal separation of molecular and ionic species in electrophoresis cells. The flow arises because the glass cell walls pick up induced negative charges when placed in contact with an aqueous electrolyte. These charges form a layer that is polarized by the applied cell voltage, setting up ionic countercurrents that distort the electrophoretic separation band. However, a recently developed process that applies a methyl cellulose coating to the cell walls can reduce the electro-osmotic flow mobility to nearly zero (see figure). With the coated cells, the migrating sample band presents a sharp planar edge; and distinct, fractional, electrophoretic separations are possible.

A number of attempts have been made to control electro-osmotic flow by applying low-charge polymeric coatings to the wall material. Dextran, cellulose, and other polysaccharides have shown promise in this area. These polymers contain a high proportion of hydroxyl groups that are readily solvated by water, leaving only a small residual charge. However, the success of these coatings ultimately depends on their ability to adsorb to the wall surface.

With the new process, the bond between the polymer and the glass substrate is significantly enhanced by the application of a layer of a silane (gamma-glycidyloxypropyltrimethoxysilane) that acts as an intermediate coupling agent. The silane alters the morphology of the glass surface and provides additional



Electro-osmotic Mobility of a Glass Capillary is sharply reduced by a coating of methyl cellulose. A stable protective layer is formed after approximately a 10-minute exposure to the methyl cellulose solution.

hydroxyl groups that enhance the bond between the methyl cellulose and the surface. It is conjectured that the silane structure extends the range of interaction of polarizable groups between the components. Another possibility is that an oxirane ring provided by the silane is subjected to nucleophilic attack, yielding a covalent bond between the polymer and the surface.

To form the coatings, the glass cell capillary is thoroughly cleaned by ultrasonics and soaking, first in alcoholic sodium hydroxide and then in aqua regia. Final precleaning is carried out in a plasmod glow

discharge chamber. The intermediate coupling agent is applied in a 30-minute soak in a methyl alcohol/silane solution. Following this, the capillary is dried under a stream of pure helium gas and is baked in a vacuum oven at 60° C. The methyl cellulose layer is formed during a 10-minute soak period. The final step is a thorough water flush.

The electro-osmotic mobility can be determined by measuring the flow velocity at various points along the cross section of the migrating sample band. This is done with a microelectrophoresis instrument that has a traveling microscope with a calibrated graticule in the field of vision. Since the osmotic flow changes direction at a point known as the "stationary level," the velocity at that point is that of the true electrophoretic flow. This can be subtracted from the measured velocity at the cell wall to determine the electro-osmotic mobility. The measured mobilities of coated cells were between zero and -0.18 $\mu\text{-cm-V}^{-1}\text{-s}^{-1}$, which is significantly lower than with uncoated cells.

This work was done by William J. Patterson of **Marshall Space Flight Center**. Further information may be found in NASA TM-X-73311 [N76-26343] "Development of Polymeric Coatings for Control of Electro-Osmotic Flow in ASTP MA-011 Electrophoresis Technology Experiment," a copy of which may be obtained at cost from the New England Research Application Center [see page A7].

MFS-23554

Electrically-Nonlinear Composite Material

A low-temperature sinter of a semiconductor and a polymer resin is useful in the manufacture of circuit boards, cables, and electroexplosive devices.

Caltech/JPL, Pasadena, California

Diallyl phthalate resin when used as a binder in combination with a semiconducting powered-boron nitride, silicon carbide, or other metal oxide produces a resistive and electrically-nonlinear composite material that can be sintered and molded into a desired shape at low temperatures [250° F (120° C)]. This composite material can absorb large amounts of heat and can withstand repeated exposure to electrostatic discharges with little deteriorating effects. These characteristics offer significant advantages over the currently-used, high-temperature-sintered, metal-oxide semiconducting materials.

The new material is prepared according to the following procedure:

- Dissolve the resin in a solvent (acetone).

- Mix the resin solution with the metal oxide (5 to 50 percent resin).
- Add a suitable catalyst (only in the case of silicone carbide).
- Evaporate the acetone in a hot-water bath.
- Grind the remaining solid material into a powder suitable for molding.
- Press a measured quantity of the powder into a suitable mold [pressure of 5,000 to 50,000 psi (35×10^6 to 350×10^6 N/m²) is required].
- Sinter the mixture for 15 minutes at 250° F (120° C).

This procedure is particularly suitable in the manufacture of electroexplosive devices (EED's), which are inherently susceptible to inadvertent activation by electrostatic discharges and high-voltage

currents. EED's equipped with shunts or heat sinks made of the resin/metal-oxide material are able to resist the discharge of a 500-picofarad capacitor charged to 25K volts and can absorb the heat generated when 1 ampere of current or 1 watt of power is applied to the bridge wire of the EED for 5 minutes.

This work was done by Vincent J. Menichelli of Caltech/JPL. For further information, Circle 21 on the TSP Request Card.

This invention is owned by NASA, and a patent application has been filed. Inquiries concerning nonexclusive or exclusive license for its commercial development should be addressed to the Patent Counsel, NASA Resident Legal Office-JPL [see page A8]. Refer to NPO-13858.

Books and Reports

These reports, studies, and handbooks are available from NASA as Technical Support Packages (TSP's) when a Request Card number is cited; otherwise they are available from one of NASA's Industrial Application Centers or the National Technical Information Service.

Effects of Hydrogen on Iron/Nickel/Cobalt Alloy

Susceptibility of this iron-based alloy to hydrogen at high temperatures and pressures

A commercially available alloy, Incoloy 903, has been considered as a candidate for various high-pressure, high-temperature applications. A recent study of its properties in hydrogen and in helium atmospheres under very extreme

environments indicates that the alloy can be degraded by gaseous hydrogen, particularly at elevated temperatures. The study also reports that water vapor added to the hydrogen environment can cause reductions in the low-cycle fatigue life of this material.

Specimens of the alloy that were cut from hot-rolled parent material were tested, along with welded specimens, in hydrogen and hydrogen/water-vapor environments up to 5,000 psig (34.5×10^6 N/m²) and at temperatures to 1,400° F (760° C). The tensile properties, low-cycle fatigue life, and creep-rupture characteristics were compared with the results of similar tests in air and helium atmospheres.

The major degradation in mechanical properties occurred in the

creep-rupture characteristics, which were reduced by more than 50 percent in both the parent and welded specimens. Tensile properties were negligibly affected except for ductility, which was reduced by 25 to 50 percent at temperatures above 1,000° F (538° C). Low-cycle fatigue life was not affected by hydrogen unless water vapor was added at 1,400° F. The water caused sharp reductions in low-cycle fatigue life, indicating that oxidation or other reactions were occurring due to the disassociation of water at the specimen surface.

This work was done by J. A. Harris and J. Mucci of Pratt & Whitney Aircraft for Marshall Space Flight Center. To learn how to obtain a copy of the report, Circle 22 on the TSP Request Card. MFS-23369

Kinetic Studies of Stress-Corrosion Cracking

Realistic lifetimes of D6AC steel under stress and corrosion environments

Environmentally-enhanced crack growth in high-strength steels has been observed by many investigators. However, the use of time-to-failure curves for stress-corrosion cracking processes may lead to incorrect estimates of the structural life, if the material is strongly dependent upon the prestress levels. To prevent the premature failure of structures, the phenomena of subcritical crack growth in the presence of a corrosive environment must be characterized. A newly developed technique characterizes the kinetics of the crack-growth rates (da/dt) and the intermediate arrest times caused by load-level changes.

In essence, the procedure treats a specimen to a hardness of Rc44 and subjects it to fatigue precracking in air. The specimen is then loaded in a creep machine with a corrosive environment present at the tip of the crack and is set to an initial stress intensity. The initial incubation time, prior to stress-corrosion cracking, is then determined. (Incubation time is given as the time to the first measurable change in the compliance-versus-time curve.) As cracking occurs, the stress intensity increases under constant load. After a steady-state crack-growth condition is achieved, load shedding is accomplished in either of two ways.

In the first method, sufficient load is removed to reduce the stress intensity by an amount ΔK . The final stress intensity on removal of the load is K_F . The process results in an incubation period followed by crack extension. In the second method, the load is reduced to zero after steady-state crack growth is achieved. The stress intensity is then increased to the value K_F . The difference between K_F and the steady-state stress intensity is equal to ΔK . This method also results in an incubation time followed by crack extension. In both cases, a steady-state crack-growth condition is achieved following a crack-arrest period.

Incubation time and crack-growth rates are determined by compliance techniques. Crack-opening displacement is measured with a clip gage, excited at 10 Vdc. The output from the clip gage is fed into a high-gain amplifier. After amplification, the signal is coupled to the y-axis of an x-y recorder. The sensitivity of the components in the system is adjusted to allow a 0.001-in. (0.0025-cm) increase in crack-opening displacement of the recorder pen on the y-axis to be magnified to 6 in. (15 cm) or greater. The x-axis is coupled to a ramp generator to allow 15 in. (38 cm) displacement of the recorder pen in 24 hours.

The system monitors crack-opening displacement versus time. In nearly all cases, the start of crack extension is discontinuous, and the incubation time is measured to within 1 percent. All drift over a 24-hour period and greater is eliminated so that no extrapolation techniques are required for analysis.

Several characteristics of subcritical crack growth in a corrosive environment were determined, using this method:

- Load shedding under stress-corrosion cracking conditions causes a temporary arrest in crack growth.
- The period of crack arrest depends on the amount of load shed and the baseline stress intensity of the specimen. The greater the amount of load shed, the longer the incubation period; the higher the baseline stress intensity, the shorter the incubation period for the same level of load shedding.
- Load shedding through a zero-load condition results in a shorter incubation time than when the same amount of load is shed without passing through a zero-load condition.
- The crack-growth rates following incubation caused by load shedding depend on the amount of load shed and the baseline load level. Crack-growth rates are lower following greater reduction in load levels.
- The "resistance" to stress-corrosion cracking depends on the fracture toughness and yield strength of the specimens of the particular alloy tested.

This work was done by Pascal J. Noronha of Marshall Space Flight Center. Further information may be found in NASA TM-X-64923 [N75-21434] "Kinetic Studies of the Stress Corrosion Cracking of D6AC Steel," a copy of which may be obtained at cost from the New England Research Application Center [see page A7].
MFS-23259

Life Sciences



Hardware, Techniques, and Processes

- 359 Hearing-Aid Tester
- 360 Multichannel Implantable Telemetry System
- 361 Batteryless Implanted Echosonometer
- 362 Prosthetic Urinary Sphincters
- 364 Cooling Vest
- 364 Longitudinally-Vibrating Surgical Microelectrode
- 366 Real-Time Video Display for Angiocardiographic Studies

Books and Reports

- 368 Liquid-Circulating Garment Controls Thermal Balance

Hearing-Aid Tester

The amplifier and battery are checked automatically by a miniature circuit contained within the hearing aid.

Lyndon B. Johnson Space Center, Houston, Texas

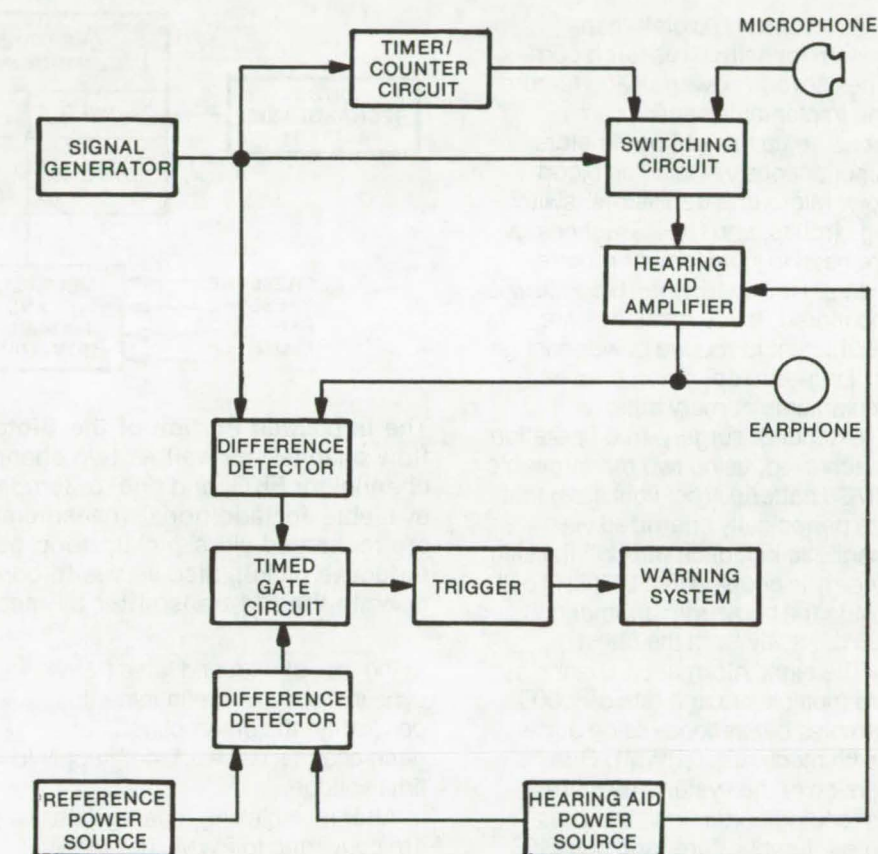
A new circuit can be incorporated directly into a hearing-aid package to provide continuous interrogation of its operating status. When a malfunction develops, the circuit automatically provides a visual signal to alert the wearer. The circuit saves time and effort by eliminating the need for periodic bench checks and will pick up defects that might otherwise go unnoticed.

Hearing aids often develop malfunctions that are undetected by the wearer. Periodic inspection will uncover these abnormalities; however, the problems may arise so gradually that they are not noticed or are mistaken for further loss of hearing. Even if inspections are carried out, they require bulky and expensive test equipment and usually require that the hearing aid be removed.

Twice per hour, the new circuit automatically performs a 0.5-second evaluation of the hearing-aid amplifier and battery. If the battery output is low or if the amplified sound signal is too low or distorted, a flashing indicator is latched and remains on until the hearing aid is switched off or a reset button is pushed. The test circuit is powered by an independent battery supply with a lifetime three times that of the hearing-aid battery.

The new circuit is shown in the accompanying block diagram. A square-wave oscillator generates a signal that is fed to the input of an electronic switch. The same signal passes through an interval timer and ripple counter and is stepped down to a 500-ms pulse every half hour. This pulse opens the electronic switch that couples the oscillator signal to the hearing-aid amplifier. The microphone output is blocked during this period.

The oscillator output is converted to a sinusoidal wave and is fed to the input of a differential amplifier to be compared with the hearing-aid amplifier output after amplitude and



Hearing Aids Are Automatically Checked by this circuit that applies a half-second test signal every 30 minutes. If the hearing-aid output is distorted or too small or if its battery is too low, a warning lamp is activated. The test circuit is incorporated directly into the hearing-aid package.

phase adjustments have been made. If the signals match in amplitude and frequency, the output of the differential amplifier will be zero. If not, any degradation in the amplified signal will appear as a difference signal that is converted to a dc voltage by an integrating circuit. This voltage, along with the output of another difference detector that checks the hearing-aid battery against a reference, is fed to a timed gate circuit. Any malfunction of the amplifier or battery supply of the hearing aid will be recorded as an output signal of the gate circuit. This signal closes a latch that activates

the warning indicator. The wearer can switch the lamp off by pressing a pushbutton that resets the latch or by opening the main power switch.

This work was done by Roger Kessinger, John T. Polhemus, and John G. Waring of Martin Marietta Corp. for **Johnson Space Center**. For further information, Circle 23 on the TSP Request Card.

This invention is owned by NASA, and a patent application has been filed. Inquiries concerning license for its commercial development should be addressed to the Patent Counsel, Johnson Space Center [see page A8]. Refer to MSC-14916.



Multichannel Implantable Telemetry System

Eight parameters, including blood flow, are sensed simultaneously, using a power source that is rechargeable without surgery.

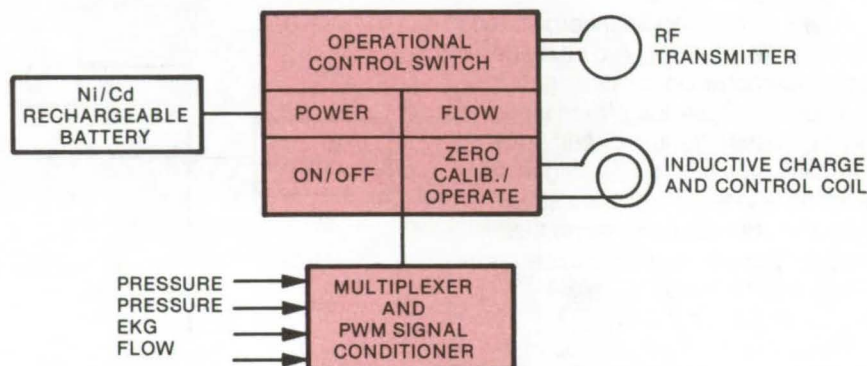
Ames Research Center, Moffett Field, California

A multiplexed biotelemetry system for animal research combines several power-saving features. The implantable sensor can measure up to eight parameters simultaneously, including blood flow. Microamp transistors, switching circuits, and CMOS technology are used to lower power requirements. However, when blood flow is monitored, these measures are insufficient to reduce power enough for long-term operation from an implantable primary battery.

Extended, surgery-free operation is achieved, using two rechargeable Ni/Cd batteries (penlight size) that are periodically energized via magnetic induction through the skin. Energy is coupled to a 250-kHz coil inside the body from another coil 2.5 cm away from the chest.

The eight information channels are multiplexed at a rate of 1,000 samples per second, using pulse-width modulation (PWM). One version of the system measures ascending aortic flow, two pressures, temperature, and one EKG parameter. One channel is subcommutated to provide deep-body temperature and engineering-voltage measurements.

A block diagram of the signal conditioner, multiplexer, and telemetry transmitter is shown. Incoming analog data on the eight channels are sequentially sampled by CMOS switches, one switch at a time. A decade counter clocks each switch for a 100- μ s period, at a rate of 10 equal-interval segments (words) per frame. Every tenth word is blanked out from the transmitted PWM signal for frame synchronization. One channel is permanently grounded for an accurate zero reference. If the data at the multiplex input were to exceed ± 1.7 volts, the leading and trailing edges of the pulse (PWM word) would be obliterated, resulting



The Implanted Portion of the Biotelemetry System: Connections for a flow channel, as well as two channels for pressure measurement, one channel for EKG, and one for temperature as shown. Spare channels are available for additional measurements. The nickel-cadmium batteries are recharged via a pickup loop positioned just beneath the skin. The inductive pickup also serves to control the implanted electronics and to operate the FM transmitter by means of an operational control switch.

in the loss of data and false frame sync indication. To eliminate this possibility, the preamplifiers for each channel use a ± 1.4 -V supply to limit voltage.

After multiplexing, analog data are converted to PWM. The PWM waveform is initiated at the beginning of each ramp and ends when the ramp equals the analog signal presented to the comparator. Since no input voltage ideally represents a 50-percent PWM duty cycle (depending on component tolerances and ramp signal jitter), channel 1 is permanently grounded for reference purposes and is used as a "zero" reference in the demodulator to correct for variations. Small errors in PWM generation, telemetry transmission, and demodulation are simultaneously corrected.

To reduce wiring and complexity, the case of the pressure cell is inserted in the apex of the left ventricle. It serves as one EKG electrode; the ground contact located on the ascending aorta is the

other. The resulting EKG signal approximates the maximal QRS vector generated by the heart. The demodulated analog flow signal is applied to a separate channel.

The flow probe, which consists of an air-core design, is driven via a square-wave signal via an integrated-circuit ramp generator instead of a separate oscillator, simplifying system synchronization. The field supply for the flowmeter switches the field on or off. In operation the field is sequentially switched to its on/off or calibrate modes. In the latter (calibration) mode, a resistor network provides a signal proportional to the field current. The signal is switched to the demodulator input in place of flow data in the analog output.

The telemetry switch uses a frequency discriminator to switch battery power on and off to the FM transmitter. A 243-kHz signal turns the system off, while a 258-kHz signal initiates the system via a latching configuration. Only a

momentary signal is required. The control unit for power activation is held 2 to 15 cm from the implanted pickup coil to activate the circuit. Since the implanted coil is placed in

the left thoracic cavity just under the ribs, transcutaneous spacing is 2 to 3 cm in the laboratory animals used.

This work was done by Thomas B. Fryer, Ernest P. McCutcheon, and

Harold Sandler of Ames Research Center and Edwin L. Carlson and William Freund of Stanford University. For further information, Circle 24 on the TSP Request Card. ARC-11079

Batteryless Implanted Echosonometer

Power is inductively coupled to the instrument, thus obviating battery recharging or replacement.

Ames Research Center, Moffett Field, California

A miniature ultrasonic echosonometer implanted within a laboratory animal does not use a built-in active power source. It instead obtains energy from an RF power oscillator that is electromagnetically transduced via an induction loop to a power-receiving loop located just under the animal's skin. The RF energy is converted to suitable dc levels; the dc is used to drive the remaining stages of the echosonometer.

This method of powering the echosonometer offers significant advantages over those in which a battery is part of an implanted package intended for long-term real-time studies. Periodic battery reactivation (or replacement) is not necessary, and no leads project through the skin of the animal under observation, thus avoiding infection that often arises at such sites.

Output data from an ultrasonic transducer (stitched to the organ under study) are amplified and fed to a signal induction loop also located immediately beneath the skin. A signal receiver loop outside the body of the animal is held opposite the transmitter loop. Data are induced into the receiver loop and are fed to processing equipment and a readout instrument. Since the ultrasonic transducer is implanted immediately next to the organ of interest, signal attenuation is minimized and beam alignment is easier to maintain. The echosonometer can image organs, vessels, and tissues and is safe for long periods of real-time observation.

Figure 1 illustrates the major components of the echosonometer relative to the epidermal layer and

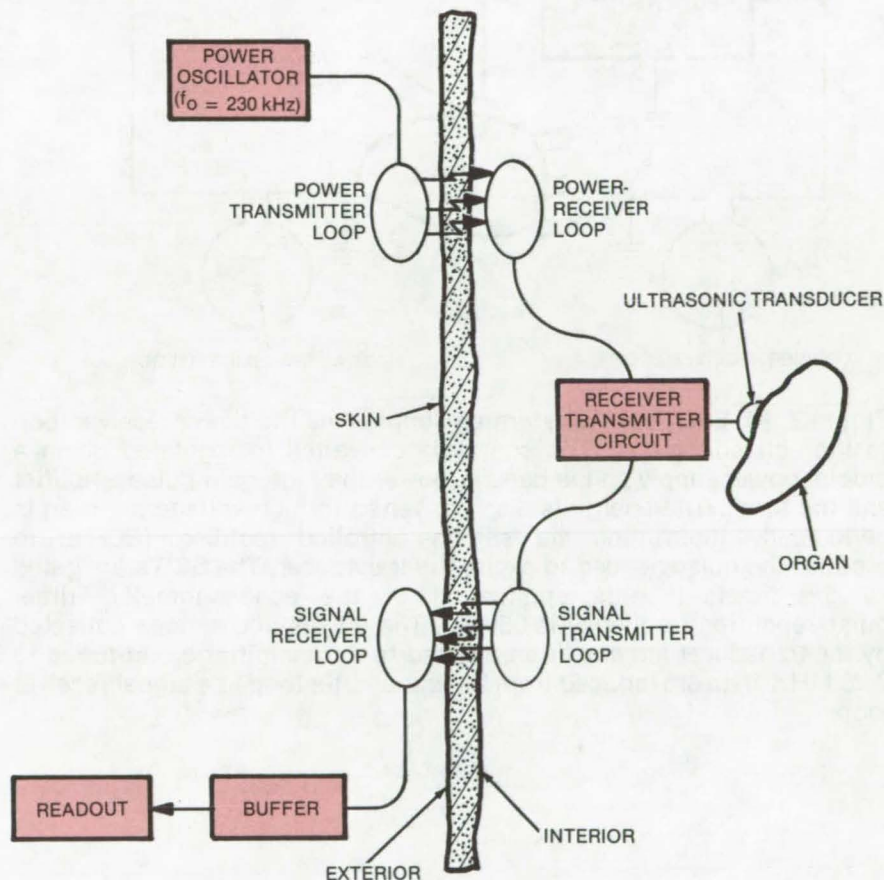


Figure 1. The **Bioimplanted Echosonometer** draws power from a power oscillator. The oscillator outputs RF energy at 230 kHz to a transmitter loop. Energy transferred via a receiver loop is converted to low-voltage dc and to high-voltage pulses for further use by the remainder of the receiver/transmitter and the ultrasonic transducer, respectively.

the organ under study. The instrument comprises a power receiver/data transmitter, an ultrasonic transducer, and a receiving loop and a transmitting loop. A circuit in the receiver/transmitter generates a stream of high-voltage pulses that are fed to a piezoelectric crystal

transducer. The transducer oscillates at an ultrasonic frequency; reflection of the ultrasonic energy from interfaces in the organ generates a return echo signal in the transducer. The time between a transmitted ultrasonic burst and a received echo indicates the depth of

(continued next page)

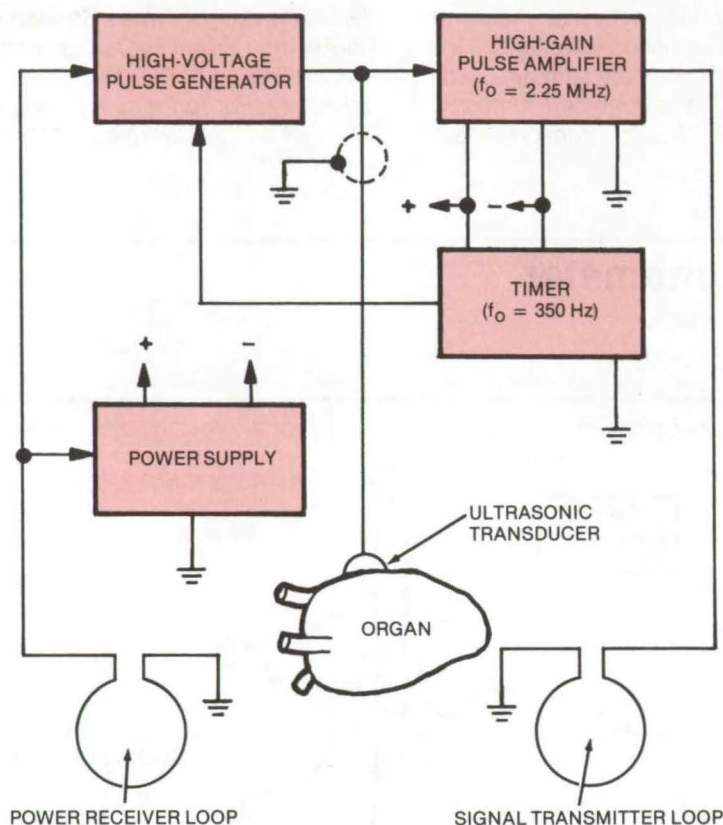


Figure 2. **RF Energy Is Transformer-Coupled** via the power receiver loop to the echosonometer. The energy is converted to regulated dc in a bipolar power supply and is used to power the high-gain pulse amplifier and the timer. The energy is also converted to high-voltage dc, then is periodically interrupted via silicon-controlled rectifiers (SCR's) to produce the pulse needed to excite the transducer. The SCR's are gated by the timer; in this application of the echosonometer, timer pulse-repetition frequency is 350 Hz. The pulses and echoes collected by the transducer are amplified and fed to a transmitter broad-tuned to 2.25 MHz. Data are induced from the transmitter loop to a signal receiver loop.

energy penetration in the organ.

Pulse rate of the high-voltage pulse generator (Figure 2) is controlled by a timer, an astable NOR-gate-configured multivibrator. Output of the multivibrator is differentiated, then buffered to source clock pulses to the generator. The pulses, in turn, trigger the generation of a high-voltage pulse into the transducer.

High-frequency energy, induced into the power receiver loop, is directly coupled to the primary winding of a transformer having two secondary windings. One of the secondaries is connected to a bipolar low-voltage dc source that powers the timer and amplifier. The other secondary, with many more turns than that of the low-voltage winding, is converted to dc that is used to charge a capacitor. A pair of silicon-controlled rectifiers, fired by the timer, rapidly discharges the capacitor through the transducer to ground. During the period between pulses, echoes from the organ under study are collected by the transducer, are amplified, and then are induced into the signal transmitter loop.

This work was done by Gilbert K. Kojima of Ames Research Center. For further information, Circle 25 on the TSP Request Card.

This invention is owned by NASA, and a patent application has been filed. Inquiries concerning nonexclusive or exclusive license for its commercial development should be addressed to the Patent Counsel, Ames Research Center [see page A8]. Refer to ARC-11035.

Prosthetic Urinary Sphincters

Proposed reliable new devices require minimal surgery for implant.

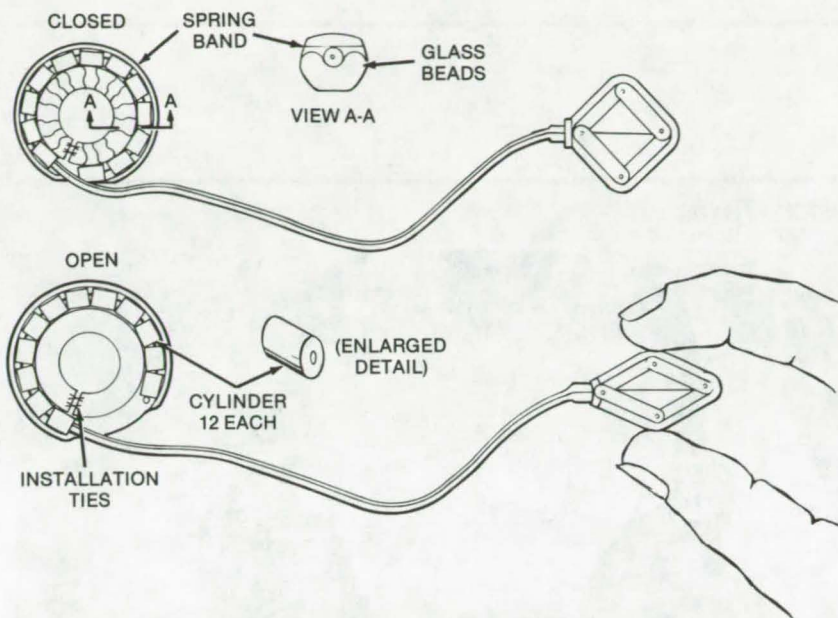
Marshall Space Flight Center, Alabama

A number of prosthetics have been proposed to take the place of nonfunctioning urinary sphincters, the ring-shaped muscles that dilate or contract body openings. These prosthetics can assist the victims of certain congenital defects, neurogenic bladder disease, stroke, multiple sclerosis, and accidents.

Each of five new devices is compared to a standard design in the illustrated chart.

One of the new devices is shown in the figure. It is a spring-cuff system that includes a cuff filled with very small glass beads (used in place of a fluid to avoid the problem of leakage). The beads evenly dis-

tribute the urethra compression over any irregularities. The urethra is held closed by a calibrated spring. The compression is released by tension in the cord from the actuator mechanism, which is held in a squeezed position for the duration of urination. The tension itself straightens out the cylinders, thus opening



The **Spring-Cuff Prosthetic** shown above is one of five proposed devices that can take the place of urinary sphincters.

Criteria	Press/ Relieve Bulb	Pressure Band	Bourdon Tube	Spring Cuff	Vise
Minimum Surgery for Implantation					
Simplicity for Maximum Reliability					
Ease of Adjusting Urethral Compression					
Minimum Compression Drift					
Flexibility of Connecting Tube					
Manufacturability					
Susceptible to Blood Contamination					
Ease of Installation Assembly					
Minimum Cuff Size					
Minimum Operator Size					
Adaptable to Male or Female					
IMPROVEMENT SAME LOSS					

A Comparison of Five New Prosthetic Sphincters is made with a standard design (the Scott-Bradley-Timm design).

up the spring band. The adjustment of urethral compression would be made during installation by selecting the right calibrated spring band and adjusting the cord to remove any excessive slack.

The other concepts include a press/relieve bulb, a pressure band, a Bourdon tube, and a vise. The press/relieve bulb concept would employ an SBT (Scott-Bradley-Timm) cuff and tube but with a larger capacity. The bulb would be squeezed to close the urethra, and a check valve would hold the fluid in the cuff. Overpressure is relieved by a small valve in the poppet head of the check valve and is bled back to the bulb through a small hole in the stem.

The pressure-band concept comprises a cuff filled with very small glass beads as in the spring-cuff design. To close the urethra, a cord attached to the pressure band keeps the cuff compressed against the urethra by a U-shaped spring.

The Bourdon-tube approach would use a cuff filled with glass beads and an SBT bulb. The cuff itself would be a Bourdon tube that would require a very low bulb volume to open it.

The vise concept employs a glass-filled "pad" on the cuff housing and another one on a piston attached to the cuff. The urethra is compressed, using a calibrated coil spring. To urinate, an activation mechanism pulls the piston off the urethra. ®

This work was done by Curtis R. Helms and Harold M. Smyly of **Marshall Space Flight Center**. For further information, Circle 26 on the TSP Request Card.

Inquiries concerning rights for the commercial use of this invention should be addressed to the Patent Counsel, Marshall Space Flight Center [see page A8]. Refer to MFS-23717.



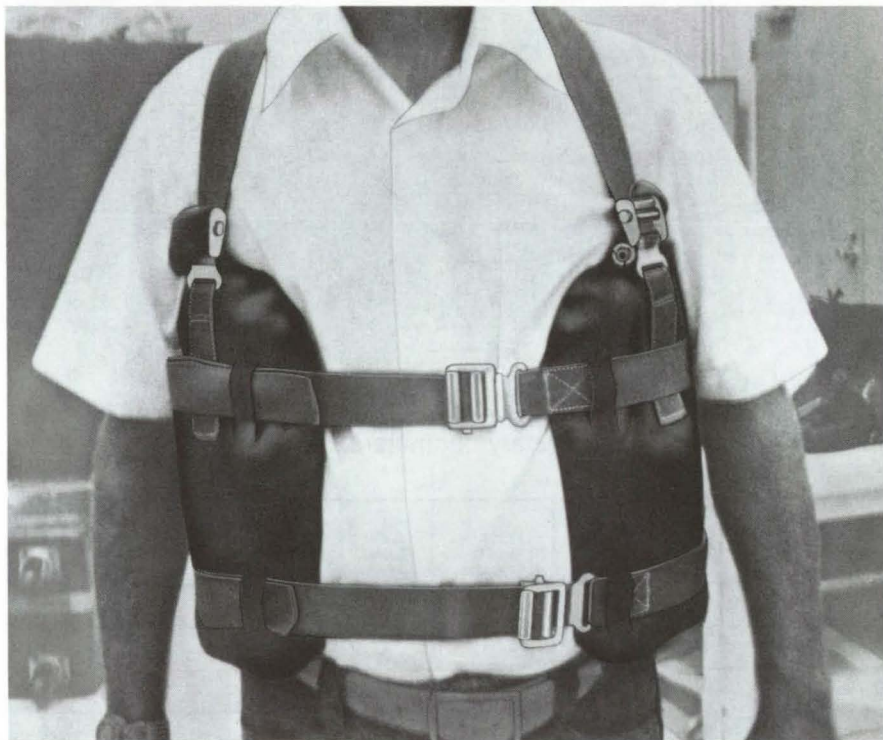
Cooling Vest

Liquid-filled garment protects wearer in hot environments.

Lyndon B. Johnson Space Center, Houston, Texas

A cooling vest, filled with chilled water, was developed to keep astronauts' body temperatures at an acceptable level during extravehicular rescues. Because it is an uncomplicated protective system and potentially inexpensive, it could well find use in other environments where heavy protective clothing is worn during physical exertion. For instance the vest could be worn by firemen underneath heat-resistant garments. The chilled water would absorb metabolic heat generated as the firefighter works. Normally this heat is trapped between his skin and the insulative clothing, making it difficult for him to function effectively. Possible applications include racing-car drivers and actors wearing "sealed" costumes under hot lights.

The vest, shown in the photograph, was developed as a substitute for more-complicated cooling systems that included water circulation, ice bags, or other special features that required support systems. This simpler garment is made from a heat-sealable urethane material put together in sections, using flat-pattern construction techniques. It is essentially a flexible container that is strapped or tied onto the wearer and is filled with cold water that absorbs body heat.



The **Cooling Vest**, worn as shown above, is made from neoprene-coated nylon and is fitted with adjustable straps. Filled with chilled water, it absorbs body heat generated during physical exertion.

The simple construction technique and durable materials make this vest relatively inexpensive to manufacture; its ease of use and effectiveness suggest that it would be well received for many applications.

*This work was done by Joseph Kosmo and James O'Kane of Johnson Space Center and Jack Coverdale of ILC. No further documentation is available.
MSC-16771*

Longitudinally-Vibrating Surgical Microelectrode

Longitudinal vibrations make electrode needle penetrate artery walls without dimpling.

Caltech/JPL, Pasadena, California

A microelectrode has been modified by attaching it to the cone of a miniature loudspeaker to impart longitudinal vibrations. This vertical

micromotion results in easier penetration into the relatively tough tissue of arterial walls, and allows more precise control over the depth of

penetration because the wall is penetrated but not pushed down. A similar approach could be taken with other probes or needles that are

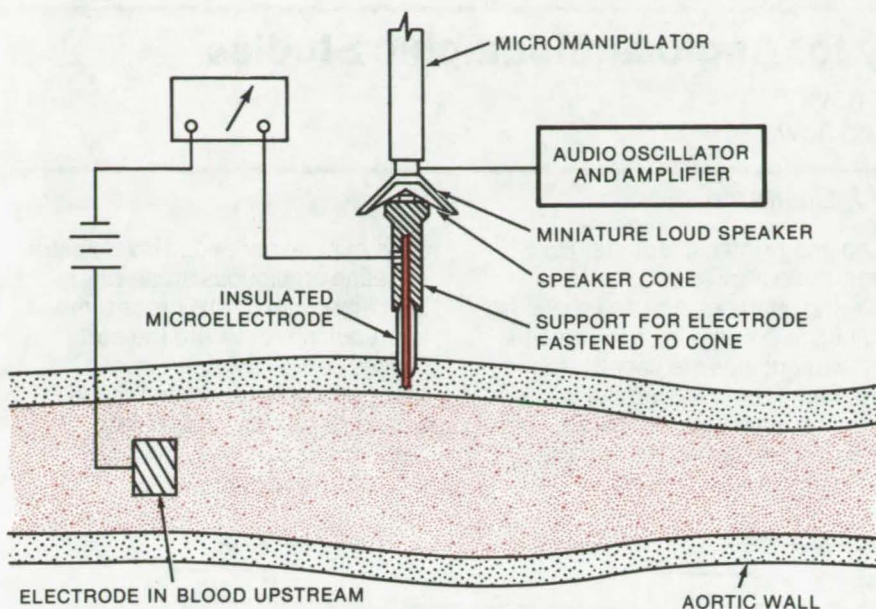


Figure 1. **Oxygen Content in Arterial Walls** is measured with a small electrode. Using a conventional nonvibrating electrode, a dimple of appreciable diameter forms in the tissue as soon as the electrode begins to penetrate the wall. With a vibrating microelectrode as shown in the apparatus above, only a minor dimple appears.

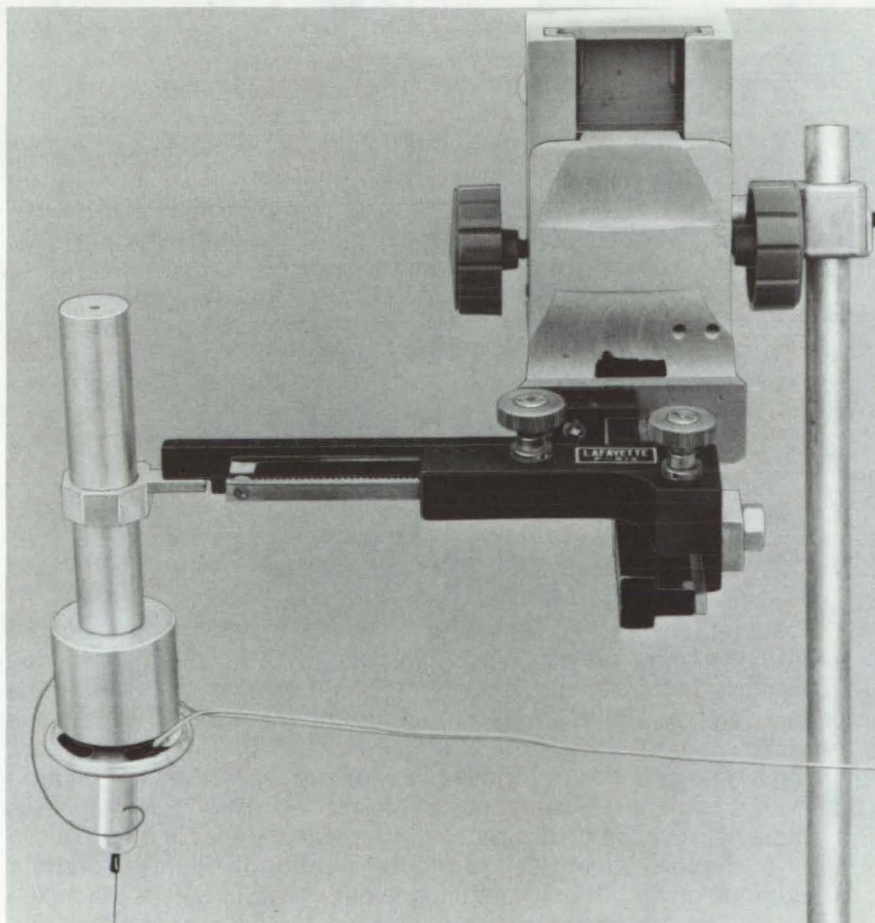


Figure 2. The **Vibrating Microelectrode** has been successfully used to make accurate oxygen-content measurements in arterial walls.

used to penetrate membranes, especially when it is important to avoid distortion around the point of the insertion.

The new microelectrode was developed in the course of a study on the possible causes of atherosclerosis, in which a series of measurements were made of the oxygen content within different layers of the arterial wall. In a typical measurement, as illustrated in Figure 1, a glass-insulated microelectrode is attached to a micromanipulator and is inserted a measured distance through the wall of the artery. The electrode tip has a diameter of 1 to 2 microns, and it was found impossible to penetrate the arterial wall without causing a surface indentation. This dimpling artificially induces a change in the oxygen content in that localized area of the wall.

This problem was substantially overcome by imparting small longitudinal vibrations to the needle. As shown in Figure 2, the electrode is vibrated by a loudspeaker that is excited by an audio amplifier connected to a power amplifier. A permanent-magnet loudspeaker is used because the concentric distance between the coil and the magnet insures minimal side motion.

This work was done by Cyril Feldstein of Caltech/JPL and Donald W. Crawford and Evangelyn W. Kanabus of the University of Southern California. For further information, Circle 27 on the TSP Request Card.

Inquiries concerning rights for the commercial use of this invention should be addressed to the Patent Counsel, NASA Resident Legal Office-JPL [see page A8]. Refer to NPO-13910.

Real-Time Video Display for Angiocardiographic Studies

Size and shape of the left ventricular cavity are correlated with blood pressure and flow.

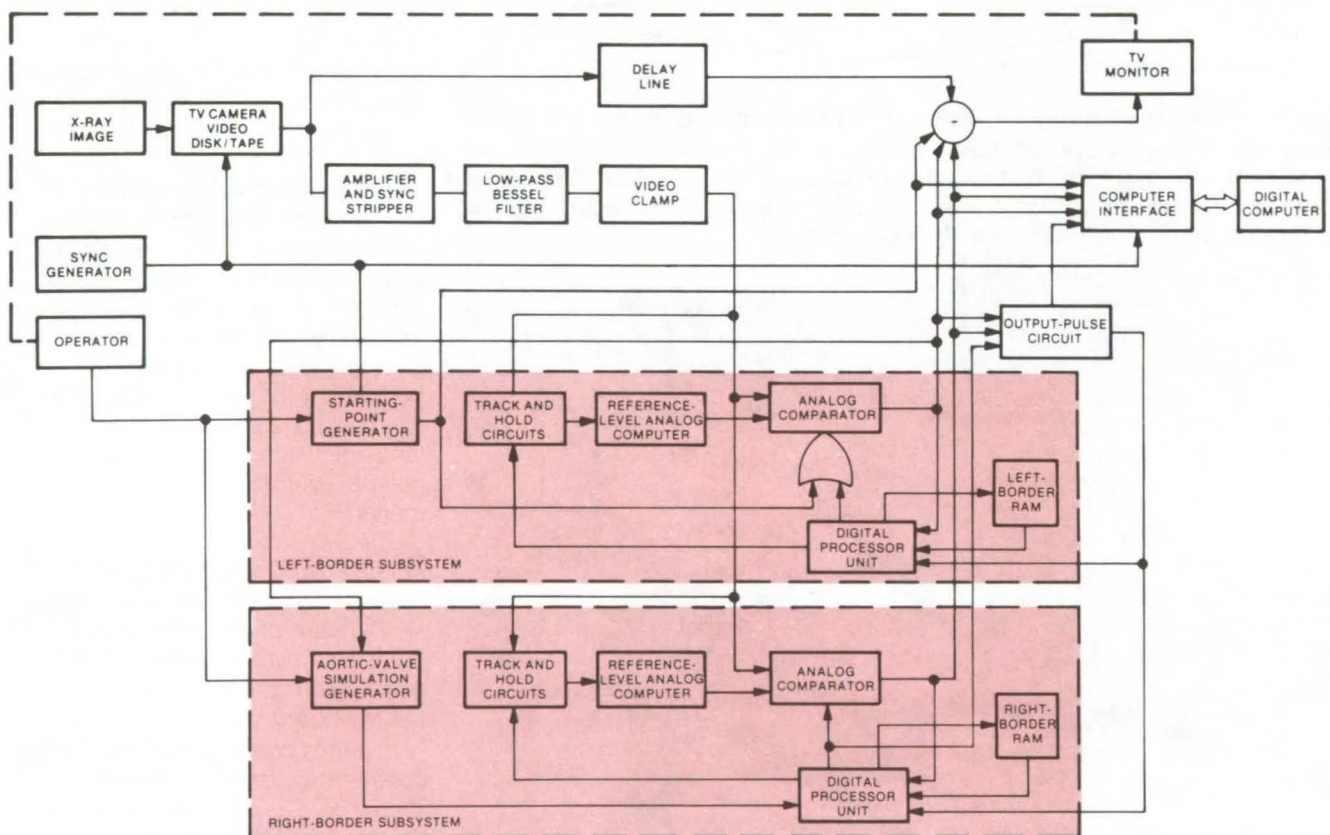
Ames Research Center, Moffett Field, California

Of the several methods of measuring the dimensions and volume of the cardiac chamber, angiocardiography has proved to date to be the most readily available and reliable. In this technique, a suitable radiopaque liquid is injected into the left ventricle, and an X-ray silhouette of the ventricle is displayed on the face

of an image intensifier tube. However, radiographic information showing chamber size and shape is difficult to develop from this image.

Heart outlines are usually traced manually to define chamber borders properly, even with films of excellent quality. More advanced or partially automated systems demand the

skills of an experienced investigator to define ambiguous areas where the diaphragm or ribs cross the heart outline, or where the aorta passes behind the heart image. Many attempts have been made to automate cardiovascular data-gathering procedures, with emphasis on developing an



The **Real-Time Contour Detector** and data acquisition system: The X-ray image is stored for subsequent processing on film, termed a cineangiogram, that is converted into a video format via a TV camera. The video signal from the camera is fed to the system. Camera timing signals are generated by a sync generator. Before a contour algorithm is applied, several preprocessing operations are performed on the input signal to improve the signal-to-noise ratio and to restore the video dc level. The signal is amplified, and sync pulses that are present in the video signal are stripped off in an amplifier and sync stripper. A 1-MHz low-pass Bessel-function filter suppresses the upper frequencies that do not contain relevant contour information. The filtered signal is then clamped for dc-level restoration. For display and visual feedback, the input video signal is also passed through a delay line that equalizes total delay of the low-pass filter and the logic circuit used in the contour detection. The delayed signal is applied to a summation amplifier where the detected contour pulses are mixed into the video signal with the correct time relation. The composite video signal is the system output signal and is used to display the X-ray image with the detected border on the TV monitor.

automated border recognizer. Yet in most methods, a computer must decipher the digitized image, thus making online and real-time operation impracticable.

The figure shows a new real-time contour detector and data acquisition system. The X-ray image at an image intensifier is converted into video format by a TV camera. The video signal is preprocessed in the sync stripper, filter, and clamp before passing to a left-border subsystem and a right-border subsystem. For display the video signal is also passed through a delay line and is applied to a summation amplifier where the detected contour pulses are mixed with the video signal and are displayed on a TV monitor. Both subsystems include:

- Track and hold circuits for sampling the brightness levels of predetermined points,
- A reference-level computer circuit,
- A brightness-level comparator,
- A processor that controls the comparator,

- A field memory for temporary storage of border-point coordinates,
- A computer interface, and
- A digital computer for real-time online operation.

Each subsystem detects the contour of one side of the chamber by comparing the brightness level of selected sample points to a dynamic reference level. The first sample point and reference level are set by the operator. The first point in the video field that causes a change in the brightness comparator is the first border point. The position of the border point is fed to the digital processor that uses this data (and the preceding point) and an algorithm to determine an "expectation window" for the next border point. The processor also defines three sample points to be used to calculate the reference level for the next border point. The border-point coordinates are stored in a random-access memory (RAM).

A separate track-and-hold circuit samples and holds the voltage level

at each of the processor-defined sample points. The set of voltages is fed to the dynamic-reference-level analog computer circuit that generates a new reference level. This is used for detection of the next border point. The left-border and right-border subsystems are nearly identical, except the right-border half includes an aortic-valve simulator. This is necessary because the X-ray contrast material injected into the patient flows into the aorta, making it impossible to obtain an outline of this portion of the heart.

*This work was done by Harold Sandler of **Ames Research Center** and Johan H. C. Reiber of Stanford University. For further information, Circle 28 on the TSP Request Card.*

This invention is owned by NASA, and a patent application has been filed. Inquiries concerning license for nonexclusive or exclusive rights for its commercial development should be addressed to the Patent Counsel, Ames Research Center [see page A8]. Refer to ARC-10985.



Books and Reports

These reports, studies, and handbooks are available from NASA as Technical Support Packages (TSP's) when a Request Card number is cited; otherwise they are available from one of NASA's Industrial Application Centers or the National Technical Information Service.

Liquid-Circulating Garment Controls Thermal Balance

Human thermoregulatory system is modeled.

Experimental data and a mathematical model of the human thermoregulatory system have been used to investigate the use of a liquid-circulating garment (LCG) to control thermal balance. The test data were gathered from a series of experiments in which environmental and metabolic conditions were varied as

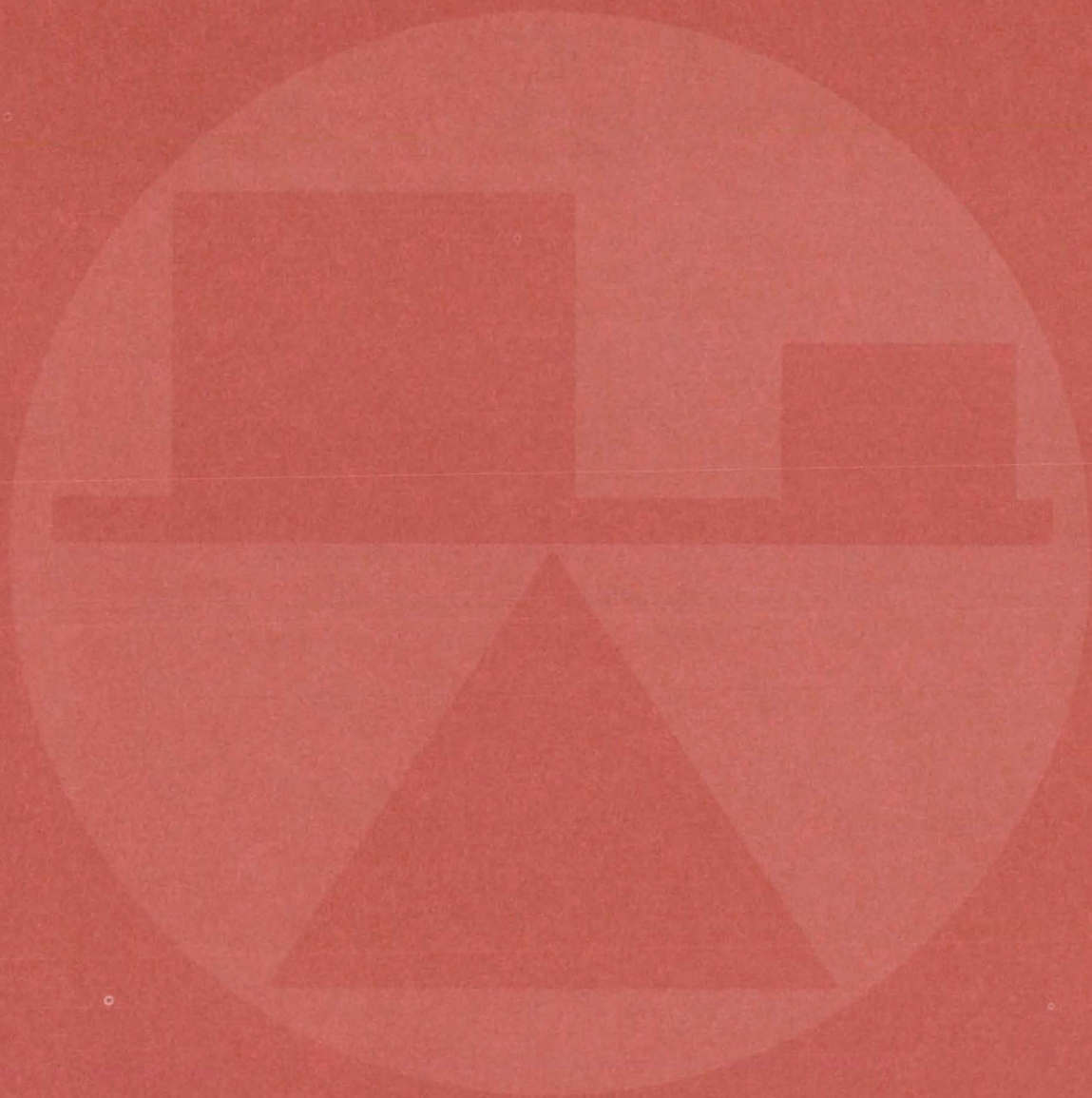
a function of LCG flow rate, LCG inlet temperature, net environmental heat exchanger, surrounding-gas ventilation rate, ambient pressure, metabolic rate, and subjective-vs.-obligatory control of LCG cooling.

A comfort band based upon total body heat storage was shown to be an effective means of quantitating thermal comfort. Test conditions associated with thermal comfort produced a nearly-rectilinear increasing relationship between metabolic rate and LCG heat dissipation; off-comfort conditions produced curvilinear or discontinuous results attributed to sweating, shivering, vasoconstriction, and vasodilatation. Thermal comfort can be provided by controlling the LCG flow rate at a fixed inlet temperature or by controlling the inlet temperature with fixed flow rate; the latter is more effective.

The mathematical model of the thermoregulatory system proved useful for interpreting the test data and for generating trends and relationships between physiological variables. It can be used as an accurate simulator of such variables as sweat rate, skin temperature, core temperature, and convective, radiative, evaporative, and LCG heat loss.

This work was done by Lawrence H. Kuznetz of Johnson Space Center. Further information may be found in NASA TM-X-58190 [N77-19756], "Control of Thermal Balance by a Liquid Circulating Garment Based on a Mathematical Representation of the Human Thermoregulatory System" [\$13.50]. A copy may be purchased [prepayment required] from the National Technical Information Service, Springfield, Virginia 22161. MSC-16727

Mechanics



Hardware, Techniques, and Processes

- 371 Measuring Solar-Cell Quality
- 372 Solar-Cell Measurements in the Field
- 373 Allowable Bending Loads for Mechanical Fasteners
- 375 Interpreting Honeycomb Climbing-Drum Peel Tests
- 376 Compressibility Measurement of Fluid-System Ullage
- 378 Instrument Measures Dynamic Pressure Fluctuations
- 380 Radiographic Detection of Cracks
- 381 Cost-Effective Actuator Tester
- 382 Multichannel Temperature Sensor
- 383 Improved Radiant-Heat Oven
- 384 Fireman's Lamp

Books and Reports

- 385 Ultrasonic Detection of Bearing Defects

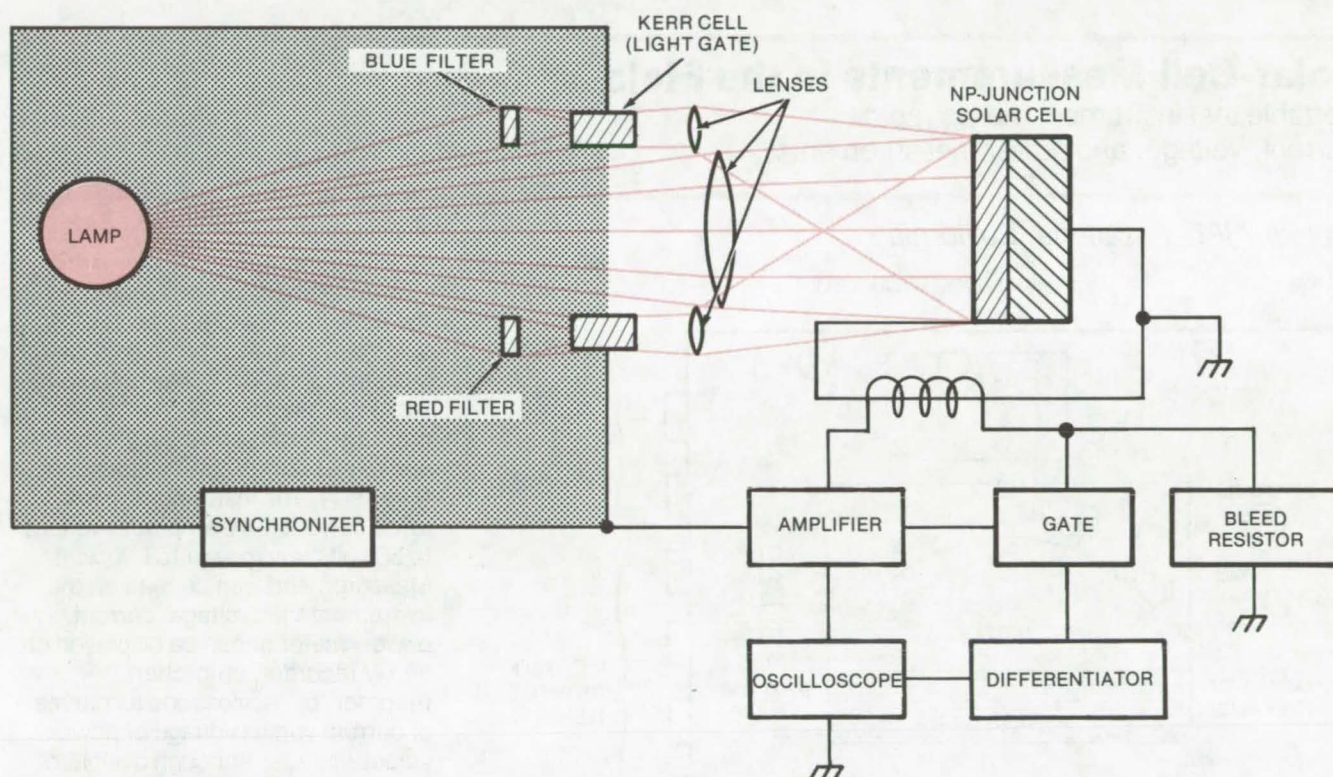
Computer Programs

- 385 Analysis of Aircraft Motions
- 386 Subsonic Wind-Tunnel Performance
- 386 Particle Trajectories in Radial-Inflow Turbines
- 387 Design of Minimum-Weight Structures

Measuring Solar-Cell Quality

Test system illuminates solar cells to ensure that minority-carrier lifetime (a performance indicator) is at the proper value.

Caltech/JPL, Pasadena, California



Laboratory Version of Test System, shown here, incorporates amplifier and differentiator to measure actual values. Production-line version merely compares cell output with that of a reference. Both versions, however, use simulated Sunlight and pulsed red and blue light to evoke response from cell.

An automatic method for checking the quality of solar cells promises to make cell manufacture more economical, efficient, and reliable. The method is based on the measurement of minority-carrier lifetime — a good indicator of cell future performance. A cell, as it comes off the production line, is exposed to light, and its behavior is compared with that of a cell of known high quality. If the newly made cell doesn't measure up, it is rejected.

Because the method is fast and automatic, it should make it easier for manufacturers to produce the millions of solar cells that will be needed for electrical power in the future.

The quality control system shines beams of red and blue light alternately on a cell to be tested. (The cell output for blue light gives information about the minority-carrier lifetime in the n layer of the cell; red light generates information about the p layer.) The cell is connected in reverse parallel to the reference cell, which is illuminated with the same light. Thus, if the minority carrier lifetime in the new cell is the same as that in the reference, there is no output from the combined cells. If there is an output, its magnitude indicates the extent of the deviation of the test cell.

The system is flexible enough to be adapted easily to testing a variety of solar cells. For example, it can be

used for back-surface field cells ($n^+ pp^+$ junctions) as well as for more conventional types (np junctions).

A somewhat more complex system has been developed for scientific (instead of production) measurements of solar cells. Instead of giving simple go/no-go or relative measurements, the scientific version (see figure) provides actual values of minority-carrier lifetime and diffusion length.

Like the production model, the scientific version uses a synchronizer to illuminate the cell with alternate beams of blue and red light and simultaneously illuminates the cell with simulated Sunlight (to produce realistic conditions within the semiconductor material). For the blue



and red light separately, the cell output passes through a differentiator (which produces an output proportional to minority-carrier diffusion length) and through an amplifier (with an output proportional to minority-carrier lifetime). The two

outputs are displayed on an oscilloscope.

This work was done by Oldwig von Roos of United Technical Services for **Caltech/JPL**. For further information, Circle 29 on the TSP Request Card.

Inquiries concerning rights for the commercial use of this invention should be addressed to the Patent Counsel, NASA Resident Legal Office-JPL [see page A8]. Refer to NPO-14100.

Solar-Cell Measurements in the Field

Portable test instrument makes rapid current, voltage, and power measurements

Caltech/JPL, Pasadena, California

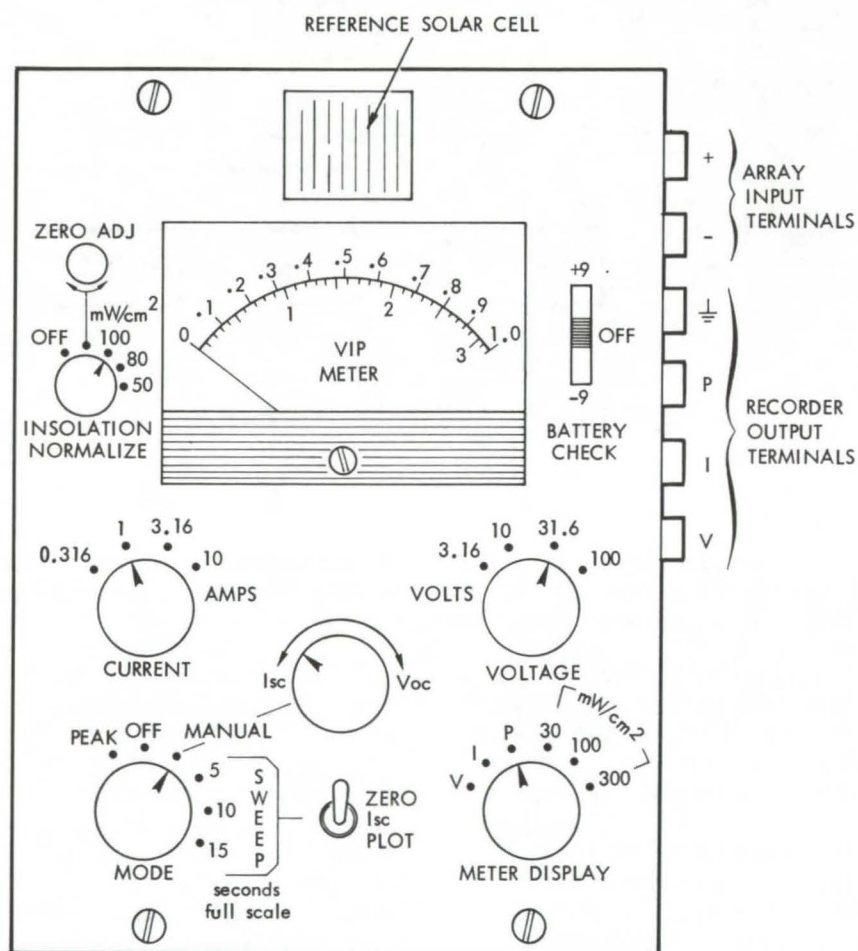


Figure 1. **Solar-Cell Arrays Are Checked** for voltage, current, and power output by this portable test instrument. A reference solar cell is included that allows the array current and voltage to be normalized to a standard illumination level.

A portable instrument measures the performance of photovoltaic solar-cell arrays in the field as well as in the laboratory. Measuring only 5 by 7 by 2 inches (12.5 by 17.5 by 5 cm), the instrument is easy to carry and use at out-of-the-way locations (Figure 1). The instrument reads array current to 10 amperes, voltage to 50 volts, and power to 500 watts. Measurements can be read on the instrument VIP (voltage/current/power) meter or can be displayed on an x-y recorder, strip-chart recorder, or oscilloscope as curves of current versus voltage or power versus voltage. Although designed primarily for solar cells, the instrument can be used for other dc sources, such as batteries and fuel cells.

Since photovoltaic solar-cell arrays are simple, reliable, and highly developed, they are expected to dominate in low-power solar-energy conversion for the foreseeable future. Consequently, a portable instrument for evaluating array performance should become more and more useful.

The compact instrument contains circuitry that allows peak current, voltage, and power to be measured in a fraction of a second, thereby minimizing heat dissipation. The power measurement is made by analog multiplication of current and voltage.

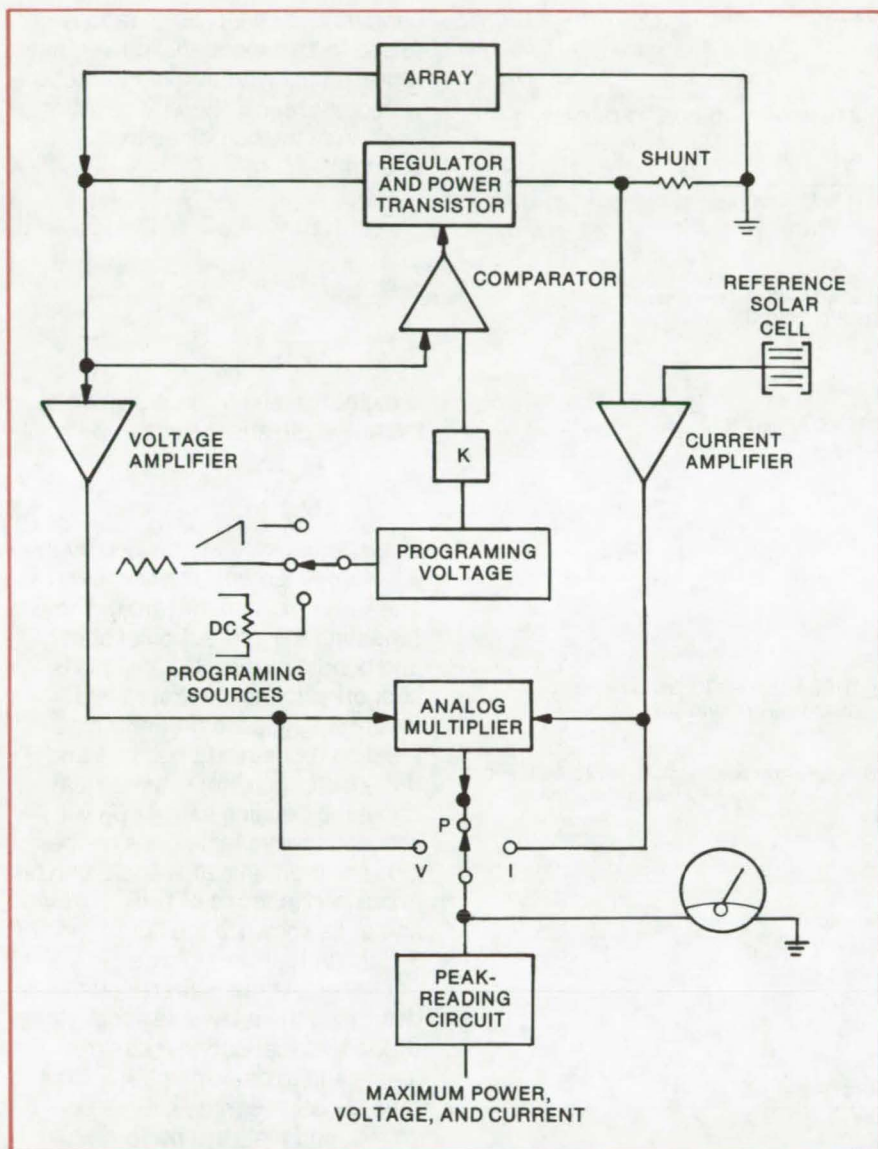


Figure 2. The **Meter Measures Array Performance** by regulating the voltage across the array, simulating an actual load. Current is measured across a shunt in series with a closed-loop series-transistor regulator. The low-level voltage and current are amplified and applied to a multiplier for power measurement. The peak-reading circuit stores the maximum voltage, current, and power level during each sweep.

A power transistor controls the loading of the solar array (Figure 2). A variable-voltage regulator drives the power transistor so that the solar-array output voltage varies linearly with a low-level programming voltage. The programming voltage can be controlled manually by the user (for dc measurements) or automatically by a constant dV/dt ramp voltage generator (for compatibility with an external strip-chart recorder) or a voltage oscillator (for peak reading). As the programming voltage sweeps over its range a peak-reading circuit stores the peak value of current, voltage, or power during a sweep.

So that measurements can be related to a standard illumination level, the instrument contains a built-in reference solar cell and circuitry that determines the ambient light level and allows the array current, and voltage to be scaled up or down accordingly.

This work was done by Ronald G. Ross, Jr., of Caltech/JPL. For further information, Circle 30 on the TSP Request Card.

Inquiries concerning rights for the commercial use of this invention should be addressed to the Patent Counsel, NASA Resident Legal Office-JPL [see page A8]. Refer to NPO-14067.

Allowable Bending Loads for Mechanical Fasteners

Modified shear-loading setup used to determine allowable bending moments

Marshall Space Flight Center, Alabama

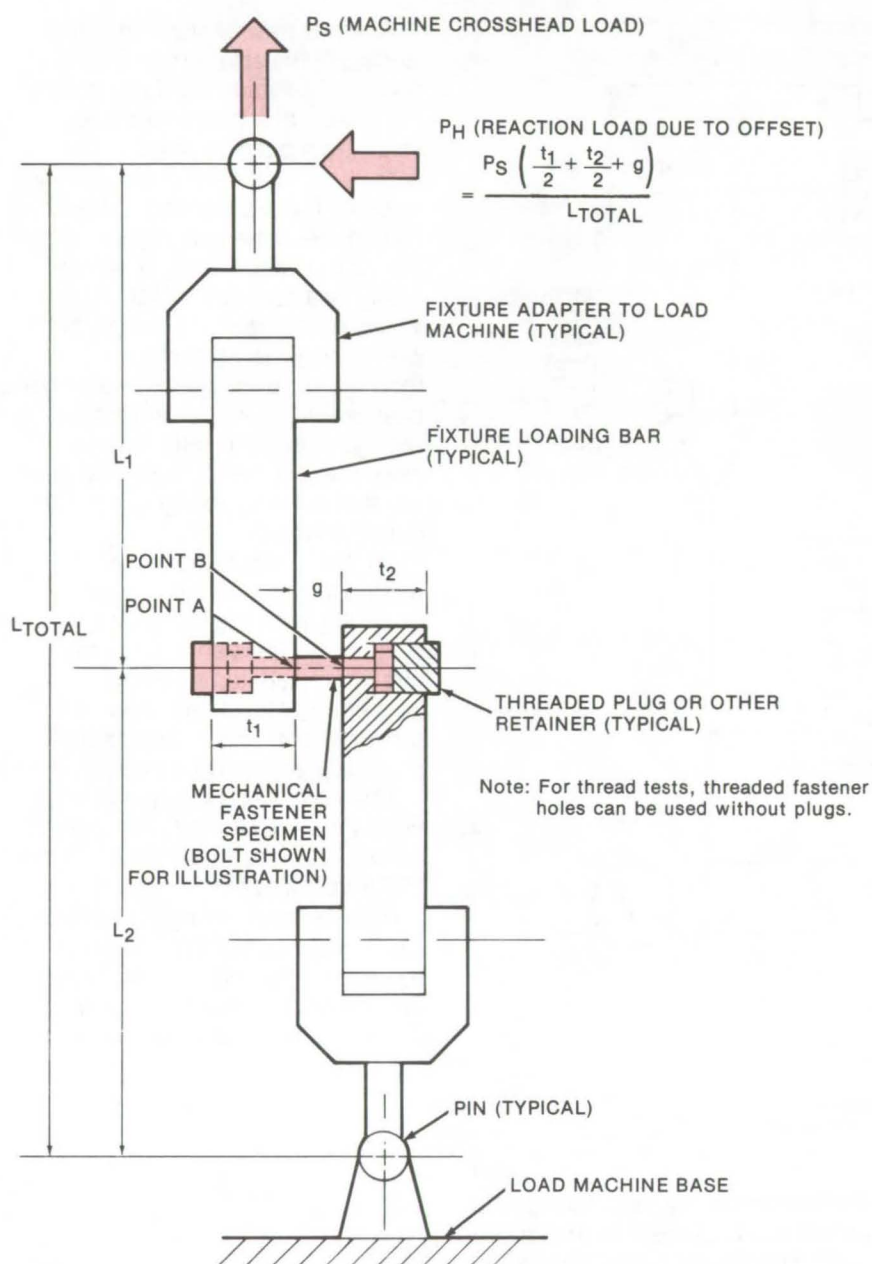
Allowable tension and shear loads, and their interaction, can be determined for bolts and pins by direct testing. However, it is difficult to establish pure bending loads directly with testing. This is because

the specimens are small, and shear loads are introduced during the tests.

A useful way around these problems has been employed to verify the allowable loads for threaded

bolts used in the Skylab program. The effects of shear load are separated by an analysis of its interaction with other loads. The interaction analysis combines separate ratios (actual-load to allowable-loads) for

(continued on next page)



The **Test Setup** above is used to determine allowable shear and bending loads on mechanical fasteners. With no gap ($g = 0$), the bending-moment load on the fastener would be zero, since the load would be transferred by pressure between the fixture bars and the fastener prying. By making measurements at three nonzero values of g and by measuring P_S to determine the allowable shear load, the bending moment can be determined.

bending and shear. Each ratio is raised to an exponential power that represents the degree of interaction with other ratios, thereby denoting a fraction of the combined load strength:

$$R_S^y + R_M^z = 1.0$$

where

$$R_S = \frac{P_{Sact}}{P_{Sall}}$$

is the actual shear force divided by the allowable shear force and

$$R_M = \frac{M_{act}}{M_{all}}$$

is the actual moment divided by the allowable moment (the unknown). The y and z exponents are unknowns reflecting the interaction of shear and bending loads. When a pin is supported in the illustrated test fixture, M_{act} is the greater of the bending moments at points A and B. If the fastener is not symmetrical about the bending axis, M_{act} will produce the highest stress on the pin. The moments at A and B can be expressed in terms of t_1 , t_2 , L_1 , L_2 , and g , as shown in the figure, and of P_S , the actual shear force.

The test fixture is first used to determine the allowable shear yield by load-vs.-deflection measurements and to determine P_{Sall} . The ratio equation contains three unknowns, and tests are performed at three different gap values (g) in order to solve for M_{act} .

Procedures can be simplified by assuming y to be 3.0, which is consistent with common practice for the interaction of shear and tension loads. This reduces the number of tests required to two.

This work was done by Ronald D. Ferdie and Raymond J. Steele of IBM Corp. for **Marshall Space Flight Center**. For further information, Circle 31 on the TSP Request Card.
MFS-23430

Interpreting Honeycomb Climbing-Drum Peel Tests

Results are related to bond flatwise tension, in-plane tension, and shear tests.

Marshall Space Flight Center, Alabama

Existing analytical methods for interpreting climbing-drum peel tests for the bond of honeycomb sandwiches are not always adequate. The relationship of climbing-drum peel tests to other tests performed on the same adhesive are difficult to define. This is primarily because the calculations of adhesive forces are not precise, and the interactions of the adhesive stresses are not clear.

Drum-peel tests have been made more meaningful by using approximations to derive analytical expressions that relate several failure modes to the peel-test results. Failures due to bond flatwise tension, in-plane tension, and shear are related to adhesive weight and method of bond cure. These factors, and test configurations, are shown to contribute interdependently to the results of climbing-drum peel tests.

Using the test setup in Figure 1, an average peeling load is determined for the drum as it moves up the specimen. Conventionally, this is related to an effective drum-peel bending moment M_{peel} . Analysis of the test shows that the average peeling load may be related to the actual bending moment and to horizontal shear forces. The identification of these actual loads at the peel line allows the development of a clearer picture of the possible failure modes of the adhesive lines.

The measurements resulting from a drum peel test are caused by the several loadings, which produce an interaction at the core/adhesive/facesheet interface, particularly at the points A and B shown in Figure 2. The interaction is produced by:

a. A flatwise tension loading of the attached facesheet pulling from the rest of the specimen,

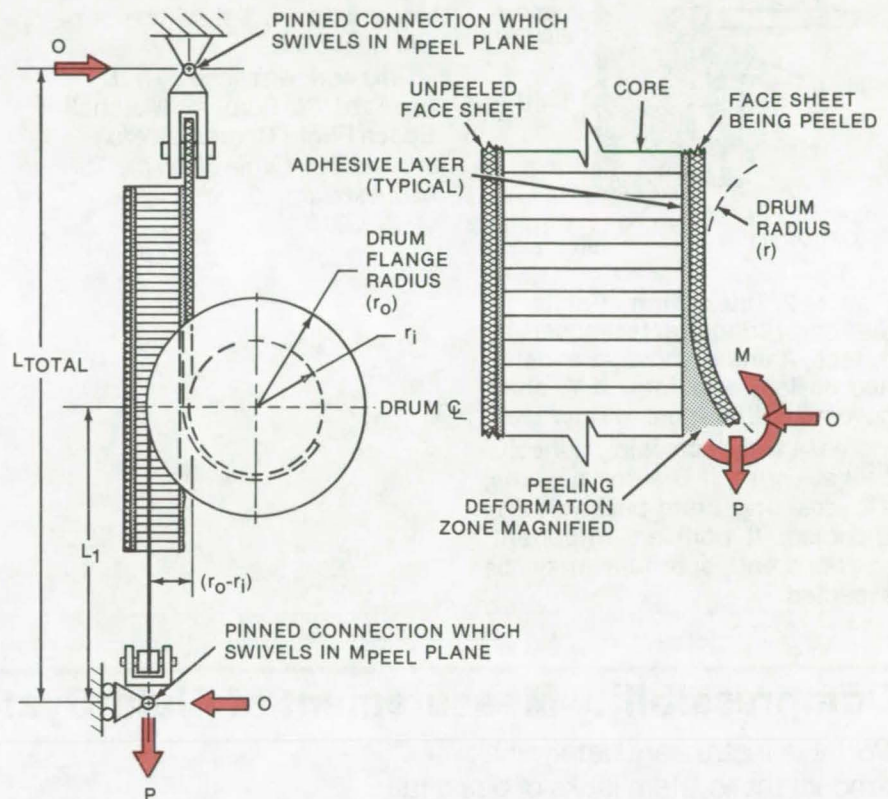


Figure 1. In the **Climbing-Drum Peel Test**, one facesheet of the test sample is attached to the drum, and the force on the cables necessary to roll the drum up continuously and to separate the facesheet from the core is recorded. This force is converted to a bending moment on the attached facesheet.

- An in-plane tension loading on the composite facesheet and adhesive, and
- Horizontal shear stresses at the core/adhesive/facesheet interface.

The combined effects of these forces can be expressed by using nondimensional coefficients termed "stress" or "load" ratios, one for each of the three types of load. Each coefficient or ratio may be derived from the actual loads determined by

using the analysis of the drum-peel tests. The ratios are defined such that when the sum of their squares equals unity at some point, failure will occur.

The resulting analysis shows that test configuration and adhesive thickness are important parameters in interpreting test results. More interestingly, mechanisms resulting in failures at points A or B in Figure 2 are shown to act both independently and in combination.

(continued on next page)

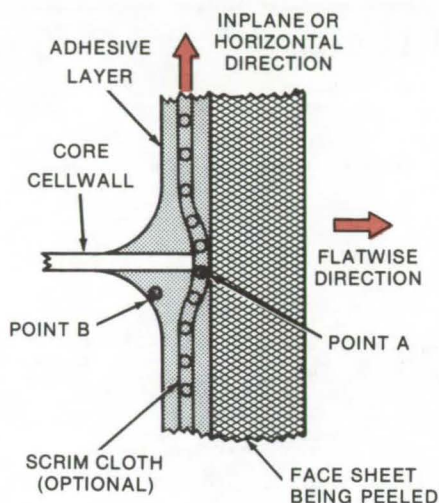


Figure 2. **Interaction Points** at the core/adhesive/facesheet interface, A and B above, are identified as failure points. If A alone governs, drum-peel values will increase with increasing adhesive peel strength; if B alone governs, a decreasing drum-peel value is expected. If both are important, an apparent optimum may be expected.

Recognition of these two different modes points out the importance of determining the actual weight-to-thickness ratio for the adhesive, the facesheet thickness, and the core geometry to use drum-peel test results properly. In designing a test experiment, fixture dimensions as shown in Figure 1 should be carefully controlled.

This work was done by R. D. Ferdie of IBM Corp. for **Marshall Space Flight Center**. For further information, Circle 32 on the TSP Request Card. MFS-23319

Compressibility Measurement of Fluid-System Ullage

Portable instrument determines amount that system lacks of being full.

Lyndon B. Johnson Space Center, Houston, Texas

A convenient self-contained instrument measures the volume of free gas or air trapped in closed fluid systems, such as lubricating-oil lines or hydraulic brakes. The air/oil ratio is important in closed-loop pressurized lube-oil systems because too much oil causes excessive drag in the gear case and too much air can lead to inadequate lubrication.

The test meter consists of a transparent cylinder, a piston, and a pressure gage, as shown in Figure 1. The cylinder is filled with the system liquid and is connected to the system under test. The operator reads the pressure P_1 , moves the piston to change the volume of liquid in the cylinder by an amount ΔV_1 , and then reads the new pressure P_2 . Because the liquid in the cylinder

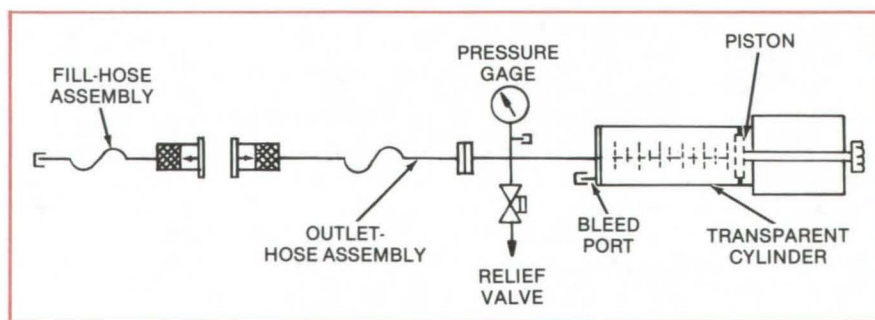


Figure 1. **Portable Compressibility Test Unit** determines the volumes of fluid and gas in a closed fluid system and can also be used to dispense or extract precise quantities of fluid. This schematic, Figure 2 shows the principle, and shows a production model.

and in the fluid line is incompressible, the change in volume of cylinder liquid will equal the change in gas volume in the system; i.e.

$$\Delta V_l = V_{g1} - V_{g2}$$

where V_{g1} and V_{g2} are the volumes of the gas at pressures P_1 and P_2 . Moreover, by Boyle's law

$$P_1 V_{g1} = P_2 V_{g2}$$

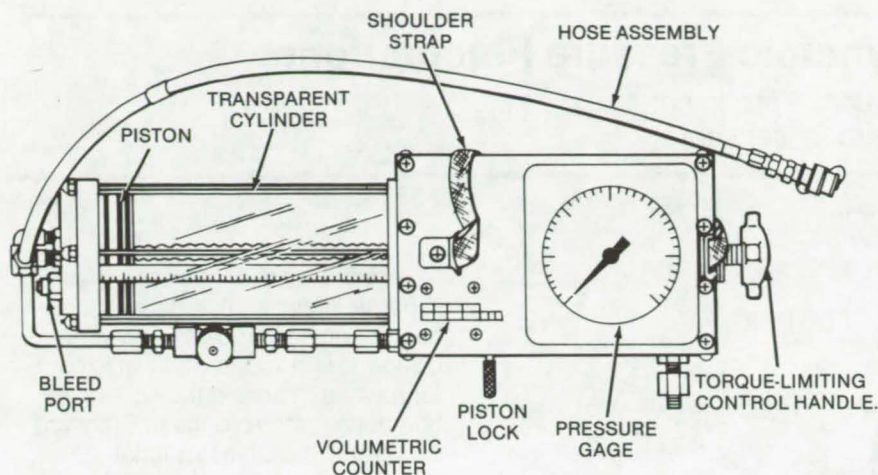


Figure 2. Drawing of **Production Model** compressibility unit developed for measuring ullage in the lube-oil systems of the Space Shuttle Orbiter auxiliary power unit shows details of the transparent cylinder, piston, and lead screw. Use of a transparent plastic is made possible by an assembly that reduces compressive and tensile loading of the cylinder to reduce the risk of cracking/crazing by oil under excessive pressure.

therefore the volume of gas in the system at the original pressure is given by

$$V_{g1} = \Delta V_1 P_2 / (P_2 - P_1)$$

If the total volume of the system is known, then measuring the volume of gas in the system also indicates the amount of liquid in the system.

Accurately measured quantities of liquid can be added to the system or removed from it by moving the piston in the calibrated cylinder of the measuring instrument.

The instrument includes many refinements for simplicity, versatility, and accuracy:

- A counter that measures ΔV_1 in 1-cm³ increments, either added or subtracted;

- A lock that holds the piston position to within 1 cm³;
- A relief valve to protect the cylinder and the system under test;
- A calibration port that allows the gage to be calibrated in the unit;
- A handle to hold the unit;
- A slip clutch in the handle that can be set to a specific torque (or pressure) — used with care, this clutch makes the relief valve redundant; and
- A shoulder strap to make handling easy.

As developed for measuring ullage in the lube-oil systems of the Space Shuttle Orbiter auxiliary power unit (see photos), this compressibility unit weighs 23 lb (10 kg), measures 21 by 7 by 6 in. (53 by 18 by 15 cm), and has a fluid capacity of 1,000 cm³ with a volumetric accuracy of ± 5 cm³. It operates at absolute pressures from zero to 20 psig (100×10^3 to 240×10^3 N/m² absolute) with a gage accuracy of ± 0.5 percent of full scale.

*This work was done by Donald A. Dzienis of United Technologies Corp. and Earl C. See of Rockwell International Corp. for **Johnson Space Center**. No further documentation is available.*
MSC-16640

Drilling Technique for Crystals

Small holes can be drilled in fragile crystals without cleaving or breaking them, using a new drilling technique. The crystal is supported on a flat holder and is advanced toward the drill at a slow controlled rate. Very slow drill speeds are used to limit heat buildup and strain on the crystal. The technique has been applied successfully on several organic crystals and should have general applicability.
(See page 402.)

Solar Meter With Silicon Photocell

An instrument with a simple silicon photovoltaic cell measures the light falling on a given spot — including direct Sunlight and light that has been scattered, reflected, and reradiated. The cell is 2 inches in diameter and generates about 0.5 volt. Its current varies directly with the light input. The cell is mounted on a heat sink to keep temperature errors to a minimum and is enclosed in a protective glass dome.
(See page 299.)

Conditional Sampling Analysis for Turbulent Flows

An analysis shows how conditional sampling measurements on turbulent flows can be incorporated into flow models. The measurements are obtained using a triggering probe and sampling probes that are activated only when a preset discriminating criterion is satisfied. Conditional sampling averages are related to the conventional averages present in flow models through an additional weighted averaging process.
(See page 414.)



Instrument Measures Dynamic Pressure Fluctuations

Pressure probe is used to measure fluctuations in hot, high-pressure environments too severe for sensors.

Lewis Research Center, Cleveland, Ohio

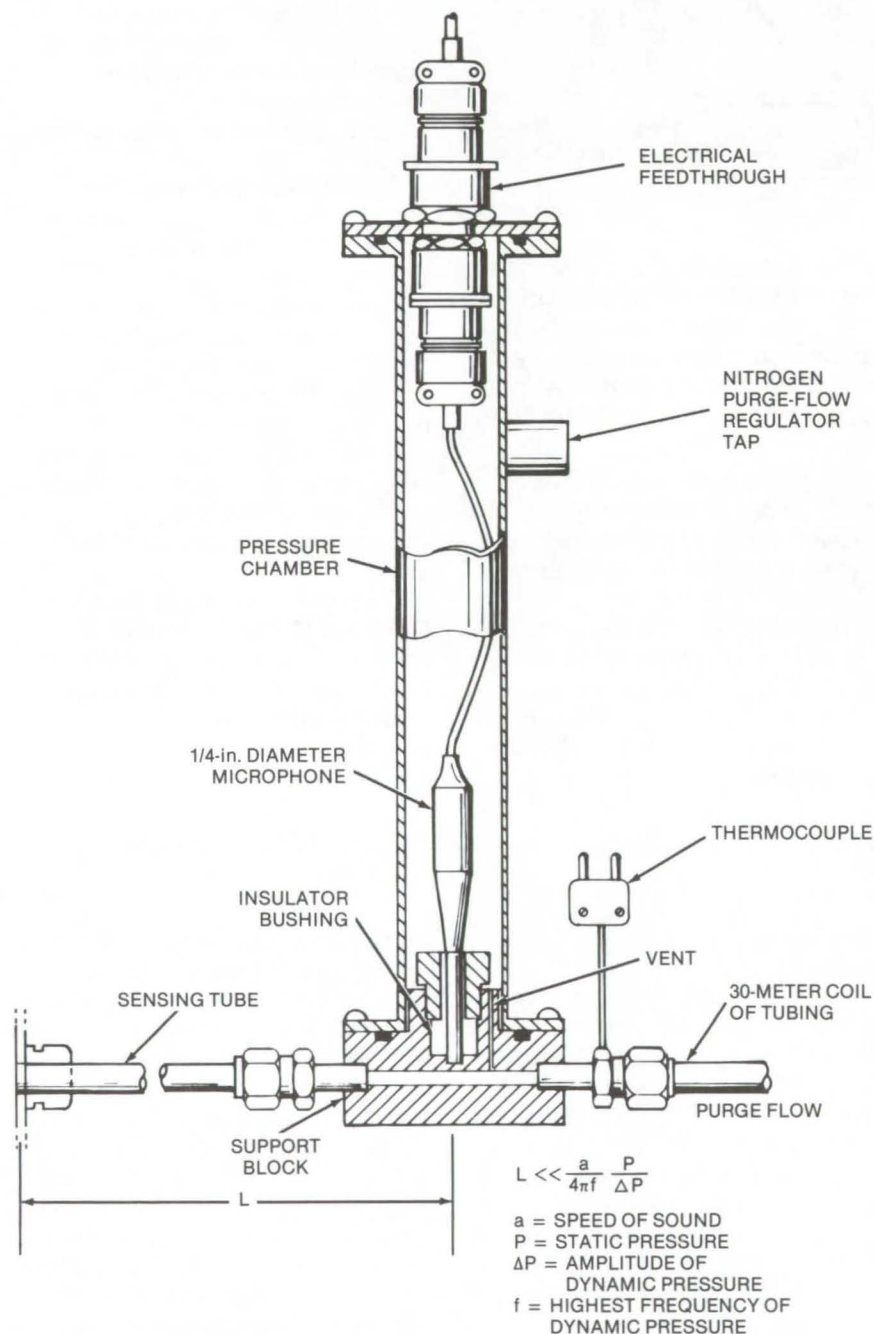


Figure 1. **Pressure Probe Sensor** is used to detect fluctuations in a high-temperature high-pressure duct. Direct contact between the sensor and the duct is avoided by using a sensing tube to tap into the duct. The purge gas tube includes 30 meters of coiled tubing so that it acts as an "infinite" line, eliminating pressure reflections.

An instrument to measure dynamic pressure fluctuations in a heated, pressurized gas flow was designed and successfully utilized for measurements in the core of an operating turbofan engine. Standard spectral and statistical signal-analysis techniques were applied to separate and identify acoustic fluctuations from other pressure fluctuations.

The instrument incorporates the principle of "infinite line" to remotely measure dynamic pressure in a severe-environment gas stream. A sensor detects pressure fluctuations that are transmitted to it through a tube from the point of measurement in a duct (Figure 1). The tube is installed in the duct as a wall static tap. Upon passing the sensor, the fluctuations progress through a 30-meter coil of flexible tubing, the "infinite line," and are subsequently dissipated to eliminate reflections that would otherwise result in reinforcement and cancellation of the incident signal.

The sensor, a 1/4-in. (0.635-cm) pressure-response microphone, is flush mounted in the sensing line through a support block and is housed in a pressure chamber. Pressure is balanced across the microphone with a venthole connecting the pressure chamber and the sensing line. The microphone electrical cable passes through a bulkhead connector in the chamber cap. The microphone is protected from harmful duct gases by a steady flow of nitrogen controlled with a pressure-differential regulator. The regulator follows system pressure by means of a feedback signal from the duct to maintain a slight positive differential pressure between the regulator output and the duct. The nitrogen purge flow is sufficient to protect the delicate microphone but has negligible effect on the measured dynamic signal.

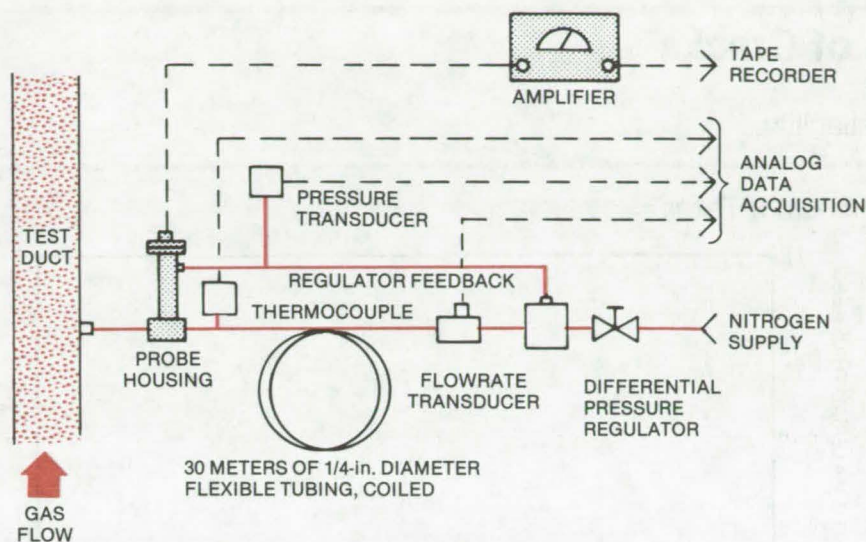


Figure 2. **Instrument Support Equipment** includes a pressure transducer to monitor static purge gas pressure, a thermocouple to measure purge gas temperature, and a flowmeter for purge-gas flow.

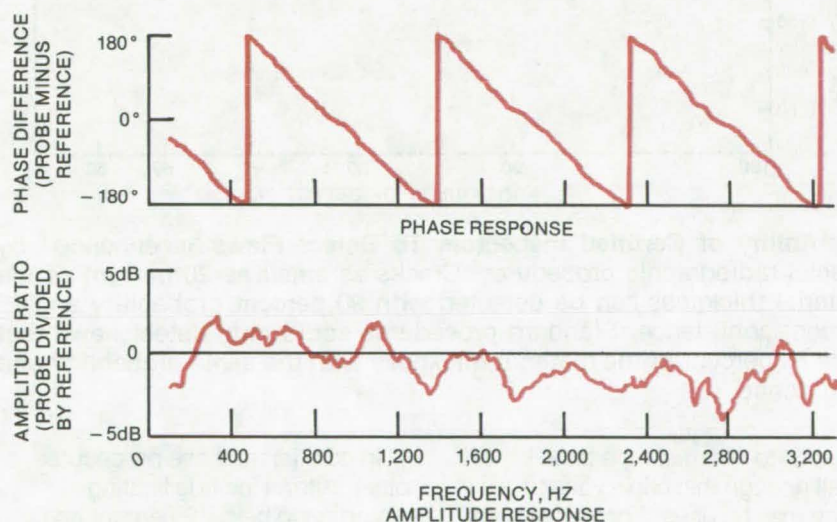


Figure 3. **Typical Data Obtained** with the probe are shown in the phase-response and amplitude-response graphs above.

Instrument support items include a thermocouple, pressure transducer, and flow-rate transducer to monitor sensing-line temperature, static pressure, and purge flow, respectively; a microphone power supply; and a signal-recording equipment (Figure 2).

Instrument frequency response is determined in an acoustic progressive-wave facility using a conventional 1/4-in. (0.635-cm) microphone as reference for basis of comparison. Typical amplitude-ratio and phase-shift plots are shown in Figure 3. Instrument-recording system accuracy is maintained by periodic sensitivity adjustment of level-recording equipment by impressing a known pressure signal at the tip of the sensing tube with a pressure signal generator.

The instrument may find application in sensitive measurement of dynamic pressure in severe environments such as high-pressure and high-temperature gas flow, particle and moisture entrained flow, and generally, in situations where a sensor cannot be directly exposed to the medium in which measurements are to be made.

This work was done by James W. Coats, Paul F. Penko, and Meyer Reshotko of **Lewis Research Center**.

Further information, consisting of data obtained through use of this instrument, may be found in:

NASA TM-X-73587 [N77-17064], "Core Noise Measurements of a YF-102 Turbofan Engine," and NASA TM-X-73535 [N77-11053], "Core Noise Source Diagnostics on a Turbofan Engine Using Correlation and Coherence Techniques."

Copies of these reports may be obtained at cost from the New England Research Application Center [see page A7].
LEW-12808

Radiographic Detection of Cracks

New procedures that give improved images can locate flaws with high reliability.

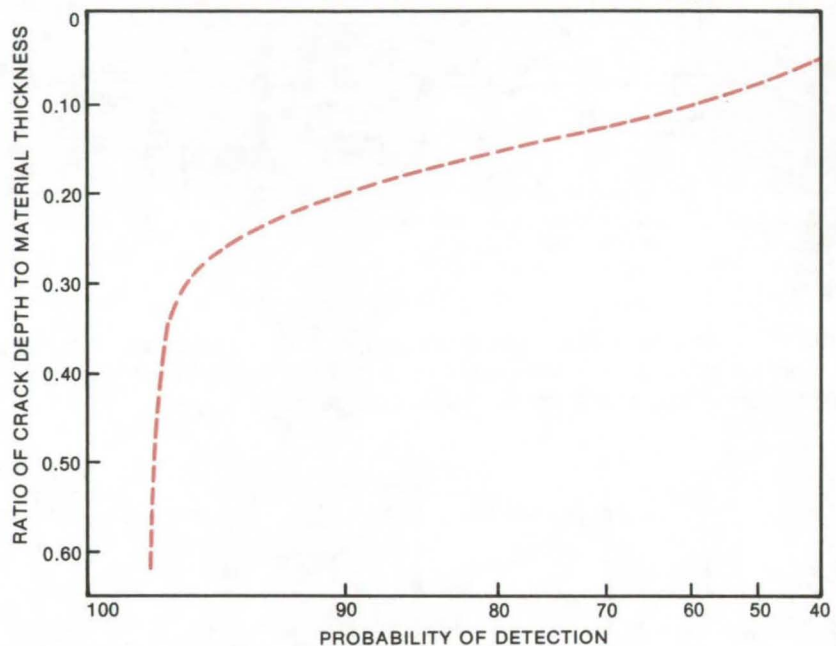
Lyndon B. Johnson Space Center, Houston, Texas

A new study finds that X-ray radiographic techniques can reliably detect material cracks if proper imaging procedures and criteria for selecting qualified inspectors are followed. Although radiographic methods have been used widely to inspect materials for anomalies, they have generally not been used for crack detection because of the supposed insensitivity of radiography to tight material cracks. However, the new study finds that radiographic images can be enhanced to the point where cracks as small as 20 percent of the material thickness can be detected reliably (see figure). This can be compared with 70 percent of the thickness when conventional radiographic procedures are used.

This increased sensitivity is obtained by improving several image characteristics, such as contrast, sharpness, contrast ratio, and distortion, by optimizing beam parameters and geometry. In addition, guidelines for the certification of qualified inspectors have been established that include testing candidates on their ability to locate flaws in prepared specimens.

The beam voltage is the most important factor that affects image quality. It was found that contrast ratio improves as the voltage range is decreased, up to the limit where internal scattering begins to reduce the image quality. This effect seems to be a result of higher sensitivity of the film emulsion to the longer wavelengths generated at lower voltages.

The image "unsharpness" factor, which measures blurring due to the penumbra effect caused by the finite size of the beam focal spot, can also be improved by either decreasing the size of the spot or by increasing its distance from the film. Of these possibilities, it is preferable to decrease the size since this allows



The Ability of Certified Inspectors To Detect Flaws is enhanced by special radiographic procedures. Cracks as small as 20 percent of the material thickness can be detected with 90 percent probability and 95 percent confidence. Standard procedures could only detect flaws that were 70 percent of the material thickness with the same probability and confidence.

the spot-to-film distance to be kept small enough that a low voltage range may be used. Focal spots less than 1.5 mm in diameter (preferably less than 0.5 mm) are necessary to obtain good image definition. Maximum tolerable unsharpness was set at 0.0005 in.

The divergence of the X-ray beam can also affect the ability to consistently locate cracks, since maximum sensitivity is obtained when the beam is parallel to the largest crack dimension. Tests indicated that a beam angle of up to 6° (12° total arc) could be tolerated with no noticeable loss of image clarity. For larger beam angles, small flaws in test specimens were overlooked by the inspectors.

In addition to these procedures, other criteria include limiting distortion to below 2 percent and maintaining contrast ratio at 8 percent for every 2 percent change in material thickness. A total of eight image-related criteria were established along with four guidelines for selecting inspectors. When these procedures are followed, cracks as small as 20 percent of the material thickness can be located with 90 percent probability and 95 percent confidence.

This work was done by Frank E. Sugg of Rockwell International Corp. for Johnson Space Center. For further information, Circle 33 on the TSP Request Card. MSC-16541

Cost-Effective Actuator Tester

A plug-in module and preprogrammed function cards convert a breadboard electrohydraulic actuator for simulated testing.

Lyndon B. Johnson Space Center, Houston, Texas

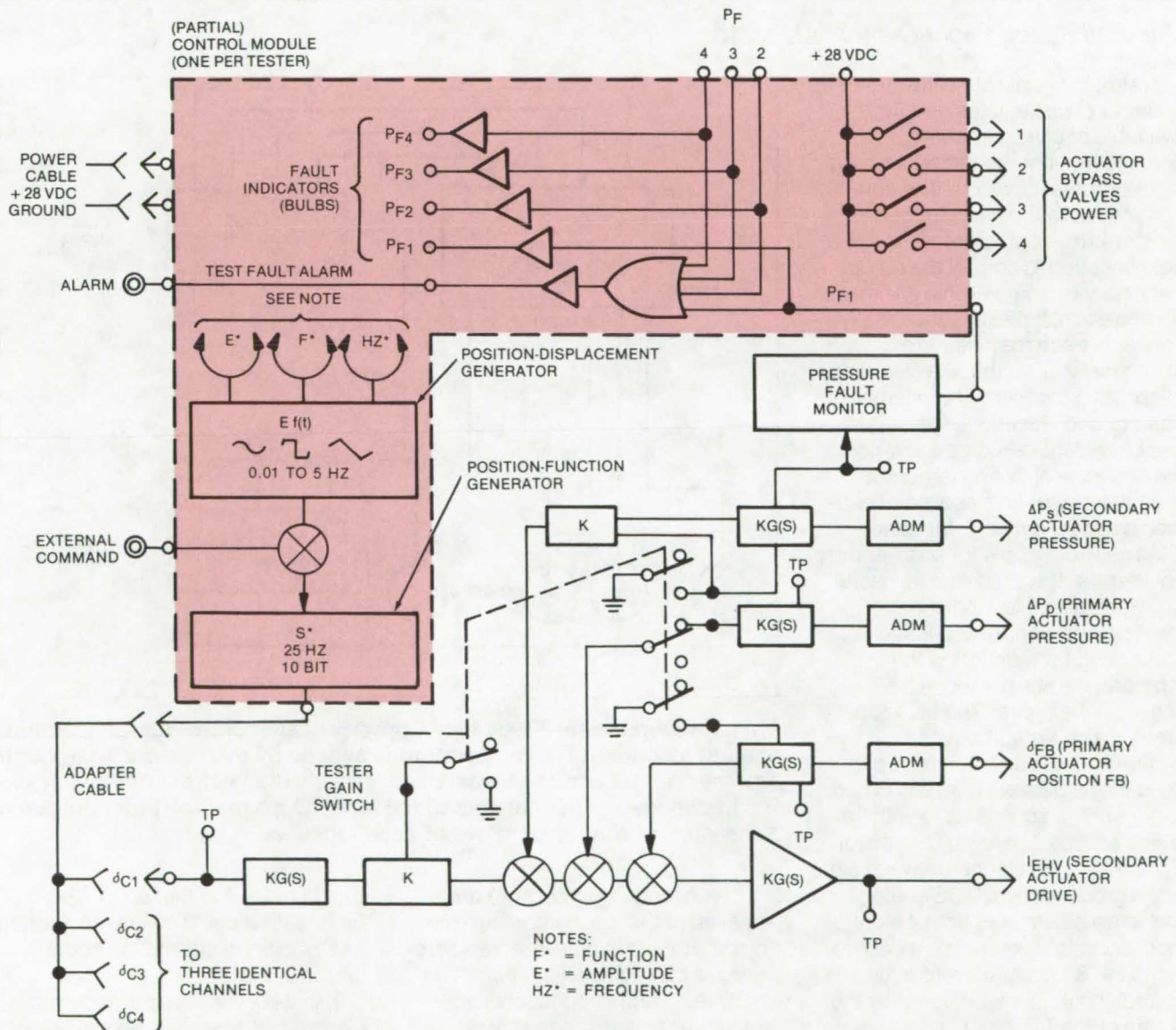
A group of preprogrammed plug-in cards and a control module will convert the breadboarded control electronics of an actuator assembly to an actuator tester. The tester, as shown, utilizes the electronic, control, and hydraulic systems of the breadboard actuator into which it is installed. The plug-in testing kit is

more cost-effective than previous methods since it permits quick field conversion of a breadboard actuator/control electronics unit but still retains the digital quantization and signal-sampling characteristics of the control unit. After change-over, the actuator test cycles may be performed with only external

electric and hydraulic power connected. A built-in multimode function generator supplies the waveforms that are used to drive the actuators.

The four-element kit consists of:

- a control module,
- servocontrol cards,
- an adapter cable, and



The **Cost-Effective Actuator Tester** shown is for one interface channel of a four-channel system. It utilizes the breadboard electronics with temporary plug-in alterations for electronic simulation. The signal and the functional relationship from command signal input to the actuator interface are shown. Cards not used during testing are removed, and a plug-in controller module is substituted in their place.

(continued next page)

•a test-point panel.

The control module plugs into chassis connectors vacated by unused cards, and it contains power, signal, and indicator functions. Four servo switches (one per card) alter actuator loop gain. An adapter jumper cable patches power and command signals for tester operation, and the plug-in test panel

accesses test points for instrumentation analysis.

The electronic breadboard interfaces with four different actuator types, of which there are six separate actuator units. This tester modification uses one breadboard unit to control four redundant secondary actuators of a single drive unit. Adaptation of the control loops for a

particular actuator type is accomplished by the switches that are mounted on each of the four card assemblies.

This work was done by Gerald F. Kopp and Charles E. Wyllie of Honeywell Inc. for Johnson Space Center. For further information, Circle 34 on the TSP Request Card. MSC-16324

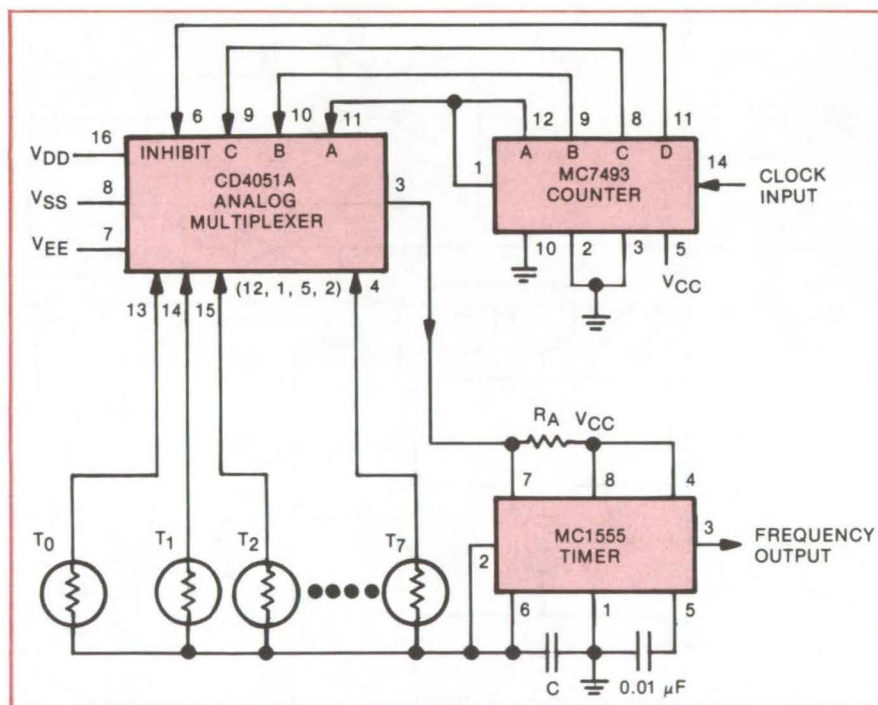
Multichannel Temperature Sensor

Inexpensive circuit monitors the temperature at eight locations and converts it to frequency.

Marshall Space Flight Center, Alabama

A simple temperature-to-frequency converter uses readily available and inexpensive components to monitor the temperature at eight or more locations. The converter uses thermistors (negative temperature-coefficient resistors) at each location to control the output frequency of a single-chip IC timer. An analog multiplexer sequentially connects each thermistor to the timing network so that the frequency becomes a measure of the temperature at each location. The circuit has been considered as a low-cost method for monitoring temperatures in solar heating-and-cooling experiments and as a means for generating control signals for solar-energy converters. It should also be useful in other data-collection and temperature-control applications.

A circuit for monitoring the temperature at eight locations is shown in the figure. The MC1555 timer is a one-chip frequency generator that can be used to produce single pulses or, as wired here, to generate a square wave with frequency set by capacitor C, resistor R_A , and the resistance between pin 7 and ground. The CMOS analog multiplexer connects one of eight input ports to an output port according to the 3-bit digital word at its control input. The word is set by the output of the TTL binary counter. Only the first three digits are needed, the fourth being used to strobe the inhibit input of the multiplexer. A separate clock is provided to advance the counter.



This **Temperature-to-Frequency Converter** can monitor the temperature at eight locations. The temperature is sensed by thermistors T_0 through T_7 . The counter and multiplexer sequentially connect the thermistors to the frequency-control network of the timer IC, so that the timer output is a measure of the temperature at each location.

Thermistors T_0 through T_7 are installed at the locations where the temperature is to be sensed and are wired to the multiplexer inputs. The multiplexer output connects to pin 7 of the timer. During each clock cycle, the timer frequency will be a measure of the temperature at one of the eight locations, as sensed by

the thermistor at that point. The timer output could be counted during each clock period and the count stored in a latch.

This work was done by Kenneth A. Kadrmas of Marshall Space Flight Center. For further information, Circle 35 on the TSP Request Card. MFS-23749

Improved Radiant-Heat Oven

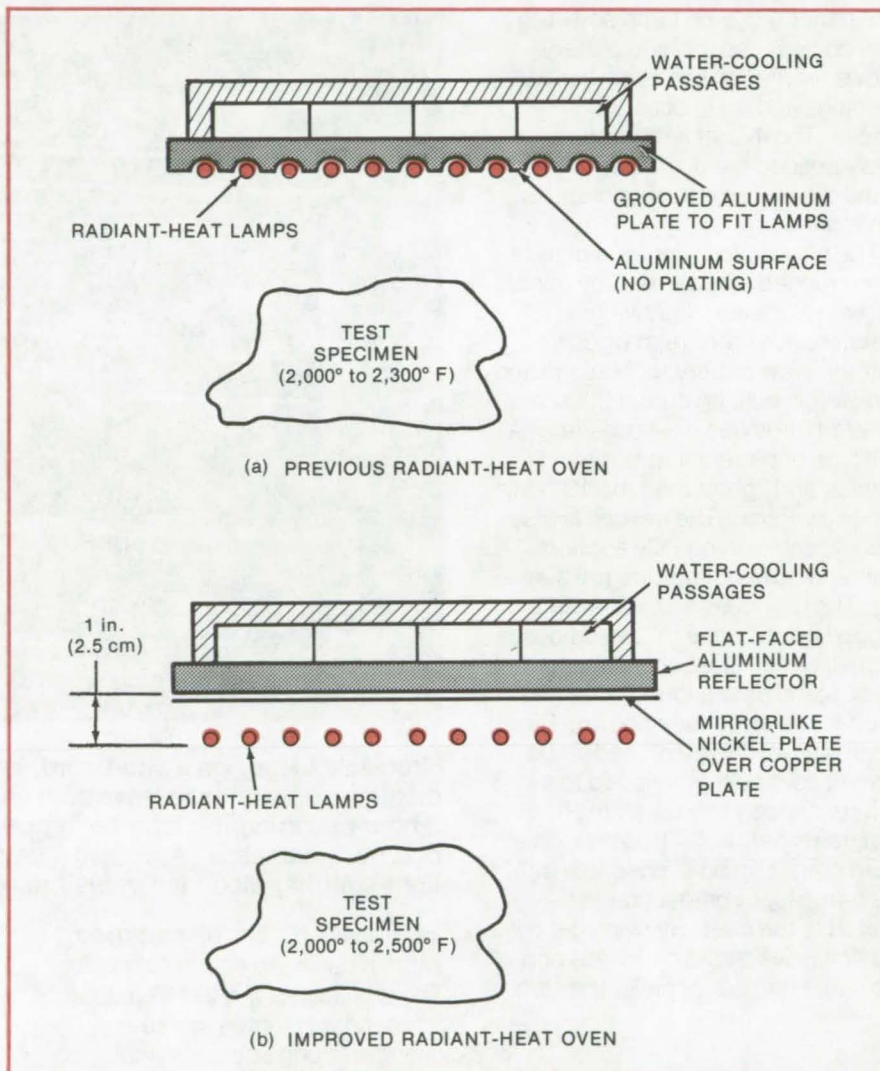
New reflector arrangement produces higher temperatures from less power and prolongs lamp life.

Lyndon B. Johnson Space Center, Houston, Texas

A greatly-improved radiant-heat oven materially increases lamp life and reduces electrical power requirements, yet heats test articles to higher temperatures with fewer lamp failures and lower cooling-water requirements than previous ovens. The new oven design permits longer operating time at test-article temperatures above 2,000° F (1,100° C) and peaks of 2,500° F (1,400° C) have been achieved with minimal loss of lamps. In ovens for brazing, heat treating, and high-temperature aerospace testing, the improved design offers significant savings in cost and energy.

In the previous oven design, shown in part (a) of the figure, the good fit between lamp and reflector absorbed at least half of the lamp output to keep the lamps cool enough to continue operating. This arrangement required up to one-third more power to get the same heat input to the test article; the extra power was absorbed by the water in the reflector. This design required lamp replacement about every five cycles when heating a test article to 2,300° F (1,300° C).

As shown in part (b) of the figure, the new oven arrangement utilizes aluminum reflectors that are plated with copper and then a very-high-luster nickel plate to produce a mirror surface. The lamps are mounted about an inch from the reflector, which reflects the major portion of the lamp output into the test article instead of absorbing energy to keep the lamps from melting. The water-cooled reflector is chemically treated inside to maintain maximum heat exchange from reflector to water.



A new **Radiant-Heat Oven** design (b) greatly lengthens lamp life and reduces power requirements by as much as 20 percent over former designs. The high-intensity oven can heat articles to 2,500° F repeatedly with a minimum of maintenance. Reflectors in previous ovens (a) relied on absorbing at least half of the lamp output to maintain lamp life and required lamp replacement every fifth run.

The new design made 51 runs to specimen temperatures of 2,300° F with no lamp replacements and 15 percent less power input. During this 51-test sequence, the specimen temperature was over 2,000° F for 10 minutes of each 67-minute test.

This work was done by Lloyd D. Beckerle and Amador R. Reyes of Rockwell International Corp. for Johnson Space Center. No further documentation is available.
MSC-16761

Fireman's Lamp

Rugged lamp used by miners is adapted for firefighters by use of lightweight battery.

Marshall Space Flight Center, Alabama

A miner's clip-on lamp powered by a compact space-age battery allows firemen to see in darkened buildings and/or in obscuring smoke. The 4-watt lamp frees a badly needed hand and can withstand the extreme environments of firefighting.

The new system consists of the same rugged light as used by miners but with a smaller, lightweight, maintenance-free, rechargeable battery. New battery technology and knowledge built up during the space program provided a 3-hour-life gel-cell type of battery that is much smaller and lighter than the 10-hour miner's version. The gel cell is also rechargeable, is equally economical, and does not require rewatering. The new cells are placed in a rugged plastic case that also houses a small circuit and light-emitting diode to indicate a low charge and need to recharge (see photo). The small battery can be placed in the turnout coat pocket, clipped to a belt, or clipped to a breathing-apparatus harness. The lamp, on a short cord, can be clipped to a belt, the harness, or onto a bracket riveted to the coat. By using gel cells (basically lead-acid batteries) and the same number of cells, the same



Fireman's Lamp, on a short cord, is clipped to belt, coat, or harness of breathing apparatus to leave both hands free. The battery, a gel cell with 3-hour operating life, can be slipped into the coat pocket or clipped to belt or harness. A small battery-monitor circuit including a light-emitting diode indicates the need to recharge.

lamp assembly can be employed, without having to obtain new bulbs. The unit utilizes a 4-V/1-A bulb with a redundant filament for safety, giving a strong adequate light.

This work was done by W. J. Britz and W. W. Varnedoe, Jr., of Marshall Space Flight Center. No further documentation is available. MFS-23783

Attaching Strain Gages by Ultrasonic Plastic Welding

Ultrasonic plastic welding may replace epoxy for bonding encapsulated strain gages to metallic surfaces. A layer of thermoplastic film is placed between the strain gage and the surface, and pressure and ultrasound are applied; the plastic melts, flows, and forms a permanent bond, generally within 3 to 6 seconds. The technique also may be used to cure adhesives and for attaching other sensors to structural parts.
(See page 408.)

Vacuum Mounting for Piezoelectric Transducers

A housing that consists of a vacuum chuck and a transducer mounting with an O-ring-sealed couplant chamber holds piezoelectric transducers to nonporous surfaces for ultrasonic or acoustic-emission testing. The housing has a flexible rubber diaphragm that provides sound isolation even on nonflat surfaces. It can also be used to apply tensile or compressive stress during testing.
(See page 393.)

Gearless Speed-Reduction Motor

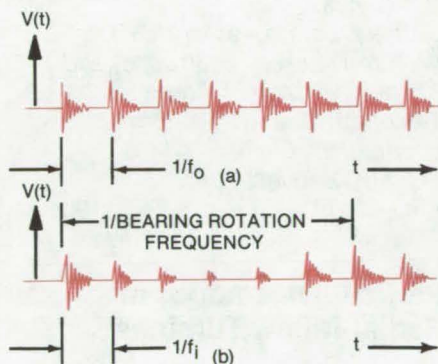
A proposed electric motor has an output shaft that rotates much more slowly than its commutation shaft. The motor uses no gears or pulleys; instead it has a magnetized rotor that rolls around the inside surface of a circular stator. Speed reductions of 1,000 to 1 or better are possible, and since frictional losses are small, the motor is efficient.
(See page 337.)

Books and Reports

These reports, studies, and handbooks are available from NASA as Technical Support Packages (TSP's) when a Request Card number is cited; otherwise they are available from one of NASA's Industrial Application Centers or the National Technical Information Service.

Ultrasonic Detection of Bearing Defects

Vibration and stress waves warn of failure and indicate its nature.



Ultrasonic Vibration Waveforms such as these are generated by defects in the outer race (a) and inner race (b) of a ball bearing.

The vibrations and stress waves emitted by defective bearings can be monitored to obtain an early warning of impending bearing failure. In an extensive experimental study, various sensors detected the noises at frequencies from 10 Hz to 1 MHz, and their outputs were displayed as

functions of time and frequency. Correlation of the results with known faults in the bearings showed that these measurements can discriminate between defective and acceptable bearings and can help identify the nature of the defect. Discrete faults as small as about 0.003 inch (0.075 mm) have been discerned by all the sensors used. Faults of about 0.001 inch (0.025 mm) were not obviously discernable.

Vibration and stress waves in the ultrasonic frequency range contain the information of primary value; in fact, the count rate of signals above 100 kHz is the strongest indication of failure propagation, with larger changes in this quantity than those of other methods. Therefore, the selection of a suitable sensor is critical to the utility of the system. Sensor selection and instrumentation are discussed at length in the report on this study.

Excessive vibration and noise in a bearing can be traced to a surface fault that causes an impact to occur every time a defect is passed. The impact duration is generally quite short (on the order of 10 μ s for a 207-size bearing with a surface fault about 10 mils (0.25 mm) wide]. The frequency content of this impact extends well beyond the 100-kHz range and in some cases could even extend into the MHz range. This impact initiates a stress wave in the bearing system. Since the bearing system made of steel is a high Q structure, multiple reflection of the stress wave causes the bearing to resonate. Vibration and noise are the end products of this process.

Some characteristic frequencies employed for bearing-defect detection are the ball-pass frequencies for a discrete outer-race defect, inner-race defect, and ball defect. These frequencies are associated with the number of impacts per unit of time or the number of times a rolling element rolls over a defect either on the races or on the rolling element itself.

The accompanying waveforms show typical signals in the time domain that would result from a single fault located on a raceway. In waveform (a) the decaying sinusoids repeat according to the ball-pass frequency for an outer-race fault, f_o . The decaying sinusoids relate to a natural resonance, and the individual ringdowns are quite alike in both amplitude and time duration. The wave in (b) shows the signal caused by an inner-race fault; though the sinusoids occur according to the ball-pass frequency for an inner-race fault, f_i , the individual bursts are not the same in amplitude or time duration.

This work was done by L. C. Ensor and C. C. Feng of ENDEVCO for **Marshall Space Flight Center**. Further information may be found in NASA CR-144130 [N76-15462], "A Study of the Use of Vibration and Stress Wave Sensing for the Detection of Bearing Failure," a copy of which can be obtained at cost from the New England Research Application Center [see page A7].
MFS-23446



Computer Programs

These programs may be obtained at very reasonable cost from COSMIC, a facility sponsored by NASA to make new programs available to the public. For information on program price, size, and availability, circle the reference letter on the COSMIC Request Card in this issue.

Analysis of Aircraft Motions

Aircraft motion derived from air-traffic-control data

Ames Research Center, in cooperation with the National Transportation Safety Board, has developed a technique for deriving time histories

of aircraft motion from air-traffic-control (ATC) radar records. Radar range and azimuth data are used along with the downlinked altitude data to derive an expanded set of data that includes airspeed, lift, and attitude angles (pitch, roll, and heading). This technique should prove useful as a source of data in

(continued on next page)

the investigation of commercial airline accidents and in the analysis of accidents involving aircraft that do not have onboard data recorders (e.g., military, short-haul, and general aviation).

The aircraft motions are determined by first smoothing raw radar data. These smoothed results, in combination with other available information (wind profiles and aircraft performance data), are used to derive an expanded set of data. The program uses a cubic least-squares fit to smooth the raw data. This moving-arc procedure provides a smoothed time history of the aircraft position, the inertial velocities, and accelerations. Using known winds, these inertial data are transformed to aircraft stability axes to provide true airspeed, thrust-drag, lift, and roll angle. Further derivation, based on aircraft-dependent performance data, can determine the aircraft angle of attack, pitch, and heading angle. Results of experimental tests indicate that values derived from ATC radar records, using this technique, agree favorably with airborne measurements.

This program is written in FORTRAN IV to be executed in the batch mode and has been implemented on a CDC 6000-series computer with a central memory requirement of 64K octal 60-bit words.

This program was written by R. C. Wingrove of Ames Research Center. For further information, Circle A on the COSMIC Request Card.
ARC-11132

Subsonic Wind-Tunnel Performance

Estimations for design and analysis of subsonic wind tunnels

Previous techniques used for the design and loss prediction of the components of subsonic wind tun-

nels have been improved and combined in a new computer program. Design guidelines for diffusers, contractions, corners, and the inlets and outlets of nonreturn tunnels are given in the program manual. The program is applicable to compressible flow through most closed- or open-throated, single-, double-, or non-return wind tunnels or ducts. A comparison of calculated performance with that actually achieved by several existing facilities produced generally good agreement.

The method of loss analysis used by the program is a synthesis of theoretical and empirical techniques. Generally, the algorithms used are those that have been substantiated by experimental tests. The basic flow-state parameters are determined from input information about the reference-control section and the test section. These parameters were derived from standard relationships for compressible flow.

The local flow conditions, including Mach number, Reynolds number, and friction coefficient, are determined for each end of each component section. The loss in total pressure caused by each section is calculated in a form nondimensionalized by both test section and local dynamic pressure. The individual losses are based on the nature of the section, local flow conditions, and input geometry and parameter information. The loss forms for typical wind-tunnel sections considered by the program include: constant area ducts, open throat ducts, contractions, constant area corners, diffusing corners, diffusers, exits, flow straighteners, fan nacelles, and screens.

Inputs consist of data describing each section, the section type, the section end shapes and dimensions, and parameters that vary from section to section. Outputs from the program consist of a tabulation of the performance-related parameters for each section of the wind-tunnel circuit and the overall performance values, which include the total circuit length, the total pressure losses

and energy ratios for the circuit, and the total operating power required. If requested, the output also includes an echo of the input data, a summary of the circuit characteristics, and plotted results on the cumulative pressure losses and the wall pressure differentials.

The program is largely selfchecking and selfprotecting, thus minimizing undetected and wasteful user errors. Judicious, iterative use of this program can simplify energy and performance optimization for subsonic duct flow.

This program is written in FORTRAN IV to operate in the batch mode and has been implemented on an IBM 360 with a central memory requirement of 82K (decimal) of 8-bit bytes.

This program was written by William T. Eckert, Jean Jope, and Kenneth W. Mort of Ames Research Center. For further information, Circle B on the COSMIC Request Card.
ARC-11138

Particle Trajectories in Radial-Inflow Turbines

Five programs help predict service life.

A package of five computer programs can be used to study the trajectories of particles in radial-inflow turbines. Particle erosion in gas-turbine engines is important because significant decreases in the operating life and rated performance can result from engine operation in dusty environments. Radial-inflow turbines have been used and are being considered for many commercial applications. These engines will at times exhibit incomplete filtering of incoming air, leading to the ingestion of erosive-size particles that could seriously degrade engine performance. A designer can predict the areas of the turbine that will be most affected by particle ingestion by using the programs described below.

Five computer programs solve the equations of motion of a particle in a gas-flow field for various parts of the turbine. They include:

•**PARDIM**, which determines the trajectory of particles in inward-flowing free vortices or in whirling flows that have no radial components but do have axial components. The solution is essentially a three-dimensional one; but instead of allowing particles to bounce, solutions are stopped when the particle passes boundaries of the fluid flow. The gas flow is based on the conservation of momentum, the conservation of mass, and the isentropic flow relations. The force of gravity acting on the particle can be included.

•**SCRL2D**, which determines the trajectory of a particle in a scroll. Gas flow is assumed to be uniform throughout the scroll, so that the solution is two-dimensional. The particle is allowed to bounce off the scroll wall, and the solution stops when the particle enters the nozzle region of flow. The force of gravity acting on the particle can be included.

•**STATOR**, which determines the trajectory of a particle in a stator. The solution neglecting the gravity force is three-dimensional, and the particle may bounce off any of the four surfaces that surround the channel. The program is restricted by a constant spacing from hub to shroud.

•**ROTOR**, which determines the trajectory of a particle in a radial-inflow turbine rotor. The gas-flow solution is based on a quasi-orthogonal method. The results of the fluid solutions are stored in arrays that specify the gas velocity vectors at the intersection points of the quasi-orthogonals and streamlines. A Runge-Kutta technique is used to integrate the three-dimensional equations of motion of the particle.

•**VANPY**, which determines the trajectory of a particle in an inward-turning vortex. The fluid-flow solution is based on the principle of constant momentum along the

streamlines, although the momentum may be different for different streamlines. The variation in the radius of curvature of the streamlines between the hub and shroud is taken to be linear.

In tracing the particles all the way through a radial-inflow turbine, the constantly changing nature of the flow requires that each region of the flow be considered individually.

Generally, all the programs will calculate several similarity parameters that are useful in relating different particles that have similar trajectories.

These programs are written in FORTRAN IV for execution in the batch mode and have been implemented on an IBM 360 with a central memory requirement of approximately 180K (decimal) of 8-bit bytes.

This program was written by W. B. Clevenger, Jr., and W. Tabakoff of the University of Cincinnati for Lewis Research Center. For further information, Circle C on the COSMIC Request Card.
LEW-12561

Design of Minimum-Weight Structures

Approximation concepts code for efficient structural synthesis

Finite-element techniques, mathematical programming methods, and an innovative collection of approximation techniques are combined in a program for finding efficient minimum-weight optimum designs for a significant class of structural synthesis problems. In the program, ACCESS-1, ("Approximation Concepts Code for Efficient Structural Synthesis") attention is focused on two- and three-dimensional structural systems made from isotropic materials that can be idealized using truss, triangular-membrane, and shear-panel elements. Multiple static loading conditions are considered, and stress, displacement, and member size constraints are

included. ACCESS-1 is a research-oriented program that implements a collection of approximation concepts to achieve efficient structural synthesis. Although the program was developed to test performance of various techniques of structural synthesis, it could be used in production to aid in the design of minimum-weight structural systems.

ACCESS-1 contains three types of finite elements: truss elements, isotropic constant-strain triangular-membrane elements, and isotropic shear-panel elements. Structural weight is minimized by modifying the cross-sectional areas of the truss elements and the thicknesses of the membrane and panel elements. Design constraints may be imposed on nodal displacements, tensile and/or compressive stresses in truss elements, von Mises combined stresses in the membrane and panel elements, together with minimum and maximum bounds on cross-sectional areas of the truss elements, and on thickness of the membrane and panel elements. Design-variable linking is employed to reduce the number of independent design variables.

At each stage during the iterative design process, the number of stress constraints is reduced by a specialized regionalization scheme, defined by finite-element groups linked to independent design variables. The number of stress constraints is further reduced using the 'throwaway' concept in which redundant or very inactive constraints are temporarily ignored. The number of displacement constraints considered during each stage is reduced by temporarily deleting displacement constraints that are neither critical nor potentially critical. First-order Taylor series expansions of the displacement and stress response quantities, in terms of linked reciprocal variables, are used to construct explicit linear approximations of the surviving inequality constraints. The objective function expressed in terms of the linked reciprocal variables is



nonlinear but explicit. Optimization is carried out by either a technique based on a modified feasible directions method or by a sequence of unconstrained minimizations based on an extended interior penalty function formulation and a modified Newton method minimizer.

It is assumed that the topological form, the geometrical configuration, and the structural materials to be used are preassigned parameters. It is also assumed that the structure can be idealized using the following three types of finite elements: truss members of uniform cross section, isotropic constant-strain triangular-membrane elements of uniform

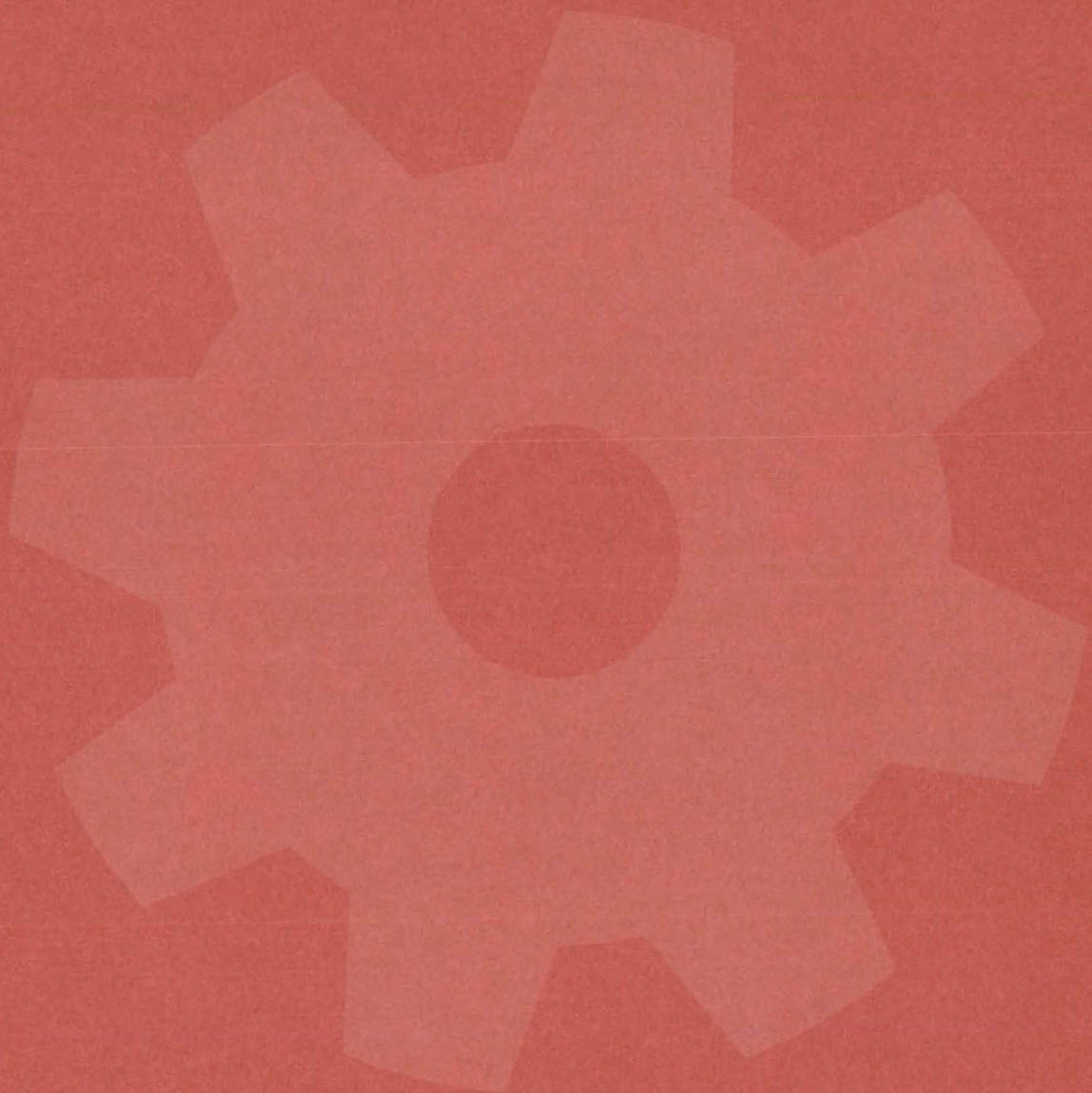
thickness, and isotropic symmetric shear-panel elements of uniform thickness. The objective function is taken to be the total weight of the finite-element idealization of the structure. The largest problem that can currently be accommodated would involve 300 finite elements (100 of each type), 300 displacement degrees of freedom, 120 design variables, and 5 distinct loading conditions.

Currently there are two machine versions of ACCESS-1 available. The IBM version is written in FORTRAN for the IBM H Compiler to be executed in the batch mode and has been implemented on an IBM 360

with a central memory requirement of approximately 380K (decimal) 8-bit bytes. The CDC version is written in FORTRAN for the CDC FTN Compiler to be executed in the batch mode and has been implemented on a CDC 6600 operating under NOS with a central memory requirement of approximately 250K (octal) 60-bit words.

*This program was written by Hirokazu Miura and Lucien A. Schmit, Jr., of the University of California, Los Angeles, for **Langley Research Center**. For further information, Circle D on the COSMIC Request Card. LAR-11994/LAR-12209*

Machinery



**Hardware,
Techniques, and
Processes**

- 391 Gearless Speed-Reduction Motor
- 392 Overhead-Handling, Universal-Positioning Device
- 393 Vacuum Mounting for Piezoelectric Transducers
- 394 Plaster Core Washout Tool
- 394 Flat-Package DIP Handling Tool
- 395 High Gantry for Lifting and Handling

Gearless Speed-Reduction Motor

Light compact unit lowers shaft speed by 1,000:1 or more.

Goddard Space Flight Center, Greenbelt, Maryland

A proposed "rolling" electric motor has an output shaft that rotates much more slowly than its commutation shaft. Speed reductions of 1,000 to 1 or better are practical. The motor uses no gears or pulleys to reduce speed. It is therefore less bulky and, since frictional losses are reduced, more efficient.

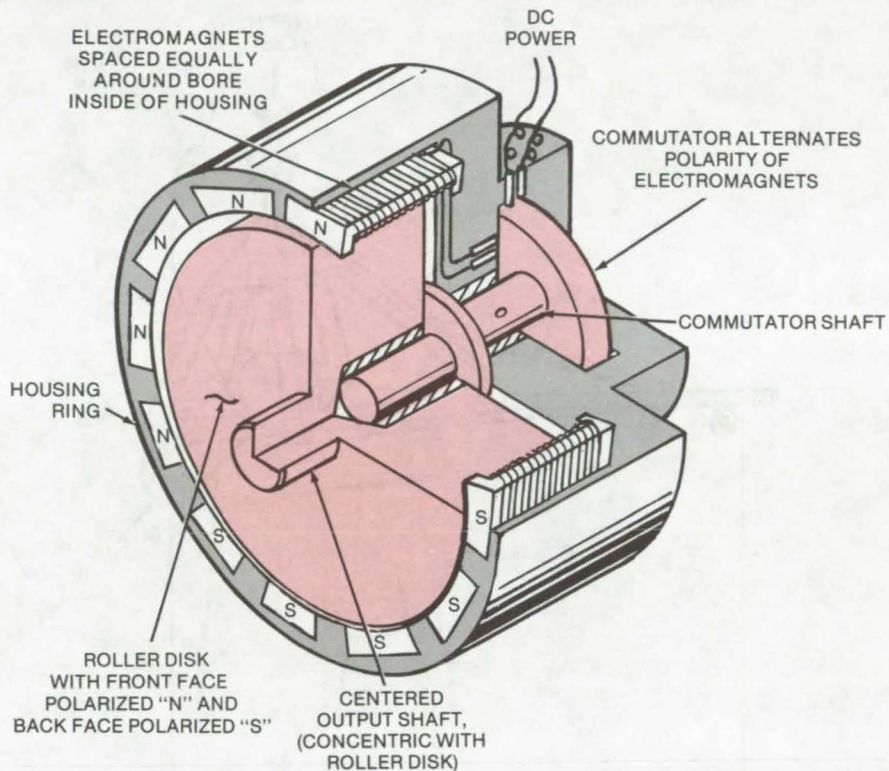
The motor contains a magnetized roller disk (one end being a south pole and the other end a north pole) that fits within a slightly-larger housing ring. The roller disk is the rotor, and the housing ring is the stator. The inside of the housing ring is fitted with several electromagnets (see figure). The output shaft of the motor is an integral part of the roller disk and is off center from the commutator shaft.

As the commutation shaft rotates, its slipring energizes and changes the polarity of the electromagnets spaced around the bore. (Any of the standard methods of changing polarity can be used, whether ac or dc.) Half the electromagnets push the disk, and half of them pull it. The roller disk thus rolls around the inside surface of the housing ring — a smaller wheel rolling inside a larger one. Because the output shaft does not rotate about the housing centerline but "oscillates" about this center, a universal joint or a similar coupling is needed to transmit power. An alternate approach would be to allow the housing to oscillate so that the shaft would have pure rotation.

The ratio of the commutation shaft rpm to the output shaft rpm, R , is determined by the relationship between the housing-ring diameter and roller-disk diameter, according to the formula:

$$R = \frac{RD}{HR-RD}$$

where: HR is the housing-ring diameter and RD is the roller-disk diameter.



To Produce Low-Speed Rotation, a high-speed commutator shaft rolls a disk around the inside surface of a housing ring. The output shaft, with its axis displaced from that of the commutator shaft, turns with the disk but at reduced speed.

For example, if the bore diameter is 3 in. (7.5 cm) and the bore is 0.005 in. (0.125 mm) larger than the roller, the speed reduction is 600:1.

If the roller-disk diameter is reduced to less than one-half of the housing diameter, then R becomes less than 1. In this case the output shaft rotates faster than the commutator, and the device acts as a gearless speed-enhancing motor.

The output speed can be varied by changing the difference between the housing and disk diameters — for example, by using a tapered roller that can be moved in or out of the ring.

In addition to the savings in weight

and bulk, this type of motor promises improved efficiency through the reduction of friction and the direct contact between the electromagnets of the stator and rotor (no airgap).

This work was done by Jesse Madey of Goddard Space Flight Center. For further information, Circle 36 on the TSP Request Card.

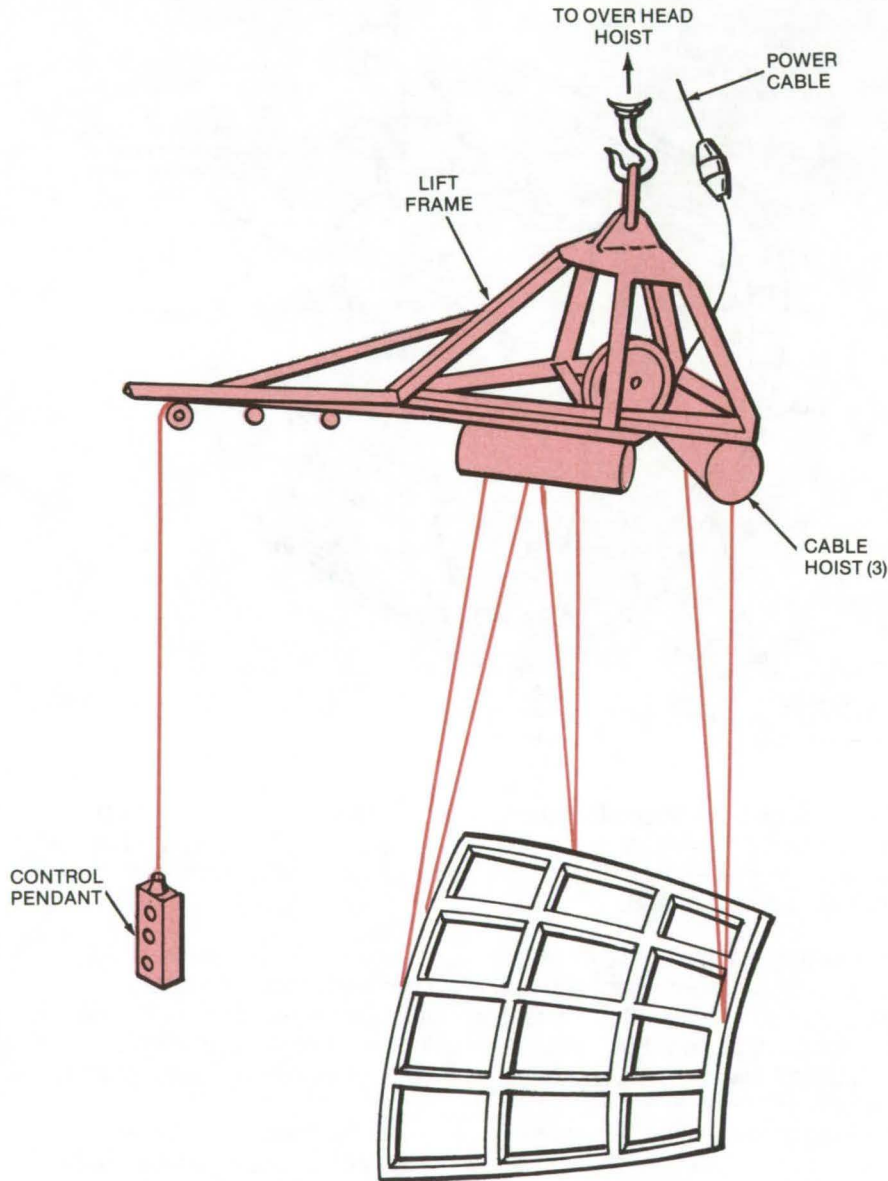
This invention is owned by NASA, and a patent application has been filed. Inquiries concerning nonexclusive or exclusive license for its commercial development should be addressed to the Patent Counsel, Goddard Space Flight Center [see page A8]. Refer to GSC-12138.



Overhead-Handling, Universal-Positioning Device

Lift-and-rotate mechanism
reorients suspended payloads

Marshall Space Flight Center, Alabama



A novel lift-and-rotate mechanism can raise a payload and reorient it while it is suspended in space. The mechanism is itself suspended from one overhead lift point and is operated from a single pendant/reel control panel.

As seen in the figure, three cable hoists are suspended at 120° intervals around a frame assembly. The cables are attached to three nonco-linear points on the payload. Each hoist is suspended from the lift frame with a device that keeps its cable drum facing the lift point during the operation. The hoists can be operated singly, in tandem, or all together from a control-switch panel suspended from a cable attached to the lift mechanism.

The hoist should be useful in a variety of industrial applications where a single overhead hoist must be used to reorient a suspended load. The lift capacity and the size of the mechanism would be determined by the application.

*This work was done by M. Johnson and R. Mann of Martin Marietta Corp. for **Marshall Space Flight Center**. For further information, Circle 37 on the TSP Request Card.*
MFS-23434

Unique **Overhead-Handling Device** can lift and reorient a suspended payload. An existing model has been used to orient and position a 20-foot-square control panel; other models can be constructed in sizes to meet particular applications.

Vacuum Mounting for Piezoelectric Transducers

Housing seals tightly but can be quickly attached and removed from a test specimen.

Lyndon B. Johnson Space Center, Houston, Texas

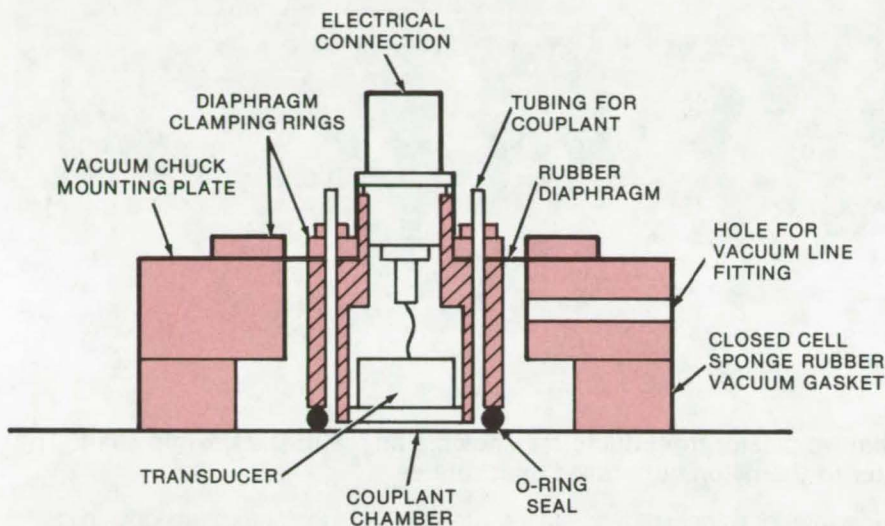


Figure 1. **Vacuum-Attached Transducer** for nonporous surfaces has a rubber diaphragm that lets it adjust to nonflat surfaces. Tubes admit and remove a liquid acoustic couplant.

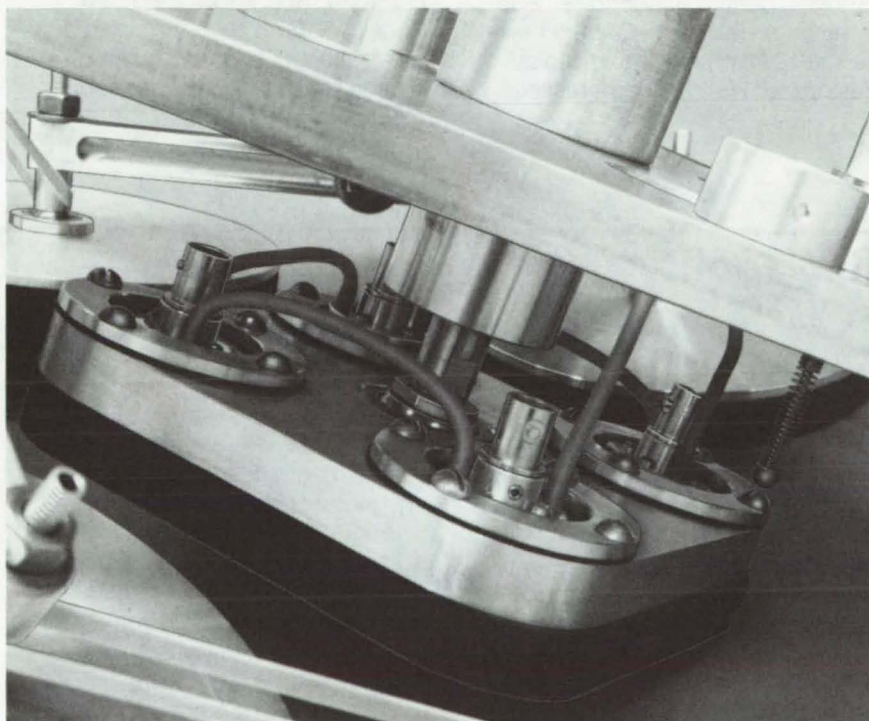


Figure 2. **Four Transducers** in vacuum housings perform rapid ultrasonic testing during production runs.

A special housing couples piezoelectric transducers to nonporous surfaces for ultrasonic or acoustic-emission testing. The housing provides sound isolation even on nonflat surfaces. It can be quickly attached and quickly removed and therefore allows rapid testing. Vacuum sealing eliminates the need for permanent or semipermanent bonds, viscous coupling liquids, weights, magnets, adhesive tape, or springs that are ordinarily used.

The housing consists of a vacuum chuck and a transducer mounting with an O-ring-sealed couplant chamber (Figure 1). Liquid acoustic couplant can be introduced through a tube leading into the chamber between the transducer and the nonporous surface and can be removed by applying air pressure through a tube. Only a small amount of couplant remains after removal, so that cleanup after testing is minimal, and the possibility of contaminating the test specimen is greatly reduced. A flexible rubber diaphragm lets the transducer tilt and move vertically to conform to curved or irregular surfaces.

The vacuum chuck can be used to apply tensile or compressive stress to the surface during testing. In one application, four housings have been mounted in a single fixture (Figure 2) for fast product-quality evaluation.

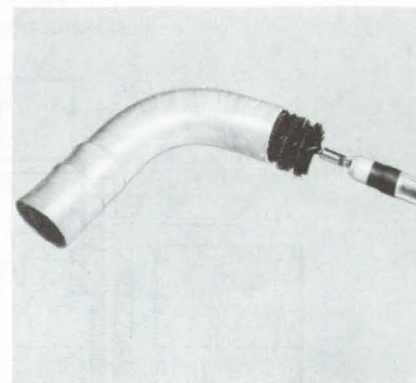
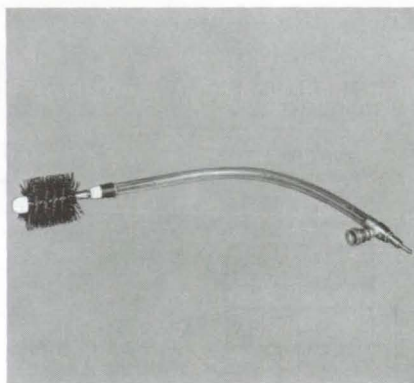
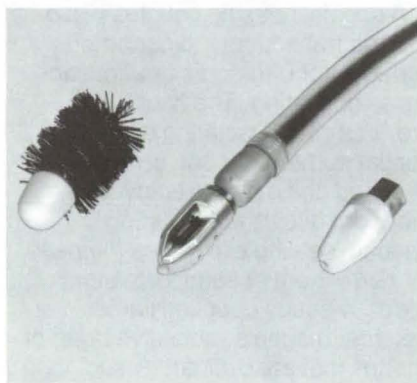
This work was done by David A. Tiede of Rockwell International Corp. for **Johnson Space Center**. No further documentation is available.
MSC-16480



Plaster Core Washout Tool

Rapid removal of soluble plaster cores from parts

Lyndon B. Johnson Space Center, Houston, Texas



The **Cutterheads and Brush** used to remove plaster from ducts are shown along with the flexible shaft. The shaft outer plastic sleeve supplies water to the nylon cutterhead as it rotates.

A new tool removes the water-soluble plaster lining from a Kevlar/epoxy duct. It is powered by pressurized water or air. A rotating plastic cutterhead with a sealed end fitting connects to a flexible shaft that allows the tool to be used with curved ducts. Plaster and other foreign debris are removed from the

duct interior without damage to the plastic duct walls.

Two types of nylon cutting heads, a cleaning brush, and a flexible shaft comprise the tool (see figure). In removing debris, either cutterhead or the brush is attached to the flexible shaft, which may be driven by pressurized liquid or compressed

air. The shaft has an inner sleeve and an outer sleeve; the latter directs the water to the cutterhead as the cutter operates.

This work was done by Robert M. Heisman, Andrew R. Keir, and Kuniyoshi Teramura of Rockwell International Corp. for Johnson Space Center. No further documentation is available.
MSC-16635

Flat-Package DIP Handling Tool

Inexpensive tool prevents contamination and bent leads.

Goddard Space Flight Center, Greenbelt, Maryland

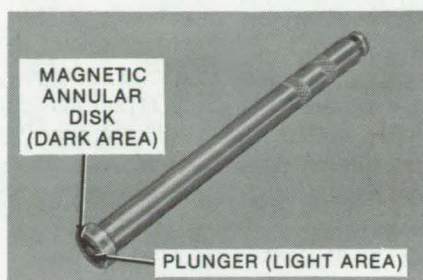
The simple and inexpensive tool shown here can facilitate the handling of integrated-circuit flat packages and prevent contamination and bent leads. The tool, which uses magnetic attraction to retain the package, requires no vacuum equipment, hoses, or other attachments. It is easily operated with one hand.

Routine handling of integrated-circuit packages for testing and assembly can often pose a problem because they are susceptible to electrostatic damage and contamination by skin oils when picked up

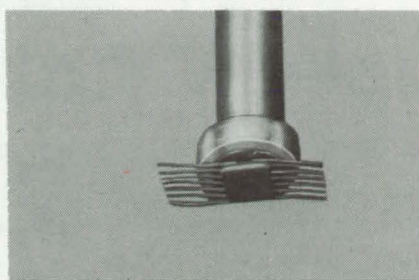
with an ungloved hand. Even if the handler wears gloves, there is the danger of bending the delicate leads. Tweezers, though widely used, can scratch or bend the leads.

Spring-loaded clamping tools are available for dual-in-line packages (DIP's); however, flat packages are not shaped for handling in this way. Vacuum-holding devices are often used, but they have several drawbacks including the need for a bulky and noisy vacuum pump and a hose connection between the pump and work area.

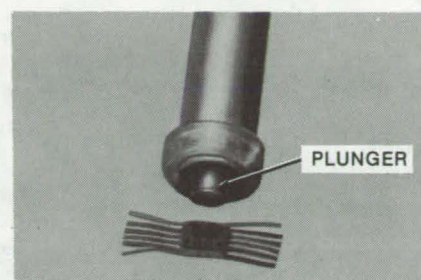
The magnetic tool has a non-magnetic outer case with a central spring-loaded plunger that is flush with an annular magnetic disk. The magnet retains the integrated circuit, and the plunger releases the IC by pushing it away from the magnet. Some flat-pack IC's have cases made of a magnetizable material. The tool can lift these devices by their cases. Other flat packs can be retained by magnetic attraction to their Kovar leads. Kovar (29 percent Ni, 17 percent



(a)



(b)



(c)

Handling Tool [a] Retains Flat-Package Integrated Circuits by magnetic attraction to their cases or Kovar leads (b). A manually operable plunger can be extended to release the IC (c).

Co, 53 percent Fe) is sufficiently magnetic for the IC to be lifted in this way.

This work was done by Evangelos Angelou and Robert Fraser of Goddard Space Flight Center. No

further documentation is available. GSC-12201

High Gantry for Lifting and Handling

Modified standard gantry with optional air mounts lifts heavy load to heights between 14 and 30 feet.

Goddard Space Flight Center, Greenbelt, Maryland

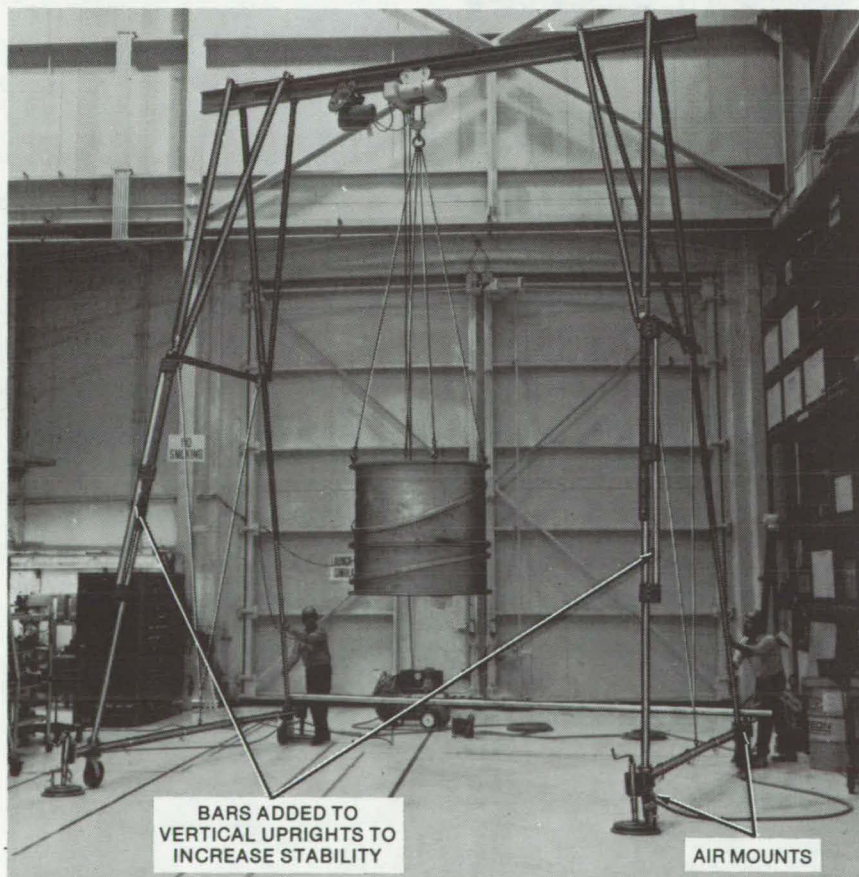


Figure 1. This **High Gantry** is adjustable from 14 to 30 feet and has been tested at 6,000 lb without yielding. Optional air mounts permit sensitive equipment to be moved easily over smooth surfaces, such as docks and shop floor surfaces, and over rougher terrain with the aid of plastic, plywood, or sheet metal that is taken up and laid down.

A standard gantry has been inexpensively modified with standard pipes to allow the lifting of heavy loads to distances higher than previously obtainable by commercial gantries. The addition of air mounts permits expensive and sensitive equipment to be moved smoothly and safely not only over worker areas, such as docks and shop floor surfaces, but also over moderately rough surfaces (if a plastic, plywood, or sheet-metal floor is taken up and laid down). Rougher terrain can be traversed by the use of wheels.

As shown in Figure 1, bars are added to the vertical uprights for the greater stability needed for higher uses of the gantry. An optional back pipe also makes the legs more stable under heavy loads and makes the gantry easier to move. The side bars are pulled up level with 7-by-19 cables 0.25 inch (0.64 cm) in diameter, thus allowing the air mounts to ride evenly on the floor. The side bars themselves are adjustable to any height between 14 and 30 feet (4 and 9 meters). A new portable erector platform (Figure 2) allows the gantry to be raised in the field, particularly in situations where horizontal assembly is impossible.



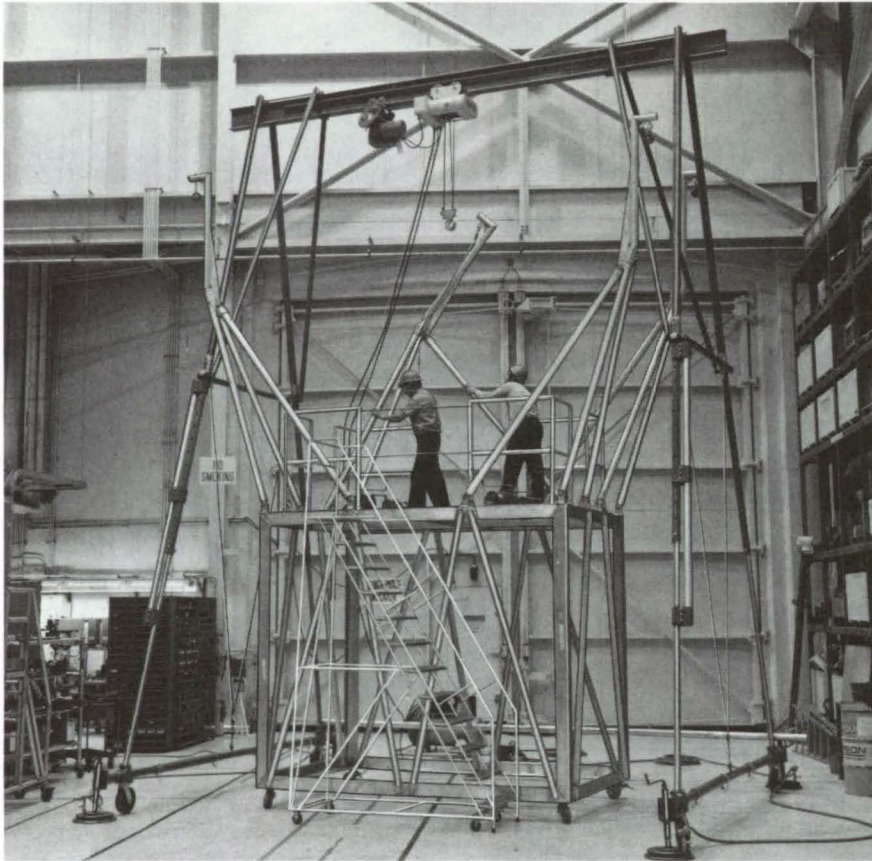
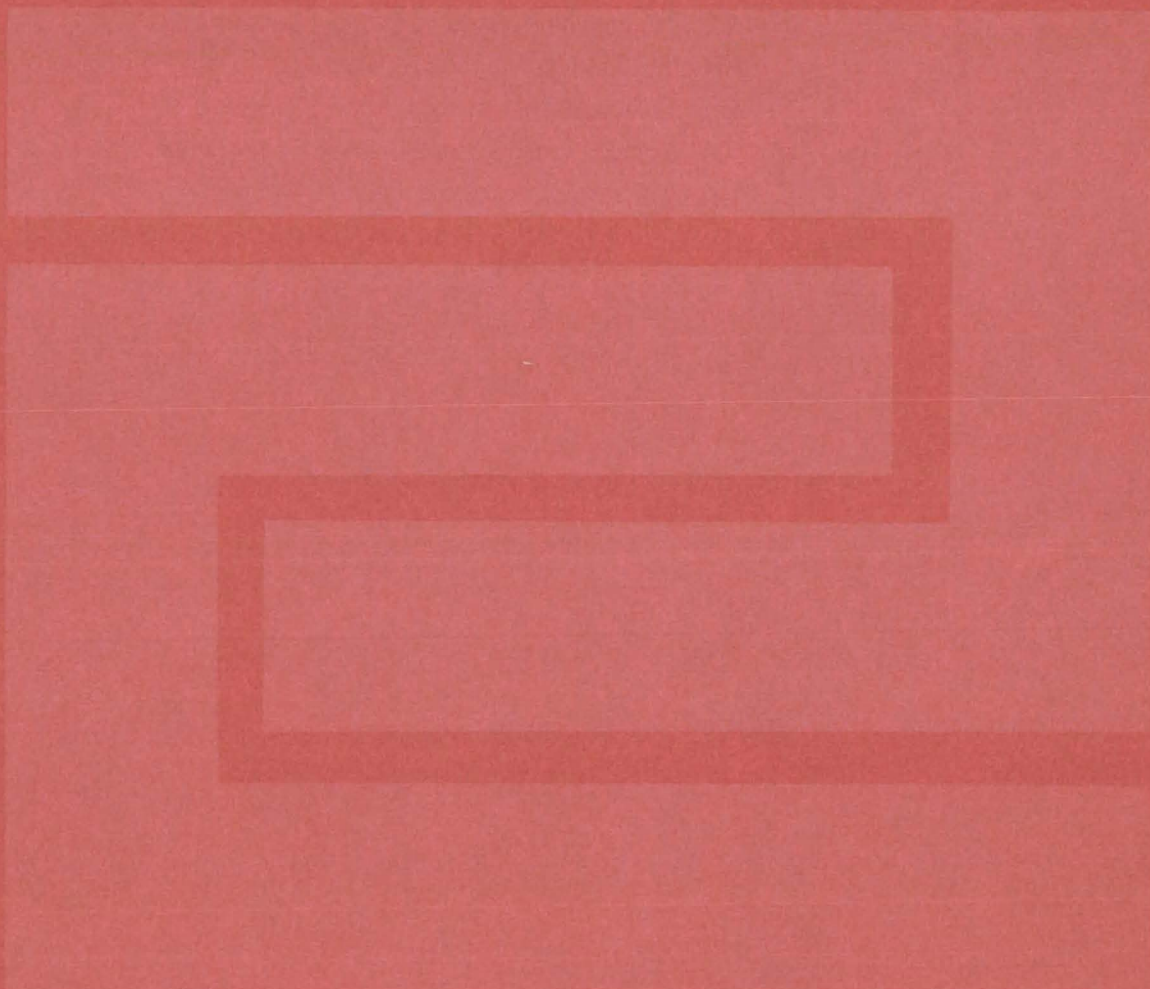


Figure 2. An optional **Portable Erector Platform** raises the gantry in the field. Because of the extreme high use, this gantry could not be jacked up on itself nor was there enough room to assemble it horizontally.

This gantry has been tested up to 6,000 pounds (2,700 kg) without yielding. The operating load at 30 feet has been set at 2,000 pounds (900 kg). On the basis of computer simulations, it has been estimated that higher loads of up to 15,000 pounds (6,800 kg) can be lifted by changing appropriately the size of the pipes and air mounts.

*This work was done by James J. Kerley, Jr., and William T. Tereniak of **Goddard Space Flight Center**. For further information, Circle 39 on the TSP Request Card.*
GSC-12235

Fabrication Technology



Hardware, Techniques, and Processes

- 399 Vacuum-Assisted Impregnation of Materials
- 400 Low-Reflection Silicon Solar Cells
- 401 Ion-Beam Sputtering Increases Solar-Cell Efficiency
- 402 Drilling Technique for Crystals
- 403 Modular Multiapertures for Light Sensors
- 404 Arc-Starting Aid For GTA Welding
- 404 Restoration of Bearings
- 406 Potting Procedure for Electronic Components
- 406 Uniform Spray Coating for Large Tanks
- 408 Attaching Strain Gages by Ultrasonic Plastic Welding

Vacuum-Assisted Impregnation of Materials

A liquid impregnant is forced through tiny voids and cracks to improve the effectiveness of protective coatings.

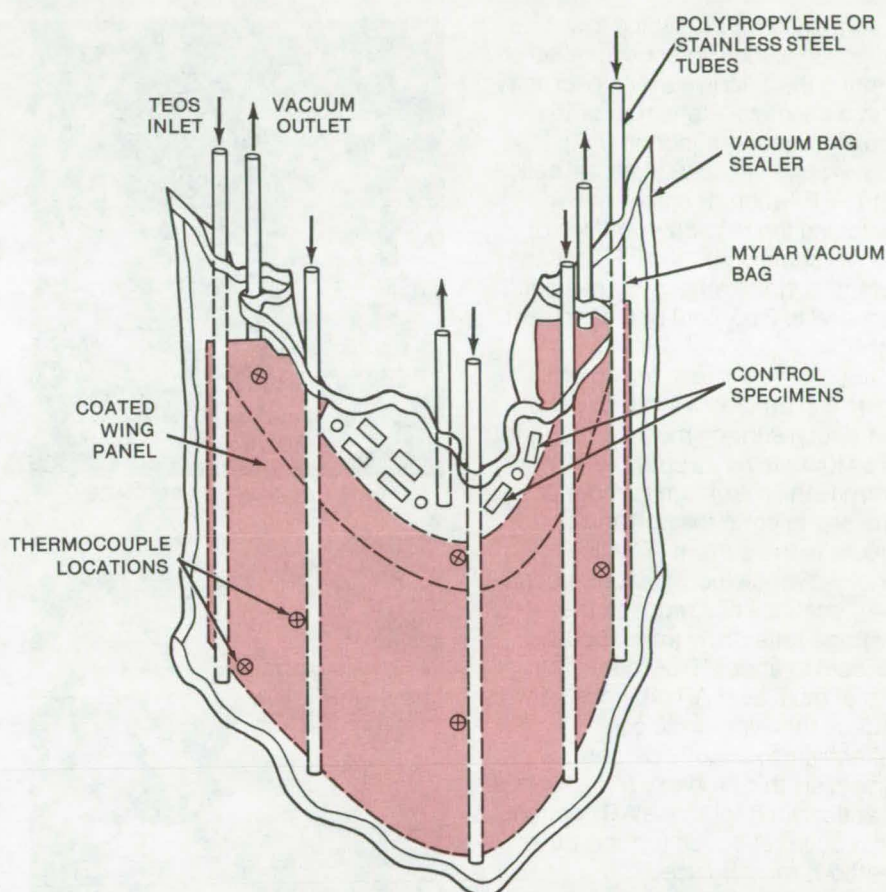
Lyndon B. Johnson Space Center, Houston, Texas

A vacuum-assisted liquid-impregnation treatment for silicon-carbide reinforced carbon-carbon systems improves the resistance of the silicon-carbide coating to attack by oxygen at elevated temperatures. The treatment fills tiny voids, pores, and cracks in the coating to enhance its effectiveness as a barrier. It may be adapted to reduce the porosity of other materials as well.

Tests on silicon-carbide coated parts, prior to treatment by the new techniques, showed substantial reductions in strength at temperatures near 1,300° F (704° C) as oxygen penetrated defects in the coating to react with the carbon substrate. In the new technique, defects are filled through forced impregnation of liquid tetraethyl orthosilicate (TEOS) followed by firing in air at 2,300° F (1,260° C) to form an oxygen-impervious solid.

Five impregnations and cures are carried out in the vacuum-bag setup shown in the figure. An expanded Teflon-mesh material is packed around the part and control specimens to improve the flow of TEOS around and through the coated surfaces. This procedure diminishes the amount of TEOS required, thereby reducing costs. Since it is a closed system, it decreases the hazard of handling toxic and flammable materials.

The coated parts were tested in oxygen at temperatures to 2,500° F (1,371° C). No detrimental effects to the basic coated system were found. The technique might also be applied to sintered silicon-carbide bodies to increase their density and to make them more resistant to hot gases for use in jet engines.



The Effectiveness of the Silicon-Carbon Coating Is Improved for this wing panel by forcing liquid tetraethyl orthosilicate through pores and cracks in the coating, using this vacuum-bag setup. Five impregnations are carried out, with each followed by curing in air at 2,500° F. System performance is optimized by separating the outlet tubes from the specimens by at least 3 inches. The vacuum outlets are spaced at 2-foot intervals; the liquid inlets are a foot apart.

*This work was done by Donald C. Rogers and David M. Shuford of Vought Corp. for **Johnson Space Center**. No further documentation is available.*

Inquiries concerning rights for the commercial use of this invention should be addressed to the Patent Counsel, Johnson Space Center [see page A8]. Refer to MSC-16785.



Low-Reflection Silicon Solar Cells

Pretreatment with chemical etchant reduces reflectivity to 2 percent.

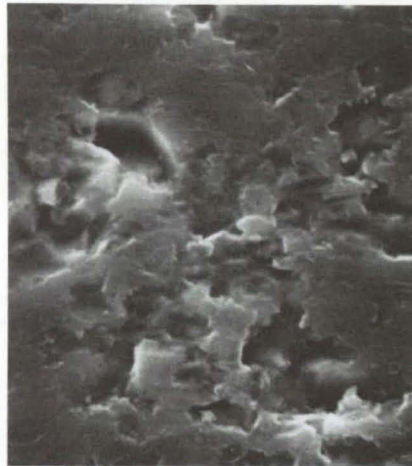
Lewis Research Center, Cleveland, Ohio

A method for producing low-reflection silicon solar cells relies on altering the silicon surface geometry with a chemical etchant prior to applying an antireflection (AR) coating and encapsulating the cell with FEP Teflon. By properly matching the refractive indices of the AR coating and the FEP encapsulant, surface reflectivity has been reduced to 2 percent of the incident light.

In order to achieve maximum solar-cell efficiency, reflectivity of the silicon surface must be reduced to as low a level as possible. This permits the maximum number of photons to enter the cell and contribute to the current. The use of single-layer dielectric antireflection (AR) coatings has reduced the average reflectivity from about 35 percent to about 10 percent. The use of multilayer AR coatings can reduce the average silicon reflectivity to about 7 percent. However, this probably represents a practical limit for these AR coatings. To reduce reflection further, other methods must be used.

Physically altering the geometry of the silicon surface has been found effective in further reducing silicon reflectivity. A grooved or texturized surface permits multiple reflection of incident light, increasing chances for photon capture and transmission and thus reducing optical reflection losses. Surface modification through chemical processing has fewer difficulties and is the least costly of the techniques investigated (e.g., ultrasonics).

A grooved or texturized surface can be produced by using an orientation-dependent chemical etch on an initially-clean saw-cut, lapped or polished silicon starting surface. A 60/40 volume percent hydrazine/water mixture containing a trace of catechol heated to



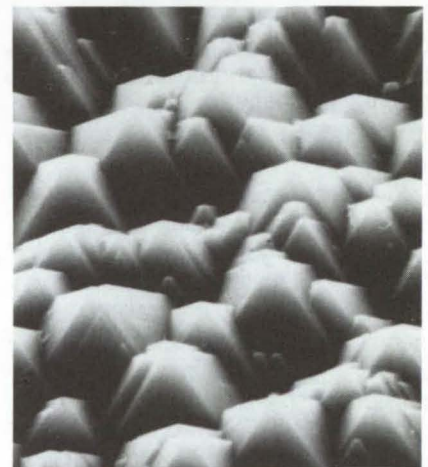
ORIGINAL SAW-CUT SURFACE



AFTER 1 MIN. OF HYDRAZINE
HYDRATE ETCHING



AFTER 6 MIN. OF HYDRAZINE
HYDRATE ETCHING



AFTER 15 MIN. OF HYDRAZINE
HYDRATE ETCHING

The Development of a Texturized Surface can be followed from the 1800X scanning-electron-microscope photographs above. The resulting pyramidal irregularities direct much of the reflected radiation back onto the surface where it is mostly absorbed.

between 230° and 239° F (383 and 388 K) and applied to a <100> silicon surface will etch the surface in from 5 to 10 minutes. The resulting surface is velvet in appearance and consists of a myriad of pyramidal etch figures. By overcoating this velvet surface with a dielectric layer of proper thickness (about 550 to 600 Å), such as Ta₂O₅ or TiO_x, and laminating this system

in FEP Teflon, a reflectivity of about 2 percent is achieved. The refractive indices of the dielectric layer and the FEP Teflon must be matched to achieve this low reflectivity.

The reduced reflection achieved with this system occurs at all wavelengths and results in improved short circuit current and spectral response. Improved collection efficiency is also expected from this

structure due to the generation of carriers closer to the cell junction.

This work was done by Cosmo R. Baraona and Henry W. Brandhorst, Jr., of **Lewis Research Center**. Further information may be found in

NASA TM-X-71715 [N75-24119], "V-Grooved Silicon Solar Cells," a copy of which may be obtained at cost from the Technology Application Center, Albuquerque, New Mexico 87131 [see page A7]. LEW-12418

Ion-Beam Sputtering Increases Solar-Cell Efficiency

Heterojunction solar cells made by ion-beam sputtering have an efficiency of 12 percent.

Lewis Research Center, Cleveland, Ohio

The use of ion-beam sputtering to fabricate heterojunction solar cells has resulted in these cells reaching 12 percent efficiency. Previous evaporation fabrication techniques produced 10 percent efficiency.

These oxide-semiconductor-on-silicon (OSOS) solar cells are fabricated from various indium-tin oxide ($\text{In}_2\text{O}_3)_x(\text{SnO}_2)_{1-x}$ compositions sputtered onto p-type single-crystal silicon substrates with a neutralized argon-ion beam. High-temperature processing or annealing is not required.

Compared to conventional silicon solar cells, the oxide-semiconductor-on-silicon (OSOS) structure has a number of advantages. The high optical transparency and low electrical resistivity greatly simplify making front contacts. The oxides exhibit indices of refraction in the right range to provide an inherent antireflection coating. The effective zero-depth junction eliminates any surface dead layer and improves the response at short wavelengths.

In conventional-junction solar cells, as the base doping increases, the dark current and lifetime decrease, and the efficiency tends to be lower. In the OSOS cells, as the base doping decreases, the dark current decreases, allowing the lifetime, collection depth, radiation resistance, and efficiency to increase. In addition, the ion-beam sputtering technique is compatible with low-cost continuous fabrication and requires no high-temperature processing.

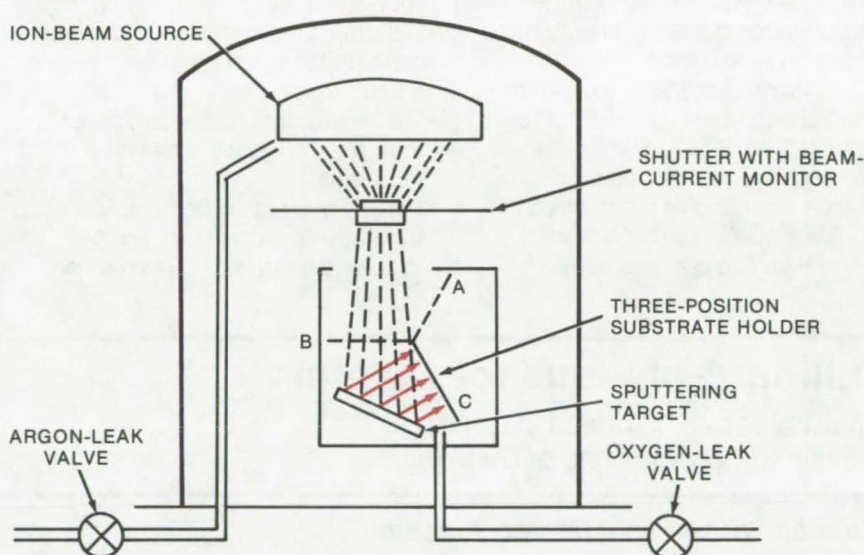


Figure 1. The **Deposition Apparatus** for fabricating ion-beam-sputtered solar cells has a three-position substrate holder. In position A, the ion beam will clean the sputter target; in position B, the ion beam etches away oxide exposed through the mask, together with a small amount of the silicon; in position C, the sputtered particles are directed at the cell substrate.

The major fabrication step is depositing the oxide semiconductor film onto a silicon wafer. An ion-beam sputtering technique is utilized in which a neutralized argon beam strikes a cold-pressed power target, sputtering the material onto a silicon substrate.

The back surface of the silicon wafer is metalized with vapor-deposited aluminum to provide a back contact for the completed cell and to insure good thermal contact to the substrate holder during deposition. Sputtering targets are prepared by cold pressing powder mixtures of the desired proportions

of indium and tin oxide. The silicon wafers are attached to the substrate holder behind a thin stainless-steel mask with 3-mm (0.12-in.) holes to define the solar-cell area. The system is then evacuated.

With the substrate holder in position A (Figure 1), the ion beam is activated and used to sputter-clean the target. Then the holder is moved to position B, and the oxide exposed through the mask is etched away together with a small amount of silicon. In the deposition position (position C), the target and substrate angles are adjusted to minimize sputtered-particle path length, yet

(continued on next page)

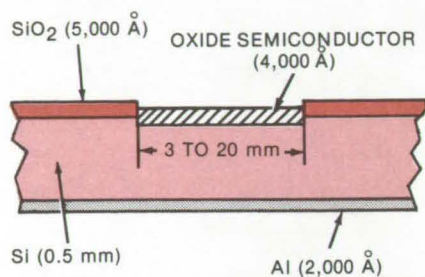


Figure 2. Oxide-Semiconductor-on-Silicon configuration is formed by ion-beam-sputtering various indium-tin oxide compositions into a p-type single-crystal silicon substrate.

provide nearly uniform coverage. Oxygen is introduced, and actual deposition takes place.

The silicon substrates were maintained at a temperature of 662° to 752° F (623 to 673 K) during the deposition, which took approximately 1 hour to give the desired 400-Å film. Cells were made with indium-tin oxide compositions

ranging from 10 to 70 percent tin oxide. Contact to the front surface of the cell was made with a gold-point probe after fabrication was completed.

The final configuration is shown in Figure 2. This type of deposition offers several economic and technical advantages for solar-cell fabrication:

- No high-temperature processing is required.
- The energy of the ion beam is in the proper range to maximize the ratio of target mass removed to total energy input; the energy of sputtered atoms impinging on the substrate is low enough to diminish concern for surface damage or resputtering.
- Targets require no special preparation. New targets are easily fabricated.
- Source and substrate temperatures, system pressure, sputter rate, and beam energy can all be

independently varied, allowing many options for process optimization. Reproducible deposition rates are assured once the system is calibrated for a particular material.

- The ion beam may also be used to sputter-clean the substrate surface prior to deposition without breaking the vacuum.
- The ion beam can be readily scaled up in size to accommodate large-scale production.

This work was done by Dorothea E. Burk, Joel B. DuBow, and James R. Sites of Colorado State University for Lewis Research Center.

Further information may be found in NASA CR-135149 [N77-16248], "Industrial Ion Source Technology," a copy of which may be obtained at cost from the New England Research Application Center [see page A7].
LEW-12895

Drilling Technique for Crystals

Small holes can be drilled in fragile crystals without cleaving or breaking.

Marshall Space Flight Center, Alabama

While instruments exist for cleaving, grinding, and polishing organic crystals, there is also a need for a method of drilling the fragile crystals without cleaving or breaking them. If a hole could be drilled in a seed crystal, for example, the seed could be suspended in its growth solution by a rod inserted in the hole. The other end of the rod could be attached to a wall of the growth cell, away from the immediate neighborhood of the growing crystal. Fixing the crystal in this way would allow growth to proceed in all directions and also allow the crystal to be more easily observed. This support method would also be useful in zero-gravity growth experiments, to prevent the seed from drifting inside its container.

A new hole-drilling technique uses a special crystal driller in which the drill bit rotates at a fixed position

while the crystal slowly advances toward the drill. The technique has been used successfully for single crystals of Rochelle salt, triglycine sulfate, N-acetylglycine, and L-alanine and should have general applicability. It uses very slow drill speeds, of the order of 30 rpm, to limit heat buildup and to reduce strain on the crystal. In one application, in which a 0.046-cm-diameter hole was to be drilled, the crystal advancement speed was 0.306 cm/h. Drilling was stopped after each 0.15 to 0.20 cm of advance to clean out the accumulated drill chips.

The crystal is supported on a flat holder, using silver paint. It is important to provide good rear support when drilling completely through a crystal and to use a slow drill speed at the moment of breakthrough. Otherwise, the unbalanced

strain could cause breakage. The holder should have a hole that can accept the drill bit when breakthrough occurs. After the drilling operation, the crystal may be removed with a razor blade, and the excess silver paint can be cleaned off with acetone.

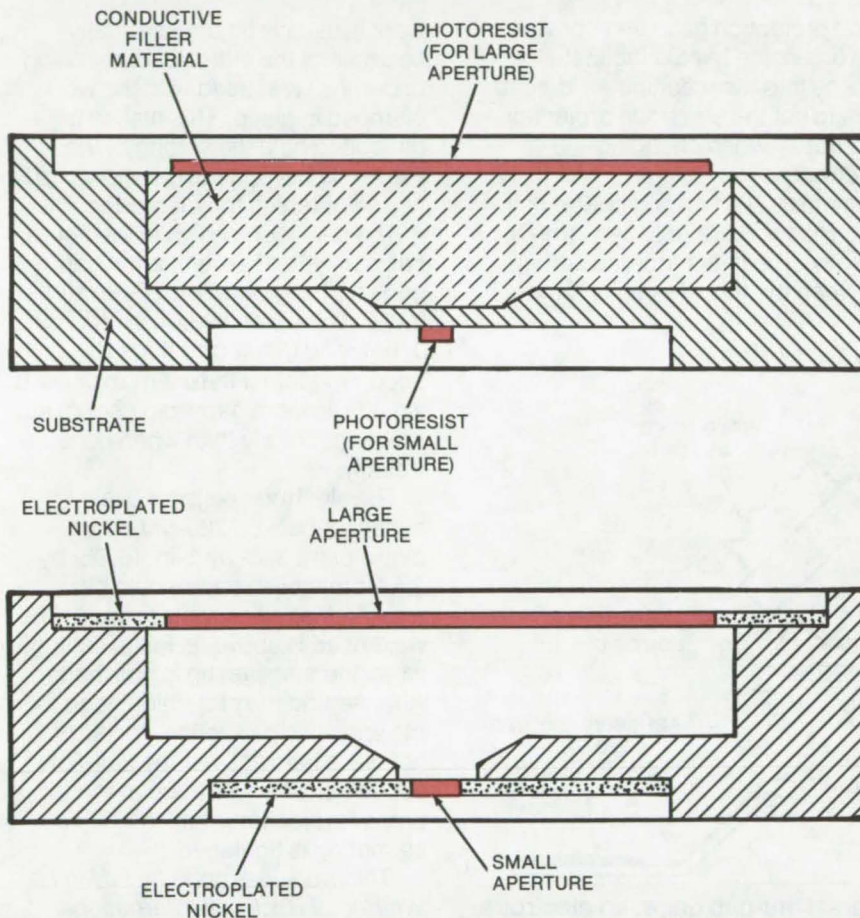
This work was done by Tom Hunter and Ichiro Miyagawa of the University of Alabama for Marshall Space Flight Center. Further information may be found in NASA CR-143886 [X75-10234], "Investigation of Crystal Growth From Solutions," a copy of which may be obtained at cost from the New England Research Application Center [see page A7].

Inquiries concerning rights for the commercial use of this invention should be addressed to the Patent Counsel, Marshall Space Flight Center [see page A8]. Refer to MFS-23580.

Modular Multiapertures for Light Sensors

One-piece construction eliminates alignment and assembly difficulties.

Marshall Space Flight Center, Alabama



Large and Small Apertures Are Prelined by photoresist and then formed by electroplating outside the photoresist areas. In the final module (bottom), the filler material in the aperture cavity has been removed to provide a fixed spacing between aperture masks.

In light-sensor systems, it is often necessary to limit the viewing angle by placing apertures of decreasing size over the sensor. However, aligning and assembling aperture masks poses difficult problems. The masks — which can be as thin as 0.0003 in (0.0075 mm) — must be handled delicately and must be

positioned and spaced precisely in their supporting structure.

Electroforming multiaperture masks as a unit eliminates these problems. Developed for Sun and star sensors for attitude and bearing control in spacecraft, the process can also be used for masks in automation and surveillance systems

when a precise, wide-angle field of view is needed.

A beryllium copper substrate, machined to the proper dimensions, is the supporting structure for the aperture masks (see figure). A cavity in the substrate is filled with a conductive material, and a layer of photoresist is deposited on it. (To ensure a uniform coating, the photoresist is applied by dip coating or centrifugal spinning.) The photoresist is exposed to define the dimensions of the large aperture (in much the same way that a contact print is made), and the photoresist outside the aperture outline is etched away.

A layer of nickel 0.0003 to 0.0007 inch (0.0075 to 0.0175 mm) thick is electroplated around the photoresist. This layer becomes the large-aperture sheet. After plating, the filler and photoresist are dissolved away.

Next, the small aperture is delineated on the opposite face of the substrate by a layer of acid-resistant material with a small-aperture shaped hole at its center. The substrate material at this center hole is etched away by an acid that does not attack the nickel mask on the large-aperture face.

When the apertures have been formed, the entire unit is flashed with black chrome. Finally, a quartz window is bonded in the large aperture, and a discardable plastic disk is placed over the small aperture to protect the frail aperture edges and to keep contamination out of the module.

This work was done by Anthony A. Rizzo of TRW, Inc., for **Marshall Space Flight Center**. For further information, Circle 40 on the TSP Request Card.
MFS-23249

Arc-Starting Aid for GTA Welding

A three-in-one handtool improves arc initiation on gas tungsten arc, automatic skate-welding machines.

Lyndon B. Johnson Space Center, Houston, Texas

A novel handtool that combines an arc-gap gage, an electrode-tip sander, and an electrode projection gage effectively improves arc initiation on gas tungsten arc (GTA), automatic skate-welding machines. The tool makes it easy for the operator to polish electrode tips and to set exactly the initial arc gap before each weld pass. The elec-

trode projection gage and convenient extension handle facilitate access into the machine weld-head area to set the electrode projection accurately when changing electrodes.

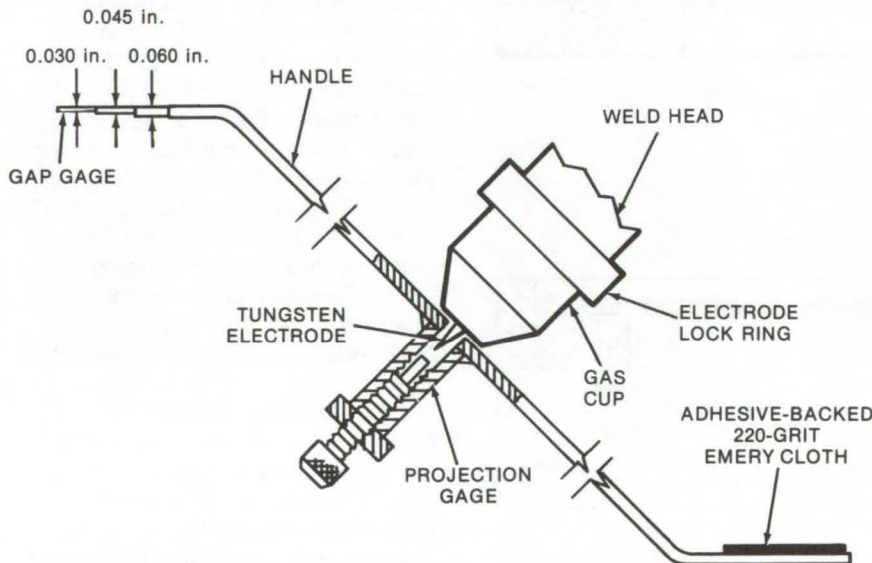
In most GTA welding operations, electrode tips are polished infrequently. The initial arc-gap setting between the tungsten tip and the

work is usually adjusted visually because of the difficulty of reaching under the weld head with the work clamped in place. This makes it difficult to hold the setting of the electrode beyond the gas-flow cup while tightening the clamping.

The new tool, shown in the figure, has a universal arc-initiation gap gage that is ground with three steps: 0.030, 0.045, and 0.060 in. (0.762, 0.124, and 0.152 cm) thick to accommodate different machines. It would allow arc gaps to be set much more accurately than when done visually.

The electrode polisher uses adhesive-backed 220-grit emery cloth. Extra 3/8- by 1-in. (0.95- by 2.54-cm) polish pads would be provided for quick replacement. The weld head is above its initial setting when the tungsten tip is polished. After setting the projection gage to the specified projection, the flat handle is held against the gas-flow cup to hold the electrode at the proper projection while the clamping is tightened.

This work was done by Edwin L. Whiffen of Rockwell International Corp. for Johnson Space Center. No further documentation is available.
MSC-19495



Three-in-One Handtool combines a universal arc-gap gage, an electrode-projection gage, and an electrode polisher to improve arc initiation on GTA automatic skate-welding machines. The tool, shown being used to set the electrode projection, has an extension handle that allows easy access to the weld-head area.

Restoration of Bearings

Raceway grinding and roller replacement makes wornout bearings "like new."

Lewis Research Center, Cleveland, Ohio

A process has been developed that restores wornout ball and roller bearings to their original quality and thereby doubles their operating life. Essentially, the process consists of grinding the raceways to an oversize but original quality condition and

installing new oversize balls or rollers. An evaluation of the process for restoring expensive, frequently-replaced aircraft bearings resulted in the restoration of 90 percent of the replaced bearings at less than 50 percent of new-bearing costs.

Rolling-element bearings are being required to operate at constantly increasing speeds and temperatures. With the development of modern-aircraft gas-turbine engines and other high-speed turbine-driven machinery, the rapidly rising costs

of engine and transmission bearings have made the reconstitution of replaced bearings an economic necessity.

Bearing refurbishment has been practiced for both military and commercial aircraft for the past 20 years. Usually, bearing refurbishment consists of disassembly, cleaning, inspection, and, if no dimensional discrepancies, flaws, or imperfections are evident, reassembly for further service. In some cases, new rolling elements are installed. In some cases, raceways are polished to remove minor imperfections and blemishes. However, polishing must be carried out with quality control equivalent to new-bearing finishing, lest raceway geometry and surfaces be distorted. Usually, any significant removal of raceway material is avoided. The U.S. Army Aviation Systems Command experience indicates that as many as half of the bearings replaced are scrapped because of raceway surface damage or dimensions beyond the allowable tolerances.

Investigation has shown that less than 10 percent of the usually-scrapped aircraft bearings have failed from classical rolling-element fatigue, which, because of the depth of fatigue damage, precludes any form of refurbishment or restoration. Thus, over 90 percent of these usually scrapped bearings are candidates for restoration by this new process.

This new process constitutes approximately the last 30 percent of new-bearing manufacturing operations. Essentially, the process consists of the following steps:

- Bearings are disassembled into component parts, are visually inspected, and race hardness is measured. The components are either accepted for restoration or scrapped.

- As necessary, the bearing faces, bores, and outer diameters are ground and/or plated to original dimensions.
- Inner and outer raceways are ground to a depth not less than 0.002 in. (0.05 mm). Surface finish is maintained to original specifications.
- Separators are stripped of plating, inspected, reworked as required to accept oversize rolling elements, and are replated.
- Bearings are assembled with new rolling elements of a size equal to the size of the original rolling elements plus twice the depth of regrounding.

Throughout the restoration process, all inspection and quality-control procedures, fixtures and gages, and similar components must be equal in quality to those used in original manufacture of the bearings. Bearings restored by this process have an expected operating life equal to original bearings.

This new process was applied experimentally to 529 bearings comprising three different types (split-inner-ring ball bearings, cylindrical roller bearings, and angular-contact ball bearings) removed at overhaul from helicopter engines and transmissions. These bearings, under normal circumstances, would not be reinstalled for use in the aircraft nor refurbished for later reuse. The purpose of the pilot program was: (a) to establish the restorable yield of these bearings and (b) to demonstrate the technical and economic feasibility of the restoration process by restoring 50 sets of each of the three bearing types.

The following results were obtained:

- Greater than a 90-percent yield can be achieved by the restoration process.
- During endurance tests with the three bearing types, no failures

occurred that could be related to the restoration-by-grinding process.

- The estimated cost to restore rolling-element bearings by this process ranges from 27 to 47 percent of new-bearing cost, depending on bearing size and complexity.
- Maintenance and replacement policies and practices should not be adversely affected by the utilization of restored bearings.

Restoration by grinding can decrease costs by salvaging most of those bearings that current refurbishment programs cannot restore to usable bearings. This process restores bearings to original manufacturing accuracy because restoration is done by grinding on the same machines and by the same techniques as new bearings.

This work was done by Richard J. Parker and Erwin V. Zaretsky of Lewis Research Center and Heinz Hanau of Industrial Tectonics, Inc. Further information may be found in:

NASA TN-D-8486 [N77-23495], "Life Analysis of Restored and Refurbished Bearings," and NASA TM-X-73440 [N76-26512], "Evaluation of Ball and Roller Bearings Restored by Grinding."

Copies of these reports may be obtained at cost from the New England Research Application Center [see page A7].

In addition, information on this technique is available in Report USAAVSCOM-TR-76-27, "Bearing Restoration by Grinding," prepared for Joint Army-NASA Seminar, Army Aviation Systems Command, Directorate for Product Assurance, 12th and Spruce Streets, St. Louis, Missouri 63166.

Inquiries concerning rights for the commercial use of this invention should be addressed to the Patent Counsel, Lewis Research Center [see page A8]. Refer to LEW-12631.



Potting Procedure for Electronic Components

A silicone rubber band and a modified heat cycle improve component dimensional stability.

Lyndon B. Johnson Space Center, Houston, Texas

Several methods and products used for embedding (potting) electronic components already exist. In certain instances, however, the potting process must be modified to effect a match more closely between the component, potting medium, and thermal environment. In one such situation — embedding a data bus coupler in an aluminum housing — the potting resin was required to have the following specifications:

- A dielectric constant of 3 or less,
- The capability of operating from -55° to 125° C,
- Good moisture resistance, and
- Good thermal conductivity.

Several epoxy casting resins failed to meet the specifications; excess contraction of the resins caused stresses on the component that, in turn, caused the transformer impedance characteristic to vary with temperature.

The low-temperature performance of the potted transformer was improved by surrounding it prior to casting with a room-temperature-vulcanizing silicone rubber and by curing the rubber in a modified thermal cycle. A resin having the thermal properties desired is then used to pot the transformer. A two-stage heat-curing cycle is used to lengthen the molecular chain of the cured resin structure. The thin coat

of silicone rubber, applied around the coil, minimizes coil-to-resin adhesion and thus lowers the stresses between the transformer and potting compound.

The potting procedure follows this sequence:

1. Clean the wound coil,
2. Apply a primer,
3. Apply the silicone rubber, and
4. Encapsulate: Precure the resin at $70^{\circ}\pm 5^{\circ}$ C, then a final resin cure at $100^{\circ}\pm 5^{\circ}$ C.

This work was done by Anthony G. Rubino and Julius Zimmerman of The Singer Co. for Johnson Space Center. For further information, Circle 41 on the TSP Request Card. MSC-16290

Uniform Spray Coating for Large Tanks

Spiral technique applies layer of polyurethane insulation to outside of cylindrical tank.

Marshall Space Flight Center, Alabama

A new system for spraying polyurethane foam insulation on a large cylindrical tank allows close control of the thickness and uniformity of the insulating layer. The tooling applies foam to the end of the tank as well as to its sides — the tank rotates on a turntable, while moving spray guns apply overlapping spirals of foam (see Figure 1). The speeds are adjusted so that mechanical properties of the foam are not degraded at the overlap joint. This process, developed specifically for the thermal protection system of the external tank [10 feet (3 meters) in diameter] on the Space Shuttle, can be used for uniformly coating any large cylindrical object.

The foam-spraying system utilizes a turntable and adapter to support and rotate the tank when it is vertical. The table is inside a plastic-covered frame (see Figure 2). The

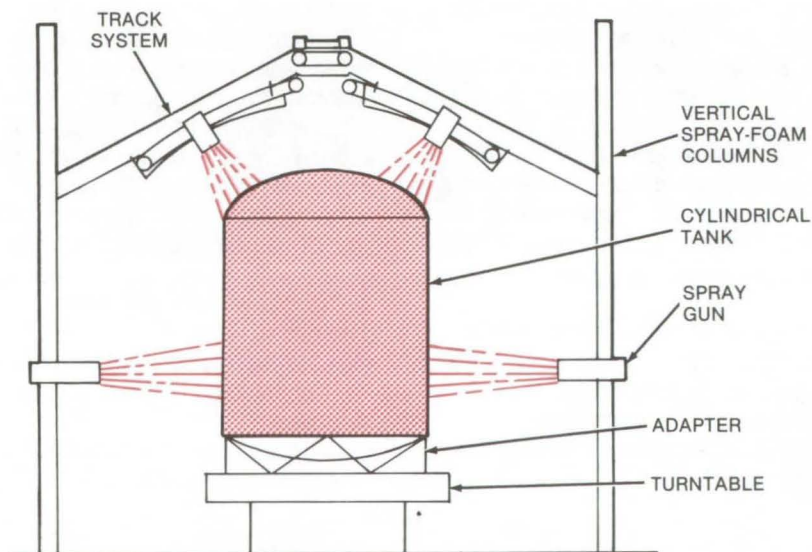


Figure 1. Tooling for Spraying polyurethane foam on the side wall and the end of 10-foot-diameter cylindrical tank includes rotating turntable and moving spray guns.

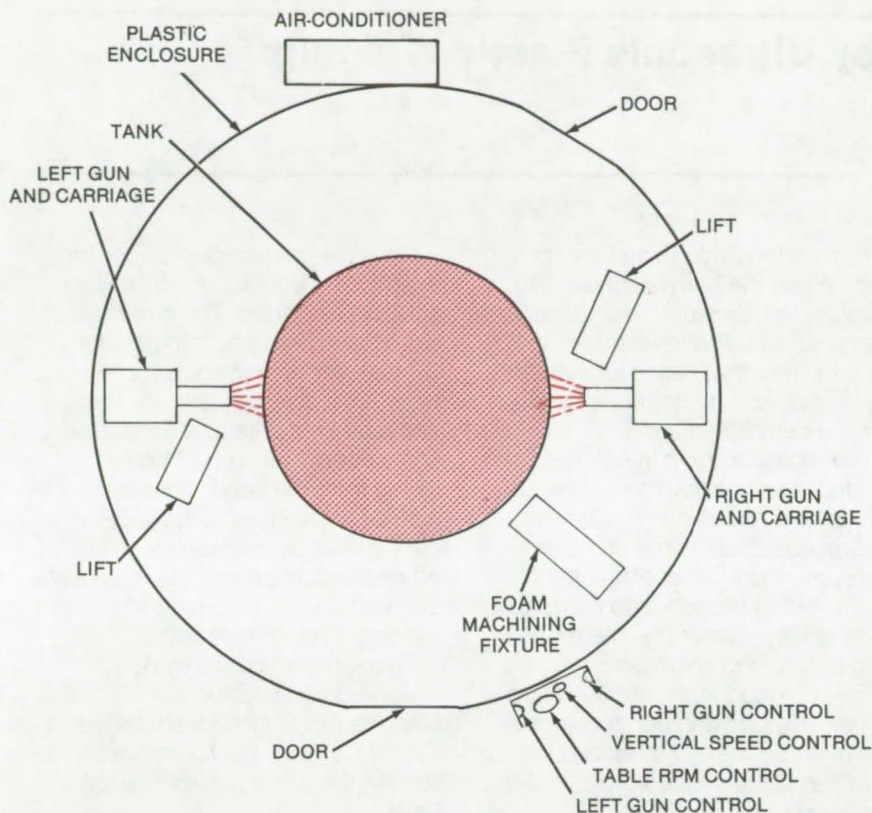


Figure 2. **Spray Facility** is located inside a plastic enclosure with an exhaust system to remove fumes and spray mist, and a hot-air supply to heat the tank. Only the masked spray-gun operators are allowed inside the enclosure during spraying.

enclosure is equipped with a hot-air supply for heating the tank both internally and externally and with an exhaust system to remove fumes and spray mist. The tooling associated with the application of foam to the 10-foot tank is shown in Figure 1.

Each remotely-operated spray gun is attached to an oscillator mounted on a carriage. The carriage is in turn secured to a support-and-drive mechanism on a tool column

that moves the gun vertically at a constant speed. There are two gun positions within the enclosure, 180° apart, with the guns directed toward the vertical centerline of the tank. The vertical speed of the two guns is synchronized and is controlled from the operator's control panel. The vertical speed of the guns is variable within the limits of 0 to 24 in./min (0 to 60 cm/min). The rotational speed of the tank is variable within the range from 0 to 2 rpm.

A one-man elevator is used to lift the gun operator as the spray gun is elevated. The gun operators must use air-breathing equipment to avoid breathing foam and solvent fumes. No other people are permitted inside the enclosure during the spray operation.

The spiral spray-foam technique is used to insulate bulkheads with a gun-and-track system similar to the vertical tool columns but positioned over the bulkhead. This approach utilizes two spray guns on oscillators attached to carriages. The carriages are moved from base to apex, at a given distance from the bulkhead surface, by a track-and-drive mechanism similar to a "welding skate." The traversing speed of the two guns is synchronized.

With gun material output, gun speed, and turntable rpm constant, the thickness of the applied foam would increase as the gun approaches the apex. Therefore, thickness in this area is controlled by varying the traversing speed of the spray gun and the turntable rpm simultaneously, which automatically varies the amount of foam deposited on a unit area of the substrate.

The rotational speed of the turntable, traversing speed of the spray guns, and remote controls for operation of the spray guns are controlled by a single operator at a station outside the spray booth.

This work was done by James M. Carter of Marshall Space Flight Center. For further information, including details of the foam application equipment, Circle 42 on the TSP Request Card.
MFS-23097

Radiographic Detection of Cracks

Inspectors can detect material cracks reliably, using X-ray radiography if beam parameters are optimized. Beam voltage, spot size, and beam divergence can be adjusted to enhance the radiographic image. When correct procedures are followed, cracks as small as 20 percent of the material thickness can be detected. (See page 380.)

Allowable Bending Loads for Mechanical Fasteners

The allowable bending loads for threaded bolts and other fasteners can be verified with a modified shear-loading setup. The effects of shear load, which normally complicate these measurements, are separated by an analysis of the interaction of shear with other loads. The test procedure is effective even when the specimen is small. (See page 373.)

Fast Thermal-Response Chamber

A new wall structure can keep chambers at constant, uniform temperature, yet allows them to be cooled rapidly if necessary. The wall structure, used in a fast-response cloud chamber, has a surface heater and a coolant shell separated by foam insulation. The wall is lightweight and requires relatively little power. (See page 342.)

Attaching Strain Gages by Ultrasonic Plastic Welding

Faster, simpler technique
requires no heat or adhesives.

Marshall Space Flight Center, Alabama

Ultrasonic plastic welding has been suggested as an improved method for bonding encapsulated strain gages to metallic surfaces. By applying pressure and ultrasound, reliable bonds may be produced within 3 to 6 seconds, without the application of heat. Presently, epoxy adhesives are used to attach the strain gages, but this method requires careful control of the ambient temperature and humidity as well as an extended curing cycle that can last several hours.

Ultrasonic plastic welding is an established method for structural bonding in the aerospace industry. In a typical configuration, electrical energy at 60 Hz is converted to electrical energy at 20,000 Hz and then to mechanical vibratory energy at 20,000 Hz. The mechanical energy

is transmitted through an ultrasonic horn. When the horn is adjacent to the parts to be welded, the vibratory energy sets up frictional forces in the joint area that cause local heating. The plastic melts, flows, and forms a permanent bond.

The most common injection-molded materials can be ultrasonically welded. Weldability depends on parameters such as melting temperature, the modulus of elasticity, the coefficient of friction, and thermal conductivity. Generally, the more rigid the plastic, the easier it is to weld. Low-modulus materials such as polyethylene and polypropylene can often be welded, provided the horn can be positioned close to the joint area.

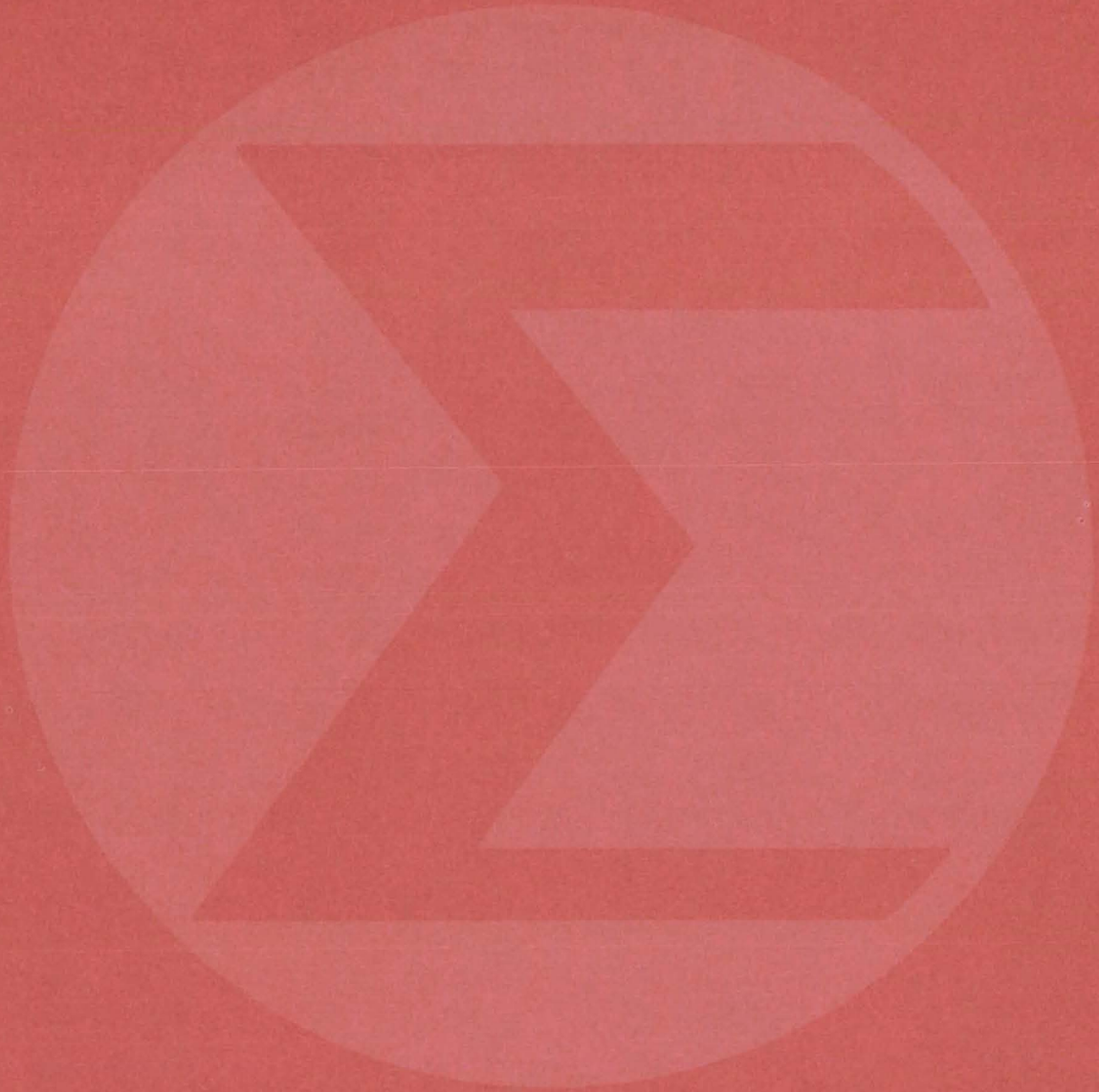
To bond the strain gage, the metal surface would be lightly abraded

(using 320-grit abrasive paper for example), degreased with a Freon solvent, and dried. The strain gage would then be taped into position with a layer of thermoplastic film between it and the surface. The application of pressure and ultrasonic energy for a short period would form the bond. The technique also might be used to simplify the curing of epoxy adhesives and for other attachment problems, such as bonding cryogenic temperature sensors to structural parts.

*This work was done by A. T. Sheppard and L. Silbert of Martin Marietta Corp. for **Marshall Space Flight Center**. For further information, Circle 43 on the TSP Request Card.*

MFS-23433

Mathematics and Information Sciences



Hardware, Techniques, and Processes

- 411 Programmable Convolution via the Chirp Z-Transform With CCD's
- 412 Edge-Following Algorithm for Tracking Geological Features
- 413 Classification Accuracy Improvement
- 414 Conditional Sampling Analysis for Turbulent Flows

Books and Reports

- 414 Reliability Analysis for Data Management Systems

Computer Programs

- 415 Vector Sweep
- 416 PERT TIME III
- 416 Document Retrieval and Reporting

Programable Convolution via the Chirp Z-Transform With CCD's

Programable filtering is done in the frequency domain instead of the time domain.

Langley Research Center, Hampton, Virginia

The transversal filtering operation is fundamental to many analog signal-processing functions. A promising solution to the problem of programable transversal filters is filtering by convolution in the frequency domain rather than in the time domain. The programable filtering is accomplished through the use of the chirp z-transform (CZT) with charge-coupled devices (CCD's).

The CZT is an algorithm for computing the discrete Fourier transform (DFT). The CZT gets its name from the fact that it can be implemented by premultiplying the time signal with a chirp (linear FM) waveform, filtering in a chirp convolution filter, and postmultiplying with a chirp waveform. Convolution can be achieved with the DFT, using the CZT algorithm, multiplying by the transform of the desired impulse response, and performing the inverse DFT. This is shown schematically in Figure 1. When the DFT is implemented, using the CZT, Figure 2 results. However, two of the multiplication operations "cancel", resulting in Figure 3.

The DFT can be performed using the CZT and employing either CCD's or acoustic surface-wave devices. However, the CZT lends itself naturally to implementation with CCD transversal filters. Although CCD technology is only about 5 years old, with further refinements with regard to modularity and on-chip multiplication of input/output data through the use of digital-to-analog multipliers, the CCD/CZT has the potential for

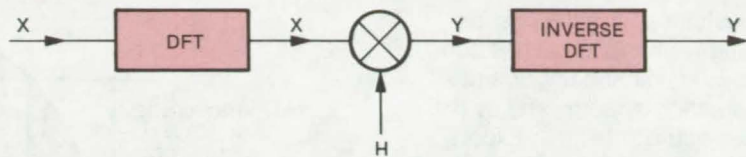


Figure 1. **Convolution Filtering** in the frequency domain can be performed using discrete Fourier transforms (DFT's). The time-domain signal is operated upon with the DFT and is multiplied by the transform of the desired impulse response (H). The signal is reconverted to the time domain by the inverse DFT.

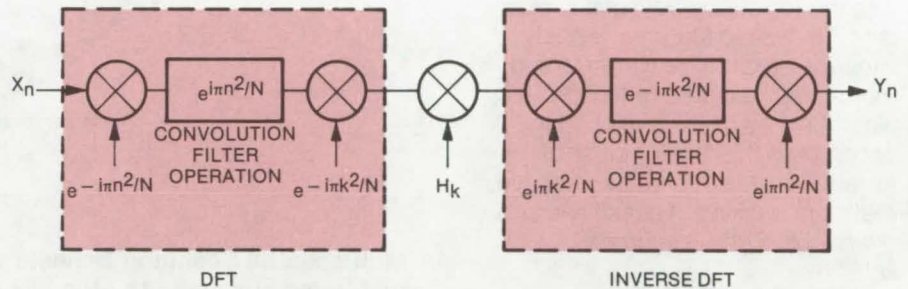


Figure 2. The **Chirp Z-Transform** can be used to compute the DFT in Figure 1. The time signal is multiplied by a linear FM waveform, filtered in a chirp convolution filter, and multiplied by another FM waveform. The inverse DFT is performed similarly.

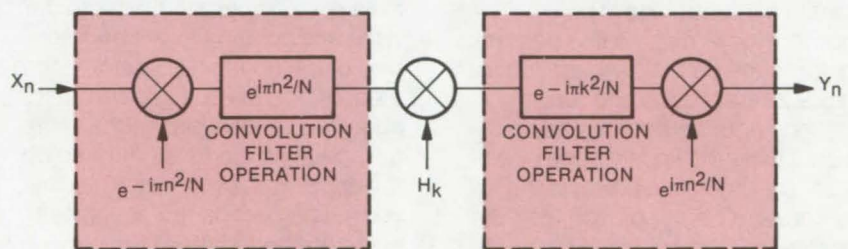


Figure 3. The **Reduced Expression** above derives from the expression in Figure 2. The multiplication operations commute, and the complex conjugates multiply to equal 1, or "cancel out."

becoming a general-purpose, standard, off-the-shelf component.

This work was done by Dennis D. Buss of Texas Instruments Inc. for **Langley Research Center**. For further information, Circle 44 on the TSP Request Card.

Title to this invention has been waived under the provisions of the National Aeronautics and Space Act [42 U.S.C. 2457(f)], to Texas Instruments, Inc., Dallas, Texas 75222. LAR-12109



Edge-Following Algorithm for Tracking Geological Features

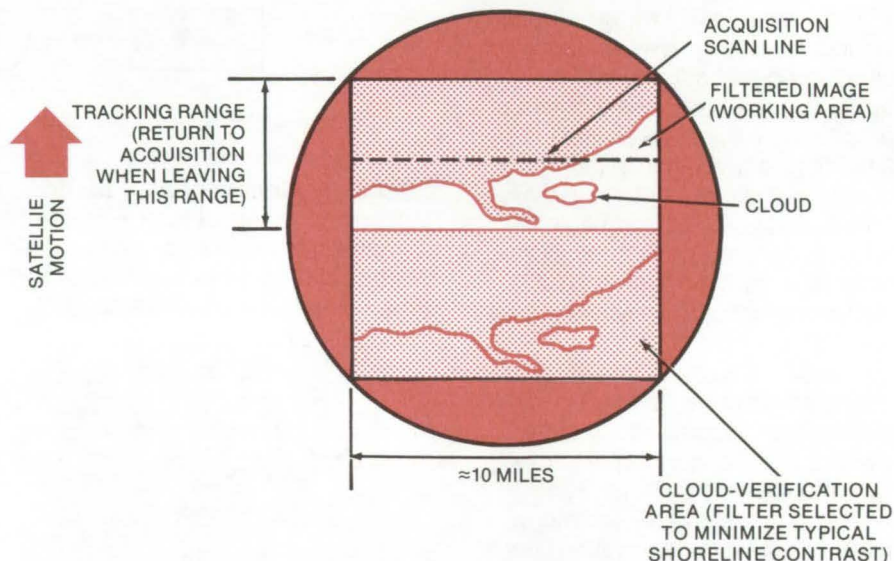
Geological patterns are detected and followed from Earth resources satellites.

Langley Research Center, Hampton, Virginia

The usefulness of satellites for monitoring water pollution has been limited by the pointing uncertainties of the detection systems and by the data rates of the satellites. Expensive, high-resolution cameras are required, and the vast quantities of imagery data generated require lengthy data reduction. A way to point satellite cameras at an area of interest accurately, while suppressing the registration of scenes that lack the desired features, would allow less-expensive cameras and more-simplified data reduction. An algorithm has been developed to accomplish this for one class of terrain features; it permits effective, real-time tracking of coastlines and rivers from Earth resources satellites.

The new development is a sequential edge-tracking algorithm employing circular scanning. It can be implemented with an image-dissector camera and a small quantity of electronics. The algorithm looks along a line perpendicular to the path of the satellite for a high-contrast edge and, upon detecting one, determines its orientation. Using the known edge orientation, the algorithm predicts the position of another point on the edge and moves to that point. If the camera is still on the edge, the process is repeated. The edge is tracked until the contrast becomes so low as to indicate that a coastline or river is no longer being tracked, or until the edge leaves the field of view of the detector. It then commences to search for a new edge.

A video camera scanning in a circular pattern over a high-contrast edge will generate a signal that will be, on first approximation, a periodic square wave having the same frequency as the scanning rate. Interpreting the fundamental-frequency sine and cosine coefficients of the Fourier-series expansion of the video signal as the



A Multispectral Scanning Scheme using two-color measurements with two filtered images of the same scene reduces data-reduction requirements. The upper image is used to identify the water/land interface, and the lower image emphasizes the cloud boundaries.

horizontal and vertical components of a vector results in the vector always being perpendicular to the edge and pointing to the brighter side of the edge. The vector length is greatest for sharp, high-contrast edges and is at a maximum when the scanning circle is centered on the edge. However, not all sharp, contrasting edges are coastlines; some are boundaries between forest and rock, desert and irrigated land, cloud and land, or cloud and water. The algorithm with the addition of optical filters to the scanning system, can distinguish between shorelines and other types of edges.

One multispectral scanning scheme is shown in the diagram; in this case a two-color measurement is made with one camera, and two filtered images of the same scene are provided. The upper image, with a 7,500-Å filter, distinguishes between water and land interfaces, since water reflects very little at this wavelength, thus providing high contrast at the land/water interface and therefore a long vector. The

lower image, with a 4,000-Å filter, minimizes the land/water interface, providing a short vector for these edges, thereby emphasizing the interface of cloud edges with the surface scene by not significantly affecting the cloud interface vector.

The edge-tracking algorithm, besides being useful as a geodesic, cartographic, and meteorological tool, might also be adaptable for the positioning of parts on an automated assembly line, the detection of flaws or other features of items on a conveyor belt, or in diagnostic medicine as a contour enhancement means for the analysis of thermographs or X-ray images.

This work was done by John C. Tietz of Martin Marietta Corp. for Langley Research Center. For further information, Circle 45 on the TSP Request Card.

Inquiries concerning rights for the commercial use of this invention should be addressed to the Patent Counsel, Langley Research Center [see page A8]. Refer to LAR-12051.

Classification Accuracy Improvement

Newly developed software significantly reduces multispectral processing time.

Langley Research Center, Hampton, Virginia

The processing system designed for the MIDAS (prototype Multivariate Interactive Digital Analysis System) program must process vast amounts of data obtained from multispectral sensors, such as those found on Skylab, ERTS, EOS, SEOS, and on several airborne systems. A major objective of the program is to minimize delays inherent in such processing systems and, essentially, to allow the operator to enter the system with a reel of tape and, in a short time, to obtain a color classification map of the area of interest.

An airborne scanner typically will gather data over a 20- to 30-mile (30- to 50-km) flight in about 15 minutes on one reel of magnetic tape. These data would currently require about 15,000 minutes of computer processing, or 6 weeks based on a 40-hour workweek. With one computer doing the processing, this aircraft could be used for only eight 15-minute sorties a year, which limitation is unacceptable. An

improvement made in the processing system effects higher accuracy in the classification of the pixels, resulting in a significantly-reduced processing time.

The classifier, which classifies the pixels into categories, executes a maximum-likelihood decision, assuming a multimodal Gaussian multivariate distribution. This assumption has been well justified by more than 100 experiments involving multispectral data. A digital implementation of the algorithms was chosen rather than analog or hybrid. The basic calculation to be performed is:

$$\ln\{pr(X)\}$$

where X is the input data vector (the vector of bytes in a pixel). The probability density function is Gaussian:

$$\ln\{pr(X)\}_i = -\frac{1}{2} \{(X - M_i)^T \Theta_i^{-1} (X - M_i) + \ln|\Theta_i| + n \ln(\pi/2)\}$$

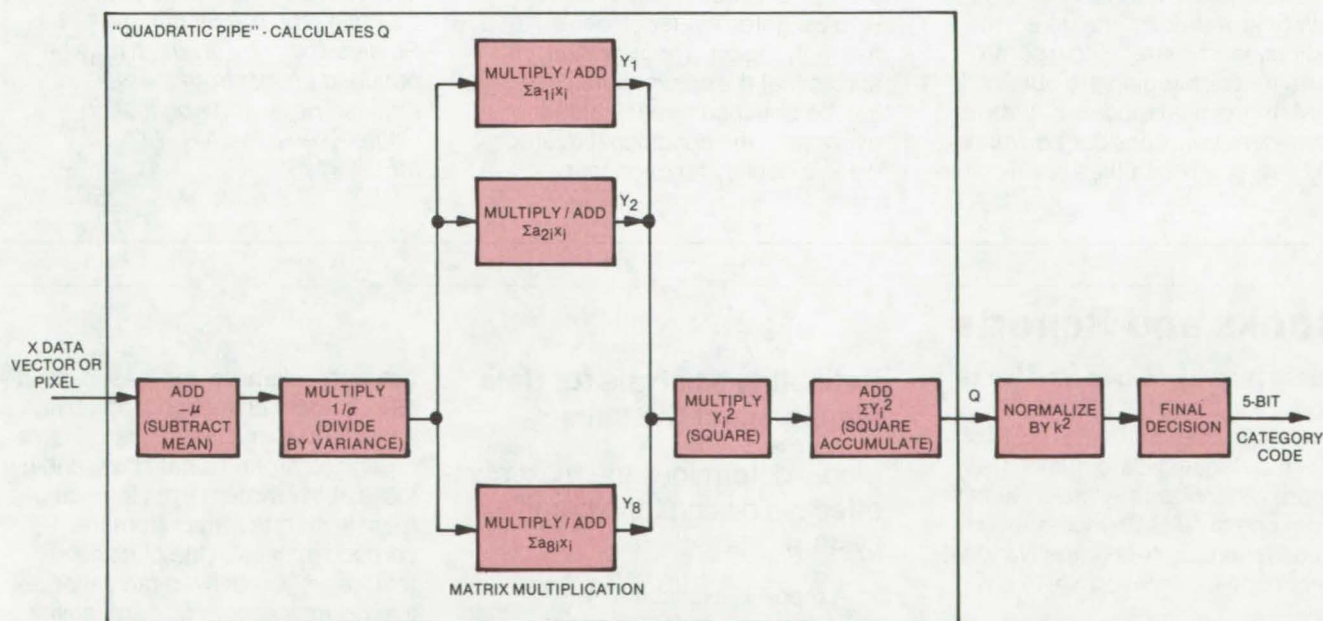
where vector M_i is the expected value of the X vector in category i ; Θ_i is the variance/covariance matrix for category i ; and n , called the number of channels, is the dimension of X , M , and Θ . With m being the number of categories into which the data can be classified, i ranges from 1 to m .

The most difficult calculation in the equation is the quadratic term:

$$Q_i = (X - M_i)^T \Theta_i^{-1} (X - M_i)$$

The classifier accepts each pixel, calculates Q , performs a normalization step, and then makes the final decision as to which, if any, of the categories the pixel belongs. The process is illustrated in the diagram. The organization of the "pipeline" was based upon the desired speed of calculation plus the available circuit hardware.

The shorter processing time effected by this improvement, in addition to increasing the allowable



The **MIDAS Classifier** is a processing scheme developed to reduce the computer time required to convert data from multispectral sensors into color classification maps. In the process, a Gaussian maximum-likelihood decision is made to divide the data pixel into categories. This decision requires the calculation of a quadratic term Q , described in the text. The scheme outlined above can help to reduce processing costs by a factor of 20.

(continued next page)

scanning time in flight, can reduce the processing costs considerably. This improvement to the present system can reduce processing costs by a factor of 20 or more and was designed to demonstrate that a better processing system will

materially assist in practical, economic realization of the benefits of remote sensing.

*This work was done by Roland Kistler and Frank Kriegler of the Environmental Research Institute of Michigan for **Langley Research***

Center. For further information, Circle 46 on the TSP Request Card. *Inquiries concerning rights for the commercial use of this invention should be addressed to the Patent Counsel, Langley Research Center [see page A8]. Refer to LAR-12102.*

Conditional Sampling Analysis for Turbulent Flows

Weighted averages are related to conventional averages for use in flow models.

Marshall Space Flight Center, Alabama

A new analysis of conditional sampling averages for turbulent flows shows how the conditional averages can be related to conventional averages and incorporated into existing flow models. The analysis thus allows the vast quantities of data generated by conditional sampling to be analyzed in a coherent way.

Conditional sampling measurements are usually made using two or more probes; one is a triggering probe, and the others are sampling probes. When a predetermined discriminating criterion is satisfied at the triggering probe, the electronics initiate sampling measurements at the other probes. In this way, the flow field is divided into different regions, and average flow parameters for each region are obtained.

Mathematical models of turbulent flows generally consider conventionally averaged quantities in which un-

weighted measurements are used. In these measurements, many of the details of the flow field that are present in the conditional averages are hidden.

The conditional time averages are obtained by using a weighting factor that takes different values depending on whether the discriminating criterion is satisfied. Thus, for example, the weighting factor might be "1" if the triggering probe is within a turbulent flow layer and "0" if it is outside. In this way, averages are biased in favor of measurements taken within the flow layer.

A complete set of conditional averages is collected by breaking the flow into infinitesimal regions, with weighted averages determined for each region. The new analysis shows that the conventional average can be obtained as a weighted average of the conditional averages, using a density function that

expresses the probability that the flow will be in each of the infinitesimal regions. Thus, the relationship between the two averages amounts to a second averaging process.

The concept is demonstrated for turbulent flow around a flat plate. Under certain conditions, approximations for the conditional averages can be made, and simplified relations for the second averaging can be obtained. Examples of the simplifications for special flows are given, in the documentation cited below.

*This work was done by F. C. Wang of **Marshall Space Flight Center.** Further information may be found in NASA TM-X-64886 [N74-34696], "On Conditional Sampling for Turbulent Flow Studies," a copy of which may be obtained at cost from the New England Research Application Center [see page A7]. MFS-23126*

Books and Reports

These reports, studies, and handbooks are available from NASA as Technical Support Packages (TSP's) when a Request Card number is cited; otherwise they are available from one of NASA's Industrial Application Centers or the National Technical Information Service.

Reliability Analysis for Data Management Systems

Model determines the most cost-effective design for a complex system.

A report is available that describes a new approach for modeling computer-controlled data management systems. The approach uses a computer model, and can determine the configuration with

optimum reliability and least cost. It differs from conventional reliability analysis in that it considers systems organized around a data bus, and it looks at the system from the equipment level rather than from the component level. One of its novel features is an ability to rank alternative designs according to reliability and cost. This is especially helpful if additional funds for improving reliability become available once a project has passed the initial design stage.

Data management systems that must function over long unattended periods are often too complex to be modeled directly from the component level. In addition, reliability data for each component are very often not available. Even if this approach can be applied, it cannot always determine the most cost-effective design if the system is very sophisticated.

The report gives a detailed description of the model, including its application to a 12-stage system for managing an unmanned 2-1/2 year mission. The system consists of a computer, a computer-interface unit, and 10 data-interface units, all communicating over a single data bus. It is required to have a reliability of 0.978 at the end of the mission.

Each stage may consist of any number of redundant units. An algorithm is used to determine the optimum redundancies that will meet the mission reliability requirements without adding unnecessarily to its cost.

The model generated a set of graphs showing how the various redundancy allocation sequences for the 12 stages compared in reliability and cost. The best design could be read directly from these graphs. A striking result of this analysis was that several of the more expensive configurations actually showed lower reliability, while other sequences gave only insignificant increases in reliability for large additional outlays.

Each item of equipment was also described by a failure-rate model, which assumed that its reliability decreased exponentially with time after a short "infant mortality period." A final wear-out period could also be included if necessary. The analysis determined the reliability of each possible system configuration as a function of time over the entire mission and calculated the mean time to failure, with and without the wear-out period.

*This work was done by Yao-Hui Huang of Sperry Support Services for **Marshall Space Flight Center**. To learn how to obtain a copy of the report, Circle 47 on the TSP Request Card.*
MFS-23208

Computer Programs

These programs may be obtained at very reasonable cost from COSMIC, a facility sponsored by NASA to make new programs available to the public. For information on program price, size, and availability, circle the reference letter on the COSMIC Request Card in this issue.

Vector Sweep

Calculating radiation of classical geometric shapes

The program Vector Sweep is a numerical procedure for calculating radiation/geometrical configuration factors and/or space-environmental heat-flux histories. It can accommodate complex systems of diverse geometric shapes residing in an unlimited variety of mutual shadowing conditions. The basic analytical device is a finite-difference employment of the unit-sphere method of calculating configuration factors. However, geometric profile boundaries and shadowing conditions are correctly recognized and quantified, virtually without limitation. An extension of the basic approach is combined with computational procedures of the Space Vehicle Radiant Energy Program (Saint Nero), a previously developed program, for

rapid calculation of space-environmental radiant-heat-flux histories in computations involving vehicle-induced shadowing.

The program employs a systematic procedure in which visible receiver geometries are searched out, projected on the base plane, integrated, and assigned appropriate configuration-factor values in a series of finite differential increments of base-plane angular displacement. Point configuration factors are thus accumulated in the process of rotating a cutting plane about the base-plane orthogonal. Moreover, the point configuration factors for all visible receiver geometries (or portions thereof) are simultaneously computed in a single 180° sweep of the cutting plane. Receiver profile boundaries and shadowing conditions are correctly recognized and accommodated without limitation.

Space-environmental heat-flux computations require that the pertinent space energy sources be located with respect to all emitter elemental areas and relocated at successive intervals of simulated flight time. The vehicle/Sun, vehicle/planet, and velocity vectors must therefore be represented in terms of coordinate systems originating at each emitter area element.

The vernal equinox is the common reference point employed for locating the Sun with respect to the planet and, subsequently, the vehicle with respect to the planet. Current provisions accommodate only the planet Earth, although the procedures in this program are generally applicable to any planet in the solar system.

Configuration, receiver, emitter, flight simulations, and space-heating options are provided as part of the computer program. This program has been designed to incorporate maximum versatility while imposing few demands on the engineering analyst. Input instructions are detailed and are accompanied by annotated master input formats. Printed output data are tabulated and labeled. Optional tape outputs are provided for selected computational and/or display purposes.

This program was developed on a CDC CYBER 70 computer and requires a minimum core requirement of 65K octal 60-bit words.

*This program was written by C. L. Moutrie and R. F. O'Neill of General Dynamics Corp. for **Lewis Research Center**. For further information, Circle E on the COSMIC Request Card.*
LEW-12281



PERT TIME III

Automated "Program Evaluation and Review Technique" system

PERT TIME III, a Program Evaluation Review Techniques system, is an automated aid for monitoring and scheduling the various activities within a particular project. It provides management with the means to evaluate accurately the status of a project and helps to control time, cost, and manpower. It will point up current and potential problem areas to allow adjustment, refinement, and rescheduling.

The PERT system utilizes a time-oriented network structure. The network represents the flow of work activities. Time estimates are created for the work elements of the network, and the flow between network elements is established. The time estimates, together with the data on network flow, are prepared as input to the system. The activities are read and linked together into paths. The start events and end events of the paths are found. Expected and allowed completion dates, slack time, and time remaining are computed for all uncompleted activities.

Errors such as looping paths, uncompleted activities followed by completed activities, uncompleted activities used as starts, and end events with no scheduled completion dates are identified and bypassed if possible. The activities of the project may be input entirely on cards or from cards and a tape or data cell generated by a previous run. Output is in the form of up to 21

fixed reports and up to 20 variable reports, schedule and resource plots, and an updated activity tape or data cell.

The network timespan is limited to a 30-year period from starting date to latest completion date. There can only be 500 starts for every 1,100 activities. One path cannot contain more than 700 branches, and the network cannot have more than 10,000 paths.

The minimum core required for the network is 52K octal plus 1K octal for each 230 activities or events. The system operates in batch mode, using the CDC FTN compiler, and has a plotting option, using a Calcomp or Varian.

*This program was written by the Systems Engineering Division of **Langley Research Center**. For further information, Circle F on the COSMIC Request Card. LAR-11887*

Document Retrieval and Reporting

Acquisition, storage, and retrieval of ASRES-ASRDI documents

This system of computer programs provides for the acquisition, storage, retrieval, and dissemination of information in the form of bibliographic citations of technical documents. The system, called ASRES (ASRDI Safety Reporting/Retrieval System), was developed by the NASA Aerospace Safety Research and Data Institute (ASRDI) for computerized management of aerospace-safety literature citations. The system should be applicable to any

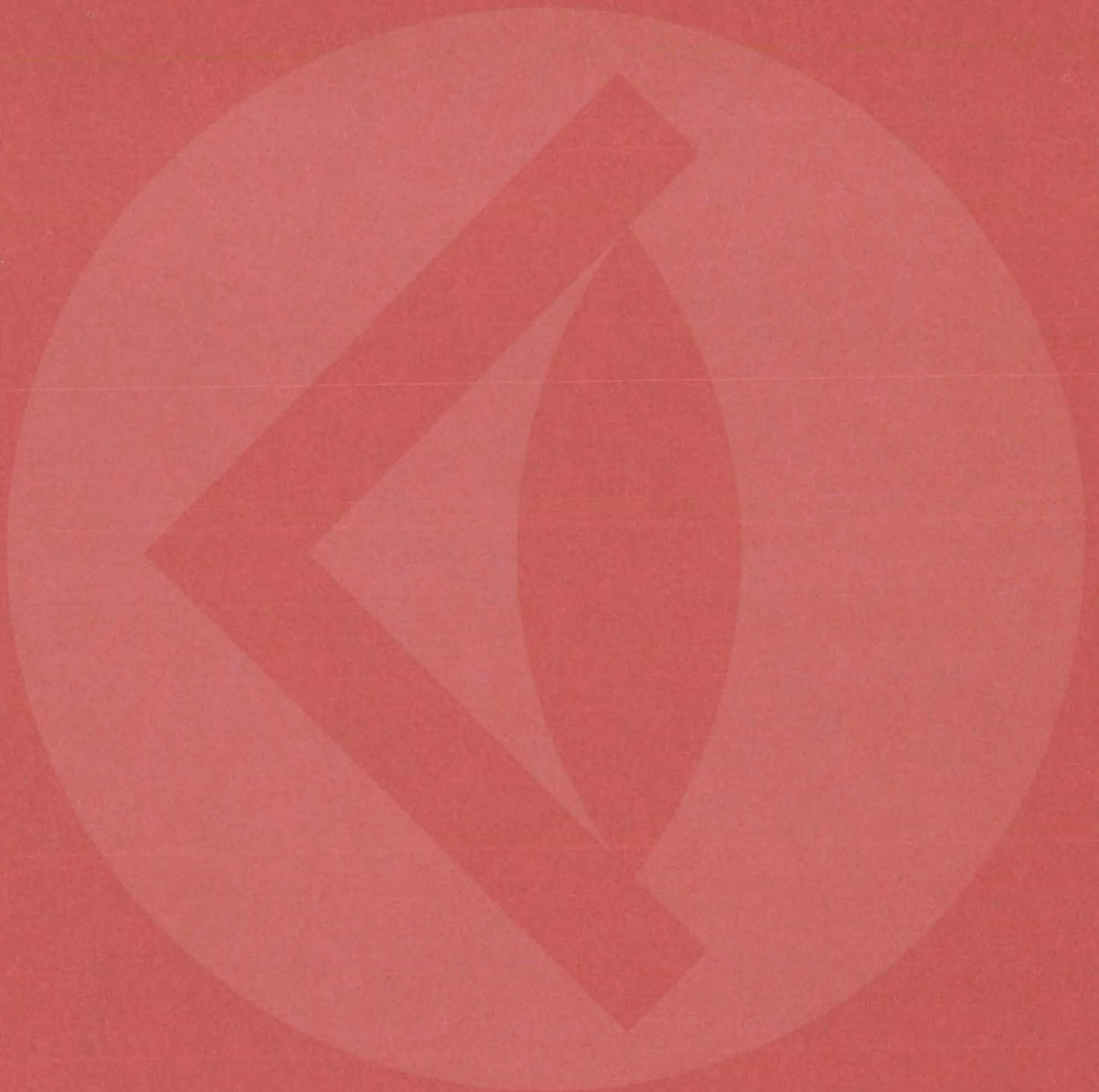
definable body of technical literature consisting of up to 32,750 citations. Persons with little or no computer experience can operate ASRES. Only a very basic understanding of data management, Boolean algebra, set theory, and the terms used in the indexes of the subject collection is necessary to use ASRES.

ASRES consists of five basic elements. First, all incoming data are inspected, discrepancies are reported, and errors are repaired. The data are converted to a highly usable format and placed into user accesses. The user can interactively search the data base and initiate retrieval of the desired information. The retrieved information is displayed in a format suitable for bibliographic publication. ASRES also provides for the retrieval of selected distribution lists that match the topic of the retrieved information. Unique features of the system include the retrieval on three levels of subject terms, including linked terms that increase the selectivity of the yield and user-controlled field expansion that allows indexes to be generated that specifically relate to sets of information.

ASRES is written in FORTRAN and was developed for the IBM 360/TSS (Time-Sharing System) with a central memory requirement of approximately 200K of 8-bit bytes. ASRES can accommodate only one user at a time and is not designed for simultaneous multiple-user access.

*This program was written by James J. Pelouch, Jr., of **Lewis Research Center**. For further information, Circle G on the COSMIC Request Card. LEW-12401*

SUBJECT INDEX



ACOUSTIC EXCITATION

Longitudinally-vibrating surgical microelectrode
page 364 NPO-13910

ACOUSTIC MEASUREMENTS

Doppler techniques for measuring fluid velocities
page 347 MFS-23289

ACOUSTICS

Ultrasonic detection of bearing defects
page 385 MFS-23446

ACTUATORS

Cost-effective actuator tester
page 381 MSC-16324

ADHESIVE BONDING

Attaching strain gages by ultrasonic plastic welding
page 408 MFS-23433

Interpreting honeycomb climbing-drum peel tests
page 375 MFS-23319

AEROSOLS

Portable aerosol-particle counter
page 346 LEW-12130

AIR POLLUTION

Dust-contamination monitor
page 338 MFS-23702

Portable aerosol-particle counter
page 346 LEW-12130

AIR TRAFFIC CONTROL

Analysis of aircraft motions
page 385 ARC-11132

AIRCRAFT ACCIDENT INVESTIGATION

Analysis of aircraft motions
page 385 ARC-11132

AIRCRAFT WAKES

Optical scanning system for laser velocimeter
page 335 LAR-12143

ALGORITHMS

Edge-following algorithm for tracking geological features
page 412 LAR-12051

Programable convolution via the chirp z-transform with CCD's
page 411 LAR-12109

ALKENES

Fire and acid-resistant polyamide fibers
page 353 MSC-16074

ALUMINUM

Tough strong iron alloys for cryogenic service
page 352 LEW-12726

ANALOG TO DIGITAL CONVERTERS

Inexpensive pulse-train converter measures analog voltage
page 305 LEW-12912

ANGIOGRAPHY

Real-time video display for angiocardigraphic studies
page 366 ARC-10985

ANTENNA ARRAYS

"Printed-circuit" rectenna
page 323 NPO-13886

ANTENNA DESIGN

Emergency-vehicle VHF antenna
page 325 MFS-23638

ANTIREFLECTION COATINGS

Low-reflection silicon solar cells
page 400 LEW-12418

Solar meter with silicon photocell
page 299 NPO-14136

APERTURES

Modular multiapertures for light sensors
page 403 MFS-23249

APPROXIMATION

Design of minimum-weight structures
page 387 LAR-11994/LAR-12209

ARC WELDING

Arc-starting aid for GTA welding
page 404 MSC-19495

AUDIO EQUIPMENT

Double-duty loudspeaker
page 312 MSC-16263

AUDIOLOGY

Hearing-aid tester
page 359 MSC-14916

AUTOMATIC TEST EQUIPMENT

Cost-effective actuator tester
page 381 MSC-16324

BALL BEARINGS

Restoration of bearings
page 404 LEW-12631

BANDPASS FILTERS

Extrasensitive phase-locked-loop circuit
page 307 MSC-16770

Op-amp gyrator simulates high Q inductor
page 318 MFS-23514

BATTERY CHARGERS

Multichannel implantable telemetry system
page 360 ARC-11079

BEARINGS

Ultrasonic detection of bearing defects
page 385 MFS-23446

BENDING

Allowable bending loads for mechanical fasteners
page 373 MFS-23430

BENDING MOMENTS

Interpreting honeycomb climbing-drum peel tests
page 375 MFS-23319

BIBLIOGRAPHIES

Document retrieval and reporting
page 416 LEW-12401

BINARY CODES

Changing NRZ data to biphasic logic
page 331 MSC-16688

BIOACOUSTICS

Hearing-aid tester
page 359 MSC-14916

BIOMETRICS

Batteryless implanted echosonometer
page 361 ARC-11035

Multichannel implantable telemetry system
page 360 ARC-11079

Real-time video display for angiocardigraphic studies
page 366 ARC-10985

BIOTELEMETRY

Multichannel implantable telemetry system
page 360 ARC-11079

BOLTS

Allowable bending loads for mechanical fasteners
Page 373 MFS-23430

BOOMS

Overhead-handling, universal-positioning device
page 392 MFS-23434

BORING MACHINES

Plaster core washout tool
page 394 MSC-16635

BOURDON TUBES

Prosthetic urinary sphincters
page 362 MFS-23717

BUBBLE TECHNIQUE

Bias-field equalizer for bubble memories
page 311 MFS-23189

BUS CONDUCTORS

Low-inductance bus lines
page 316 MSC-16730

CABLES

Low-inductance bus lines
page 316 MSC-16730

CAPACITORS

Capacitive connectors for digital-data lines
page 308 GSC-12238

Low-resistance current monitor
page 318 GSC-12278

CARDIOLOGY

Batteryless implanted echosonometer
page 361 ARC-11035

Real-time video display for angiocardigraphic studies
page 366 ARC-10985

CARRIAGES

High gantry for lifting and handling
page 395 GSC-12235

CASTS

Plaster core washout tool
page 394 MSC-16635

CAVITY RESONATORS

Changing Sunlight to microwaves: a concept
page 324 NPO-14068

CELLULOSE

Control of electro-osmotic flow
page 354 MFS-23554

CHANNELS [DATA TRANSMISSION]

Reliability analysis for data management systems
page 414 MFS-23208

CHARGE COUPLED DEVICES

Programable convolution via the chirp z-transform with CCD's
page 411 LAR-12109

CHEMILUMINESCENCE

Simplified ozone detection by chemiluminescence
page 351 LAR-11405

CHIRP

Programable convolution via the chirp z-transform with CCD's
page 411 LAR-12109

CHROMIUM ALLOYS

Effects of hydrogen on iron/nickel/cobalt alloy
page 355 MFS-23369

CIRCUIT BOARDS

Electrically-nonlinear composite material
page 355 NPO-13858

CIRCUIT BREAKERS

Versatile solid-state relay
page 304 MFS-23632

CLASSIFIERS

Classification accuracy improvement
page 413 LAR-12102

CLOCKS

Extrasensitive phase-locked-loop circuit
page 307 MSC-16770



CLOTHING

Liquid-circulating garment controls thermal balance
page 368 MSC-16727

CLOUD CHAMBERS

Fast-response cloud chamber
page 342 MFS-23588

COATING

Potting procedure for electronic components
page 406 MSC-16290

Uniform spray coating for large tanks
page 406 MFS-23097

Vacuum-assisted impregnation of materials
page 399 MSC-16785

CODING

Changing NRZ data to biphasic logic
page 331 MSC-16688

COLOR PHOTOGRAPHY

Laser produces color images from digital data
page 337 GSC-12198

COMMUNICATION CABLES

Low-inductance bus lines
page 316 MSC-16730

COMMUNICATION SATELLITES

Emergency-vehicle VHF antenna
page 325 MFS-23638

Satellite-based interference analyzer
page 326 GSC-12150

COMMUTATORS

Gearless speed-reduction motor
page 391 GSC-12138

COMPOSITE MATERIAL

Electrically-nonlinear composite material
page 355 NPO-13858

COMPRESSIBILITY

Compressibility measurement of fluid-system ullage
page 376 MSC-16640

COMPUTER STORAGE DEVICES

Bias-field equalizer for bubble memories
page 311 MFS-23189

CONDUCTORS

Capacitive connectors for digital-data lines
page 308 GSC-12238

CONTAMINANTS

Dust-contamination monitor
page 338 MFS-23702

CONTROL UNITS [COMPUTERS]

Reliability analysis for data management systems
page 414 MFS-23208

CONTROLLERS

Cost-effective actuator tester
page 381 MSC-16324

CONVOLUTION INTEGRALS

Programable convolution via the chirp z-transform with CCD's
page 411 LAR-12109

CORRELATION DETECTION

Extrasensitive phase-locked-loop circuit
page 307 MSC-16770

CORROSION PREVENTION

Vacuum-assisted impregnation of materials
page 399 MSC-16785

CORROSION RESISTANCE

Fire and acid-resistant polyamide fibers
page 353 MSC-16074

COSTS

PERT TIME III
page 416 LAR-11887

COUPLING CIRCUITS

Inexpensive pulse-train converter measures analog voltage
page 305 LEW-12912

CRACK INITIATION

Kinetic studies of stress-corrosion cracking
page 356 MFS-23259

Radiographic detection of cracks
page 380 MSC-16541

CRANES

Overhead-handling, universal-positioning device
page 392 MFS-23434

CREEP TESTS

Kinetic studies of stress-corrosion cracking
page 356 MFS-23259

CRYOGENICS

Tough strong iron alloys for cryogenic service
page 352 LEW-12726

CURRENT REGULATORS

Low-resistance current monitor
page 318 GSC-12278

Simple constant-current-regulated power supply
page 309 LEW-12894

CUTTERS

Plaster core washout tool
page 394 MSC-16635

CUTTING

Drilling technique for crystals
page 402 MFS-23580

DATA CONVERTERS

Changing NRZ data to biphasic logic
page 331 MSC-16688

DATA LINKS

Multichannel implantable telemetry system
page 360 ARC-11079

DATA REDUCTION

Edge-following algorithm for tracking geological features
page 412 LAR-12051

DATA STORAGE

Bias-field equalizer for bubble memories
page 311 MFS-23189

DATA TRANSMISSION

Capacitive connectors for digital-data lines
page 308 GSC-12238

Changing NRZ data to biphasic logic
page 331 MSC-16688

DEFECTS

Ultrasonic detection of bearing defects
page 385 MFS-23446

DEMODULATORS

Extrasensitive phase-locked-loop circuit
page 307 MSC-16770

DIFFERENTIAL THERMAL ANALYSIS

Fast-response cloud chamber
page 342 MFS-23588

DISPLACEMENT MEASUREMENT

Design of minimum-weight structures
page 387 LAR-11994/LAR-12209

DISPLAY DEVICES

Laser produces color images from digital data
page 337 GSC-12198

DOCUMENT STORAGE

Document retrieval and reporting
page 416 LEW-12401

DOCUMENTS

Document retrieval and reporting
page 416 LEW-12401

DOMESTIC SATELLITE COMMUNICATION SYSTEMS

Satellite-based interference analyzer
page 326 GSC-12150

DOPPLER EFFECT

Doppler techniques for measuring fluid velocities
page 347 MFS-23289

DRILLING

Drilling technique for crystals
page 402 MFS-23580

DRILLS

Plaster core washout tool
page 394 MSC-16635

DUST

Dust-contamination monitor
page 338 MFS-23702

ECHOCARDIOGRAPHY

Batteryless implanted echosonometer
page 361 ARC-11035

EDGES

Edge-following algorithm for tracking geological features
page 412 LAR-12051

ELECTRIC BATTERIES

Fireman's lamp
page 384 MFS-23783

ELECTRIC CONNECTORS

Capacitive connectors for digital-data lines
page 308 GSC-12238

ELECTRIC CONTACTS

Hall-effect toggle switch
page 300 MSC-16354

Individual control of relays in a matrix
page 302 NPO-14095

Magnetic rotary switch
page 301 MSC-16624

ELECTRIC DISCHARGE

Safe handling practices for electrostatic-sensitive devices
page 320 MSC-16642

ELECTRIC MOTORS

Gearless speed-reduction motor
page 391 GSC-12138

ELECTRIC POTENTIAL

Low-resistance current monitor
page 318 GSC-12278

ELECTRIC POWER PLANTS

"Solar ponds"
page 343 NPO-13581

ELECTRIC POWER SUPPLIES

Precision voltage source without precision parts
page 314 GSC-12182

Simple constant-current-regulated power supply
page 309 LEW-12894

ELECTRIC RELAYS

Individual control of relays in a matrix
page 302 NPO-14095

Versatile solid-state relay
page 304 MFS-23632

ELECTROCARDIOGRAPHY

Batteryless implanted echosonometer
page 361 ARC-11035

ELECTRODEPOSITION

Modular multiapertures for light sensors
page 403 MFS-23249

ELECTRODES

Longitudinally-vibrating surgical
microelectrode
page 364 NPO-13910

ELECTROENCEPHALOGRAPHY

Multichannel implantable telemetry system
page 360 ARC-11079

ELECTROFORMING

Modular multiapertures for light sensors
page 403 MFS-23249

ELECTROHYDRAULIC CONTROL

Cost-effective actuator tester
page 381 MSC-16324

ELECTROMAGNETIC INTERFERENCE

Satellite-based interference analyzer
page 326 GSC-12150

ELECTROMAGNETIC WAVE FILTERS

Op-amp gyrator simulates high Q inductor
page 318 MFS-23514

ELECTRON GUNS

Simple constant-current-regulated power
supply
page 309 LEW-12894

ELECTRONIC CONTROL

Versatile solid-state relay
page 304 MFS-23632

ELECTRONIC EQUIPMENT TESTS

Cost-effective actuator tester
page 381 MSC-16324

Hearing-aid tester
page 359 MSC-14916

Measuring solar-cell quality
page 371 NPO-14100

Solar-cell measurements in the field
page 372 NPO-14067

ELECTRONIC PACKAGING

Potting procedure for electronic components
page 406 MSC-16290

ELECTROPHORESIS

Control of electro-osmotic flow
page 354 MFS-23554

ELECTROPLATING

Modular multiapertures for light sensors
page 403 MFS-23249

ELECTROSTATIC CHARGE

Safe handling practices for electrostatic-
sensitive devices
page 320 MSC-16642

EMBEDDING

Potting procedure for electronic components
page 406 MSC-16290

ENCAPSULATING

Low-reflection silicon solar cells
page 400 LEW-12418

Potting procedure for electronic components
page 406 MSC-16290

ENERGY DISSIPATION

Liquid-circulating garment controls thermal
balance
page 368 MSC-16727

ENVIRONMENTAL MONITORING

Radiometer gives true absorption and
emission coefficients
page 339 NPO-13677

EROSION

Particle trajectories in radial-inflow turbines
page 386 LEW-12561

ETCHANTS OR ETCHING

Low-reflection silicon solar cells
page 400 LEW-12418

FAILURE ANALYSIS

Reliability analysis for data management
systems
page 414 MFS-23208

FASTENERS

Allowable bending loads for mechanical
fasteners
page 373 MFS-23430

FATIGUE [MATERIALS]

Ultrasonic detection of bearing defects
page 385 MFS-23446

FILTERS

Op-amp gyrator simulates high Q inductor
page 318 MFS-23514

FINITE DIFFERENCE THEORY

Vector sweep
page 415 LEW-12281

FINITE ELEMENT METHOD

Design of minimum-weight structures
page 387 LAR-11994/LAR-12209

FIRE FIGHTING

Fireman's lamp
page 384 MFS-23783

FLAME RETARDANTS

Fire and acid-resistant polyamide fibers
page 353 MSC-16074

FLOW DISTRIBUTION

Conditional sampling analysis for turbulent
flows
page 414 MFS-23126

Control of electro-osmotic flow
page 354 MFS-23554

FLOW MEASUREMENT

Conditional sampling analysis for turbulent
flows
page 414 MFS-23126

Optical scanning system for laser
velocimeter
page 335 LAR-12143

FLUID DYNAMICS

Doppler techniques for measuring fluid
velocities
page 347 MFS-23289

FLUIDS

Compressibility measurement of
fluid-system ullage
page 376 MSC-16640

FLUTTER

Inexpensive solid-state monitoring circuit
page 310 LEW-12848

FLUX QUANTIZATION

DC transformer uses magnetoresistors
page 313 MFS-23659

FOREST FIRE DETECTION

Radiometer gives true absorption and
emission coefficients
page 339 NPO-13677

FORMING TECHNIQUES

Modular multiapertures for light sensors
page 403 MFS-23249

FRONT CRANES

High gantry for lifting and handling
page 395 GSC-12235

GARMENTS

Cooling vest
page 364 MSC-16771

Liquid-circulating garment controls thermal
balance
page 368 MSC-16727

GAS FLOW

Instrument measures dynamic pressure
fluctuations
page 378 LEW-12808

GAS PRESSURE

Instrument measures dynamic pressure
fluctuations
page 378 LEW-12808

GAS TUNGSTEN ARC WELDING

Arc-starting aid for GTA welding
page 404 MSC-19495

GAS TURBINE ENGINES

Particle trajectories in radial-inflow turbines
page 386 LEW-12561

GAS-METAL INTERACTIONS

Effects of hydrogen on iron/nickel/cobalt
alloy
page 355 MFS-23369

GEODESY

Edge-following algorithm for tracking
geological features
page 412 LAR-12051

GRINDING [MATERIAL REMOVAL]

Restoration of bearings
page 404 LEW-12631

GROUND HANDLING

High gantry for lifting and handling
page 395 GSC-12235

GROUND SUPPORT EQUIPMENT

High gantry for lifting and handling
page 395 GSC-12235

GROUND-AIR-GROUND COMMUNICATIONS

Emergency-vehicle VHF antenna
page 325 MFS-23638

GYRATORS

Op-amp gyrator simulates high Q inductor
page 318 MFS-23514

HALL EFFECT

Hall-effect toggle switch
page 300 MSC-16354

Magnetic rotary switch
page 301 MSC-16624

HANDLING EQUIPMENT

Flat-package DIP handling tool
page 394 GSC-12201

High gantry for lifting and handling
page 395 GSC-12235

Overhead-handling, universal-positioning
device
page 392 MFS-23434

HEARING

Hearing-aid tester
page 359 MSC-14916

HEART DISEASES

Real-time video display for
angiocardigraphic studies
page 366 ARC-10985

HEAT FLUX

Vector sweep
page 415 LEW-12281

HEAT STORAGE

"Solar ponds"
page 343 NPO-13581

HEAT TRANSFER

Fast-response cloud chamber
page 342 MFS-23588



HEAT TREATMENT

Improved radiant-heat oven
page 383 MSC-16761

HEATING EQUIPMENT

Window-mounted auxiliary solar heater
page 344 MFS-23719

HELICAL ANTENNAS

Emergency-vehicle VHF antenna
page 325 MFS-23638

HIGH STRENGTH

Tough strong iron alloys for cryogenic service
page 352 LEW-12726

HIGH TEMPERATURE TESTS

Improved radiant-heat oven
page 383 MSC-16761

HOLDERS

Vacuum mounting for piezoelectric transducers
page 393 MSC-16480

HONEYCOMB STRUCTURES

Interpreting honeycomb climbing-drum peel tests
page 375 MFS-23319

HUMAN FACTORS ENGINEERING

Liquid-circulating garment controls thermal balance
page 368 MSC-16727

HUMAN TOLERANCES

Liquid-circulating garment controls thermal balance
page 368 MSC-16727

HYDRAULIC FLUIDS

Compressibility measurement of fluid-system ullage
page 376 MSC-16640

HYDROGEN EMBRITTLEMENT

Effects of hydrogen on iron/nickel/cobalt alloy
page 355 MFS-23369

ILLUMINATING

Fireman's lamp
page 384 MFS-23783

IMAGING TECHNIQUES

Laser produces color images from digital data
page 337 GSC-12198

IMPEDANCE MATCHING

Low-inductance bus lines
page 316 MSC-16730

IMPLANTED ELECTRODES [BIOLOGY]

Multichannel implantable telemetry system
page 360 ARC-11079

IMPREGNATING

Vacuum-assisted impregnation of materials
page 399 MSC-16785

INCONEL [TRADEMARK]

Effects of hydrogen on iron/nickel/cobalt alloy
page 355 MFS-23369

INDUCTION MOTORS

Gearless speed-reduction motor
page 391 GSC-12138

INDUCTORS

Op-amp gyrator simulates high Q inductor
page 318 MFS-23514

INFORMATION RETRIEVAL

Document retrieval and reporting
page 416 LEW-12401

INFRARED DETECTORS

Radiometer gives true absorption and emission coefficients
page 339 NPO-13677

INITIATORS [EXPLOSIVES]

Electrically-nonlinear composite material
page 355 NPO-13858

INKS

Inkjet color-printer control interface
page 327 LAR-12103

INSOLATION

Solar meter with silicon photocell
page 299 NPO-14136

INSULATION

Potting procedure for electronic components
page 406 MSC-16290

INTERFACES

Inkjet color-printer control interface
page 327 LAR-12103

INTERFACIAL TENSION

Interpreting honeycomb climbing-drum peel tests
page 375 MFS-23319

ION BEAMS

Ion-beam sputtering increases solar-cell efficiency
page 401 LEW-12895

IONIZATION CHAMBERS

Fast-response cloud chamber
page 342 MFS-23588

IRON ALLOYS

Effects of hydrogen on iron/nickel/cobalt alloy
page 355 MFS-23369

Tough strong iron alloys for cryogenic service
page 352 LEW-12726

KINETICS

Kinetic studies of stress-corrosion cracking
page 356 MFS-23259

LASER DOPPLER VELOCIMETERS

Doppler techniques for measuring fluid velocities
page 347 MFS-23289

Optical scanning system for laser velocimeter
page 335 LAR-12143

Portable aerosol-particle counter
page 346 LEW-12130

LIGHTING EQUIPMENT

Fireman's lamp
page 384 MFS-23783

LIQUID COOLING

Cooling vest
page 364 MSC-16771

Liquid-circulating garment controls thermal balance
page 368 MSC-16727

LOUDSPEAKERS

Double-duty loudspeaker
page 312 MSC-16263

LUBRICANTS

Compressibility measurement of fluid-system ullage
page 376 MSC-16640

LUMINOUS INTENSITY

Simplified ozone detection by chemiluminescence
page 351 LAR-11405

MACHINING

Drilling technique for crystals
page 402 MFS-23580

MAGNET COILS

Double-duty loudspeaker
page 312 MSC-16263

MAGNETIC DOMAINS

Bias-field equalizer for bubble memories
page 311 MFS-23189

MAGNETIC STORAGE

Bias-field equalizer for bubble memories
page 311 MFS-23189

MAGNETORESISTIVITY

DC transformer uses magnetoresistors
page 313 MFS-23659

MAGNETS

Magnetic rotary switch
page 301 MSC-16624

MANDRELS

Plaster core washout tool
page 394 MSC-16635

MANPOWER

PERT TIME III
page 416 LAR-11887

MATRICES [CIRCUITS]

Individual control of relays in a matrix
page 302 NPO-14095

MEMBRANE STRUCTURES

Design of minimum-weight structures
page 387 LAR-11994/LAR-12209

METAL FILMS

Capacitive connectors for digital-data lines
page 308 GSC-12238

METAL OXIDE SEMICONDUCTORS

Safe handling practices for electrostatic-sensitive devices
page 320 MSC-16642

METAL-GAS SYSTEMS

Effects of hydrogen on iron/nickel/cobalt alloy
page 355 MFS-23369

MICROCRACKS

Radiographic detection of cracks
page 380 MSC-16541

MICROELECTRONICS

"Printed-circuit" rectenna
page 323 NPO-13886

MICROPHONES

Instrument measures dynamic pressure fluctuations
page 378 LEW-12808

MICROWAVE TRANSMISSION

"Printed-circuit" rectenna
page 323 NPO-13886

MINORITY CARRIERS

Measuring solar-cell quality
page 371 NPO-14100

MOLDING MATERIALS

Plaster core washout tool
page 394 MSC-16635

MONITORS

Inexpensive solid-state monitoring circuit
page 310 LEW-12848

Low-resistance current monitor
page 318 GSC-12278

MOTORS

Gearless speed-reduction motor
page 391 GSC-12138

MULTISPECTRAL BAND SCANNERS

Edge-following algorithm for tracking geological features
page 412 LAR-12051

MULTISPECTRAL PHOTOGRAPHY

Classification accuracy improvement
page 413 LAR-12102

NICKEL

Tough strong iron alloys for cryogenic service
page 352 LEW-12726

NICKEL ALLOYS

Effects of hydrogen on iron/nickel/cobalt alloy
page 355 MFS-23369

NIOBIUM

Tough stron iron alloys for cryogenic service
page 352 LEW-12726

NOISE SPECTRA

Satellite-based interference analyzer
page 326 GSC-12150

NONAQUEOUS ELECTROLYTES

Fireman's lamp
page 384 MFS-23783

NONDESTRUCTIVE TESTS

Cost-effective actuator tester
page 381 MSC-16324

Hearing-aid tester
page 359 MSC-14916

Radiographic detection of cracks
page 380 MSC-16541

OILS

Compressibility measurement of fluid-system ullage
page 376 MSC-16640

OMNIDIRECTIONAL ANTENNAS

Emergency-vehicle VHF antenna
page 325 MFS-23638

OPERATIONAL AMPLIFIERS

Op-amp gyrator simulates high Q inductor
page 318 MFS-23514

OPTICAL DATA PROCESSING

Classification accuracy improvement
page 413 LAR-12102

Differential optical proximity detector
page 340 NPO-13939

OPTICAL EQUIPMENT

Differential optical proximity detector
page 340 NPO-13939

Laser produces color images from digital data
page 337 GSC-12198

OPTICAL MEASURING INSTRUMENTS

Differential optical proximity detector
page 340 NPO-13939

Faster optical-spectra recording and analysis
page 336 MSC-16729

OPTICAL RADAR

Multiline radar scan
page 330 MFS-23252

OPTICAL RANGE FINDERS

Differential optical proximity detector
page 340 NPO-13939

OPTICAL SCANNERS

Optical scanning system for laser velocimeter
page 335 LAR-12143

OSCILLATIONS

Inexpensive solid-state monitoring circuit
page 310 LEW-12348

OSCILLATORS

Extrasensitive phase-locked-loop circuit
page 307 MSC-16770

OSMOSIS

Control of electro-osmotic flow
page 354 MFS-23554

Ovens

Improved radiant-heat oven
page 383 MSC-16761

OXIDES

Ion-beam sputtering increases solar-cell efficiency
page 401 LEW-12895

OZONE

Simplified ozone detection by chemiluminescence
page 351 LAR-11405

OZONOMETRY

Simplified ozone detection by chemiluminescence
page 351 LAR-11405

PANELS

Design of minimum-weight structures
page 387 LAR-11994/LAR-12209

PARTICLE BEAMS

Portable aerosol-particle counter
page 346 LEW-12130

PARTICLE DENSITY (CONCENTRATION)

Portable aerosol-particle counter
page 346 LEW-12130

PARTICLE SIZE DISTRIBUTION

Portable aerosol-particle counter
page 346 LEW-12130

PARTICLE TRAJECTORIES

Particle trajectories in radial-inflow turbines
page 386 LEW-12561

PCM TELEMETRY

Multichannel implantable telemetry system
page 360 ARC-11079

PEELING

Interpreting honeycomb climbing-drum peel tests
page 375 MFS-23319

PERFORMANCE PREDICTION

Reliability analysis for data management systems
page 414 MFS-23208

PERMALLOYS [TRADEMARK]

Bias-field equalizer for bubble memories
page 311 MFS-23189

Pert

Pert time III
page 416 LAR-11887

PHASE LOCK DEMODULATORS

Extrasensitive phase-locked-loop circuit
page 307 MSC-16770

PHOTOGRAPHIC EQUIPMENT

Laser produces color images from digital data
page 337 GSC-12198

PHOTOGRAPHIC RECORDING

Laser produces color images from digital data
page 337 GSC-12198

PHOTOMETERS

Solar meter with silicon photocell
page 299 NPO-14136

PHOTOVOLTAIC CELLS

Solar-cell measurements in the field
page 372 NPO-14067

Solar meter with silicon photocell
page 299 NPO-14136

PICKOFFS

Bias-field equalizer for bubble memories
page 311 MFS-23189

PIEZOELECTRIC TRANSDUCERS

Vacuum mounting for piezoelectric transducers
page 393 MSC-16480

PINS

Allowable bending loads for mechanical fasteners
page 373 MFS-23430

PLASTERS

Plaster core washout tool
page 394 MSC-16635

PLASTIC COATINGS

Uniform spray coating for large tanks
page 406 MFS-23097

PLETHYSMOGRAPHY

Multichannel implantable telemetry system
page 360 ARC-11079

PLUNGERS

Flat-package DIP handling tool
page 394 GSC-12201

POLYAMIDE RESINS

Fire and acid-resistant polyamide fibers
page 353 MSC-16074

POROSITY

Vacuum-assisted impregnation of materials
page 399 MSC-16785

PORTABLE EQUIPMENT

Portable aerosol-particle counter
page 346 LEW-12130

Solar-cell measurements in the field
page 372 NPO-14067

POSITIONING

Overhead-handling, universal-positioning device
page 392 MFS-23434

POTTING COMPOUNDS

Potting procedure for electronic components
page 406 MSC-16290

POWER SUPPLY CIRCUITS

Low-inductance bus lines
page 316 MSC-16730

Precision voltage source without precision parts
page 314 GSC-12182

PRESSURE REDUCTION

Subsonic wind-tunnel performance
page 386 ARC-11138

PRESSURE SENSORS

Instrument measures dynamic pressure fluctuations
page 378 LEW-12808

PRESSURE WELDING

Attaching strain gages by ultrasonic plastic welding
page 408 MFS-23433

PRINTED CIRCUITS

"Printed-circuit" rectenna
page 323 NPO-13886

PRINTERS

Inkjet color-printer control interface
page 327 LAR-12103

PROBABILITY THEORY

Measurement of bit-error rate
page 328 MSC-12743

PROJECT MANAGEMENT

Pert time III
page 416 LAR-11887

PROSTHETIC DEVICES

Prosthetic urinary sphincters
page 362 MFS-23717



PROTECTIVE CLOTHING Cooling vest page 364	MSC-16771	Solar meter with silicon photocell page 299	NPO-14136	SCANNING Multiline radar scan page 330	MFS-23252
PROTECTIVE COATINGS Potting procedure for electronic components page 406	MSC-16290	RANDOM NOISE Measurement of bit-error rate page 328	MSC-12743	SCHEDULING PERT TIME III page 416	LAR-11887
Vacuum-assisted impregnation of materials page 399	MSC-16785	READERS Differential optical proximity detector page 340	NPO-13939	SEALERS Vacuum-assisted impregnation of materials page 399	MSC-16785
PROXIMITY Differential optical proximity detector page 340	NPO-13939	RECTIFIERS "Printed-circuit" rectenna page 323	NPO-13886	SEALING Potting procedure for electronic components page 406	MSC-16290
PSEUDONOISE Measurement of bit-error rate page 328	MSC-12743	REDUNDENCY Reliability analysis for data management systems page 414	MFS-23208	SEMICONDUCTOR DEVICES Hall-effect toggle switch page 300	MSC-16354
PUBLIC ADDRESS SYSTEMS Double-duty loudspeaker page 312	MSC-16263	REFLECTANCE Low-reflection silicon solar cells page 400	LEW-12418	Magnetic rotary switch page 301	MSC-16624
PULSE DURATION MODULATION Inkjet color-printer control interface page 327	LAR-12103	REFLECTORS Improved radiant-heat oven page 383	MSC-16761	Safe handling practices for electrostatic- sensitive devices page 320	MSC-16642
PULSE FREQUENCY MODULATION TELEMETRY Measurement of bit-error rate page 328	MSC-12743	RELIABILITY Reliability analysis for data management systems page 414	MFS-23208	SEMICONDUCTORS [MATERIALS] Ion-beam sputtering increases solar-cell efficiency page 401	LEW-12895
PYRANOMETERS Solar meter with silicon photocell page 299	NPO-14136	REMOTE SENSORS Classification accuracy improvement page 413	LAR-12102	SEPARATED FLOW Control of electro-osmotic flow page 354	MFS-23554
		Edge-following algorithm for tracking geological features page 412	LAR-12051	SERVOMECHANISMS Cost-effective actuator tester page 381	MSC-16324
RADAR DATA Analysis of aircraft motions page 385	ARC-11132	RESIN BONDING Attaching strain gages by ultrasonic plastic welding page 408	MFS-23433	SHEAR STRENGTH Allowable bending loads for mechanical fasteners page 373	MFS-23430
RADAR EQUIPMENT Multiline radar scan page 330	MFS-23252	RESISTANCE THERMOMETERS Multichannel temperature sensor page 382	MFS-23749	SHEAR STRESS Interpreting honeycomb climbing-drum peel tests page 375	MFS-23319
RADAR SCANNING Multiline radar scan page 330	MFS-23252	RESISTORS Low-resistance current monitor page 318	GSC-12278	SIGNAL TO NOISE RATIOS Measurement of bit-error rate page 328	MSC-12743
RADIAL FLOW Particle trajectories in radial-inflow turbines page 386	LEW-12561	RESTORATION Restoration of bearings page 404	LEW-12631	SILANES Control of electro-osmotic flow page 354	MFS-23554
RADIANT HEATING Improved radiant-heat oven page 383	MSC-16761	RIGID MOUNTING Vacuum mounting for piezoelectric transducers page 393	MSC-16480	SIMULATION Op-amp gyrator simulates high Q inductor page 318	MFS-23514
RADIATION DISTRIBUTION Vector sweep page 415	LEW-12281	ROLLER BEARINGS Restoration of bearings page 404	LEW-12631	SIMULATORS Cost-effective actuator tester page 381	MSC-16324
RADIATION MEASURING INSTRUMENTS Radiometer gives true absorption and emission coefficients page 339	NPO-13677	ROTATING DISKS Gearless speed-reduction motor page 391	GSC-12138	SINGLE CRYSTALS Drilling technique for crystals page 402	MFS-23580
RADIO FREQUENCY INTERFERENCE Satellite-based interference analyzer page 326	GSC-12150	ROTORS Gearless speed-reduction motor page 391	GSC-12138	SINTERING Electrically-nonlinear composite material page 355	NPO-13858
RADIO RELAY SYSTEMS Emergency-vehicle VHF antenna page 325	MFS-23638	SAMPLING Conditional sampling analysis for turbulent flows page 414	MFS-23126	SKY RADIATION Solar meter with silicon photocell page 299	NPO-14136
RADIO TELEMETRY Measurement of bit-error rate page 328	MSC-12743	SATELLITE ANTENNAS Satellite-based interference analyzer page 326	GSC-12150	SLITS Modular multiapertures for light sensors page 403	MFS-23249
RADIOGRAPHY Radiographic detection of cracks page 380	MSC-16541	SATELLITE SOLAR ENERGY CONVERSION Changing Sunlight to microwaves: a concept page 324	NPO-14068	SOLAR CELLS Ion-beam sputtering increases solar-cell efficiency page 401	LEW-12895
Real-time video display for angiocardiographic studies Page 366	ARC-10985	Differential optical proximity detector page 340	NPO-13939	Low-reflection silicon solar cells page 400	LEW-12418
RADIOMETERS Radiometer gives true absorption and emission coefficients page 339	NPO-13677			Measuring solar-cell quality page 371	NPO-14100
				Solar-cell measurements in the field page 372	NPO-14067

SOLAR COLLECTORS

Multichannel temperature sensor
page 382 MFS-23749

"Solar ponds"
page 343 NPO-13581

Window-mounted auxiliary solar heater
page 344 MFS-23719

SOLAR ENERGY

Ion-beam sputtering increases solar-cell
efficiency
page 401 LEW-12895

Low-reflection silicon solar cells
page 400 LEW-12418

Measuring solar-cell quality
page 371 NPO-14100

Solar meter with silicon photocell
page 299 NPO-14136

"Solar ponds"
page 343 NPO-13581

Solar-cell measurements in the field
page 372 NPO-14067

Window-mounted auxiliary solar heater
page 344 MFS-23719

SOLAR ENERGY CONVERSION

Changing Sunlight to microwaves: a concept
page 324 NPO-14068

Multichannel temperature sensor
page 382 MFS-23749

SOLAR HEATING

Window-mounted auxiliary solar heater
page 344 MFS-23719

SOLAR POWER SOURCES

Changing Sunlight to microwaves: a concept
page 324 NPO-14068

SOLAR RADIATION

Solar meter with silicon photocell
page 299 NPO-14136

SPATIAL FILTERING

Programmable convolution via the chirp
z-transform with CCD's
page 411 LAR-12109

SPECTRA

Faster optical-spectra recording and
analysis
page 336 MSC-16729

SPRAYING

Uniform spray coating for large tanks
page 406 MFS-23097

SPUTTERING

Ion-beam sputtering increases solar-cell
efficiency
page 401 LEW-12895

STATIC ELECTRICITY

Safe handling practices for electrostatic-
sensitive devices
page 320 MSC-16642

STATORS

Gearless speed-reduction motor
page 391 GSC-12138

STRAIN GAGES

Attaching strain gages by ultrasonic plastic
welding
page 408 MFS-23433

STRESS ANALYSIS

Design of minimum-weight structures
page 387 LAR-11994/LAR-12209

STRESS CORROSION CRACKING

Kinetic studies of stress-corrosion cracking
page 356 MFS-23259

STRESS WAVES

Ultrasonic detection of bearing defects
page 385 MFS-23446

STRUCTURAL DESIGN CRITERIA

Design of minimum-weight structures
page 387 LAR-11994/LAR-12209

STRUCTURAL WEIGHT

Design of minimum-weight structures
page 387 LAR-11994/LAR-12209

SUBSONIC WIND TUNNELS

Subsonic wind-tunnel performance
page 386 ARC-11138

SUPERCONDUCTING POWER**TRANSMISSION**

Changing Sunlight to microwaves: a concept
page 324 NPO-14068

SUPERCONDUCTIVITY

DC transformer uses magnetoresistors
page 313 MFS-23659

SURFACE FINISHING

Uniform spray coating for large tanks
page 406 MFS-23097

SURGICAL INSTRUMENTS

Longitudinally-vibrating surgical
microelectrode
page 364 NPO-13910

SURVIVAL EQUIPMENT

Fireman's lamp
page 384 MFS-23783

SWITCHES

Hall-effect toggle switch
page 300 MSC-16354

Magnetic rotary switch
page 301 MSC-16624

SWITCHING CIRCUITS

Precision voltage source without precision
parts
page 314 GSC-12182

Versatile solid-state relay
page 304 MFS-23632

SYNTHETIC FIBERS

Fire and acid-resistant polyamide fibers
page 353 MSC-16074

TELEVISION SYSTEMS

Real-time video display for
angiocardiographic studies
page 366 ARC-10985

TEMPERATURE CONTROL

Cooling vest
page 364 MSC-16771

Multichannel temperature sensor
page 382 MFS-23749

TEMPERATURE DISTRIBUTION

Multichannel temperature sensor
page 382 MFS-23749

TEMPERATURE GRADIENTS

Fast-response cloud chamber
page 342 MFS-23588

TEMPERATURE MEASURING

INSTRUMENTS
Multichannel temperature sensor
page 382 MFS-23749

TEMPERATURE SENSORS

Multichannel temperature sensor
page 382 MFS-23749

TENSILE STRENGTH

Allowable bending loads for mechanical
fasteners
page 373 MFS-23430

THERMAL CONTROL COATINGS

Fast-response cloud chamber
page 342 MFS-23588

THERMAL MAPPING

Radiometer gives true absorption and
emission coefficients
page 339 NPO-13677

THERMAL RESISTANCE

Fire and acid-resistant polyamide fibers
page 353 MSC-16074

THERMISTORS

Multichannel temperature sensors
page 382 MFS-23749

Radiometer gives true absorption and
emission coefficients
page 339 NPO-13677

THERMOREGULATION

Fast-response cloud chamber
page 342 MFS-23588

TIME

PERT TIME III
page 416 LAR-11887

TITANIUM

Tough strong iron alloys for cryogenic
service
page 352 LEW-12726

TOUGHNESS

Tough strong iron alloys for cryogenic
service
page 352 LEW-12726

TRAJECTORY ANALYSIS

Particle trajectories in radial-inflow turbines
page 386 LEW-12561

TRANSDUCERS

Multichannel implantable telemetry system
page 360 ARC-11079

TRANSFORMERS

DC transformer uses magnetoresistors
page 313 MFS-23659

TRANSISTOR LOGIC

Changing NRZ data to biphasic logic
page 331 MSC-16688

TRANSMISSION LINES

Low-inductance bus lines
page 316 MSC-16730

TRUSSES

Design of minimum-weight structures
page 387 LAR-11994/LAR-12209

TURBOFAN ENGINES

Instrument measures dynamic pressure
fluctuations
page 378 LEW-12808

TURBULENT FLOW

Conditional sampling analysis for turbulent
flows
page 414 MFS-23126

ULLAGE

Compressibility measurement of
fluid-system ullage
page 376 MSC-16640

ULTRASONIC RADIATION

Batteryless implanted echosonometer
page 361 ARC-11035

ULTRASONIC TEST

Ultrasonic detection of bearing defects
page 385 MFS-23446

Vacuum mounting for piezoelectric
transducers
page 393 MSC-16480



ULTRASONIC WAVE TRANSDUCERS

Batteryless implanted echosonometer
page 361 ARC-11035

ULTRASONIC WELDING

Attaching strain gages by ultrasonic plastic
welding
page 408 MFS-23433

URINATION

Prosthetic urinary sphincters
page 362 MFS-23717

VANADIUM

Tough strong iron alloys for cryogenic
service
page 352 LEW-12726

VECTOR ANALYSIS

Vector sweep
page 415 LEW-12281

VELOCITY MEASUREMENT

Doppler techniques for measuring fluid
velocities
page 347 MFS-23289

Optical scanning system for laser
velocimeter
page 335 LAR-12143

VESTS

Cooling vest
page 364 MSC-16771

VIBRATION

Longitudinally-vibrating surgical
microelectrode
page 364 NPO-13910

Ultrasonic detection of bearing defects
page 385 MFS-23446

VIDEO DATA

Real-time video display for
angiocardiographic studies
page 366 ARC-10985

VOLTAGE CONVERTERS (DC TO DC)

DC transformer uses magnetoresistors
page 313 MFS-23659

Inexpensive pulse-train converter measures
analog voltage
page 305 LEW-12912

Precision voltage source without precision
parts
page 314 GSC-12182

VOLTAGE GENERATORS

Precision voltage source without precision
parts
page 314 GSC-12182

VOLTAGE REGULATORS

Inexpensive pulse-train converter measures
analog voltage
page 305 LEW-12912

Precision voltage source without precision
parts
page 314 GSC-12182

VOLTMETERS

Inexpensive pulse-train converter measures
analog voltage
page 305 LEW-12912

VORTICES

Optical scanning system for laser
velocimeter
page 335 LAR-12143

WARNING SYSTEMS

Double-duty loudspeaker
page 312 MSC-16263

WATER POLLUTION

Edge-following algorithm for tracking
geological features
page 412 LAR-12051

WELDABILITY

Tough strong iron alloys for cryogenic
service
page 352 LEW-12726

WELDED JOINTS

Arc-starting aid for GTA welding
page 404 MSC-19495

WELDING MACHINES

Arc-starting aid for GTA welding
page 404 MSC-19495

WINCHES

Overhead-handling, universal-positioning
device
page 392 MFS-23434

WINDOWS [APERTURES]

Modular multiapertures for light sensors
page 403 MFS-23249

WIND TUNNEL MODELS

Subsonic wind-tunnel performance
page 386 ARC-11138

WIND TUNNEL NOZZLES

Subsonic wind-tunnel performance
page 386 ARC-11138

WIND TUNNEL TESTS

Subsonic wind-tunnel performance
page 386 ARC-11138

WORKING FLUIDS

Compressibility measurement of
fluid-system ullage
page 376 MSC-16640

X-RAY INSPECTION

Radiographic detection of cracks
page 380 MSC-16541

National Aeronautics and
Space Administration

Washington, D.C.
20546

Official Business
Penalty for Private Use \$300

SPECIAL FOURTH-CLASS RATE
BOOK

FOURTH-CLASS MAIL
POSTAGE & FEES PAID
NASA
WASHINGTON, D.C.
PERMIT No. G 27

NASA

*Space-technology experience was used to design
a weight-recording system for logging trucks.*

*Using this electronic measurement and
display system, truckers can maximize their
loads without exceeding highway weight limits.*

